

University of Sheffield

Growth Optimisation and Characterisation of III-Nitride Materials on Silicon Substrate

Xinchi Chen

A Thesis Submitted for the Degree of Doctor of Philosophy

in

Electronic and Electrical Engineering

at

University of Sheffield

Department of Electronic and Electrical Engineering

Centre for GaN Materials and Devices

Supervisor: Dr Ian Farrer

September 2024

Abstract

III-nitride semiconductors have been demonstrated to be a crucial component in the modern fabrication of advanced optoelectronics and are poised to spearhead a new revolution in general lighting, wearable devices, and microdisplay technologies. At present, III-nitride optoelectronic devices are primarily based on c-plane polar gallium nitride (GaN) grown on (0001) sapphire or silicon carbide (SiC) substrates. Over the past few decades, this technology has witnessed rapid development and unprecedented achievements. However, it also presents certain limitations and challenges. However, it also presents certain limitations and challenges associated with GaN-based technology. Furthermore, micro-light-emitting diodes (μ LEDs), as key components of microdisplay applications, require maintaining high brightness, high resolution, and high efficiency at extremely small dimensions. However, the performance of μ LEDs produced through conventional fabrication methods is limited due to the introduction of sidewall damage by the dry etching process.

The growth of high-quality GaN on Si substrates presents significant challenges due to the inherent properties of the materials. For instance, the lattice mismatch and differences in thermal expansion coefficients between Si and GaN can easily lead to cracking issues. Additionally, Si and GaN are prone to melt-back etching during high temperature growth. These issues represent major obstacles in the development of GaN on Si substrates. This study systematically investigates and optimizes the growth process of GaN on Si, starting from the initial substrate preparation to final GaN layer growth. Ultimately, it successfully achieves crack-free, high-quality GaN on (111) Si substrates.

The performance of optical and electrical device growth on GaN-on-Si template has also been investigated. It was discovered that InGaN/GaN multiple quantum wells (MQWs) structures grown on GaN-on-Si exhibit a significant discrepancy in their optical performance when compared to InGaN MQWs grown on sapphire under identical growth conditions. The indium (In) content in the two InGaN quantum wells (QWs) was found to be significantly different by X-ray diffraction (XRD) and its fitted curves. This discrepancy can be attributed to the differing internal stress states of the two kinds of templates, which lead to different amounts of In incorporation during the growth. Furthermore, a basic AlGaIn/GaN high electron mobility transistors (HEMTs) is grown on GaN-on-Si, and its characteristics are investigated.

This study also presents a selective epitaxial growth method for μ LEDs using prefabricated microarray templates. The μ LEDs were grown on GaN-on-Si template by this approach, and the key factors influencing the growth process were investigated and optimised. Furthermore, by utilizing a mixture of H_2/N_2 ambient gas instead of the original N_2 ambient gas during the growth of quantum barriers (QBs), and a comparison with the original growth method of MQWs, provided a valuable reference point for the fabrication of μ LEDs with longer emission wavelengths in the future.

Acknowledgements

To be honest, I never imagined that I would one day be writing this acknowledgment. After countless days and nights of dedication, I have finally completed my PhD thesis. It may not be outstanding, but it represents my utmost effort and marks the end of a long and arduous PhD journey. At this moment, as I sit in front of my computer reflecting on the past few years, I feel an unexpected sense of peace. This journey has been filled with numerous challenges, starting with the laboratory fire in my first year, followed by the COVID-19 lockdowns in my second year. Just as everything seemed to be getting back on track and I was ready to realize my aspirations, a series of unforeseen and uncontrollable events unfolded, once again shaking the stability I had only just regained. These setbacks nearly left me stranded at my lowest point, but fortunately, they are now part of the past.

Pursuing a PhD has not only been a test of endurance and resilience but also a process of growth and self-discovery. During these difficult times, I received a lot of support and encouragement from many people. Without their help, I might have succumbed to the difficulties long ago. Therefore, I would like to take this precious opportunity to express my deepest gratitude to everyone who has accompanied, supported, and helped me along this path.

First and foremost, I would like to extend my sincerest thanks to my supervisor, Dr. Ian Farrer. He is a knowledgeable, rigorous, and yet incredibly kind and humorous scientist. I will never forget the moment I first sat in his office, and he said to me, "I am happy to be your supervisor." At that time, I was struggling through the lowest point of my PhD journey, and he accepted me as his "senior" PhD student during that difficult period. Over the following days, he not only taught me numerous scientific skills but also showed me how to approach problems from a broader perspective. His guidance extended beyond academics, as he also cared for my personal well-being and mental health, helping me to alleviate anxiety and navigate through one challenge after another. Though our supervisor-student relationship did not span the entirety of my PhD, I am immensely grateful to have encountered such a "true" supervisor at a critical moment. Thank you. I would also like to express my gratitude to my second supervisor, Prof. Mark Hopkinson, for his invaluable support and assistance with experimental equipment.

My heartfelt thanks also go to Dr. Chenqi Zhu. He patiently taught me how to operate the MOCVD

and generously shared his valuable experience and insights into sample growth and scientific research. His patience and selflessness not only enabled me to master the MOCVD but also helped me grow into an independent researcher. I am also deeply grateful to my group members: Dr. Peng Feng, Dr. Ye Tian, Dr. Guillem Martínez de Arriba, Dr. Jack Haggar, Mr. Ce Xu, Ms. Rongzi Ni, Dr. Xiangyu He, and Dr. Rick Smith. Thank you all for your support and assistance throughout my PhD. I feel incredibly fortunate to have worked alongside such outstanding colleagues.

A special thanks goes to Mr. Stephen Atkin, Mr. Paul Haines, and the Technical Staff Group for their diligent management and maintenance of the cleanroom facilities, which provided us with a stable environment for our experiments. I would also like to thank the staff of the EEE Department and the Postgraduate Research Student Support Team (Jack, Luke, and Imogen) for their help and support when I was struggling. I would also like to acknowledge the former group members who briefly worked with me: Dr. Jiu Ling, Dr. Shuoheng Shen, Dr. Xuanming Zhao, Mr. Wei Zhong, and Mr. Zhiheng Lin. Thank you for your contributions during my PhD journey.

I cannot forget my friends who have been by my side all these years. Your company, encouragement, and support kept me hopeful and determined in moments of despair. My heartfelt gratitude to each of you.

Finally, I would like to express my deepest gratitude to my parents. Thank you for your understanding and patience during my vulnerable times. Your unconditional love and selfless support gave me the courage and strength to stand up again after every setback. Your encouragement has been the source of my perseverance and determination. Words cannot fully convey my appreciation for all you have done for me. Thank you for your unwavering support and love. I love you both deeply.

Last but not least, I want to thank myself. I have not always been strong, but I got through it. Thank you for not giving up. Thank you for not giving up. Everything will get better.

Xinchi Chen

Sheffield, UK

September 2024

List of Publications

- [1] C Zhu, C Xu, P Feng, **X Chen**, G M de Arriba, J Bai and T Wang, “A comparison study of InGaN/GaN multiple quantum wells grown on (111) silicon and (0001) sapphire substrates under identical conditions”, *Journal of Physics D: Applied Physics*, (2022)

- [2] Y Tian, P Feng, C Zhu, **X Chen**, C Xu, V Esendag, G Martinez de Arriba and T Wang, “Nearly Lattice-matched GaN Distributed Bragg Reflectors with Enhanced Performance”, *Materials* 15, 3536 (2022).

Content

ABSTRACT	I
ACKNOWLEDGEMENTS	III
LIST OF PUBLICATIONS	V
CONTENT	VI
LIST OF FIGURES	XI
LIST OF TABLES	XVIII
CHAPTER 1 INTRODUCTION	1
1.1 HISTORY AND DEVELOPMENT OF LIGHT EMITTING TECHNOLOGY	1
1.2 CURRENT CHALLENGES OF III-NITRIDES	7
1.2.1 <i>Epitaxial Substrate</i>	7
1.2.2 <i>Crystal Quality and Morphology</i>	10
1.2.3 <i>Quantum Confined Stark Effect</i>	10
1.2.4 <i>Efficiency Droop</i>	12
1.2.5 <i>Micro-LEDs and Micro-Display Applications</i>	13
1.3 MOTIVATION AND AIMS	15
1.4 THESIS ORGANIZATION.....	17
REFERENCES.....	19
CHAPTER 2 BACKGROUND	26
2.1 SEMICONDUCTORS.....	26
2.1.1 <i>Band Structure</i>	26
2.1.2 <i>P-Type and N-Type Doped III-nitride Semiconductors</i>	29
2.1.3 <i>Recombination</i>	30
2.1.4 <i>LED Structure</i>	32
2.2 III-NITRIDE SEMICONDUCTORS	34
2.2.1 <i>Crystal Structure of III-Nitrides</i>	35
2.2.2 <i>Defects in III-Nitrides</i>	38

2.2.3	<i>Material Properties of III-Nitrides</i>	40
2.2.4	<i>Alloys and Tunable Bandgaps</i>	42
2.2.5	<i>Internal Polarizations</i>	44
2.2.6	<i>High-Electron-Mobility Transistor (HEMT)</i>	49
2.3	III-NITRIDES ON SILICON SUBSTRATES.....	53
2.3.1	<i>Lattice Mismatch</i>	53
2.3.2	<i>Thermal Expansion Coefficient Mismatch</i>	54
2.3.3	<i>Melt-Back Etching</i>	55
	REFERENCE	57
CHAPTER 3 EXPERIMENTAL TECHNIQUES		62
3.1	PRE-GROWTH TREATMENT.....	62
3.1.1	<i>Template Cleaning</i>	62
3.1.2	<i>Photo-Enhanced Chemical Etching</i>	63
3.2	METAL-ORGANIC CHEMICAL VAPOUR DEPOSITION (MOCVD)	65
3.2.1	<i>Introduction</i>	65
3.2.2	<i>Basic Principles</i>	66
3.2.3	<i>Gas System</i>	69
3.2.4	<i>MO Source System</i>	72
3.2.5	<i>Reactor System</i>	76
3.2.6	<i>Reactor Exhaust System</i>	78
3.2.7	<i>In-situ Monitoring System</i>	79
3.3	CHARACTERISATION TECHNIQUES.....	84
3.3.1	<i>Nomarski microscopy</i>	84
3.3.2	<i>X-ray Diffraction (XRD)</i>	85
3.3.3	<i>Scanning Electron Microscopy (SEM)</i>	87
3.3.4	<i>Atomic Force Microscopy (AFM)</i>	89
3.3.5	<i>Photoluminescence (PL)</i>	90
3.3.6	<i>Confocal Microscopy</i>	91
3.4	FABRICATION TECHNIQUES	93

3.4.1	<i>Thin-Film Deposition</i>	93
3.4.2	<i>Photolithography</i>	94
3.4.3	<i>Dry Etching</i>	96
	REFERENCE	100
CHAPTER 4 OPTIMISATION OF C-PLANE GAN GROWTH ON (111) SILICON		103
4.1	INTRODUCTION	103
4.2	PRE-GROWTH TREATMENT OF (111) SILICON	106
4.2.1	<i>Chemical Treatment vs. High Temperature Annealing</i>	106
4.2.2	<i>Optimisation of High Temperature Annealing</i>	110
4.3	OPTIMISATION OF ALN BUFFER LAYER GROWTH	113
4.3.1	<i>The Initial Growth Process of AlN Layer</i>	113
4.3.2	<i>Optimisation of LT&HT-AlN Growth Temperature</i>	116
4.3.3	<i>Optimisation of HT-AlN Growth</i>	117
4.4	OPTIMISATION OF ALGAN BUFFER LAYER.....	120
4.5	OPTIMISATION OF GAN GROWTH	127
4.6	CONCLUSIONS	133
	REFERENCE	134
CHAPTER 5 COMPARATIVE STUDY OF GAN-BASED OPTICAL AND ELECTRICAL DEVICES ON SAPPHIRE AND SILICON.....		136
5.1	INTRODUCTION	136
5.2	COMPARISON STUDY OF C-PLANAR LED WITH INGAN/GAN MQWS ON (0001) SAPPHIRE AND (111) SI SUBSTRATES	139
5.3	INVESTIGATING THE EFFECT OF NH ₃ AMBIENT GAS IN COOLING ON THE OPTICAL PROPERTIES OF INGAN/GAN MQWS-BASED LEDs.....	148
5.4	GROWTH OF ALGAN/GAN HEMTs ON (111) SI	153
5.5	CONCLUSIONS	160
	REFERENCE	161
CHAPTER 6 COMPARATIVE STUDY OF GAN-BASED MICRO-LEDs ON SAPPHIRE		

AND SILICON BY DIRECT EPITAXIAL APPROACH	164
6.1 INTRODUCTION	164
6.2 DIRECT EPITAXIAL OVERGROWTH METHOD FOR III-NITRIDES MLEDs ON A PATTERNED TEMPLATE.....	167
6.3 DIRECT EPITAXIAL OVERGROWTH TO ACHIEVING INGAN/GAN MQWS-BASED MLEDs ON A PATTERNED TEMPLATE.....	170
6.3.1 <i>Investigation of the Initial n-GaN Layer in InGaN/GaN μLEDs on Patterned Templates</i>	170
6.3.2 <i>Effect of Final p-GaN Growth on the Optical Properties of InGaN/GaN μLEDs on Patterned Templates</i>	172
6.3.3 <i>Comparative Analysis of 5 μm InGaN/GaN μLEDs on Sapphire and Silicon by Confined Selective Epitaxial Overgrowth</i>	176
6.3.4 <i>Effect of μLED Dimensions on InGaN/GaN μLEDs Grown on (111) Silicon</i>	181
6.3.5 <i>Fill Factor Analysis of InGaN/GaN μLEDs on Silicon</i>	185
6.4 EFFECT OF H ₂ -DOPED QUANTUM BARRIERS OF INGAN/GAN MLEDs ON PATTERNED TEMPLATES.....	190
6.4.1 <i>Impact of H₂-Doped Quantum Barriers on the Optical Properties of 5 μm μLEDs on Sapphire and Silicon</i>	191
6.4.2 <i>Impact of H₂-Doped Quantum Barriers on Optical Properties of InGaN/GaN μLEDs on Silicon</i>	194
6.5 CONCLUSIONS	200
REFERENCE	202
CHAPTER 7 CONCLUSIONS AND FUTURE WORK.....	206
7.1 CONCLUSIONS	206
7.1.1 <i>Optimisation of GaN Growth on Silicon</i>	206
7.1.2 <i>Comparative Study of Optical and Electrical Devices on Sapphire and Silicon</i>	207
7.1.3 <i>Comparative Study of μLEDs on Sapphire and Silicon by Direct Epitaxial Approach</i>	207
7.2 FUTURE WORK	209

7.2.1	<i>Enhance Quality of GaN on (111) Si</i>	209
7.2.2	<i>Integration of μLEDs and HEMTs on Silicon Substrate</i>	209
7.2.3	<i>Selective Epitaxy of μLEDs on Patterned Templates</i>	210
7.2.4	<i>H₂-Dope MQWs Growth Method</i>	210

List of Figures

<i>Figure 1-1 Schematic diagram of the quantum-confined Stark effect (QCSE).</i>	11
<i>Figure 1-2 The external quantum efficiency of a Ga_{0.85}In_{0.15}N/GaN based LED as a function of injection current. Efficiency droop occurs when the injection current is above a threshold current. The dashed curve is the ideal external quantum efficiency for a droop-free LED [76].</i>	12
<i>Figure 2-1 The energy gaps of a metal, semiconductor, and insulator. E_g represents the bandgap energy, while E_f indicates the Fermi level.</i>	27
<i>Figure 2-2 Schematic diagram of photon emission and band structures in direct and indirect bandgap semiconductor materials</i>	28
<i>Figure 2-3 The three primary types of recombination process. (A) SRH, (B) Band-to-band, and (C) Auger recombination.</i>	30
<i>Figure 2-4 Schematic representation of (A) a p-n junction under forward bias; with an accompanying energy level diagram of a p-n junction under (B) zero bias, and (C) under forward bias conditions.</i>	33
<i>Figure 2-5 Bandgap and emission wavelength at room temperature plotted as a function of the lattice constant for common semiconductor materials. Reproduced with permission [17].</i> ...	34
<i>Figure 2-6 Schematic representation of the hexagonal wurtzite crystal structure of GaN.</i>	35
<i>Figure 2-7 Schematic representation of Bravais-Miller Index in hexagonal crystal structure.</i>	37
<i>Figure 2-8 Optical microscopy images of (A) Ga-polar GaN and (B) N-polar GaN.</i>	38
<i>Figure 2-9 Diagrammatic representation of typical point defects.</i>	39
<i>Figure 2-10 Diagrammatic representation of (A) an edge dislocation and (B) a screw dislocation.</i>	39
<i>Figure 2-11 Diagrammatic representation of the (A) normal stacking sequence and (A-E) various types of basal stacking faults (BSFs) in wurtzite III-nitride semiconductors.</i>	40
<i>Figure 2-12 (A) Spontaneous polarizations in III-nitrides (Al_xIn_yGa_(1-x-y)N) alloys according to a Vegard-like rule; (B) Piezoelectric coupling constants e₃₃ (squares) and e₃₁ (dots). Reproduced with permission [40].</i>	46

Figure 2-13 Schematic representation of the polarization orientation and band structure of (A) a polar, and (B) a non-polar InGaN/GaN quantum well.	47
Figure 2-14 Schematic diagram of AlGaIn/GaN HEMT on Silicon substrate with AlGaIn buffer layer.	51
Figure 2-15 Schematic diagrams of the atomic arrangement of (A) Si atoms on the (111) Si plane and (B) Ga atoms on the (0001) GaN plane.	54
Figure 2-16 Optical microscopy image of 1.4 μm cracked GaN layer grown on (111) Si substrate	55
Figure 2-17 Cross-sectional SEM images of melt-back etching between GaN and Si. Reproduced with permission [52].	56
Figure 3-1 Schematic diagram of the regular template cleaning procedure.....	63
Figure 3-2 the custom PEC etching system employed in this study.	63
Figure 3-3 Photograph of the (A) Aixtron 3 \times 2" flip-top CCS reactor system; and (B) Thomas-Swan 3 \times 2" vertical CCS reactor system.	65
Figure 3-4 The schematic of the Aixtron 3 \times 2" flip-top CCS reactor system; (A) gas mixing cabinet; (B) electrical cabinet; (C) glove box; (D) reactor cabinet; (E) load lock; (F) power supply cabinet.....	66
Figure 3-5 Schematic representation of the deposition process and surface reactions occurring during MOCVD growth.....	67
Figure 3-6 MegaTorr PS7-PD hydrogen gas purifier; (A) photograph; (B) schematic diagram. ...	70
Figure 3-7 The in-line hydrogen gas purifier; (A) photograph; (B) schematic diagram.....	71
Figure 3-8 Simple schematic diagram of the gas delivery system in an AIXTRON MOCVD system.	72
Figure 3-9 The schematic diagram of the MO source system.	73
Figure 3-10 (A) Photograph and (B) schematic diagram of the MOCVD bubbler.....	75
Figure 3-11 The basic configuration of the reactor system; (A) thermocouple; (B) tungsten heater; (C) showerhead; (D) reactor lid; (E) optical probe; (F) Showerhead water cooling; (G) double O-ring seal; (H) susceptor; (I) quartz liner; (J) susceptor support; (K) exhaust.	77

<i>Figure 3-12 Schematic of the cross-sectional configuration of the two-plenums showerhead.</i>	<i>77</i>
<i>Figure 3-13 Heater unit of the MOCVD system; (A) photo of tungsten heater; (B) heater coil zone schematic - (Red: Zone A; Orange: Zone B; Blue: Zone C).</i>	<i>78</i>
<i>Figure 3-14 The components of the reactor exhaust system; (A) mesh filter; (B) pall filter; (C) overview of EDWARDS M150 gas reactor column; (D) overview of the scrubber heater cell contained a gas reactor column cartridge.</i>	<i>79</i>
<i>Figure 3-15 (A) The ARGUS CCS system monitoring interface in Aixtron MOCVD system, and (B) the photograph of a 3x2" susceptor with the ring areas are ladled.</i>	<i>80</i>
<i>Figure 3-16 Typical interferogram record of the two-Step GaN growth (GaN-1 and GaN-2 part).</i>	<i>82</i>
<i>Figure 3-17 The fundamental principle of the Leytec Epicurve.</i>	<i>83</i>
<i>Figure 3-18 (A) Schematic illustration of a basic DIC system, and (B) the photograph of the Leica DMLM microscope system.</i>	<i>84</i>
<i>Figure 3-19 Schematic illustration of the X-ray diffraction with Bragg's law.</i>	<i>85</i>
<i>Figure 3-20 Photo of the Bruker D8 X-ray diffractometer.</i>	<i>86</i>
<i>Figure 3-21 (A) Schematic structure of an EBL-SEM system and (B) the photograph of a Raith 150 EBL series SEM system which used in this project. Adapted with permission [23].</i>	<i>87</i>
<i>Figure 3-22 (A) Schematic diagram of an AFM system and (B) the AFM system used in this project.</i>	<i>89</i>
<i>Figure 3-23 Schematic diagram of a custom-built PL system.</i>	<i>91</i>
<i>Figure 3-24 (A) Photograph of confocal microscopy system (WITec 300R) and (B) the schematic illustration of a confocal microscopy system.</i>	<i>92</i>
<i>Figure 3-25 (A) The photograph of Plasma-Therm 790 series PECVD system and (B) the schematic illustration of a PECVD system.</i>	<i>93</i>
<i>Figure 3-26 The equipment of the coating process; includes the spinner, timer and photoresist. ...</i>	<i>95</i>
<i>Figure 3-27 The Karl Suss MJB3 UV400 series mask aligner in yellow room.</i>	<i>96</i>
<i>Figure 3-28 (A) The photograph of Plasma-Therm Shuttlelock RIE system and (B) the schematic illustration of a RIE system.</i>	<i>97</i>

Figure 3-29 (A) The photograph of Oxford Instruments Plasmalab System 100 which used in this project and (B) the schematic illustration of a ICP system.	98
Figure 4-1 the optical microscope images of four samples (A, B, C, D) with different pre-treatment methods under two different annealing temperatures.	109
Figure 4-2 the Full-Width Half-Maximum (FWHM) values for (002) AlN vs. surface preparing annealing Time, which determined by Bruker X-ray diffraction rocking curve measurements.	112
Figure 4-3 Structure of AlN buffer layer on Si substrate.	114
Figure 4-4 The gas flow used for TMA and NH ₃ for the (A) NH ₃ nitridation and (B) TMA pre-flow method.	114
Figure 4-5 Relation between the 002 AlN FWHM values and the different growth temperature differences for the HT-AlN layers relative to the LT-AlN.	117
Figure 4-6 Structure of GaN on Si.	121
Figure 4-7 Optical microscopy images of Group A; (A ₁) 500nm AlGa _N ; (A ₂) 700nm AlGa _N and (A ₃) 800nm AlGa _N . The red line serves to highlight the cracks.	123
Figure 4-8 Optical microscopy images of Group B; AlGa _N layer with (B ₁) 29% Al content; (B ₂) 26% Al content and (B ₃) 22.5% Al content.	124
Figure 4-9 XRD ω -2 θ scan aligned on AlN of Sample B ₁ (red), B ₂ (blue) and B ₃ (green).	125
Figure 4-10 Optical microscopy images of Group C; (C ₁) 500nm AlGa _N with 29.5% Al; (C ₂) 700nm AlGa _N with 30% Al; (C ₃) 500nm AlGa _N with 26% Al; and (C ₄) 700nm AlGa _N with 26% Al.	125
Figure 4-11 the structure of GaN on Si with single AlGa _N layer and two-step undoped GaN layer.	128
Figure 4-12 the in-situ reflectance curve for the GaN growth part of Samples A (blue curve), B (red curve) and C (green curve).	129
Figure 4-13 Optical microscopy images at two magnifications of Samples A (A-1 & -2), B (B-1 & -2) and C (C-1 & -2).	130
Figure 4-14 (A) the in-situ reflectance for the GaN growth phase; and (B) the optical microscopy image of Sample D.	131

<i>Figure 4-15 Reflectance and curvature for the optimized growth process for GaN on Si(111). ...</i>	<i>132</i>
<i>Figure 5-1 Schematic diagram of InGaN/GaN MQWs structure with InGaN/GaN SLs on (A) GaN-on-Si template and (B) GaN-on-Sapphire template.</i>	<i>141</i>
<i>Figure 5-2 RT-PL spectra of MQWs on Si (sample A) and MQWs on sapphire (sample B).</i>	<i>142</i>
<i>Figure 5-3 the SEM images of (A) MQWs on Si template and (B) MQWs on sapphire template.</i>	<i>143</i>
<i>Figure 5-4 The RT-PL spectra of four samples (A-D).....</i>	<i>143</i>
<i>Figure 5-5 The XRD ω-2θ spectra and corresponding fitting curves for samples A (red) and B (blue). The satellite peaks of both SLs and MQWs are labelled in the figure.....</i>	<i>145</i>
<i>Figure 5-6 RT-PL spectra of Samples A, B, E and F, under the same the intensity scale.</i>	<i>149</i>
<i>Figure 5-7 The XRD ω-2θ spectra and corresponding fitting curves for samples E and F. The satellite peaks of both SLs and MQWs are labelled in the figure.....</i>	<i>150</i>
<i>Figure 5-8 Schematic of an AlGaIn/GaN HEMT structure on (111) Si substrate with an AlN interlayer.</i>	<i>154</i>
<i>Figure 5-9 Cross-sectional SEM image of an AlGaIn/GaN HEMT on (111) Si with an AlN interlayer.</i>	<i>155</i>
<i>Figure 5-10 XRD results of sample GN4337: (A) ω-2θ scan, the important peaks are labelled; XRD rocking curves of (B) (002) AlN, (C) (002) GaN, and (D) (102) GaN.</i>	<i>156</i>
<i>Figure 5-11 Electron channelling contrast image of GN4337. The image shows dislocations (spots with black-white contrast) and atomic steps (lines).....</i>	<i>158</i>
<i>Figure 5-12 Flow chart of standard fabrication process for GaN-HEMT.</i>	<i>158</i>
<i>Figure 5-13 (A) Optical image of the HEMT device H457C - (GN4337 after device); (B) Current-voltage (I-V) characteristics as a function of gate voltage.</i>	<i>159</i>
<i>Figure 6-1 SEM image of the size comparison between Mini LED and Micro LED chips [1].....</i>	<i>165</i>
<i>Figure 6-2 Comparative schematic cross-sections of display technologies: (A) TFTLCD, (B) OLED, and (C) MicroLED, illustrating the key layers and components in each technology.....</i>	<i>165</i>
<i>Figure 6-3 Schematic illustration of the preparation process for the μLED patterned template and the confined selective epitaxial overgrowth of μLEDs on the patterned template. (A) Growth of a standard GaN layer on the substrate; (B) Deposition of the SiO₂ layer; (C) Photolithography</i>	

and ICP etching; and (D) Selective epitaxial overgrowth of μ LEDs.	168
Figure 6-4 Structure schematic of (A) patterned template after overgrowth; (B) the single μ LED unit without the initial n-GaN and (C) the single μ LED unit with the initial n-GaN.	171
Figure 6-5 the standard room-temperature PL spectra of Sample A (without initial n-GaN layer) and the Sample B (with initial n-GaN layer).....	172
Figure 6-6 SEM images of GN4115: (A) top view and (B) cross-section; GN4116: (C) top view and (D) cross-section; and GN4117: (E) top view and (F) cross-section.	174
Figure 6-7 the standard room-temperature PL spectra of GN4115, GN4116 and GN4117 with different TMG flow rates for final p-GaN growth.	175
Figure 6-8 Structure schematic of (A) patterned template before overgrowth; (B) overgrown μ LEDs and (C) single μ LED unit with 5 pairs SLs and 30 pairs MQWs.	178
Figure 6-9 Plan view SEM images of (A) Sample A: 5 μ m LEDs on (0001) sapphire and (B) Sample B: 5 μ LEDs on (111) Si.....	178
Figure 6-10 Standard RT-PL spectra of 5 μ m μ LEDs on sapphire template (AX161A) and the 5 μ m μ LEDs on silicon template (AX161B).	179
Figure 6-11 the XRD results of (A) AX161A - sapphire substrate, and (B) AX161B- silicon substrate with (002) GaN and (102) GaN.	179
Figure 6-12 Schematic of a 2-inch μ LED patterned template (Si substrate) with three different dimensions.....	181
Figure 6-13 Optical images of the patterned template (Si substrate) with three different μ LED dimensions: (A) 5 μ m, (B) 10 μ m, and (C) 20 μ m, along with the corresponding SEM images after overgrowth: (D) 5 μ m, (E) 10 μ m, and (F) 20 μ m.	182
Figure 6-14 (A) RT-PL spectra of μ LEDs on Si templates with dimensions of 5 μ m, 10 μ m, and 20 μ m; and (B) a zoomed-in view of the PL spectrum for the 5 μ m μ LED.	183
Figure 6-15 RT-PL spectra of μ LEDs on the control group (sapphire template) with dimensions of 5 μ m, 10 μ m, and 20 μ m.	184
Figure 6-16 Optical microscopy images of the two μ LED patterned templates (before overgrowth) with different fill factor. (A) AX161B with fill factor of 22.9%; (B) AX161C with fill factor of 6.5%.	186
Figure 6-17 SEM top-view images of two μ LED samples (after overgrowth) with two fill factors: (A)	

<i>AX161B with a fill factor of 22.9% and (B) AX161C with a fill factor of 6.5%.....</i>	<i>187</i>
<i>Figure 6-18 (A) RT-PL spectra of AX161B and AX161C; and (B) the zoomed-in PL spectrum of AX161C.....</i>	<i>187</i>
<i>Figure 6-19 The XRD ω-2θ spectra for samples AX161B and AX161C. (A) and (B) the fast scan of AX161B and AX161C; (C) and (D) the slow scan of AX161B and AX161C.....</i>	<i>188</i>
<i>Figure 6-20 SEM cross-section images of (A) AX161B; FF: 22.9% and (B) AX161C; FF: 6.5%.</i>	<i>189</i>
<i>Figure 6-21 RT-PL spectra of (A) AX161A, (B) AX161B, (C) AX162A, and (D) AX162B μLEDs with different QB growth conditions and substrates.</i>	<i>192</i>
<i>Figure 6-22 SEM top-view images of 5μm μLEDs with different substrates and quantum barrier growth conditions after overgrowth: (A) AX161A (sapphire, N₂), (B) AX161B (silicon, N₂), (C) AX162A (sapphire, H₂/N₂), and (D) AX162B (silicon, H₂/N₂).</i>	<i>193</i>
<i>Figure 6-23 SEM images of μLEDs grown on silicon substrates with different QB conditions and fill factors (FF): (A) AX161B (N₂, 22.9%), (B) AX161C (N₂, 6.5%), (C) AX162B (H₂/N₂, 22.9%), and (D) AX162C (H₂/N₂, 6.5%)......</i>	<i>196</i>
<i>Figure 6-24 RT-PL spectra of μLEDs grown on silicon substrates with different QB conditions and fill factors (FF): (A) AX161B (N₂, 22.9%), (B) AX161C (N₂, 6.5%), (C) AX162B (H₂/N₂, 22.9%), and (D) AX162C (H₂/N₂, 6.5%)......</i>	<i>197</i>
<i>Figure 6-25 SEM images of μLEDs with different dimensions (5 μm, 10 μm, 20 μm) grown on silicon substrates under different QB conditions: (A-C) AX161C with N₂ QB, and (D-F) AX162C with H₂/N₂ QB.</i>	<i>198</i>
<i>Figure 6-26 RT-PL spectra of μLEDs with different dimensions (5 μm, 10 μm, 20 μm) grown on silicon substrates under different QB conditions: (A-C) AX161C with N₂ QB, and (D-F) AX162C with H₂/N₂ QB.....</i>	<i>198</i>

List of Tables

<i>Table 1-1 Physical properties and typical prices for 2-inch wafers of various substrate materials commonly used in growth of III-nitrides [44, 45, 49-52].</i>	8
<i>Table 1-2 Representative works from different research institutes on stress control methods, thickness and crystal quality of GaN epitaxial layers on silicon substrates.</i>	9
<i>Table 1-3 Comparison of Key Characteristics Among Micro-LED, LCD, and OLED Technologies [78].</i>	13
<i>Table 2-1 Crystal parameters of wurtzite structure III-nitrides [22-25].</i>	36
<i>Table 2-2 Electrical and thermal properties of common semiconductor materials at 300K [1, 28-35].</i>	41
<i>Table 2-3 Band gaps and corresponding emission wavelengths of typical III-nitride materials [37].</i>	44
<i>Table 2-4 Normalized figures of merit (JFoM and BFoM) of common semiconductor materials [49].</i>	50
<i>Table 3-1 The Parameters of Common MO Bubblers [13-16].</i>	75
<i>Table 4-1 the annealing perimeters of Samples A, B, C and D.</i>	108
<i>Table 4-2 The annealing parameters of samples A, B, C, D and E, under the reactor pressure of 86 mbar and annealing temperature of 1340 °C.</i>	111
<i>Table 4-3 the (002) AlN FWHM values, mean values and standard deviation of samples by two different initial processes, group A: NH₃ nitridation; group B: TMA pre-flow.</i>	115
<i>Table 4-4 The growth conditions of AlN layer by LT&HT method.</i>	116
<i>Table 4-5 the growth parameters of two different HT-AlN growth methods.</i>	118
<i>Table 4-6 the (002) AlN FWHM values of samples by two different HT-AlN growth methods.</i>	119
<i>Table 4-7 Growth Conditions of AlGaIn Buffer Layer in Different Groups.</i>	122
<i>Table 4-8 Growth conditions of GaN-1 and GaN-2 layer.</i>	128
<i>Table 5-1 the MQWs emission wavelength and FWHM of four samples A, B, C and D.</i>	144

<i>Table 5-2 the parameters of Samples A and B, inclusive of the Indium content, InGaN quantum well thickness and GaN barrier thickness of both SLs and MQWs</i>	<i>146</i>
<i>Table 5-3 the template type, cooling ambient, MQWs emission wavelength, and FWHM of Samples A, B, E and F</i>	<i>149</i>
<i>Table 5-4 the parameters of Samples A, B, E and F, inclusive of the Indium content, InGaN quantum well thickness and GaN barrier thickness of both SLs and MQWs</i>	<i>151</i>
<i>Table 5-5 FWHM Values of Sample GN4337; Including (102) AlN, (002) GaN and (102) GaN.</i>	<i>156</i>
<i>Table 5-6 FWHM values and corresponding calculated screw and edge dislocation densities for the (002) and (102) GaN reflections in samples GN4337.</i>	<i>157</i>
<i>Table 6-1 Growth conditions of p-GaN layers for three samples; including growth temperature, reactor pressure, TMG and NH₃ flow rate.</i>	<i>173</i>
<i>Table 6-2 FWHM values and corresponding calculated screw and edge dislocation densities for the (002) and (102) GaN reflections in samples AX161A and AX161B.</i>	<i>180</i>
<i>Table 6-3 The parameters of both μLED patterned templates.</i>	<i>186</i>
<i>Table 6-4 Overview of sample parameters, including substrate type, μLED dimensions, QB growth ambient gas, and NH₃ flow rate.</i>	<i>191</i>
<i>Table 6-5 Overview of μLED Samples with Different Dimensions, Fill Factors and Quantum Barrier (QB) Growth Conditions on Silicon Substrates.</i>	<i>195</i>

Chapter 1 Introduction

1.1 History and Development of Light Emitting Technology

Since our early human ancestors discovered how to make fire by drilling into wood [1], the lighting technology of human society has experienced a period of evolution from primitive flame to oil lamps, and then to electric lighting. From the discovery of the electroluminescent phenomenon of silicon carbide (SiC) in 1907 to the breakthrough of blue LEDs in 1994, the LED technology has undergone nearly a century of evolution [2].

Discovery and Application of III-V Compounds

In 1907, English scientist Henry Joseph Round discovered that applying a voltage between two contacts of SiC crystals could emit yellow light, which constituted the earliest recorded phenomenon of electroluminescence [3]. In 1936, Georges Destriau from France discovered that zinc sulphide (ZnS) powder emitted light without electrical charge, and first proposal of the term "electroluminescence" (EL) to describe this phenomenon. Given that SiC is a wide bandgap semiconductor material, its electro-optical conversion efficiency is extremely low (only 0.03%), which raises questions about its practical value [4]. In 1952, Heinrich Welker discovered III-V compounds, such as gallium arsenide (GaAs), which have superior properties not found in silicon (Si) and germanium (Ge), opening up a wide range of prospects for III-V compounds in optoelectronic devices [5]. In the same year, the electronic properties of GaAs as a III-V semiconductor were first reported [6]. Subsequently, Rubin Braunstein of RCA discovered that GaAs could emit infrared light when an electric current was applied to it in 1955. This discovery revealed the potential applications of III-V compounds in infrared optoelectronics.

In 1962, Nick Holonyak of General Electric in the United States achieved a significant breakthrough in the field of optoelectronics by fabricating the first red LED using vapour phase epitaxy (VPE) technology in GaAs substrate growth of gallium arsenide phosphide (GaAsP). This development marked the advent of visible LEDs and was a crucial milestone in the evolution of modern lighting technology [7]. However, due to the large mismatch between GaAsP and the GaAs substrate in terms of lattice constants and thermal expansion coefficients, this leads to a higher defect density in

the epitaxial materials, which seriously affects the efficiency of the LEDs which was only 0.1 lm/W. In 1968, at Bell Labs in the United States, Logan used liquid phase epitaxy (LPE) to successfully grow a PN structure by growing n-doped GaP on p-type GaP substrates doped with zinc oxide (ZnO), achieving an external quantum efficiency (EQE) of 0.1% for a green LED [8, 9]. Four years later, in 1972, the VPE technology was employed to dope GaAsP with N impurities, resulting in the successful production of orange, yellow and yellow-green LEDs [10]. In the 1980s, the luminous efficiency of AlGaAs-based red LEDs grown by LPE technology reached 10 lm/W. By the 1990s, high-brightness red/yellow aluminium gallium indium phosphide (AlGaInP) LEDs had been successfully developed, with their luminous efficacy increased to 100 lm/W in comparison to the 10 to 17 lm/W efficacy of conventional incandescent lamps. These technological breakthroughs marked the significant development of LED technology in terms of luminous efficacy and application and laid a solid foundation for the development of modern lighting technology [11].

After the successful development of red and green LEDs, the research and development of blue LEDs has become the focus of extensive academic and industrial attention, as the full set of red, green and blue primary colours of light (known as RGB colour mode) is essential for the realisation of full-colour display technology. In this background, the III-nitride semiconductor materials with excellent properties have attracted particular attention. III-nitride semiconductors, such as gallium nitride (GaN), aluminium nitride (AlN) and indium nitride (InN) and their alloys, which are direct bandgap semiconductors with large bandgaps widths, enabling them to efficiently generate the high-energy photons required for blue and ultraviolet light.

Development of GaN Epitaxial Growth

Gallium Nitride (GaN) in particular has demonstrated its unique advantages in the development of blue LEDs. Its excellent physical and chemical stability and tunable bandwidth when combined with other III-nitrides has made GaN an ideal material for the manufacture of high-performance optoelectronic devices. In 1928, Johnson first synthesised GaN using the powder method. However, the material obtained is GaN powder, which can only be used to study the crystal structure of GaN [12]. Ten years later, in 1938, scientists led by Juza and Hahn developed a process that involved introducing the ammonia (NH_3) to molten gallium at high temperatures, and successfully produced thermodynamically stable GaN films [13]. This reaction process is known as chemical vapour

deposition (CVD). However, due to the high melting point and dissociation pressure characteristics of GaN crystals, its bulk single crystal substrate is difficult to produce. Therefore, GaN epi-film is usually grown on heterogeneous substrates, but this heterogeneous epitaxial growth leads to a high dislocation density of GaN. In 1969, Maruska successfully obtained the first reported single crystal GaN film on a sapphire substrate using vapour phase epitaxy (VPE). In this process, hydrogen chloride (HCl) gas will first react with gallium metal at high temperatures to form gallium chloride (GaCl) on the sapphire substrate. These GaCl then react with ammonia (NH₃) to form a GaN film. However, the GaN films grown by this method show essentially n-type doping with high electron concentrations, typically $> 10^{19} \text{ cm}^{-3}$ [14]. This high electron concentration is caused by a high density of nitrogen vacancies and can adversely affect the electrical properties of the material. In 1983, Yoshida fabricated the first high-quality GaN films on sapphire substrates using molecular beam epitaxy (MBE), by using a high-temperature aluminium nitride (AlN) buffer layer on the sapphire before the GaN growth [15].

The year 1986 was a milestone in GaN materials research when Isamu Akasaki, Hiroshi Amano and others at Nagoya University, Japan, invented a two-step GaN growth technique using metal organic chemical vapour deposition (MOCVD) to obtain morphologically smooth GaN thin films on a low-temperature AlN buffer layer [16]. In 1991, Nakamura innovated from the traditional two-step method by using low-temperature GaN instead of AlN as a buffer layer, further improving the crystal quality of GaN films [17]. Nowadays, the two-step epitaxial growth method developed and modified by Amano and Nakamura is widely used to grow high-quality single-crystal GaN films on sapphire substrates. The successful production of high-quality GaN films provides a solid foundation for the future development of GaN-based LEDs. In addition, based on the two-step method, the scientists have developed the epitaxial lateral overgrowth (ELOG) technique, which further improves the crystal quality of GaN materials.

Development of GaN Doping Technology

The successful development of p-type doped GaN (p-GaN) films was another major breakthrough in GaN materials. Normally, silicon (Si) is the most commonly used n-type GaN dopant because Si as a donor impurity can provide additional electrons and increase the conductivity of the material, and the Si doping process is relatively mature. In contrast, the p-type doping of GaN has been a

technological bottleneck in the realisation of high-brightness GaN-based LEDs. In order to obtain low-resistance p-GaN, researchers have tried using a variety of elements as acceptor impurities, including zinc (Zn), beryllium (Be), magnesium (Mg) and calcium (Ca), and despite these efforts, the successful realisation of highly efficient p-type doping remains a major challenge [18-21].

In 1971, Pankove and his team at RCA Laboratories in the USA doped GaN with Zn as an acceptor impurity to compensate for the background electron concentration, successfully fabricated a semi-insulating GaN film, and developed a metal-insulator-semiconductor (MIS) structure of GaN-based blue LEDs, considered to be the first blue LEDs in the world [22]. Then, in 1973, Maruska used a similar method to form semi-insulating GaN films by doping GaN with Mg as an acceptor impurity and produced violet LEDs with a MIS structure. However, the limitations of the technology at the time resulted in the very low internal quantum efficiency (IQE) of GaN-based LED chips with MIS structure [23]. In 1989, Amano obtained Mg-doped GaN films by MOCVD and used the low-energy electron beam irradiation (LEEBI) method to activate the Mg acceptor in p-type GaN films to produce low-resistance p-GaN [24]. However, the LEEBI method is limited by the penetration depth of the electron beam, and therefore only presents strong p-type properties on the GaN surface. In 1992, Nakamura performed a high-temperature thermal annealing treatment on Mg-doped p-GaN films grown by MOCVD at 700°C with nitrogen. This treatment significantly improved the electrical conductivity of Mg-doped p-GaN, resulting in a reduction in resistivity from $1 \times 10^8 \Omega \cdot \text{cm}$ to $2 \Omega \cdot \text{cm}$ [25]. Meanwhile Nakamura makes the point that when Mg-doped GaN films are grown using the MOCVD, the Mg atoms tend to combine with hydrogen, ammonia, and hydrogen atoms generated during decomposition of metal-organic sources to form Mg-H neutral complexes. These Mg-H complexes passivate the Mg atoms and prevent them from acting as effective p-type acceptors, thus affecting the electrical conductivity of the material [26]. Neugebauer and Van de Walle investigated the mechanism of acceptor activation during high temperature thermal annealing and published in 1995 [27]. They used theoretical calculations to show that high-temperature thermal annealing effectively disrupts the structure of the Mg-H complex, releasing and reactivating Mg atoms that act as p-type dopants.

Development of GaN-based LEDs

Improvements in doping technology have not only enabled the manufacture of GaN p-n junctions

but have also led to the rapid development of GaN-based LEDs. In 1993, Nakamura reported a breakthrough achievement when they successfully fabricated a blue LED using a GaN/InGaN/GaN double-heterojunction (DH) structure as the active region, achieving the output power of 125 μW at 440 nm under an injection current of 20 mA, and the EQE of 0.22% [28]. In the following year, Nakamura's team achieved a notable enhancement in the IQE of blue LEDs by introducing a thin AlGaIn layer as an electron barrier layer (EBL) in DH-LEDs, resulting in high luminance of more than 1 cd, which output power was reached to the 1500 μW at 450 nm under a forward current of 20 mA, and the EQE was as high as 2.7% at room temperature [29]. In 1995, they made a further breakthrough, reporting the utilisation of InGaIn multi-quantum well (MQW) structures as the active region of high-brightness LEDs. By modulating the indium content in the compounds, these LEDs were able to emit not only blue light, but also green and yellow light at room temperature [30]. In the same year, the first white LED was successfully developed by combining an InGaIn-based blue LED with a yellow phosphor [31, 32]. This technological advance significantly extends the colour range of GaN-based LEDs and provides a technological foundation for the development of multi-colour and full-colour LEDs.

Since the beginning of the 21st century, LED technology has entered a new phase of rapid development and widespread application. While improving energy efficiency and colour quality, the cost of LEDs has decreased year by year with the expansion of production scale and the maturity of the technology, making LED lighting gradually become an economical choice for home and commercial lighting. Moreover, the progress of LED technology is not limited to traditional lighting, but is also widely used in automotive lighting, commercial displays, visible light communication (VLC), medical equipment lighting and many other fields [33, 34]. Furthermore, the reduced energy consumption of LEDs in comparison to traditional lighting sources results in a decrease in energy requirements for lighting, which in turn leads to a reduction in carbon emissions. Consequently, LEDs are regarded as a more environmentally friendly lighting technology, and their adoption has had a significant impact on global energy consumption and environmental policies.

Several countries, including the European Union (banning incandescent bulbs by 2012), the United States (implementing energy efficiency standards from 2012), China (phasing out high-wattage incandescent bulbs since 2012), and Australia (banning incandescent bulbs in 2009), have

introduced regulations to phase out inefficient incandescent bulbs in favour of energy-saving alternatives like LEDs. The objective of these bans is to reduce energy consumption, lower greenhouse gas emissions and promote the use of efficient lighting technologies.

Development of GaN-based power devices

GaN also has great potential in high power and high frequency electronics due to its wide bandgap properties. GaN has a bandgap of about 3.39 eV, which allows it to operate at higher temperatures, voltages and power levels while maintaining low leakage currents and high efficiency. In GaN/AlN heterojunctions, the lattice mismatch and polarisation effects of the two materials lead to the formation of a potential energy trap at the interface. This energy trap confines electrons to form a high-density two-dimensional electron gas (2DEG) and is becoming a fundamental requirement for the development of GaN-based high electron mobility transistors (HEMTs) [35]. In 1993, Khan's team developed the first GaN-based HEMT, marking the beginning of the use of GaN in high frequency and high power electronic devices [36]. Through in-depth studies by several research teams, the structure of GaN HEMTs has been further optimised to significantly improve the electron density and mobility of 2DEG by introducing AlGaIn as a barrier layer. Alex Lidow and his team at International Rectifier were instrumental in bringing GaN power devices to market in 1999 [37]. Moreover, since the end of the 20th century, Fujitsu in Japan has shown considerable interest and investment in the field of GaN-based HEMTs and has achieved remarkable success. Large-scale commercial production of GaN HEMTs was successfully achieved in the early 2000s, and they are being supplied to communications equipment manufacturers worldwide.

With the in-depth exploration of GaN, GaN-based photonic devices have been widely used in various fields such as power electronics, radio frequency (RF) wireless communication and solid-state lighting. The LEDs and LDs with GaN/InGaIn heterojunction structures have become the preferred choice for lighting technology due to their high efficiency, strong durability and low energy consumption. Furthermore, GaN-based HEMTs show great potential for power conversion, with the potential to offer enhanced power conversion efficiencies, reduced switching losses and faster switching speeds. These anticipated benefits suggest that GaN-based electrical devices will also become increasingly significant in the high-performance electronics market [38, 39].

1.2 Current Challenges of III-Nitrides

Since the turn of the 20th century, gallium nitride (GaN) technology has undergone significant advancements. However, the majority of these developments have been confined to c-plane GaN on sapphire substrates. Therefore, the utilisation of different substrates has become one of the concerns in developing GaN epitaxial technology. GaN-on-Si technology offers a promising avenue for combining the economic viability of silicon with the exceptional electronic properties of GaN. Nevertheless, the large-scale commercialisation of GaN-on-Si is currently hindered by a number of challenges, including cracking issues caused by severe thermal expansion coefficient mismatch and lattice mismatch between the GaN and Si [40-42]. This section will discuss the principal issues and significant challenges that have hindered the development of GaN-on-Si emitters.

1.2.1 Epitaxial Substrate

The development of GaN epitaxial growth technology has been fraught with challenges, particularly in terms of substrate selection. GaN homogeneous substrates are the most ideal substrates for GaN growth, but GaN single crystal substrates are not suitable for large-scale applications due to their considerable cost [43]. Specifically, the cost of a 2-inch free-standing bulk GaN substrate can reach as much as £2000, whereas a 12-inch silicon substrate is priced at only £80 [44, 45]. As a result, research into GaN-based semiconductor materials and devices over the last two decades has mainly been based on heterogeneous epitaxy.

SiC, sapphire, and Si are common substrates for GaN epitaxial growth. The advantages of SiC include a low lattice mismatch with GaN (3.5%) and high thermal conductivity (4.9 W/cmK), both of which enhance crystal quality and device performance. However, the high cost of SiC limits its commercial and large-scale viability [46]. Sapphire substrates are cheaper than SiC and can be manufactured in larger sizes due to the mature manufacturing process, making them the most common choice for GaN epitaxial growth. However, the 16% lattice mismatch with GaN and the very low thermal conductivity present significant challenges for GaN-on-Sapphire [46]. Sapphire acts as an insulator, which limits its use in semiconductor power electronics. In contrast, Si single crystal substrates offer significant cost advantages over SiC. Currently, Si single-crystal technology is capable of producing large-size substrates up to 12-inches in diameter, which not only reduces

the manufacturing cost of GaN-based electronics, but also improves the utilisation of Si substrates. It is particularly noteworthy that the fabrication process for GaN electronics on Si substrates is compatible with conventional CMOS technology, significantly reducing manufacturing costs and providing the technical basis for monolithic integration of GaN-on-Si-based electronics [47, 48].

Table 1-1 Physical properties and typical prices for 2-inch wafers of various substrate materials commonly used in growth of III-nitrides [44, 45, 49-52].

	Sapphire	4H - SiC	GaN	Silicon (001)
In-plane lattice constant (a_0) (Å)	4.758	3.073	3.189	5.431
Out-of-plane lattice constant (c_0) (Å)	12.991	10.053	5.185	/
Thermal expansion coefficient (10^{-6} K^{-1})	8.8 / 5.3	4.2	5.59	2.6
Thermal conductivity (W/mK)	35	490	130	149
Prices (2-inch) (£)	£50 - £100	£300 - £1000	£2000 - £3000	£10 - £35

Although GaN-on-Si technology offers a number of advantages, there are also significant challenges associated with the epitaxial growth of the material, particularly with regard to the issues of melt-back etching and surface cracking. A large number of experiments have shown that growing GaN directly on Si substrate causes severe etching of the Si substrate, due to the fact that Ga atoms can react with Si at high temperatures [53]. An effective way to avoid this problem was to first grow an AlN buffer layer on a Si substrate and then epitaxially grow GaN. As Al has no etching effect on the surface of the Si substrate, the stability of the Si substrate can be maintained during high temperature epitaxial growth by MOCVD. The lattice mismatch between Si and GaN can be up to 16.9%, resulting in a large number of dislocations in the GaN epitaxial layer, while a thermal

mismatch of 54% builds up a large amount of tensile stress in the GaN epitaxial layer during the cooling process, leading to cracking and wafer bending [53]. Over the past two decades, research in GaN-on-Si has focused on the stress control of epitaxial layer and the crystal quality improvement of GaN. In recent years, several technical routes have been proposed to control the stress of the GaN epitaxial layer and improve its crystal quality, including a) selective-area growth; b) AlN/GaN superlattice buffer layer technology; c) low-temperature AlN interlayer; d) SiN interlayer; e) graded $\text{Al}_x\text{Ga}_{1-x}\text{N}$ buffer layer [54-57]. Each of these technologies is an effective way of growing crack-free GaN crystals on Si substrate, and each has its own advantages for different applications. In addition, an in-situ curvature monitoring system has been developed for real-time tracking of wafer deformation during growth [58-61]. By obtaining curvature data from the monitoring system, the internal stresses in the epi-film can be derived using the Stoney formula and the wafer curvature, lateral wafer temperature uniformity and stress state can be systematically investigated [62]. Table 1-2 lists representative results in the field of GaN-on-Si by MOCVD from different institutes.

Table 1-2 Representative works from different research institutes on stress control methods, thickness and crystal quality of GaN epitaxial layers on silicon substrates.

Research institute	Stress control technology	Thickness of GaN (μm)	XRD FWHM (arcsec)
IMEC, Belgium [63]	AlGaIn buffer layer;	2~3	(002) 533
	SiN interlayer		(102) 415
Nagoya University, Japan [64]	GaN/AlN superlattice	9	/
Otto-von-Guericke-University, Germany [65]	SiN, AlN interlayer	14.3	(002) 252
			(102) 372
Toshiba, Japan [66]	AlGaIn buffer layer;	3	(002) 289
	SiN interlayer		(102) 256
Suzhou Institute of Nano-tech and Nano-bionics, China [67]	AlGaIn buffer layer	6	(002) 260
			(102) 270

1.2.2 Crystal Quality and Morphology

In GaN epitaxial growth, due to the lack of suitable primary substrates, epitaxial growth on heterogeneous substrates is often required, however, heterogeneous substrates can result in a significant increase in the defect density in the nitride epi-layer. GaN grown on sapphire substrates typically has a high density of threading dislocations (TDs), reaching values of 10^9 to 10^{10} cm^{-2} . These high-density dislocations are mainly due to the significant lattice mismatch and thermal expansion coefficient differences between GaN and sapphire. The high density of dislocations will strongly affect the electron mobility and optical properties of the crystal, reducing the performance of the device. In addition, the thermal expansion mismatch also generates biaxial compressive strain within the GaN film during the cooling process of MOCVD epitaxial growth, and the resulting strain-induced quantum confined stark effect (QCSE) can lead to a reduction in the luminous efficacy of the LED chip.

In case of GaN grown on Si substrates typically exhibits higher dislocation densities, with values ranging from 10^8 to 10^{10} cm^{-2} . Furthermore, the melting-back etching will bring more challenges to the growth of GaN on Si. Typically, the quality of GaN crystals grown on Si is inferior to that of GaN grown on sapphire substrates due to better thermal matching and proven growth techniques. It is important to highlight that the impact of TDs on device performance is critical. In wide bandgap semiconductors such as gallium nitride, TDs are regarded as non-radiative recombination centres, meaning that they can trap electrons and holes and prevent them from emitting light by radiative recombination, leading to lower optical efficiency of optoelectronic devices, such as LEDs and LDs, as these carriers are non-radiatively recombined before reaching the light-emitting region.

1.2.3 Quantum Confined Stark Effect

The Quantum Confined Stark Effect (QCSE) significantly affects GaN-based optical devices. In GaN and other III-nitride semiconductors, the lack of central symmetry in the lattice structure leads to strong spontaneous and piezoelectric polarisation effects, creating a built-in electric field along the c -axis (crystal growth direction) [68, 69]. The electrons and holes in a quantum well are spatially separated by the effect of this built-in electric field, which reduces the overlap of the electron-hole wave functions and thus the probability of radiative recombination. This phenomenon, known as

the Quantum Confined Stark Effect - QCSE, was observed by Miller and first reported in 1984 [70]. The built-in electric field also leads to changes in the energy levels within the quantum well, resulting in a red-shift in the emission wavelengths. As the injected current increases, the number of injected electrons and holes can partially shield the effect of the built-in electric field, leading to a blue-shift of the emission wavelength [70]. Moreover, reducing the electron-hole wave function overlap increases the lifetime of radiative recombination, which directly limits the modulation speed of the light emitting device, which is fatal for VLC applications. Similarly, a reduction in overlap leads to a decrease in the radiative recombination probability, which in turn leads to a reduction in the internal quantum efficiency (IQE).

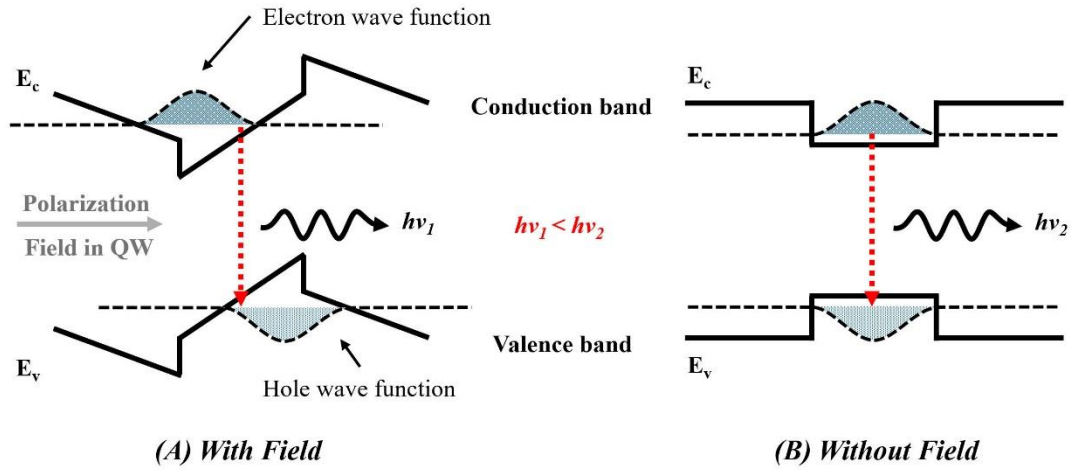


Figure 1-1 Schematic diagram of the quantum-confined Stark effect (QCSE).

It should be noted that in the InGa_N/Ga_N MQWs based optical devices, increasing the indium content provides the device with longer emission wavelengths, with a consequent enhancement of lattice mismatch, leading to an intensification of QCSE. Meanwhile, adjusting the thickness of the quantum well can mitigate the effects of QCSE to some extent, which in turn introduces more stress and may cause more problems. This means that while high indium content InGa_N/Ga_N MQWs offer the possibility of achieving long wavelength and high efficiency optical emission devices, QCSE limits the use of high indium content InGa_N and thick QWs. Therefore, the development of effective strategies to mitigate or eliminate QCSE has become a central research priority to achieve high performance optoelectronic devices.

1.2.4 Efficiency Droop

The phenomenon of efficiency droop has been widely observed and reported in the III-nitride LEDs, and this phenomenon is particularly significant at high current drives, which imposes a limitation on device performance [71]. Ideally, each electron injected into the LED can efficiently recombine with a hole and release a photon, so the optical output of an ideal LED should be linearly related to the injection current. In practice, the quantum efficiency of III-nitride LEDs typically rises to a peak initially with increasing injected current density and then decreases gradually with further increases in current density. This is known as the phenomenon of efficiency droop. Theoretically, at low current densities, due to the low carrier density injected into the active region (quantum well), most carriers can effectively participate in radiative recombination and release photons. As a result, the quantum efficiency initially increases with increasing current. However, once a certain peak current density is reached, further increases in current density will lead to the enhancement of several non-ideal effects, causing the quantum efficiency to begin to decrease. But thus now, the efficiency droop remains a widely debated topic and there is still no broad consensus on the mechanism of its origin. Researchers have proposed a variety of mechanistic models to explain the underlying causes of this phenomenon, including electron leakage [72], density-activated defect recombination [73], loss of current injection efficiency [74] and Auger recombination [75].

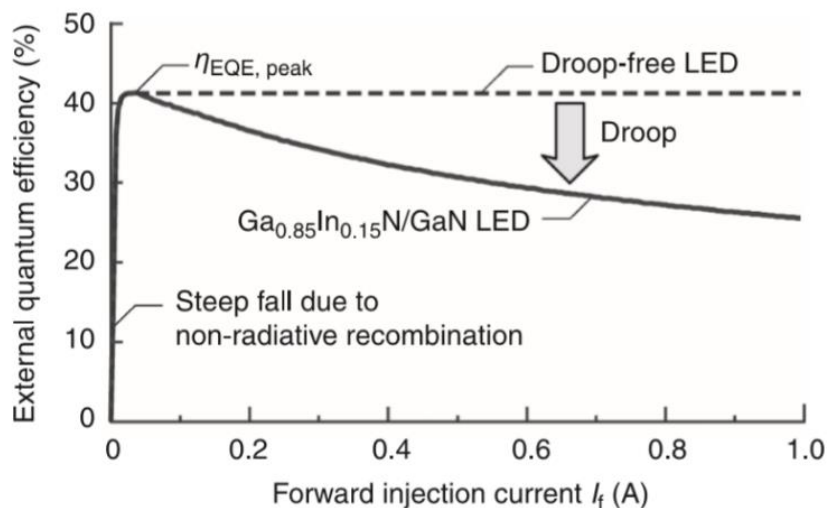


Figure 1-2 The external quantum efficiency of a $\text{Ga}_{0.85}\text{In}_{0.15}\text{N}/\text{GaN}$ based LED as a function of injection current. Efficiency droop occurs when the injection current is above a threshold current. The dashed curve is the ideal external quantum efficiency for a droop-free LED [76].

1.2.5 Micro-LEDs and Micro-Display Applications

The development of LED technology has led to new explorations into the fabrication process and applications of III-nitride LEDs. Micro-LEDs (μ LEDs) are attracting attention as an emerging display technology, and their excellent performance and extremely small size ($<100 \mu\text{m}$) are expected to be used in a wide range of applications, including visible light communication (VLC), high performance displays and optogenetic light [77].

Table 1-3 Comparison of Key Characteristics Among Micro-LED, LCD, and OLED Technologies [78].

Parameter	LCD	OLED	Micro-LED
Emission type	Backlight	Self-emissive	Self-emissive
Brightness (cd/m^2)	3000	5000	100000
Luminescent material	Inorganic	Organic	Inorganic
Contrast ratio	5000:1	∞	∞
Pixels per inch (PPI)	>300	1500-6000	1500-10000
Colour gamut	75%, NTSC	$>100\%$, NTSC	$>100\%$, NTSC
Viewing angle	Best ($\sim 178^\circ$)	Best ($\sim 178^\circ$)	Best ($\sim 178^\circ$)
Response time	5 ms, slow	10 μs , medium	0.2 ns, fast
Operating temperature	233-373K	238-358 K	15-500 K

In comparison to traditional display technologies such as organic light-emitting diodes (OLEDs) and liquid crystal displays (LCDs), GaN μ LEDs offer a number of distinctive advantages. As a self-luminous source, μ LEDs do not require a backlight, which is a necessity in traditional LCD displays. This allows for the display of truer blacks, thereby enabling the achievement of higher contrast ratios [79]. Although OLEDs are also self-luminous, μ LEDs offer superior durability and stability. The organic materials used in OLEDs are susceptible to degradation, particularly at high brightness

and high temperatures. Consequently, in order to extend their operational lifetime, OLEDs are typically operated at lower injection current densities [80]. Furthermore, μ LED technology allows for extremely high pixel densities by enabling each LED to function as an independent, precisely controlled light-emitting unit, achieving high resolutions on very small displays.

The epitaxial growth and subsequent device fabrication of μ LEDs present significant challenges due to their extremely small size in comparison to conventional LEDs. The growth of GaN on sapphire substrates typically results in a high density of defects due to a significant mismatch between the lattices of GaN and sapphire, which can lead to a range of efficiency issues for GaN-based μ LEDs. The problem is even more pronounced for GaN-based μ LEDs on Si substrates. The fabrication of conventional LEDs typically involves the combination of photolithography and dry etching processes. However, the dry etching process inevitably causes damage to the surface and sidewalls of the LEDs, which may result in the formation of non-radiative recombination centres, thereby leading to a degradation of the luminescence efficiency. In the case of regular-sized LEDs, this issue can typically be disregarded, given that the damage is relatively limited in extent in comparison to the area of luminosity. However, as the dimensions of the LED decrease, the consequences of etch damage become more pronounced, with the ratio of the sidewall to the total light-emitting area increasing exponentially with decreasing size. This has a significant impact on the overall light output [81, 82]. Our team has developed a novel μ LED growth process that is based on a selective growth, where a patterned etching is first performed on a GaN substrate followed by direct growth of the LED structure. This innovative method avoids the damage that can be caused by dry etching, which is a significant advantage [80, 83, 84].

1.3 Motivation and Aims

The ongoing advancements in semiconductor technology have significantly driven the demand for high-performance optoelectronic devices. Among these devices, III-nitride materials, such as GaN, have become indispensable components due to their superior properties, gradually supplanting traditional light sources like fluorescent lamps in the lighting industry. Furthermore, in display applications, GaN based LEDs can offer several competitive advantages over conventional LCD or OLED technologies, including high brightness, long lifespan, and high efficiency, making them an ideal choice for modern display technologies.

Silicon represents an attractive alternative substrate for the growth of III-nitrides, due to its favourable cost, large size and compatibility with existing microelectronic technologies. However, the growth of high-quality GaN on silicon substrates remains a significant challenge due to the lattice mismatch and thermal expansion coefficient mismatch between GaN and Si, which often result in high defect densities and surface cracks of GaN layer, which can lead to compromised device performance. The successful growth of group III-nitride materials on silicon substrates not only reduces production costs, but also opens up new avenues of research in electronic and optoelectronic devices.

Furthermore, the rapid advancement of display technology has resulted in a corresponding increase in market demand for high-performance and ultra-small displays. This has led to μ LED emerging as a leading candidate for next-generation display solutions. However, a key challenge lies in further reducing the size of μ LEDs while maintaining high performance. As the size of μ LEDs decreases to tens of micrometres or even smaller, the sidewall damage caused by the dry etching processes inherent in traditional μ LED fabrication becomes increasingly severe, which leads to enhanced non-radiative recombination, which ultimately results in a significant decline in μ LED efficiency.

The main motivation of this thesis is to address the existing challenges associated with the growth of c-plane GaN on (111) silicon substrates, aiming to optimise the growth process to achieve high crystal quality and minimise defects. Furthermore, this study presents a comparative analysis of the impact of diverse substrates on the performance of optical (LEDs) and electronic devices (HEMTs). Finally, an innovative selective direct epitaxy technique has enabled the fabrication of μ LEDs

without the occurrence of sidewall damage. In this study, μ LEDs on silicon substrates were grown by this method and then subjected to advanced characterisation and detailed analysis. The objective of this study is to explore and optimise the growth technology for μ LEDs on silicon, thereby contributing to the development of cost-effective, high-performance μ LEDs on silicon substrates.

1.4 Thesis Organization

Chapter 1 provides a brief overview of the development of light-emitting technologies and III-nitride semiconductor materials, discussing the recent advancements in micro-LED research. Additionally, this chapter outlines the primary motivation and research objectives of the study.

Chapter 2 offers a fundamental introduction to III-nitride semiconductors, covering their physical and chemical properties while explaining the underlying principles. This chapter also includes a comprehensive analysis of the current challenges facing III-nitride semiconductors, with a particular focus on the epitaxial growth of gallium nitride on silicon.

Chapter 3 provides an overview of the principal experimental techniques and equipment employed in this project. It covers the essential methods and primary instruments used for epitaxial growth, material characterisation, and device fabrication. Specifically, the technologies employed in this study include MOCVD for material epitaxy; XRD, SEM, optical microscopy, AFM, and PL for characterization; and various equipment for device fabrication, including PECVD, RIE, ICP, and lithography.

Chapter 4 presents a comprehensive analysis of the various steps involved in the growth of GaN on (111) silicon substrates, with a particular focus on the impact of each step on epitaxial growth. It covers the pre-treatment process of the silicon substrate, the impact of high temperature annealing in the initial step of growth, the growth of AlN and graded AlGaN buffer layers, and finally the growth of the GaN layer will be studied. XRD and optical microscopy are used to assess the crystal quality and surface morphology of the resulting GaN materials in this chapter.

Chapter 5 investigates the GaN-based optical devices and electrical devices on (0001) sapphire and (111) silicon substrates. The first part in this chapter is presents a comparative analysis of c-plane InGaN/GaN MQWs-based LEDs that had been grown under identical conditions on different substrates. This analysis was conducted with a focus on examining their PL spectra and XRD ω -2 θ curves. The second part provides a brief study of GaN/AlGaN HEMT structures grown on silicon substrate, along with corresponding XRD results and SEM images.

Chapter 6 primarily focused on the growth of GaN-based μ LEDs, which were fabricated on

patterned substrates using a direct selective area overgrowth method developed by our research group. This chapter examines the growth process of μ LEDs achieved through this overgrowth method and investigates several key factors that influence μ LED characteristics. These factors include the growth of the initial n-GaN layer and the final p-GaN layer, the substrates, μ LED dimensions, and the fill factor of the pattern. Furthermore, a comparative analysis was conducted to investigate the differences between μ LEDs grown using H_2/N_2 mixed gas as the ambient during QB layer growth and those grown using N_2 as the ambient during MQW growth.

Chapter 7 summarizes the findings of this study and explores potential directions for future research.

References

- [1] "Brief History of Human's use and control of Fire." Sacred Hearth Friction Fire. Available: <https://www.sacredhearthfrictionfire.com/history-of-fire.html> (accessed September, 2024).
- [2] E. F. Schubert, *Light-emitting diodes* (2018). E. Fred Schubert, 2018.
- [3] H. J. Round, "A note on carborundum," in *Semiconductor devices: pioneering papers*: World Scientific, 1991, pp. 879-879.
- [4] J. A. Edmond, H.-S. Kong, and C. H. Carter Jr, "Blue LEDs, UV photodiodes and high-temperature rectifiers in 6H-SiC," *Physica B: Condensed Matter*, vol. 185, no. 1-4, pp. 453-460, 1993.
- [5] C. Wilmsen, *Physics and chemistry of III-V compound semiconductor interfaces*. Springer Science & Business Media, 2013.
- [6] H. Welker, "Über neue halbleitende Verbindungen," *Zeitschrift für Naturforschung A*, vol. 7, no. 11, pp. 744-749, 1952.
- [7] N. Holonyak and S. F. Bevacqua, "Coherent (visible) light emission from Ga (As_{1-x}P_x) junctions," *Applied Physics Letters*, vol. 1, no. 4, pp. 82-83, 1962.
- [8] R. Logan, H. White, and W. Wiegmann, "Efficient Green Electroluminescence in Nitrogen-Doped GaP p-n Junctions," *Applied Physics Letters*, vol. 13, no. 4, pp. 139-141, 1968.
- [9] R. A. Logan, H. G. White, and W. Wiegmann, "Efficient green electroluminescent junctions in GaP," *Solid-State Electronics*, vol. 14, no. 1, pp. 55-70, 1971.
- [10] M. Craford, R. W. Shaw, A. Herzog, and W. Groves, "Radiative recombination mechanisms in GaAsP diodes with and without nitrogen doping," *Journal of Applied Physics*, vol. 43, no. 10, pp. 4075-4083, 1972.
- [11] T. Gessmann and E. Schubert, "High-efficiency AlGaInP light-emitting diodes for solid-state lighting applications," *Journal of applied physics*, vol. 95, no. 5, pp. 2203-2216, 2004.
- [12] W. C. Johnson, J. Parson, and M. Crew, "Nitrogen compounds of gallium. iii," *The journal of physical chemistry*, vol. 36, no. 10, pp. 2651-2654, 2002.
- [13] H. Hahn and R. Juza, "Untersuchungen über die nitride von cadmium, gallium, indium und germanium. Metallamide und metallnitride. VIII. Mitteilung," *Zeitschrift für anorganische und allgemeine Chemie*, vol. 244, no. 2, pp. 111-124, 1940.
- [14] H. P. Maruska and J. Tietjen, "The preparation and properties of vapor-deposited

- single-crystal-line GaN," *Applied Physics Letters*, vol. 15, no. 10, pp. 327-329, 1969.
- [15] S. Yoshida, S. Misawa, and S. Gonda, "Improvements on the electrical and luminescent properties of reactive molecular beam epitaxially grown GaN films by using AlN-coated sapphire substrates," *Applied Physics Letters*, vol. 42, no. 5, pp. 427-429, 1983.
- [16] H. Amano, N. Sawaki, I. Akasaki, and Y. Toyoda, "Metalorganic vapor phase epitaxial growth of a high quality GaN film using an AlN buffer layer," *Applied Physics Letters*, vol. 48, no. 5, pp. 353-355, 1986.
- [17] S. N. S. Nakamura, "GaN growth using GaN buffer layer," *Japanese Journal of Applied Physics*, vol. 30, no. 10A, p. L1705, 1991.
- [18] J. Pankove, E. Miller, and J. Berkeyheiser, "GaN blue light-emitting diodes," *Journal of Luminescence*, vol. 5, no. 1, pp. 84-86, 1972.
- [19] J. Pankove, M. Duffy, E. Miller, and J. Berkeyheiser, "Luminescence of insulating Be-doped and Li-doped GaN," *Journal of Luminescence*, vol. 8, no. 1, pp. 89-93, 1973.
- [20] H. Maruska, W. Rhines, and D. Stevenson, "Preparation of Mg-doped GaN diodes exhibiting violet electroluminescence," *Materials Research Bulletin*, vol. 7, no. 8, pp. 777-781, 1972.
- [21] O. Lagerstedt and B. Monemar, "Luminescence in epitaxial GaN: Cd," *Journal of Applied Physics*, vol. 45, no. 5, pp. 2266-2272, 1974.
- [22] J. Pankove, E. Miller, and J. Berkeyheiser, "GaN electroluminescent diodes," in *1971 International Electron Devices Meeting, 1971: IEEE*, pp. 78-78.
- [23] H. Maruska, D. Stevenson, and J. Pankove, "Violet luminescence of Mg-doped GaN," *Applied Physics Letters*, vol. 22, no. 6, pp. 303-305, 1973.
- [24] H. Amano, M. Kito, K. Hiramatsu, and I. Akasaki, "P-type conduction in Mg-doped GaN treated with low-energy electron beam irradiation (LEEBI)," *Japanese journal of applied physics*, vol. 28, no. 12A, p. L2112, 1989.
- [25] S. Nakamura, T. Mukai, M. S. M. Senoh, and N. I. N. Iwasa, "Thermal annealing effects on p-type Mg-doped GaN films," *Japanese Journal of Applied Physics*, vol. 31, no. 2B, p. L139, 1992.
- [26] C. G. Van De Walle and J. Neugebauer, "Hydrogen in semiconductors," *Annual Review of Materials Research*, vol. 36, no. 1, pp. 179-198, 2006, doi: 10.1146/annurev.matsci.36.010705.155428.
- [27] J. Neugebauer, "Role of hydrogen and hydrogen complexes in doping of GaN," *MRS Online Proceedings Library (OPL)*, vol. 423, p. 619, 1996.
- [28] S. Nakamura, M. S. M. Senoh, and T. M. T. Mukai, "P-GaN/N-InGaN/N-GaN double-

- heterostructure blue-light-emitting diodes," *Japanese Journal of Applied Physics*, vol. 32, no. 1A, p. L8, 1993.
- [29] S. Nakamura, T. Mukai, and M. Senoh, "Candela-class high-brightness InGaN/AlGaIn double-heterostructure blue-light-emitting diodes," *Applied Physics Letters*, vol. 64, no. 13, pp. 1687-1689, 1994.
- [30] S. Nakamura, M. Senoh, N. Iwasa, and S.-i. Nagahama, "High-brightness InGaIn blue, green and yellow light-emitting diodes with quantum well structures," *Japanese journal of applied physics*, vol. 34, no. 7A, p. L797, 1995.
- [31] S. Nakamura, "Nobel Lecture: Background story of the invention of efficient blue InGaIn light emitting diodes," *Reviews of Modern Physics*, vol. 87, no. 4, pp. 1139-1151, 2015.
- [32] S. Pimputkar, J. S. Speck, S. P. DenBaars, and S. Nakamura, "Prospects for LED lighting," *Nature photonics*, vol. 3, no. 4, pp. 180-182, 2009.
- [33] C. H. Yeh, Y. L. Liu, and C. W. Chow, "Real-time white-light phosphor-LED visible light communication (VLC) with compact size," *Optics express*, vol. 21, no. 22, pp. 26192-26197, 2013, doi: 10.1364/OE.21.026192.
- [34] S. Bo, J. Xiaopeng, Y. Kam-Chuen, F. Jiajie, and M. G. Pecht, "A Review of Prognostic Techniques for High-Power White LEDs," *IEEE transactions on power electronics*, vol. 32, no. 8, pp. 6338-6362, 2017, doi: 10.1109/TPEL.2016.2618422.
- [35] H. W. Jang *et al.*, "Mechanism of two-dimensional electron gas formation in Al_xGa_{1-x}N/GaN heterostructures," *Applied Physics Letters*, vol. 81, no. 7, pp. 1249-1251, 2002.
- [36] M. Asif Khan, A. Bhattarai, J. Kuznia, and D. Olson, "High electron mobility transistor based on a GaN-Al_xGa_{1-x}N heterojunction," *Applied Physics Letters*, vol. 63, no. 9, pp. 1214-1215, 1993.
- [37] A. Lidow, M. De Rooij, J. Strydom, D. Reusch, and J. Glaser, *GaN transistors for efficient power conversion*. John Wiley & Sons, 2019.
- [38] M. Charles *et al.*, "(Invited) Epitaxy of GaN on Si (111) for Power Electronics, RF and LEDs," in *ECS Trans*, 2018 2018, vol. 86: The Electrochemical Society, Inc, 7 ed., pp. 233-247, doi: 10.1149/08607.0233ecst.
- [39] Z. Liu, *Compound semiconductor materials and devices*. San Rafael, California]: San Rafael, California : Morgan & Claypool Publishers, 2016, 2016.
- [40] A. Dadgar *et al.*, "MOVPE growth of GaN on Si – Substrates and strain," *Thin solid films*, vol. 515, no. 10, pp. 4356-4361, 2007, doi: 10.1016/j.tsf.2006.07.100.

- [41] V. N. Bessolov, M. E. Kompan, E. V. Konenkova, V. N. Pantelev, S. N. Rodin, and M. P. Shcheglov, "Epitaxy of GaN(0001) and GaN(101) Layers on Si(100) Substrate," *Technical physics letters*, vol. 45, no. 6, pp. 529-532, 2019, doi: 10.1134/S106378501906004X.
- [42] H. Ishikawa, G. Y. Zhao, N. Nakada, T. Egawa, T. Jimbo, and M. Umeno, "GaN on Si Substrate with AlGaN/AlN Intermediate Layer," *Japanese Journal of Applied Physics*, vol. 38, no. 5, pp. 492-494, 1999, doi: 10.1143/jjap.38.1492.
- [43] H. Amano, "Nobel Lecture: Growth of GaN on sapphire via low-temperature deposited buffer layer and realization of p-type GaN by Mg doping followed by low-energy electron beam irradiation," *Reviews of Modern Physics*, vol. 87, no. 4, pp. 1133-1138, 2015.
- [44] "SiC/GaN/AlN Wafer." Soka Technology. Available: <https://sokatec.com/collections/sic-gan-wafer> (accessed September, 2024).
- [45] "12" (300mm) Polished Silicon Wafer." WAFER PRO. Available: <https://waferpro.com/product/12-inch-300mm-polished-silicon-wafer/> (accessed September, 2024).
- [46] D. Zhu, D. Wallis, and C. Humphreys, "Prospects of III-nitride optoelectronics grown on Si," *Reports on Progress in Physics*, vol. 76, no. 10, p. 106501, 2013.
- [47] K. Harafuji, T. Tsuchiya, and K. Kawamura, "Molecular dynamics simulation for evaluating melting point of wurtzite-type GaN crystal," *Journal of applied physics*, vol. 96, no. 5, pp. 2501-2512, 2004.
- [48] S. Chowdhury, B. L. Swenson, M. H. Wong, and U. K. Mishra, "Current status and scope of gallium nitride-based vertical transistors for high-power electronics application," *Semiconductor Science and Technology*, vol. 28, no. 7, p. 074014, 2013.
- [49] "Silicon Wafers." Agar Scientific Ltd. Available: <https://www.agarscientific.com/tem/support-films-substrates/silicon-wafers> (accessed September, 2024).
- [50] "MSE PRO 2 inch Silicon Carbide Wafers 4H/6H P-Type SiC Substrates (Dummy Grade)." MSE Supplies LLC. Available: <https://www.msesupplies.com/en-gb/products/mse-pro-2-inch-silicon-carbide-wafers-4h-6h-p-type-sic-substrates-dummy-grade?variant=40047423356986> (accessed September, 2024).
- [51] "Sapphire Substrate 99.999% Monocrystalline 3 " ." PI-KEM Store. Available: <https://store.pi-kem.co.uk/product/sapphire-substrate-3-99-999-monocrystalline-x-1pc/> (accessed September, 2024).
- [52] M. E. Levinshtein, S. L. Rumyantsev, and M. S. Shur, *Properties of Advanced Semiconductor Materials: GaN, AlN, InN, BN, SiC, SiGe*. John Wiley & Sons, 2001.

- [53] A. Dadgar *et al.*, "Metalorganic chemical vapor phase epitaxy of gallium-nitride on silicon," *physica status solidi (c)*, no. 6, pp. 1583-1606, 2003.
- [54] J. Liu *et al.*, "Wafer-scale crack-free 10 μm -thick GaN with a dislocation density of $5.8 \times 10^7 \text{ cm}^{-2}$ grown on Si," *Journal of Physics D: Applied Physics*, vol. 52, no. 42, p. 425102, 2019.
- [55] J. Cheng *et al.*, "Growth of high quality and uniformity AlGaIn/GaN heterostructures on Si substrates using a single AlGaIn layer with low Al composition," *Scientific Reports*, vol. 6, no. 1, p. 23020, 2016.
- [56] H. Schenk, E. Frayssinet, A. Bavard, D. Rondi, Y. Cordier, and M. Kennard, "Growth of thick, continuous GaN layers on 4-in. Si substrates by metalorganic chemical vapor deposition," *Journal of crystal growth*, vol. 314, no. 1, pp. 85-91, 2011.
- [57] X. Zou, K. M. Wong, W. C. Chong, J. Ma, and K. M. Lau, "High-efficiency blue and green LEDs grown on Si with 5 micrometer thick GaN buffer," *physica status solidi (c)*, vol. 11, no. 3-4, pp. 730-733, 2014.
- [58] F. Lipski, M. Klein, X. Yao, and F. Scholz, "Studies about wafer bow of freestanding GaN substrates grown by hydride vapor phase epitaxy," *Journal of crystal growth*, vol. 352, no. 1, pp. 235-238, 2012.
- [59] S. Hearne *et al.*, "Stress evolution during metalorganic chemical vapor deposition of GaN," *Applied Physics Letters*, vol. 74, no. 3, pp. 356-358, 1999.
- [60] A. Krost, A. Dadgar, G. Strassburger, and R. Clos, "GaN-based epitaxy on silicon: stress measurements," *physica status solidi (a)*, vol. 200, no. 1, pp. 26-35, 2003.
- [61] A. Krost *et al.*, "In situ monitoring of the stress evolution in growing group-III-nitride layers," *Journal of crystal growth*, vol. 275, no. 1-2, pp. 209-216, 2005.
- [62] R. Clos, A. Dadgar, and A. Krost, "Wafer curvature in the nonlinear deformation range," *physica status solidi (a)*, vol. 201, no. 11, pp. R75-R78, 2004.
- [63] K. Cheng, M. Leys, S. Degroote, M. Germain, and G. Borghs, "High quality GaN grown on silicon (111) using a SixNy interlayer by metal-organic vapor phase epitaxy," *Applied physics letters*, vol. 92, no. 19, 2008.
- [64] S. L. Selvaraj, T. Suzue, and T. Egawa, "Breakdown enhancement of AlGaIn/GaN HEMTs on 4-in silicon by improving the GaN quality on thick buffer layers," *IEEE electron device letters*, vol. 30, no. 6, pp. 587-589, 2009.
- [65] A. Dadgar *et al.*, "Improving GaN-on-silicon properties for GaN device epitaxy," *physica status solidi c*, vol. 8, no. 5, pp. 1503-1508, 2011.
- [66] T. Hikosaka, H. Yoshida, N. Sugiyama, and S. Nunoue, "Reduction of threading

- dislocation by recoating GaN island surface with SiN for high-efficiency GaN-on-Si-based LED," *physica status solidi (c)*, vol. 11, no. 3-4, pp. 617-620, 2014.
- [67] Y. Sun *et al.*, "Room-temperature continuous-wave electrically injected InGaN-based laser directly grown on Si," *Nature Photonics*, vol. 10, no. 9, pp. 595-599, 2016.
- [68] T. Takeuchi *et al.*, "Quantum-confined Stark effect due to piezoelectric fields in GaInN strained quantum wells," *Japanese Journal of Applied Physics*, vol. 36, no. 4A, p. L382, 1997.
- [69] F. Bernardini, V. Fiorentini, and D. Vanderbilt, "Spontaneous polarization and piezoelectric constants of III-V nitrides," *Physical Review B*, vol. 56, no. 16, p. R10024, 1997.
- [70] D. A. Miller *et al.*, "Band-edge electroabsorption in quantum well structures: The quantum-confined Stark effect," *Physical Review Letters*, vol. 53, no. 22, p. 2173, 1984.
- [71] J. Cho, E. F. Schubert, and J. K. Kim, "Efficiency droop in light-emitting diodes: Challenges and countermeasures," *Laser & Photonics Reviews*, vol. 7, no. 3, pp. 408-421, 2013.
- [72] K. J. Vampola, M. Iza, S. Keller, S. P. DenBaars, and S. Nakamura, "Measurement of electron overflow in 450 nm InGaN light-emitting diode structures," *Applied Physics Letters*, vol. 94, no. 6, 2009.
- [73] J. Hader, J. Moloney, and S. Koch, "Density-activated defect recombination as a possible explanation for the efficiency droop in GaN-based diodes," *Applied Physics Letters*, vol. 96, no. 22, 2010.
- [74] L. Wang *et al.*, "Influence of carrier screening and band filling effects on efficiency droop of InGaN light emitting diodes," *Optics Express*, vol. 19, no. 15, pp. 14182-14187, 2011.
- [75] J. Iveland, L. Martinelli, J. Peretti, J. S. Speck, and C. Weisbuch, "Direct measurement of Auger electrons emitted from a semiconductor light-emitting diode under electrical injection: identification of the dominant mechanism for efficiency droop," *Physical review letters*, vol. 110, no. 17, p. 177406, 2013.
- [76] J.-J. Huang, H.-C. Kuo, and S.-C. Shen, *Nitride Semiconductor Light-Emitting Diodes (LEDs): Materials, Technologies, and Applications*. Woodhead Publishing, 2017.
- [77] M. D. Dawson and M. A. Neil, "Micro-pixelated LEDs for science and instrumentation," *Journal of Physics D: Applied Physics*, vol. 41, no. 9, p. 090301, 2008.
- [78] Z. Wang, X. Shan, X. Cui, and P. Tian, "Characteristics and techniques of GaN-based micro-LEDs for application in next-generation display," *Journal of semiconductors*,

vol. 41, no. 4, p. 041606, 2020.

- [79] Z. Fan, J. Lin, and H. Jiang, "III-nitride micro-emitter arrays: development and applications," *Journal of Physics D: Applied Physics*, vol. 41, no. 9, p. 094001, 2008.
- [80] J. Bai *et al.*, "A direct epitaxial approach to achieving ultrasmall and ultrabright InGaN micro light-emitting diodes (μ LEDs)," *ACS photonics*, vol. 7, no. 2, pp. 411-415, 2020.
- [81] M. S. Wong *et al.*, "High efficiency of III-nitride micro-light-emitting diodes by sidewall passivation using atomic layer deposition," *Optics express*, vol. 26, no. 16, pp. 21324-21331, 2018.
- [82] S. S. Konoplev, K. A. Bulashevich, and S. Y. Karpov, "From large-size to micro-LEDs: scaling trends revealed by modeling," *Physica Status Solidi (a)*, vol. 215, no. 10, p. 1700508, 2018.
- [83] Y. Cai, J. I. Hagggar, C. Zhu, P. Feng, J. Bai, and T. Wang, "Direct epitaxial approach to achieve a monolithic on-chip integration of a HEMT and a single micro-LED with a high-modulation bandwidth," *ACS applied electronic materials*, vol. 3, no. 1, pp. 445-450, 2021.
- [84] J. Bai *et al.*, "Ultrasmall, ultracompact and ultrahigh efficient InGaN micro light emitting diodes (μ LEDs) with narrow spectral line width," *ACS nano*, vol. 14, no. 6, pp. 6906-6911, 2020.

Chapter 2 Background

2.1 Semiconductors

Materials can be categorized into solid, liquid, gas, and plasma based on their physical states. The solid materials can be further divided based on their electrical conductivity into conductors, insulators, and semiconductors. Insulators exhibit extremely low electrical conductivity due to the absence of free electrons, with typical values ranging from 10^{-18} to 10^{-8} S/cm⁻¹. Conversely, conductors such as metals exhibit high electrical conductivity due to an ample number of free electrons, typically falling between 10^4 to 10^6 S/cm⁻¹ [1]. Semiconductors fall between these two categories, with conductivity that can be modulated by external means, such as temperature, applied fields, or doping, making them versatile for electronic applications.

2.1.1 Band Structure

The band structure refers to the distribution of the energy bands in a semiconductor material. It describes the energy states in which electrons are permitted to exist within the material. In isolated atoms, electrons exist in discrete energy levels. When atoms form a crystalline solid, interatomic interactions cause these discrete energy levels to overlap and spread out to form energy bands. In essence, a single crystal consists of valence and conduction bands [2-4]. The valence band is the highest occupied band and is completely filled with electrons at absolute zero temperature. In contrast, the conduction band is the energy band above the valence band and is usually empty at absolute zero temperature. The region between the two energy bands is known as the forbidden band, or 'band gap', where there are no allowed energy levels [5]. The band gap is defined as the energy difference between the bottom of the conduction band and the top of the valence band, where no energy states exist. Electrons must gain enough energy to be excited from the valence band into the conduction band to make the conductive. The size of the energy gap is a key factor in determining whether a material is a conductor, semiconductor or insulator. The energy band structure describes the energy states that electrons can occupy in a material, and the size of the band gap directly determines the conductivity of the material [6]. Figure 2.1 illustrates the energy gaps for three different types of solid-state materials.

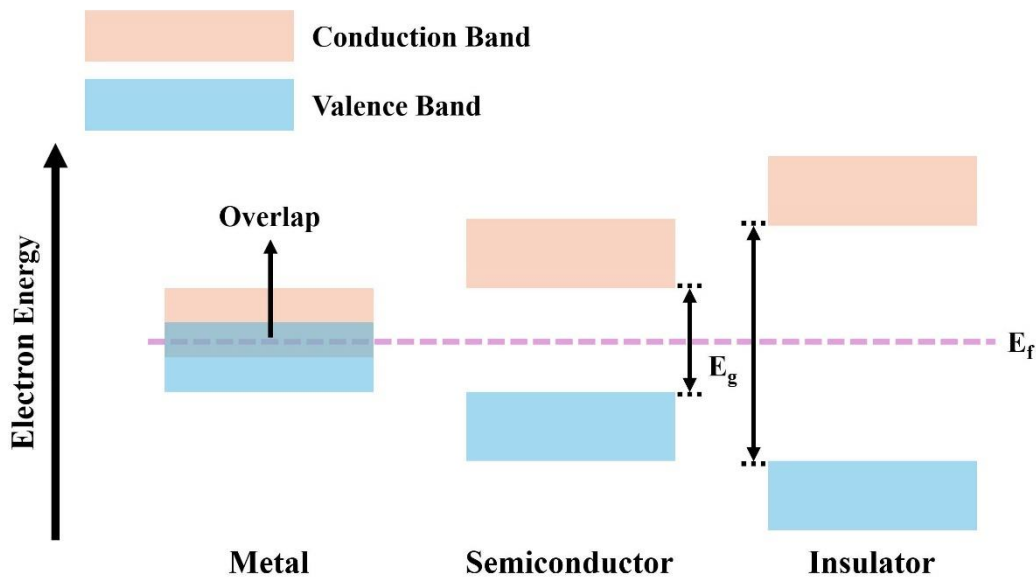


Figure 2-1 The energy gaps of a metal, semiconductor, and insulator. E_g represents the bandgap energy, while E_f indicates the Fermi level.

In insulators, electrons are usually trapped in the valence band, while the conduction band is empty, and the band gap between the two is large; it is usually difficult for electrons to gain enough energy to excite from the valence band to the conduction band, so the conductivity of such materials is negligible. However, by applying a high enough voltage to an insulator that the electric field is strong enough to strip electrons from the atoms, the conductivity of the material increases dramatically. This threshold voltage is called the breakdown voltage of the insulator.

In the case of conductors, the energy gap between the valence and conduction bands is very small, or there is an overlap between them, so this energy band structure allows electrons to move freely in a conductor, giving the material very high electrical conductivity. Semiconductors possess a band gap between insulators and conductors. Semiconductors can be made to conduct electricity under certain conditions by a series of external excitations that allow some of the electrons in the valence band to gain enough energy to cross the energy gap into the conduction band. In addition, the conductivity of semiconductor materials can be precisely controlled by doping, temperature, illumination and applied electric fields. This makes semiconductor materials a solid basis for the construction of a wide range of electronic devices.

In semiconductor energy band structures, the valence and conduction bands are located on either side of the Fermi energy level and have the highest occupied energy state and the lowest unoccupied

energy state, respectively [7]. When an electron in the valence band is excited, it gains enough energy to jump into the conduction band, leaving a hole in the valence band. When the electron in the conduction band recombines with the hole in the valence band, it can release energy equal to the difference between the two energy levels, usually in the form of a photon. Typical semiconductor band structures can be classified as direct bandgap and indirect bandgap based on the mechanism of electron transfer between the conduction and valence bands [6]. Figure 2-2 illustrates these two types of band structure.

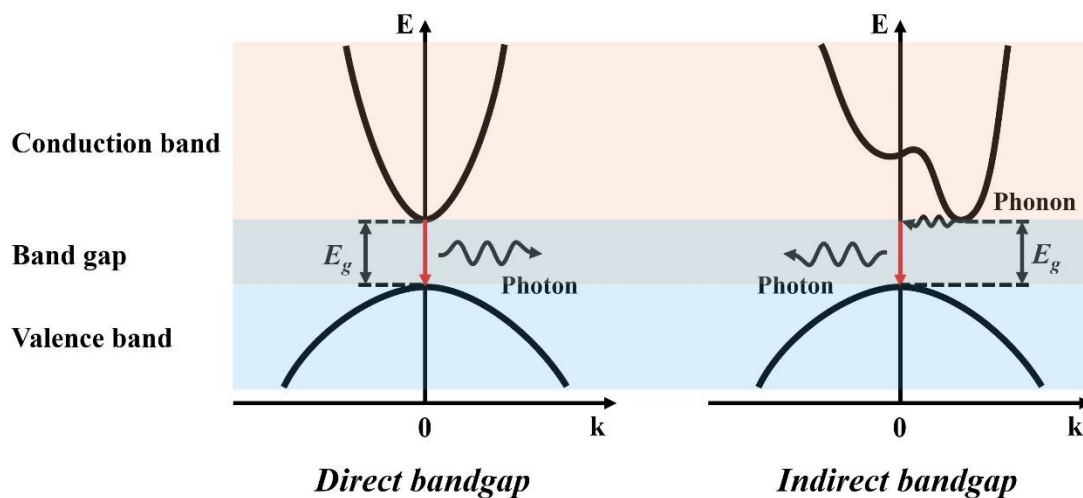


Figure 2-2 Schematic diagram of photon emission and band structures in direct and indirect bandgap semiconductor materials

In direct bandgap semiconductors, the highest point in the valence band and the lowest point in the conduction band have the same position in momentum space (k -vector). Therefore, there is no need to change the momentum of an electron as it excites into the conduction band or returns to the valence band; the transition of an electron in a direct bandgap structure is straightforward. In contrast, for indirect energy band structures, where the valence band maximum and the conduction band minimum are at different locations in momentum space, electron transitions between the two energy bands require the involvement of a third-particle to maintain momentum conservation (i.e., the k vector is constant) [8], while greatly reducing the probability of radiative recombination of electrons and holes. Since the electron-hole recombination process in direct bandgap structures does not involve any third-party particles (e.g. phonons) to assist in momentum conservation, the recombination of electron-hole pairs in direct bandgap semiconductors is much more efficient than

in indirect bandgap semiconductors, resulting in very fast recombination lifetimes, which means that the high optical efficiency in optical devices. Based on the above considerations, direct bandgap semiconductors such as gallium nitride and gallium arsenide are favoured for the manufacture of high-power emitters such as light-emitting diodes or laser diodes.

2.1.2 P-Type and N-Type Doped III-nitride Semiconductors

Intrinsic semiconductors are pure materials that have not been artificially doped, such as silicon (Si), germanium (Ge), and gallium nitride (GaN). At absolute zero, intrinsic semiconductors do not conduct electricity at all because they have no free electrons or holes to conduct current. Under thermal excitation, some of the electrons in the valence band gain enough energy to jump into the conduction band, thus making the material conductive. The electrical properties of an intrinsic semiconductor can be improved by introducing impurity atoms into a pure semiconductor, a process known as 'doping'. The doped semiconductors are classified into n-type (donor-doped) or p-type (acceptor-doped) categories, depending on the type of impurity atoms introduced. Doping introduces an extra energy level (impurity energy level) between the conduction band and the valence band, where the donor impurity adds extra electrons making it easier for electrons to be excited from the valence band to the conduction band (in the n-type), while the acceptor impurity creates extra holes (in the p-type), thus increasing the conductivity of the semiconductor. In III-nitride materials, when GaN is doped with a small amount of a Group-II element such as magnesium (Mg), the magnesium atoms replace gallium atoms and generate additional holes in the valence band. The introduction of Mg into GaN results in the material exhibiting p-type semiconductor characteristics, which are primarily influenced by free holes. Likewise, doping GaN with Group IV elements such as silicon (Si) leads to the creation of n-type semiconductors, which are dominated by free electrons. Si atoms can replace Ga atoms and provide additional electrons, allowing n-type semiconductors to have a high concentration of free electrons at room temperature [9]. Additionally, it should be noted that P-type doping is significantly more challenging than N-type doping due to the high acceptor energy level of Mg, which makes hole activation difficult. Moreover, Mg easily forms Mg-H complexes with residual hydrogen atoms from the growth process, leading to passivation and preventing the function of accepting electrons. These limitations collectively make P-type doping much more difficult compared to N-type doping.

2.1.3 Recombination

In semiconductor materials, when an electron absorbs energy and moves from the valence band to the conduction band, it creates a hole in the valence band and forms an electron-hole pair (EHP). Free electrons and holes can move freely within the semiconductor, and the excited electrons eventually return to the valence band to combine with the holes in a process known as recombination, which usually involves a release of energy. The recombination process can occur through a variety of mechanisms, but there are three primary types: Shockley-Read-Hall (SRH) recombination, radiative recombination, and Auger recombination.

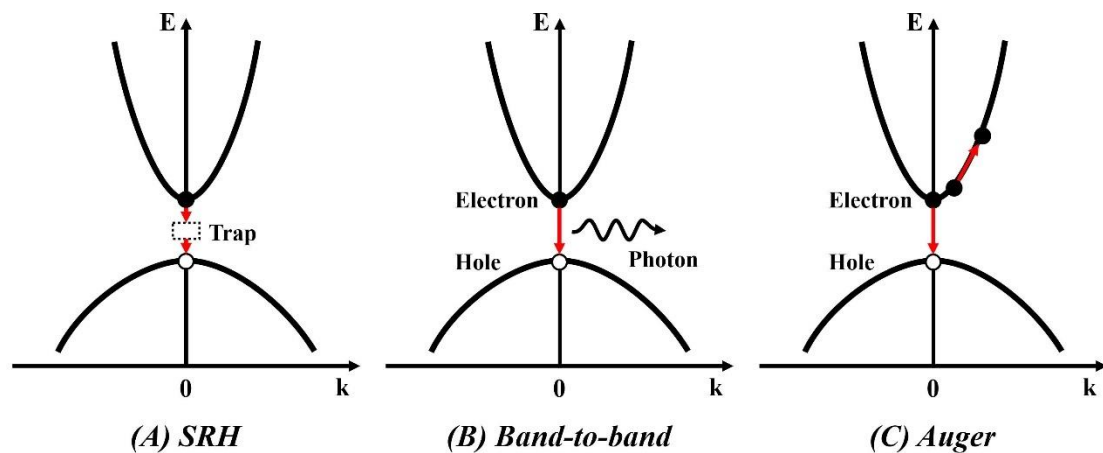


Figure 2-3 The three primary types of recombination process. (A) SRH, (B) Band-to-band, and (C) Auger recombination.

Shockley-Read-Hall (SRH) recombination is a type of non-radiative recombination and is one of the most common recombination mechanisms in semiconductors, mainly caused by defect states or impurity energy levels in the energy gap. These defect states or impurity energy levels provide an intermediate energy level between the conduction band and valence band, this intermediate energy level is called a 'trap' and is used to trap free electrons or holes. When the trap captures a free electron or hole, it changes the defect state from neutral to negatively or positively charged. The activated defect state can then trap another type of carrier, and if the defect state traps a pair of carriers (EHP), the pair will recombine in the defect state. This process usually releases energy in a non-radiative form [10, 11]. Figure 2-3A illustrates the fundamental mechanism with the SRH recombination process. The arrows in the figure illustrate the process by which free electrons can gradually descend

to the valence band. This occurs via intermediate energy levels induced by traps within the energy band.

Due to the principles underlying SRH recombination, the energy required for per transition is relatively small. The rate of SRH recombination (R_{SRH}) is contingent upon both the carrier concentration and trap density, and can be succinctly described as:

$$R_{SRH} = An \quad (2.1)$$

Where A represents the coefficient of SRH recombination and n signifies the carrier concentration.

Radiative recombination is the fundamental principle underlying the operation of light-emitting diodes (LEDs) and lasers. In this process, the energy released by the recombination of electrons and holes is emitted in the form of photons, resulting in light emission. Radiative recombination can occur by a variety of mechanisms, including band-to-band recombination, exciton recombination and donor-acceptor recombination. Each of these mechanisms involves different physical processes corresponding to different modes of electron and hole binding. Figure 2-3B illustrates band-to-band recombination, this recombination process is highly efficient as electrons can transition directly from the conduction band to the valence band without any intermediate states, and the energy of the emitted photon is determined by the band gap. In exciton recombination or donor-acceptor recombination, the energy of the emitted photon is dictated by the binding energy of the exciton or the disparity in energy levels between the impurities. The carrier recombination rate of radiative recombination (R_{Rad}) can be generally characterised as [12]:

$$R_{Rad} = Bn^2 \quad (2.2)$$

Where B represents the radiative recombination coefficient, typically in the range of 10^{-9} to 10^{-11} cm³/s for III-nitride materials and n signifies the carrier concentration.

Auger recombination is a form of non-radiative recombination characterised by a three-carrier process involving two carriers of the same type and one carrier of a different type. In this process, the energy released by the recombination of electrons and holes is not emitted as a photon. Instead, it is transferred to another electron or hole to provide additional energy. This excited electron or hole subsequently dissipates this energy in a non-radiative form, typically through processes such as heat generation or lattice vibrations. Figure 2-3C describes an Auger recombination process.

Auger recombination becomes notably pronounced at high carrier concentrations and stands as a significant contributor to efficiency degradation in high-brightness LEDs and lasers. This is primarily due to its adverse effect on reducing the number of electron-hole pairs, which is detrimental to both photovoltaic conversion and light emission [13]. The recombination rate of Auger recombination (R_{Aug}) can be expressed as follows:

$$R_{Aug} = Cn^3 \quad (2.3)$$

Where C is the Auger coefficient of recombination and n signifies the carrier concentration.

The carrier recombination lifetime is a pivotal parameter that characterizes the dynamics of carrier recombination in semiconductors and refers to the average time it takes for the excited electrons to recombine with holes. This parameter is important for understanding and designing semiconductor device characteristics as it directly affects the photovoltaic response speed and efficiency of the material. Longer recombination lifetimes mean that carriers can traverse greater distances within the semiconductor material prior to recombination, a characteristic that is advantageous for enhancing photovoltaic conversion efficiencies, such as those observed in solar cells. Conversely, for applications in general lighting, displays, and visible light communication (VLC), shorter recombination lifetime may be preferred to enhance internal quantum efficiency (IQE) and the maximum modulation bandwidth for VLC applications [14].

The total recombination lifetime (τ) of a semiconductor material can be described in terms of radiative (τ_{rad}) and non-radiative ($\tau_{non-rad}$) lifetimes, as illustrated by the subsequent equation [15, 16]:

$$\tau^{-1} = \tau_{rad}^{-1} + \tau_{non-rad}^{-1} \quad (2.4)$$

Typically, temperature and defect density are more likely to affect the non-radiative recombination process and hence the total carrier recombination lifetime.

2.1.4 LED Structure

An LED is a semiconductor device that generates light based on the recombination of electrons and holes. The fundamental configuration of the LED is a p-n junction, which is constructed upon a combination of p-type and n-type semiconductor materials. Due to the disparity in carrier

concentration between the p-type and n-type regions, carriers migrate by diffusion to areas of lower concentration to achieve equilibrium. This means that holes and electrons diffuse towards the n-type and p-type sides, respectively. This migration results in the formation of a depletion zone between these regions, accompanied by a built-in electric field spanning this region. Figure 2-4 depicts a standard operational circuit for a p-n junction-based LED.

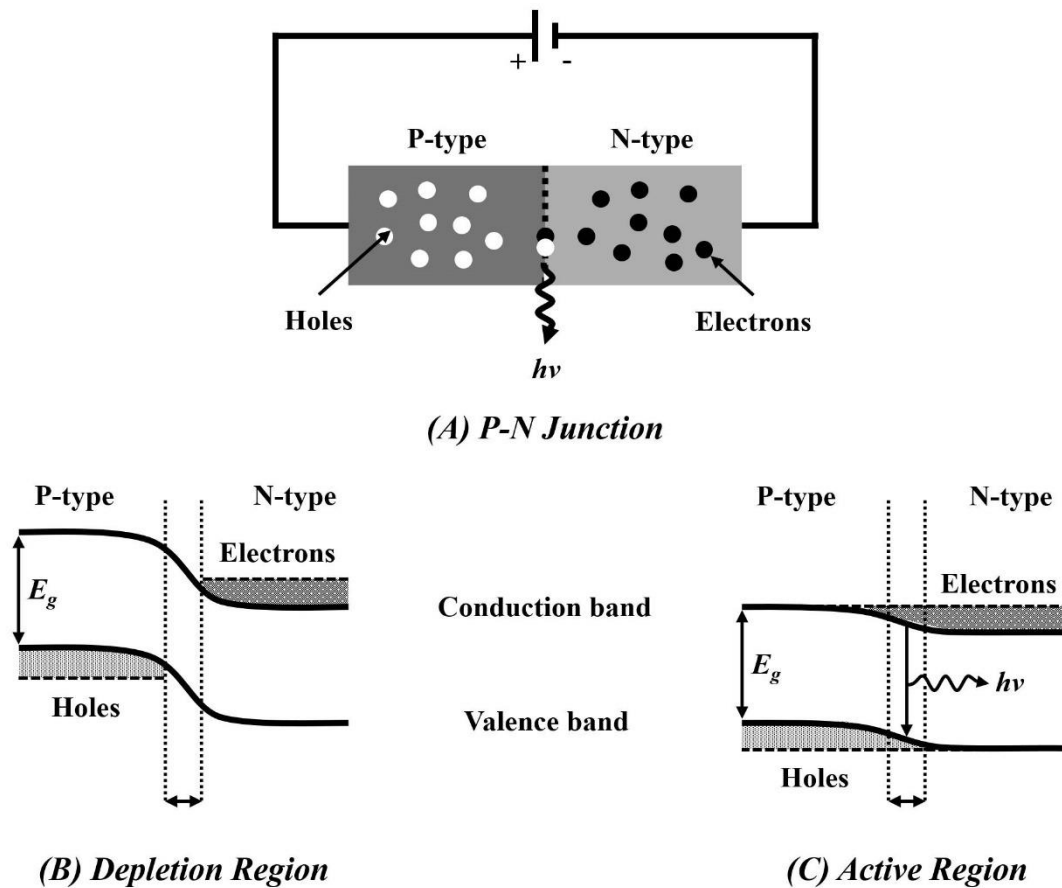


Figure 2-4 Schematic representation of (A) a p-n junction under forward bias; with an accompanying energy level diagram of a p-n junction under (B) zero bias, and (C) under forward bias conditions.

The built-in electric field inhibits carrier (electrons and holes) diffusion between the n-type and p-type regions. Once the field has attained sufficient strength, diffusion stops, and equilibrium is reached (Figure 2-4B). When a forward bias is applied to the p-n junction yield, electrons and holes are injected from the n-region and p-region, respectively, which breaks the original equilibrium state within the P-N junction, leading to a reduction of the depletion region, further diffusion of electrons and holes into the opposite region, and the formation of a new region called the active region. The electrons and holes recombine in the active region, emitting photons, as shown in Figure 2-4C.

While the emission of photons is a result of radiative recombination, the flow of current is maintained by the continuous injection of electrons and holes from the external circuit under forward bias. It can be seen that the emission of photons does not directly cause current flow; rather, both phenomena are consequences of carrier recombination in the active region.

2.2 III-Nitride Semiconductors

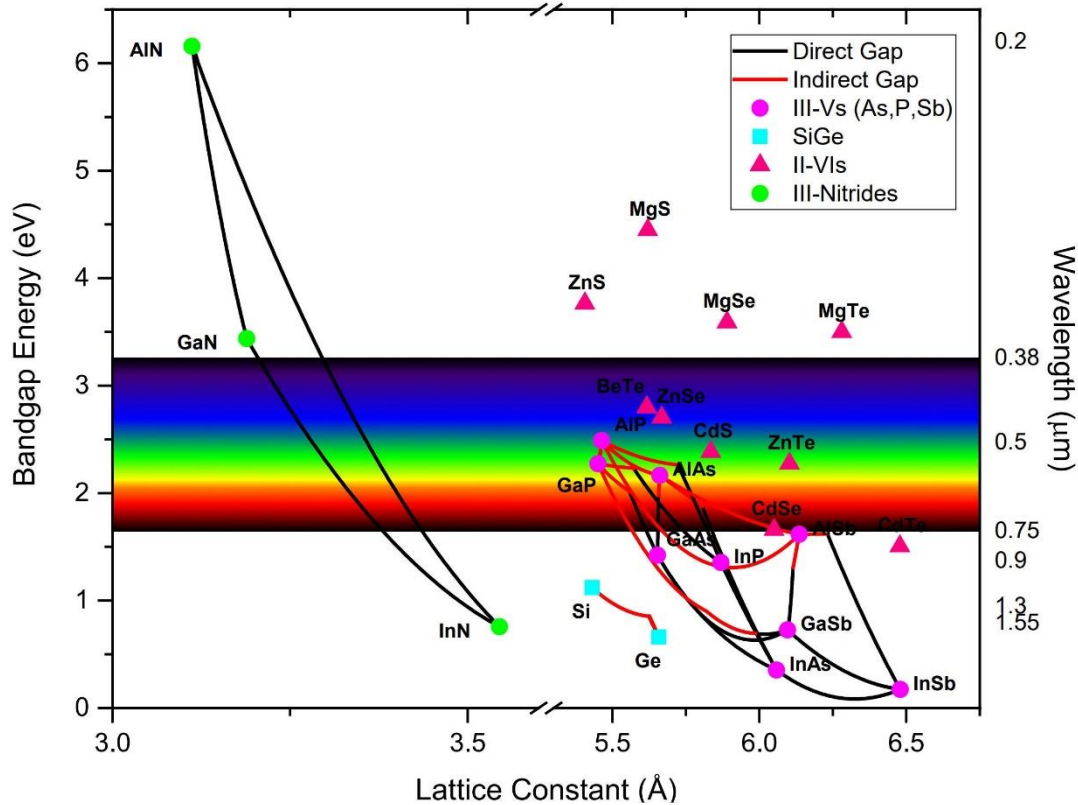


Figure 2-5 Bandgap and emission wavelength at room temperature plotted as a function of the lattice constant for common semiconductor materials. Reproduced with permission [17].

III-Nitride semiconductors, which are composed of nitrogen (N) and group III elements such as gallium (Ga), aluminium (Al), and indium (In), exhibit a range of properties that render them suitable for a variety of applications. For example, GaN and AlN are known for their wide bandgaps and high electron mobility, while InN is known for its narrow bandgap, with ternary alloys (InGaN, AlInN) ranging from the infrared to the ultraviolet wavelengths, rendering these materials suitable for optoelectronic and high-power electronic applications. Furthermore, compound semiconductors have an exceptional capacity for alloy formation, allowing for precise modification of their energy bandgap widths and relevant physical and chemical properties by adjusting of the

elemental ratios within these alloys. In optoelectronic applications, the wavelengths of light emitted by the alloys can be tuned by varying the content of each component in the alloys, enabling the development of light-emitting diodes (LEDs) and laser diodes (LDs) that can emit light across a spectrum of colours. Common III-nitride semiconductors include gallium nitride (GaN), indium nitride (InN), aluminium nitride (AlN), and their alloys such as aluminium gallium nitride (AlGaN), indium gallium nitride (InGaN), and aluminium indium gallium nitride (AlInGaN). [18]. Figure 2-5 illustrates the bandgap of III-nitride compound semiconductors, which cover a wide spectral region from the deep ultraviolet to the entire visible region up to near infrared [17].

2.2.1 Crystal Structure of III-Nitrides

III-nitride materials typically crystallise in the wurtzite structure, which is the most common phase. However, zinc blende and rock salt structures can also exist, but the rock salt structure is only stable under extremely high-pressure conditions, making it rare in natural environments. The zinc blende crystal structures can be formed on seed crystal substrates such as gallium arsenide which have their own cubic sphalerite structures. However, this zinc blende structure always exists a tendency to transform into the hexagonal wurtzite structure with more thermodynamically stability [19-21].

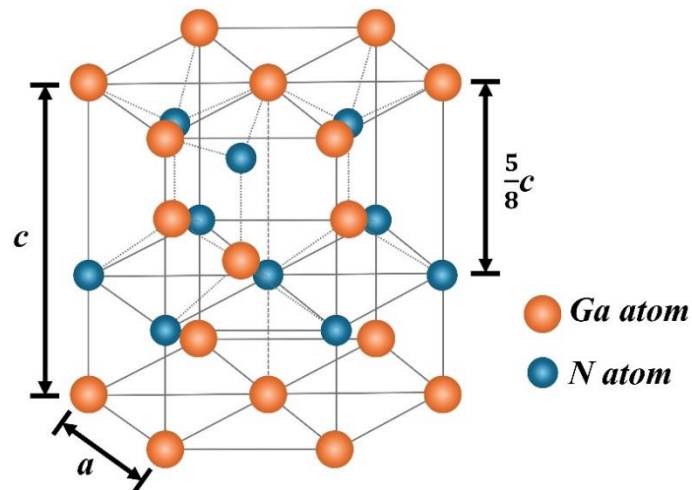


Figure 2-6 Schematic representation of the hexagonal wurtzite crystal structure of GaN.

The wurtzite structure is the most stable, prevalent and extensively utilised crystal structure within the III-nitrides. This thesis will concentrate exclusively on the study of the properties of III-nitride semiconductors with a wurtzite structure. In this structure, each nitrogen atom is bonded to four Group III atoms, forming a tetrahedral coordination. Similarly, each Group III atom is tetrahedrally

coordinated to four nitrogen atoms. This mutual tetrahedral coordination is a fundamental feature of the wurtzite structure, which has hexagonal crystal system symmetry [22]. Figure 2-6 shows a schematic of wurtzite GaN. Two interpenetrating sublattices of Ga and N atoms are staggered along the c-axis (perpendicular to the basal plane) with an offset equal to 5/8 of the cell height. Furthermore, the lattice parameters of the Wurtzite structure are defined by two key parameters: the in-plane lattice parameter (a) and the out-of-plane lattice parameter (c). The former represents the distance between adjacent atoms within the same basal plane, while the latter denotes the distance between basal planes of identical composition. Table 2-1 provides a detailed account of the lattice constants and bonding parameters of typical III-nitrides [22-25].

Table 2-1 Crystal parameters of wurtzite structure III-nitrides [22-25].

	AlN	GaN	InN
In-plane lattice constant (a_0) (Å)	3.111	3.189	3.533
Out-of-plane lattice constant (c_0) (Å)	4.982	5.185	5.705
c_0 / a_0	1.601	1.625	1.615
Bond length (Å)	1.89	1.94	2.15
Bandgap (E_g) (eV)	6.026	3.390	0.641
Bond energy (E) (eV)	2.88	2.20	1.93

The Miller indices (h, k, i and ℓ) were introduced to accurately describe the planes and directions of the lattice in hexagonal and rhombic crystal systems [26]. The indices h, k, and i represent the reciprocal of plane intercept with the a_1 , a_2 , and a_3 axes within the basal plane, respectively. It is important to note that the relationship between the three indices is:

$$h + k + i = 0 \quad (2.5)$$

Furthermore, the index ℓ represents the reciprocal of the plane intercept along the c -axis of the crystal (the axis perpendicular to the base plane). Figure 2-7 illustrates the Bravais-Miller Index coordinate system in a wurtzite unit cell.

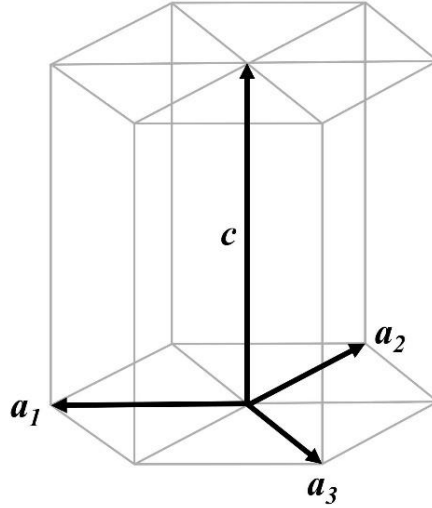


Figure 2-7 Schematic representation of Bravais-Miller Index in hexagonal crystal structure.

III-nitride crystals (GaN, AlN, and InN) can exhibit two different crystal polarities due to the lack of inversion symmetry along the c -axis. This non-centrosymmetric nature of the wurtzite structure gives rise to different polarities depending on the orientation of the atomic layers. Further, the underlying reason for the two polarities is due to the non-central symmetry in the Wurtzite structure. These two different crystal polarities are determined by the atom of the termination surface in the growth direction along the c -axis. As the example of gallium nitride, the surface terminated with the group III element atom gallium is known as the Ga-polar, and the polarity of this surface is along the c -axis in the positive direction, with a Miller index usually expressed as (0001). The other, the surface terminating with a nitrogen atom, is known as N-polar and the Miller index is expressed as (000-1), with the surface polarity in the opposite direction along the c -axis. The Ga-polar gallium nitride usually exhibits a smooth surface morphology, whereas N-polar gallium nitride has a rough surface and shows a hexagonal mound structure. The difference in surface morphology is due to the different mobility of gallium and nitrogen atoms on the surface. When growing GaN on sapphire by MOCVD, the usual growth conditions favour the formation of Ga-polar surfaces. In addition, Ga-polar gallium nitride has high chemical stability and low surface defect density compared to N-polar

gallium nitride, which leads Ga-polar gallium nitride the material of choice for the fabrication of optoelectronic and microelectronic devices. The polarity of a semiconductor material also has a significant effect on other aspects such as chemical properties, doping, crystal growth rate, defect generation and internal polarisation direction [27].

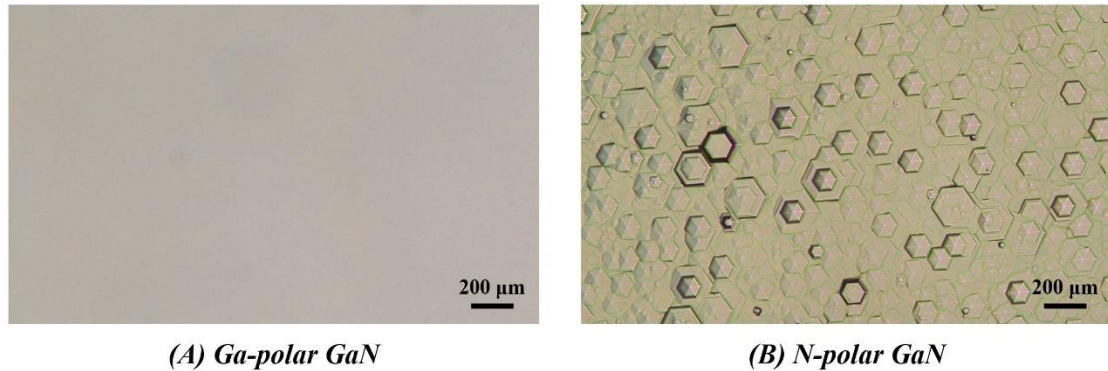


Figure 2-8 Optical microscopy images of (A) Ga-polar GaN and (B) N-polar GaN.

2.2.2 Defects in III-Nitrides

III-nitride semiconductor materials are characterised by a periodic crystal structure, where atomic positions are determined by the unit cell lattice parameters. Ideally, a perfect crystal exhibits complete periodicity. However, in practice, deviations from the ideal lattice structure occur during crystal growth due to external factors, leading to the formation of crystal defects. These defects can be classified based on their dimensionality into zero-dimensional (0D), one-dimensional (1D), two-dimensional (2D), and three-dimensional (3D) defects.

0D defects, also known as point defects, are characterised by the presence of localised irregularities, such as vacancies, interstitials, and substitutional impurities, which manifest as missing, misplaced, or foreign atoms within the crystal structure. 1D defects, or line defects, are caused by atomic displacement along a specific direction, with dislocations being the most common example. 2D defects, referred to as planar defects, occur due to atomic misalignment within a plane. The most common example of such a defect is the stacking fault. Lastly, 3D defects, or volume defects, are macroscopic in nature and involve a large volume of atoms, leading to the formation of pits, voids, and cracks. The presence of defects is a significant challenge in the field of crystalline materials, with the potential to have a significant impact on the electrical and optical properties of the material.

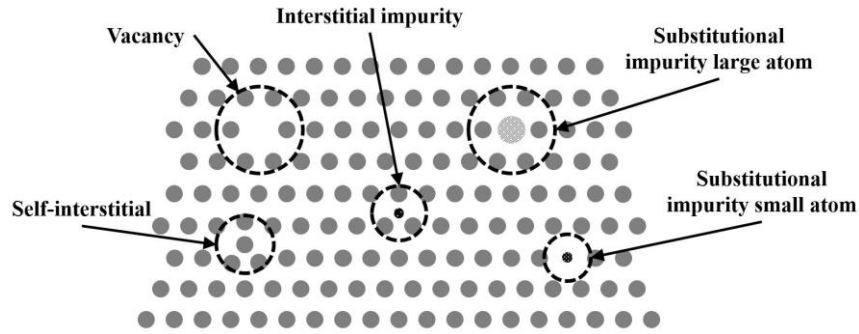


Figure 2-9 Diagrammatic representation of typical point defects.

Point defects refer to the absence of an atom at a lattice site, the presence of an atom at a non-lattice position, or the substitution of a host atom by a foreign impurity. As illustrated in Figure 2-9 Diagrammatic representation of typical point defects. Figure 2-9, there are three primary categories of point defects: vacancies, interstitials, and substitutional impurities. A vacancy is defined as the absence of an atom from its customary lattice position, resulting in an unoccupied lattice site. In III-nitride semiconductors, nitrogen vacancies and gallium vacancies are among the most frequently observed point defects. Nitrogen vacancies are a primary contributor to unintentional n-type doping in GaN, while gallium vacancies are closely associated with yellow band emission, which significantly impacts the optical properties of the material. Therefore, point defects play a crucial role in doping mechanisms, carrier concentration, and luminescence properties in III-nitride semiconductors.

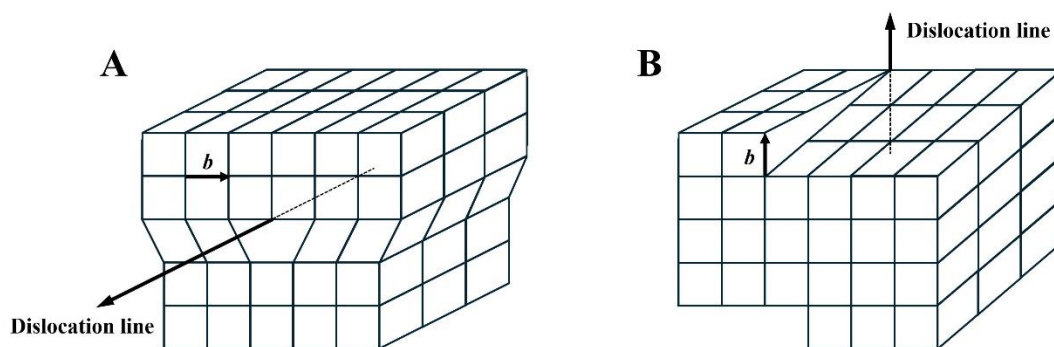


Figure 2-10 Diagrammatic representation of (A) an edge dislocation and (B) a screw dislocation.

Dislocations are one-dimensional line defects that occur when there is a misalignment of atomic planes within a crystal structure. The classification of dislocations is typically based on the spatial relationship between their Burgers vector (b) and the dislocation line. The three primary types of

dislocation are as follows: edge dislocations Figure 2-10A, screw dislocations Figure 2-10B, and mixed dislocations. For an edge dislocation, which forms when an extra atomic plane is inserted into the lattice, a local lattice distortion occurs. The Burgers vector is perpendicular to the dislocation line. In the case of screw dislocations, atomic planes undergo shear displacement, resulting in a helical structure. The Burgers vector is parallel to the dislocation line. Furthermore, a mixed dislocation exhibits characteristics of both edge and screw dislocations, representing a hybrid form of both. In III-nitride emitters, dislocations function as non-radiative recombination centre, which results in a degradation of their luminescence efficiency.

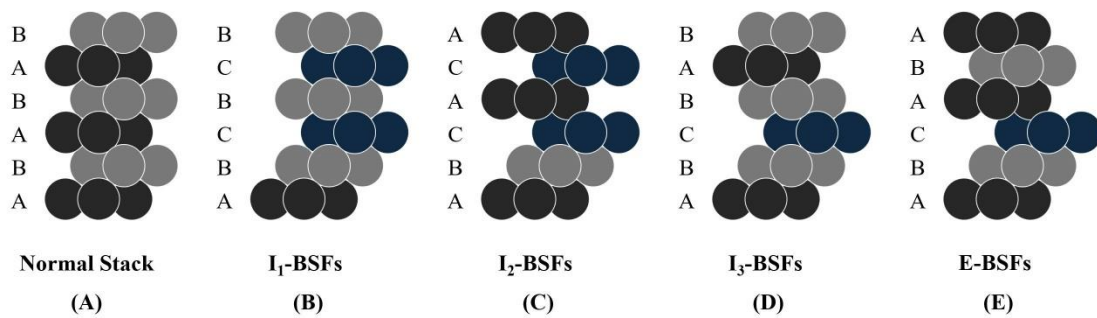


Figure 2-11 Diagrammatic representation of the (A) normal stacking sequence and (A-E) various types of basal stacking faults (BSFs) in wurtzite III-nitride semiconductors.

Stacking faults (SFs) are 2D planar defects in crystal structures, characterised by localized disruptions in the regular stacking sequence of atomic layers, thereby disrupting the periodic arrangement of the crystal lattice. In an ideal crystal, atomic layers exhibit a specific stacking sequence, such as ABABAB or ABCABC, which are also termed basal plane stacking faults (BSFs). However, when the stacking sequence is disturbed, for instance by the insertion of additional atomic layers or by the misalignment of existing layers, layer faults are formed. Depending on the specific error in the stacking sequence, stacking faults can be classified into two main types: intrinsic basal stacking faults (I-BSFs) and extrinsic basal stacking faults (E-BSFs). I-BSFs are formed when the original atomic layer is either removed or replaced by another atomic layer. In contrast, E-BSFs result from the insertion of an additional atomic layer into the original stacking sequence.

2.2.3 Material Properties of III-Nitrides

Table 2-2 presents the basic material electrical and thermal properties of GaN and other common

semiconductor materials. Electron mobility describes the speed at which electrons move under the force of an electric field, is one of the most important parameters for understanding semiconductor materials and designing semiconductors and reflects the ability of electrons to move through semiconductor materials. The electron mobility of a semiconductor material is affected by several factors including crystal structure, external temperature, electric field strength, doping concentration and defects. The reported electron mobility of GaN varies because the crystal quality of the semiconductor material affects its electron mobility and the quality of the GaN is affected by the substrate, growth technique and growth conditions. The highest reported experimental data for GaN electron mobility currently is $1245 \text{ cm}^2\text{V}^{-1}\text{s}^{-1}$, reported by D. C. Look in 2001 [28], prior to which the electron mobility of a typical GaN epitaxial layer was about $1000 \text{ cm}^2\text{V}^{-1}\text{s}^{-1}$. The table also shows that GaN has superior breakdown voltage and thermal conductivity compared to GaAs, InP and Si, has a higher melting point than other materials. The exceptional physical properties of GaN render it an optimal choice for specific applications, particularly in field of high-power and high-frequency electronics.

Table 2-2 Electrical and thermal properties of common semiconductor materials at 300K [1, 28-35].

Materials	Electron Mobility ($\text{cm}^2\text{V}^{-1}\text{s}^{-1}$)	Thermal Conductivity ($\text{W} \cdot \text{cm}^{-1}\text{K}^{-1}$)	Breakdown Field (kVcm^{-1})	Melting Point ($^{\circ}\text{C}$)
GaN	1245	2.3	5000	2500
GaAs	9400	0.55	400	1238
InP	4000	0.68	500	1062
Si	1400	1.56	300	1414

GaN also has excellent chemical and thermal stability compared to other semiconductor materials due to its unique crystal structure and chemical bonding properties. Ga-polar GaN is chemically inert and resistant to most acids and alkalis. However, some specific crystal facets and defects of

Ga-polar GaN and N-polar GaN can be etched by specific chemical reagents, such as phosphoric acid (H₃PO₄) and potassium hydroxide (KOH) [36, 37]. The majority of recent research on GaN-based LEDs is based on Ga-polar GaN. Selective etching of patterned μ LED substrates using KOH solution under UV lamp irradiation is a critical step prior to μ LED growth in this thesis.

2.2.4 Alloys and Tunable Bandgaps

Tuning the composition of alloys of III-nitride materials (e.g., AlN, GaN, and InN) in order to modify their bandgap (E_g) and lattice constants (a) is a key strategy for achieving specific electronic and optoelectronic device properties. According to Vegard's law, the lattice constants of an alloy can be considered as a linear combination of the lattice constants of its constituents [38].

For a binary alloy A_xB_{1-x} consisting of two elements A and B, the lattice constant $a_{A_xB_{(1-x)}}$ can be expressed by the equation below:

$$a_{A_xB_{(1-x)}} = xa_A + (1-x)a_B \quad (2.6)$$

where x is the molar fraction of element A in the alloy ($0 \leq x \leq 1$). a_A and a_B refer the lattice constants of the pure elements A and B, respectively.

When using Vegard's law to calculate the lattice constants of AlGa_xN or InGa_xN, the AlGa_xN (or InGa_xN) can be considered as a binary alloy system consisting of AlN (or InN) and GaN and calculated through the equation:

$$a_{Al_xGa_{(1-x)}N} = xa_{AlN} + (1-x)a_{GaN} \quad (2.7)$$

Where $a_{Al_xGa_{(1-x)}N}$ is the lattice constant of the AlGa_xN alloy, x is the mole fraction of AlN in the AlGa_xN alloy, a_{AlN} and a_{GaN} refer the lattice constants of the AlN and GaN, respectively.

For the ternary alloy system, the formulae must take into account the molar ratios of the three elements, using AlInGa_xN as an example:

$$a_{Al_xIn_yGa_{(1-x-y)}N} = xa_{AlN} + ya_{InN} + (1-x-y)a_{GaN} \quad (2.8)$$

Where $a_{Al_xIn_yGa_{(1-x-y)}N}$, a_{AlN} , a_{InN} and a_{GaN} denote the lattice constants of AlInGa_xN, AlN, InN and GaN, respectively, and x , y , and $(1-x-y)$ denote the molar fractions of AlN, InN, and GaN in the alloys, respectively.

It is important to note that Vegard's law provides an idealised linear relationship for predicting the lattice constants of alloys. However, in practice, the real lattice constants may deviate from this linear model due to the complex interactions that may exist between different elements, and the more diverse the elements in an alloy, the more likely it is that the predictions by Vegard's law will deviate from reality.

The calculation of the bandgap of semiconductor alloys is more complicated because the bandgap of an alloy depends not only on the bandgap of its constituent elements, but is also influenced by the composition, microstructure and interactions of the alloy, and is not a simple linear relationship with the constituent elements. Nevertheless, the prediction of the bandgap of an alloy can be initially estimated using Vegard's law and corrected by introducing the "bowing effect" parameter, which can be described by the following equation:

$$E_{g(x)} = xE_{g,A} + (1 - x)E_{g,B} - bx(1 - x) \quad (2.9)$$

Where $E_{g(x)}$ is the bandgap of the alloy, $E_{g,A}$ and $E_{g,B}$ represents the bandgaps of components A and B respectively. x is the proportion of component A in the alloy, and b is a bowing parameter describing the non-linear relationship of the bandgap as a function of the component proportion.

The bandgaps and corresponding emission wavelengths of typical III-nitrides are listed in Table 2-3. InN has a very narrow bandgap, and the InGaN alloy formed by combining it with GaN is able to achieve a wide range of bandgap adjustment (0.7 eV ~ 3.4 eV) by turning the In content due to the significant difference in the bandgap of the two materials, and its emission wavelength is able to cover the full spectrum of visible light (380 nm ~ 740 nm), within near-ultraviolet (UV) to part of near-infrared (NIR) range (365 nm ~ 1771 nm). Meanwhile, the bandgap width of AlGaN alloys composed of AlN and GaN can be achieved from 3.4 eV to 6.2 eV by changing the Al content, and the emission wavelength of the AlGaN can be adjusted in the deep ultraviolet (DUV) to ultraviolet (UV) region (200 nm ~ 365 nm). Thus, III-nitride materials show great potential for applications covering the spectral range from the deep ultraviolet to the near infrared due to their adjustable bandgap and excellent optoelectronic properties.

Table 2-3 Band gaps and corresponding emission wavelengths of typical III-nitride materials [37].

III-nitride Materials	Bandgap (eV)	Wavelength (nm)
GaN	3.4	365
AlN	6.2	200
InN	0.7	1771
AlGaN	3.4 ~ 6.2	200 ~ 365
InGaN	0.7 ~ 3.4	365 ~ 1771

2.2.5 Internal Polarizations

The spontaneous polarisation of the material is mainly caused by the asymmetry of the crystal structure of the material, and in the case of III-nitrides such as AlN, GaN and InN they have a non-centrosymmetric wurtzite crystal structure and therefore have a significant spontaneous polarisation effect, a phenomenon which is also known as the intrinsic polarisation of the material, which is independent of the strain state. An important cause of the polarisation phenomenon is the difference in electronegativity between atoms of group-III elements (Al, Ga, In) and nitrogen atoms. This difference in electronegativity leads to a degree of ionisation of the III-N bond, which results in the formation of an intrinsic electric dipole moment in the chemical bond. Typically, in semiconductor materials with symmetric crystal structures, such as cubic crystals, the internal electric dipole moments cancel each other out on a macroscopic scale, resulting in a total dipole moment of zero for the entire crystal system. However, this cancellation is incomplete in non-centrosymmetric crystal structures, triggering a spontaneous polarization in GaN, with the net dipole moment pointing in the [000-1] direction. For III-nitride alloys, their spontaneous polarization values P_{sp} can be estimated by interpolation using Vegard's law [39]:

$$P_{sp,Al_xGa_{(1-x)}N} = xP_{sp,AlN} + (1 - x)P_{sp,GaN} \quad (2.10)$$

where $P_{sp,AN}$ refers to the spontaneous polarisation of III nitrides (e.g. AlN or InN), $P_{sp,GaN}$ is the spontaneous polarisation of GaN, and x is the mole fraction of component A (Al or In) in the alloy.

When an external stress (compression or tension) is applied to a III-nitride material, the III-group atoms (Al, Ga, In) and the nitrogen atoms (N) are displaced from their original relative equilibrium positions. This displacement changes the charge distribution within the material, resulting in the positive and negative centres of charge no longer coinciding, thus generating electric dipole moments in the crystals, a phenomenon known as piezoelectric polarisation. The strain introduced into a crystal can usually be described as a combination of isotropic in-plane ($\varepsilon_{xx} = \varepsilon_{yy}$) and out-of-plane strains (ε_{zz}) and is calculated by comparing the lattice constants in the strained state with those in the unstrained state, the following equations can be used to express the strain:

$$\varepsilon_{xx} = \varepsilon_{yy} = \frac{(a - a_0)}{a_0} \quad (2.11)$$

$$\varepsilon_{zz} = \frac{(c - c_0)}{c_0} \quad (2.12)$$

Where ε_{xx} and ε_{zz} are the in-plane and out-of-plane strains, respectively; a and c are the lattice constants in the strained state, and a_0 and c_0 are the lattice constants in the unstrained state.

The piezoelectric polarisation density P_{pz} in a particular direction (in the z direction, for example) is related to the in-plane strain and the out-of-plane strain, which can be calculated by an equation of the following form:

$$P_{pz} = e_{31}(\varepsilon_{xx} + \varepsilon_{yy}) + e_{33}\varepsilon_{zz} \quad (2.13)$$

In this equation, e_{31} and e_{33} denote the piezoelectric constant describing the strength of the piezoelectric effect of a material in response to strain, and they represent the coefficients of piezoelectric polarisation along the direction perpendicular to these strains when in-plane and out-of-plane strains are applied, respectively.

Thus, the total polarisation value (P_{Total}) for a semiconductor material with piezoelectric properties can be described as the sum of its spontaneous (P_{sp}) and piezoelectric polarization (P_{pz}), which can be expressed by the following equation:

$$P_{Total} = P_{sp} + P_{pz} \quad (2.14)$$

In bulk semiconductor materials, an electric field is induced by internal spontaneous polarisation. This built-in electric field is usually cancelled out by the free carriers accumulated at the surface of the material, and this cancellation results in a zero macroscopic electrostatic field across the material. However, in heterostructures such as AlGaN/GaN and InGaN/GaN, the difference in spontaneous polarisation between the different material layers generates an additional electric field at the quantum well interface, which is referred to as the built-in electrostatic field. At the same time, the quantum well is sandwiched between two thicker layers of the barrier and is usually forced to adopt the same lattice constant as the barriers. Due to the mismatch in lattice constants between the quantum well material and the barrier material, the quantum well is subjected to strain, causing piezoelectric polarisation. For III-nitride materials with non-centrosymmetric lattices, this piezoelectric polarisation induced by strain will generate an additional piezoelectric field.

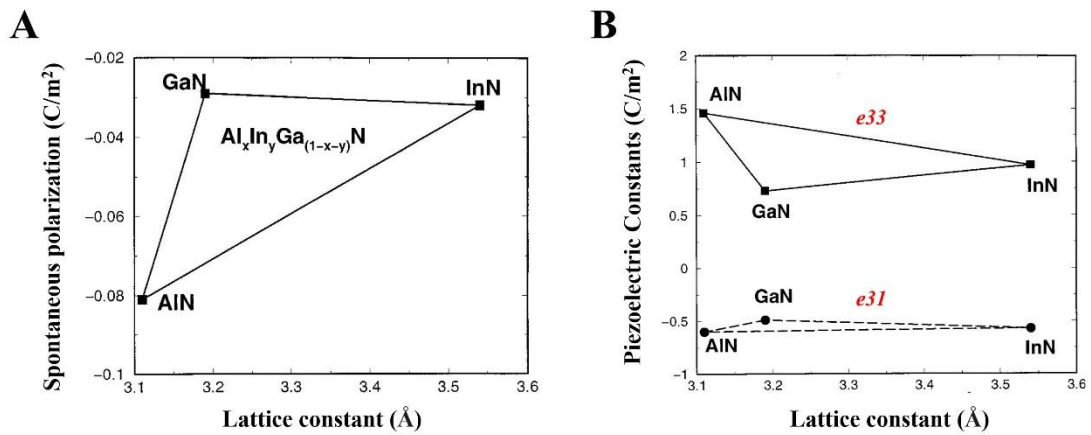


Figure 2-12 (A) Spontaneous polarizations in III-nitrides ($Al_xIn_yGa_{(1-x-y)}N$) alloys according to a Vegard-like rule; (B) Piezoelectric coupling constants e_{33} (squares) and e_{31} (dots). Reproduced with permission [40].

Figure 2-12 illustrates the spontaneous polarisation and piezoelectric coefficient of III-nitrides and their alloys as a function of lattice constant. It can be seen from Figure 2-12A that the spontaneous polarisation coefficient of AlN is about three times that of GaN, and when AlGaN and GaN form a heterostructure, the AlGaN layer will have a strong spontaneous polarisation. In addition, AlN has a slightly smaller lattice constant than GaN, so the AlGaN layer experiences tensile strain in the AlGaN/GaN quantum well. This strain induces piezoelectric polarisation in the same direction as the spontaneous polarisation, both pointing in the [000-1] direction, which enhances the overall

polarisation effect in the structure. For the InGaN/GaN heterostructure, the spontaneous polarisation of InGaN is similar of GaN, but since the lattice constant of InGaN is significantly larger than that of GaN, the InGaN layer is subjected to compressive strain in the InGaN/GaN quantum well. This compressive strain leads to the generation of a piezoelectric polarisation that is oriented in a direction opposite to the spontaneous polarisation, aligning with the [0001] orientation [40].

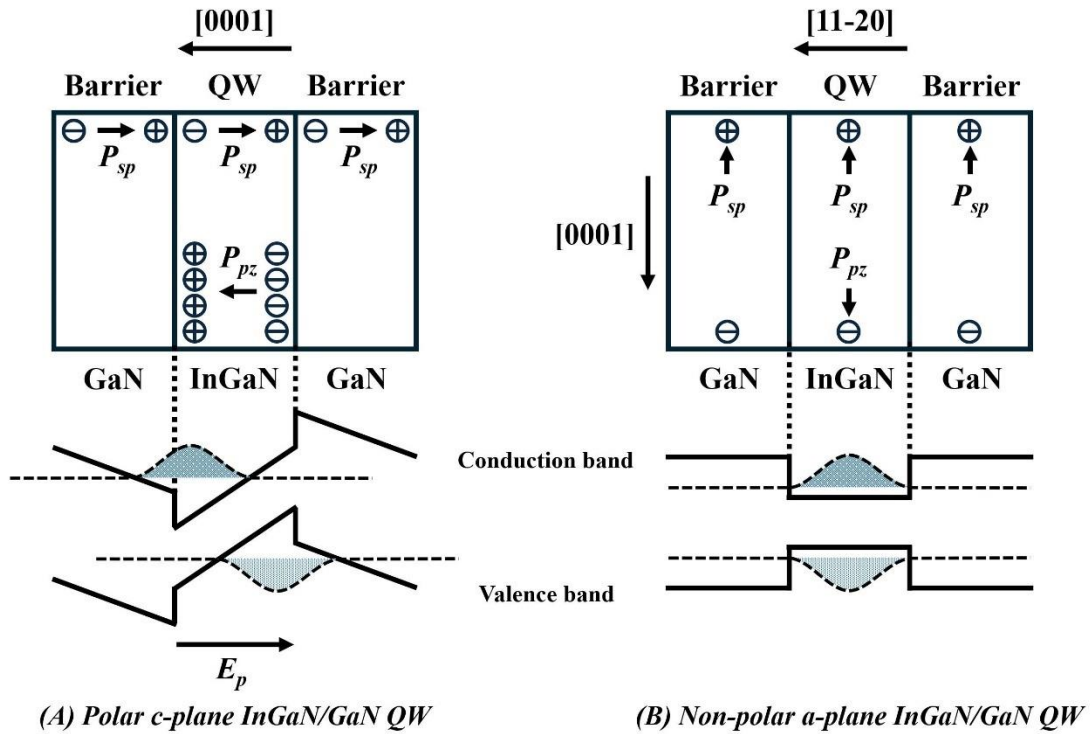


Figure 2-13 Schematic representation of the polarization orientation and band structure of (A) a polar, and (B) a non-polar InGaN/GaN quantum well.

In c-plane InGaN/GaN QW structures (Figure 2-13A), the built-in electric field generated by spontaneous polarisation and piezoelectric polarisation leads to a tilting of the energy bands in the potential well. The built-in electric field pushes electrons and holes to opposite sides of the quantum well, which causes them to separate spatially. This separation reduces the overlap of electrons and holes in the quantum well, thereby affecting their recombination efficiency and directly affects the optical efficiency of optoelectronic devices such as LEDs and LDs. This phenomenon caused by the electric field is known as the QCSE. In addition, the built-in electric field generated by spontaneous polarisation and piezoelectric polarisation is significantly reduced or eliminated in QWs with non-polar (Figure 2-13B) or semi-polar growth directions due to the symmetry of the crystal structure, which contributes to increasing the wave function overlap of electrons and holes in the quantum

wells, thus increasing the recombination efficiency and optical efficiency. This leads to the reduction of QCSE. Typically, the commonly chosen growth directions for non-polar quantum wells include the a-plane [11-20] or m-plane [10-10].

The QCSE phenomenon has a complex effect on the properties of III-nitride based heterostructures in several ways. In quantum well structures, the distortion of the energy band structure due to the built-in electric field reduces the bandgap energy, thus inducing a red-shift in the emission wavelength, as shown in the Figure 2-13A. This red-shift theoretically facilitates the achievement of longer wavelength emission, which is useful for developing the emission wavelength range of InGaN/GaN LEDs into the longer wavelength region. However, at high injection currents, the carrier concentration in the quantum well increases, leading to shielding of the built-in electric field, which reduces the energy band distortion due to QCSE, resulting in a shift of the emission wavelength towards the short wavelength direction (i.e. blue shift). This blue shift affects the wavelength stability of the device and presents a challenge for applications that require precise control of the emission wavelength. In addition, the reduced overlap of the electron and hole wavefunctions leads to a slowing of the radiative recombination process and an increase in the radiative recombination lifetime. This reduces the contribution of each carrier to the luminescence and decreases the internal quantum efficiency (IQE).

QCSE is also a major challenge for InGaN/GaN QW emitters, where the In content in the InGaN quantum well plays a critical role in realising longer emission wavelengths, in particular green and yellow luminescence. The lattice mismatch between the InGaN alloy and the GaN substrate increases with increasing In content, leading to the introduction of more strain into the quantum well, which enhances the piezoelectric effect due to the lattice asymmetry. The combined effect of the strain-induced piezoelectric polarisation and the spontaneous polarisation of the InGaN alloy itself creates a strong built-in electric field that exacerbates the QCSE. As a result, the energy band structure in the quantum well is significantly distorted, and the spatial distributions of electrons and holes are further separated, reducing their overlap integrals, which directly leads to the reduction of radiative recombination efficiency and is one of the main reasons for the lower efficiency of long-wavelength InGaN-based LEDs.

2.2.6 High-Electron-Mobility Transistor (HEMT)

Due to their unique electrical and physical properties, the III-nitrides show great potential and advantages in the field of high power and high frequency electronic devices. GaN-based HEMTs have significant advantages over GaAs-based HEMTs and other conventional HEMTs, including higher bandwidth, higher breakdown voltage, superior thermal stability and fast switching characteristics. Moreover, GaN-based HEMTs can achieve comparable cutoff frequency (f_T) and maximum oscillation frequency (f_{max}) due to their excellent electrical properties of the GaN, which is critical for RF applications and microwave frequencies [41-43].

The essence of HEMT is the utilisation of bandgap differences of semiconductor materials to form an ultrathin conductive channel with high electron mobility, known as a "two-dimensional electron gas" (2DEG). In AlGaAs/GaAs-based HEMTs, the small bandgap difference and low spontaneous polarisation require modulation doping impurities within the AlGaAs layer to form 2DEG by means of enhancing the electric field at the interface. In contrast, AlGaN/GaN-based HEMTs exhibit larger bandgap differences and significant polarisation (spontaneous and piezoelectric) effects, which can spontaneously form a 2DEG without doping. Moreover, the high carrier density and mobility in the 2DEG layer of AlGaN/GaN HEMTs result in low on-resistance, making them superior to Si/SiC-based devices for applications requiring high efficiency and high frequency [44-46].

Baliga's Figure of Merit (BFoM) and Johnson's Figure of Merit (JFoM) are two important parameters for evaluating the performance of power semiconductor devices, and are defined by the following equations:

$$BFoM = \epsilon_r \epsilon_0 \mu E_c^3 \quad (2.15)$$

Where ϵ is the permittivity of the material, ϵ_r is the relative permittivity, ϵ_0 is the permittivity of the vacuum, μ is the electron mobility and E_c is the critical electric field of the material.

$$JFoM = \frac{E_c v_{sat}}{2\pi} \quad (2.16)$$

Where E_c represents the critical electric field of the material and v_{sat} is the saturation drift velocity of the electrons.

These parameters help to theoretically quantify and comparison of the potential of different semiconductor materials for use in power device applications. The BFoM is used to evaluate the performance of semiconductor materials in power applications, with a particular focus on their efficiency in high-voltage applications [47]. This parameter combines the electron mobility, critical electric field and dielectric constant of a material to measure the ability of a material to withstand high voltages at a given electric field without breakdown. Therefore, a high BFoM value indicates that the material can achieve higher efficiency and better performance in high voltage applications. GaN-based power devices exhibit high breakdown voltages and low conduction losses, attributed to their superior material properties, which also result in a much higher BFoM for GaN than silicon and even silicon carbide, showing advantages in high voltage applications. In addition, through the use of critical electric fields and saturation drift speeds, JFoM provides a quantitative means of evaluating and comparing the suitability of different semiconductor materials for high frequency and high speed switching applications [48]. For example, GaN materials exhibit high JFoM values due to their high critical electric fields and saturation drift speeds, making GaN-based devices particularly advantageous in applications requiring fast switching and high frequency response. Table 2-4 shows the JFoM and BFoM values of common semiconductor materials including (111) Si, GaAs, SiC and GaN [49].

Table 2-4 Normalized figures of merit (JFoM and BFoM) of common semiconductor materials [49].

Materials	JFoM ($E_c \cdot v_{sat} / 2\pi$)	BFoM ($\epsilon \cdot \mu \cdot E_c^3$)
(111) Si	1	1
GaAs	7.1	15.6
SiC	260	110
GaN	760	650

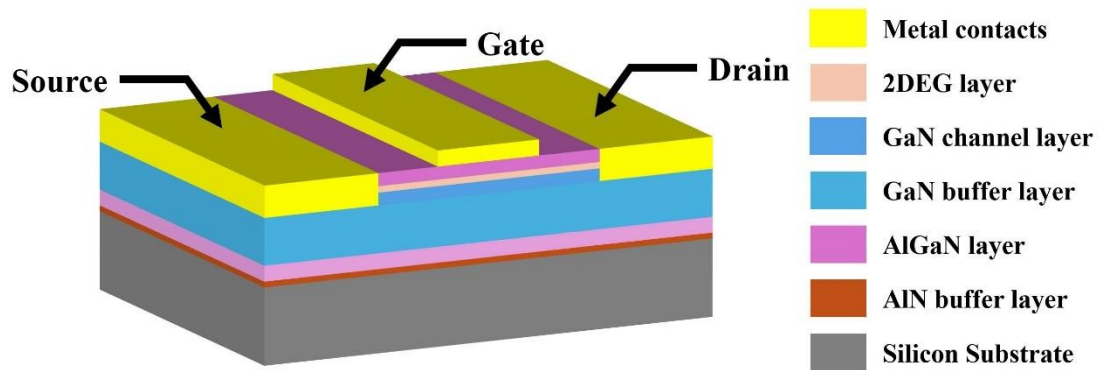


Figure 2-14 Schematic diagram of AlGaN/GaN HEMT on Silicon substrate with AlGaN buffer layer.

Figure 2-14 illustrates the basic structure of an AlGaN/GaN HEMT on Silicon substrate. In general, both sapphire and silicon can be employed as substrates for the growth of HEMT structures. Sapphire substrates are widely used due to their excellent electrical insulation and thermal stability; silicon substrates are preferred due to their lower cost and compatibility with existing silicon-based processes. Typically, AlGaN/GaN HEMT structures have a thick GaN buffer layer as the interface between the heterostructure and the substrate. The buffer layer is mainly used to reduce lattice mismatch and provide a suitable platform for growing high quality AlGaN layers, and the buffer layer must be semi-insulating to prevent breakdown at high voltages. At the interface of GaN and AlGaN, a high-density 2DEG spontaneously forms due to the polarisation difference between the materials and acts as a channel layer for HEMT to support high-speed electron transport. In addition, the HEMT structure requires three metal contacts, including two ohmic contacts and one Schottky contact. The two ohmic contacts act as the source and drain of the HEMT, and are used to provide good electrical contact and reduce the contact resistance, which is usually made of Ti/Al/Ni/Au metal stacks, while Ni/Au alloy is used to form a Schottky contact on the surface of the AlGaN layer between the source and drain as the gate contact of the HEMT, which is used to control the conductivity state of the 2DEG. When the HEMT is under zero bias, current flows through the 2DEG layer from the drain to the source and the device is in the on-state. However, when a negative bias is applied to the gate, the electric field depletes the 2DEG layer under the gate and closes the channel, cutting off the current flow, which is referred to as the off-state [50]. It is also important to note that the threshold voltage (V_{th}) of the HEMT is an important electrical characteristic that defines the minimum gate voltage required to switch the HEMT from the off-state to the on-state.

Breakdown voltage (V_{br}), on-state resistance (R_{on}) and drain current (I_{DS}) are three key metrics for evaluating HEMT performance. These parameters determine the usefulness and effectiveness of HEMTs in various applications. The breakdown voltage refers to the maximum voltage that the transistor can withstand, beyond which breakdown will occur and damage the device. This breakdown can be vertical or lateral, depending on the geometry of the device. The lateral breakdown typically occurs between the gate and drain, while vertical breakdown occurs in the vertical structure of the device, such as from the channel layer to the substrate. The lateral breakdown voltage can be effectively increased by increasing the gate-to-drain distance, while increasing the resistivity of the buffer layer or optimising the thickness and material of the buffer layer can increase the vertical breakdown voltage.

On-state resistance is the internal resistance of a device in the on-state, consisting of an ohmic contact resistance and a 2DEG channel sheet charge. The amount of on-state resistance directly affects the power dissipation and efficiency of the device. R_{on} can be effectively reduced by optimising the design of the device, such as reducing the gate-drain spacing, increasing the channel width, or using materials with higher electron mobility. However, reducing the gate-drain spacing also reduces the breakdown voltage of the device, as a shorter gate-drain spacing means that the electric field is more concentrated, which tends to initiate breakdown. The R_{on} is usually calculated by measuring the linear region in the I-V characteristic curve of the device. Also, to make it easier to compare the performance of different devices, R_{on} is usually normalised to the gate width. This can eliminate the effect of different device sizes on the resistance value.

Drain current (I_{DS}) is the current that flows from the drain to the source of a device. This parameter is a key measure of device performance and is especially critical when analysing the current drive capability and switching performance of a device. The magnitude and direction of the drain current is controlled by the gate voltage (V_{GS}), which controls current flow by affecting the concentration of charge carriers in the channel, which can be determined by following equation:

$$I_{DS} = n_s \times v_{eff} \times q \quad (2.17)$$

where n_s denotes the concentration of charge carriers in the channel and v_{eff} denotes the effective velocity of the electrons, which can be considered as the average drift velocity of the

electrons in the presence of an electric field. q is the charge of the electrons, i.e., the fundamental charge constant (approximately 1.6×10^{-19} Coulomb).

2.3 III-Nitrides on Silicon Substrates

With the rapid development of semiconductor technology, there is a growing demand for III-nitride semiconductor materials, which have a wide range of applications in high performance electronic and optoelectronic devices. Typically, these materials are grown on sapphire or silicon carbide (SiC) substrates, but the cost and size limitations of these substrates limit their potential. Silicon substrates are a more attractive alternative due to their low cost, large size and compatibility with existing silicon-based microelectronics manufacturing technologies. However, the epitaxial growth of III-nitride materials on silicon substrates presents several technical challenges, including lattice mismatch, thermal expansion coefficient differences and chemical incompatibility. The presence of these problems results in a high density of defects, such as dislocations and microcracks, which affects the quality of the epitaxial layer and subsequent device performance.

2.3.1 Lattice Mismatch

The crystal structure of silicon is cubic and the (001) silicon crystal with four-fold surface symmetry, whereas III-nitrides such as gallium nitride have a wurtzite structure with a hexagonal six-fold surface symmetry. When (0001) GaN is grown on (001) Si, two different in-plane orientations of the GaN are formed simultaneously, resulting in a rough surface morphology. Consequently, high quality GaN is not achievable on (001) Si, indicating that (001) Si is not an optimal substrate for GaN growth. Fortunately, the (111)-oriented silicon has a three-fold surface symmetry, which can be matched with the hexagonal six-fold surface symmetry of GaN, resulting in only one in-plane orientation of GaN. Therefore, when epitaxially growing GaN on a Si substrate, it is generally preferred to use (111) oriented silicon as the substrate.

It is also noteworthy that the crystal in-plane orientation relations of GaN crystals grown on (111) Si substrates are GaN [1-100] \parallel Si [-1-12] and GaN [11-20] \parallel Si [-110], which means that the mentioned intra-plane orientations of GaN and Si are parallel to each other. In addition, a lattice mismatch of about 17% exists between GaN and (111) Si, resulting in significant tensile stress

within GaN crystals in the GaN-on-Si system. The lattice mismatch of GaN on (111) Si, denoted as $f_{GaN/Si}$ can be calculated by the following equation:

$$f_{\frac{GaN}{Si}} = \frac{\left| a_{GaN} - \frac{\sqrt{2}}{2} a_{Si} \right|}{\frac{\sqrt{2}}{2} a_{Si}} = \frac{\left| 3.189 - \frac{\sqrt{2}}{2} \times 3.840 \right|}{\frac{\sqrt{2}}{2} \times 3.840} = 17\% \quad (2.18)$$

where a_{Si} is and a_{GaN} is the in-plane lattice constant of cubic Si and wurtzite GaN, respectively. ($a_{Si} = 3.840\text{\AA}$ and $a_{GaN} = 3.189\text{\AA}$).

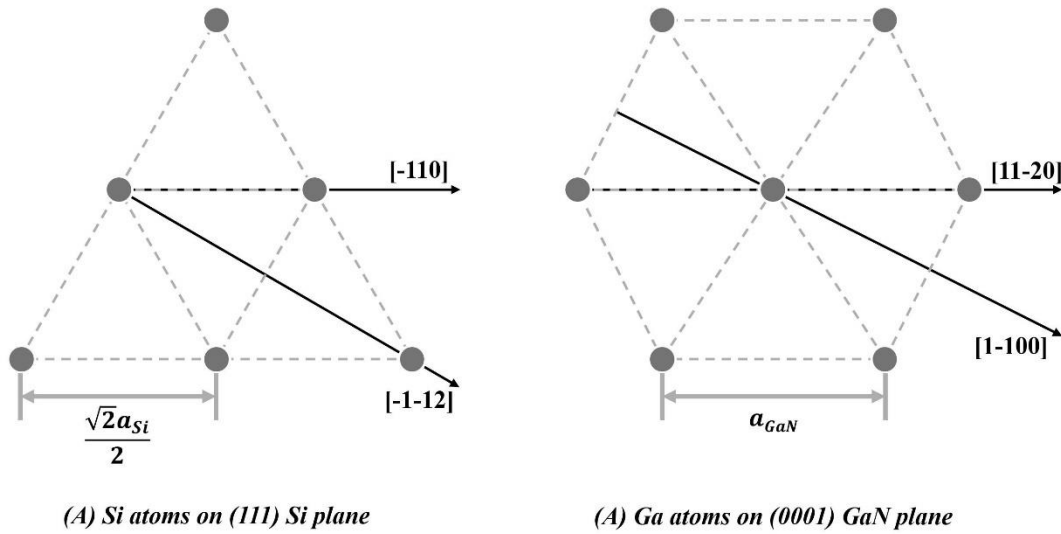


Figure 2-15 Schematic diagrams of the atomic arrangement of (A) Si atoms on the (111) Si plane and (B) Ga atoms on the (0001) GaN plane.

2.3.2 Thermal Expansion Coefficient Mismatch

The difference in thermal expansion coefficients (TEC) between GaN and Si is also a significant challenge in GaN-on-Si systems. The thermal expansion coefficient of GaN ($5.59 \times 10^{-6} \text{ K}^{-1}$) is significantly higher than that of Si ($2.59 \times 10^{-6} \text{ K}^{-1}$), resulting the thermal expansion coefficient mismatch of GaN and Si $\Delta_{GaN/Si}$ is 115%, as calculated by following equation:

$$\Delta_{GaN/Si} = \frac{TEC_{GaN} - TEC_{Si}}{TEC_{Si}} \times 100\% \quad (2.19)$$

Where TEC_{GaN} and TEC_{Si} is the thermal expansion coefficients of GaN and Si, respectively.

Such a large thermal coefficient mismatch is a major contributor to GaN surface cracking and wafer

bending due to the large tensile stresses introduced during cooling after crystal growth from high temperatures. At the same time, the accumulated stress increases with increasing GaN layer thickness, further aggravating wafer bending and GaN cracking. This issue becomes more pronounced with the increase in substrate diameter. Both the wafer bending and cracking will inevitably challenge the quality of the GaN film and the performance of the device [51]. Figure 2-16 illustrates that the serious cracking problem occurs in the case of GaN on (111) Si without any optimization.

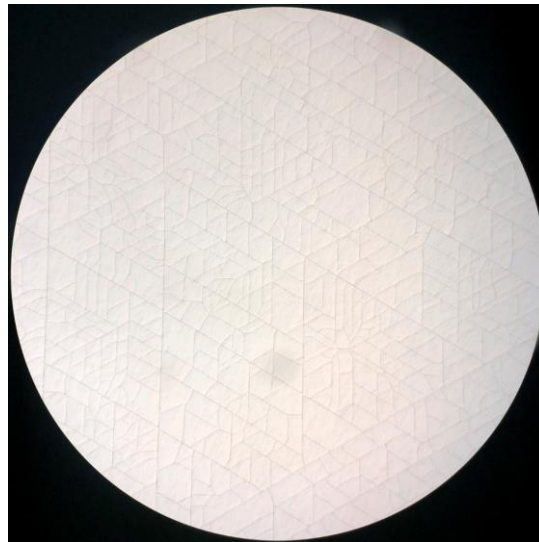


Figure 2-16 Optical microscopy image of 1.4 μm cracked GaN layer grown on (111) Si substrate

2.3.3 Melt-Back Etching

Melt-back Etching is a manifestation of the chemical incompatibility that exists between GaN and silicon substrates. Unlike sapphire and silicon carbide substrates, when gallium nitride is grown directly on a silicon substrate by metal organic chemical vapour deposition (MOCVD) at a normal GaN growth temperature ($>1000^{\circ}\text{C}$), silicon chemically reacts with gallium nitride to form a Ga-Si eutectic alloy. This reaction causes silicon to diffuse from the substrate into the GaN, damaging the Si substrate and roughening the GaN surface. This reaction is often referred to as "melt-back etching" [52, 53]. Introduction of an AlN buffer layer to physically separate the GaN and Si substrates is currently the most widely used and proven method to effectively avoid melt-back etching. It should be noted that if the thickness of the AlN buffer layer is insufficient, or if there are many pits or uncovered areas in the buffer layer, then melt-back etching will still occur at high

temperatures [54]; Therefore, optimising the thickness and surface roughness of the AlN buffer layer is the necessary to improve GaN on Si. Reducing the growth temperature below 870°C serves as an alternative strategy to prevent a reduce melt-back etching [55]. However, lower growth temperatures degrade the quality of the GaN, potentially resulting in significantly higher crystal defect densities. Figure 2-17 presents the melt-back etching phenomenon observed between GaN and Si.

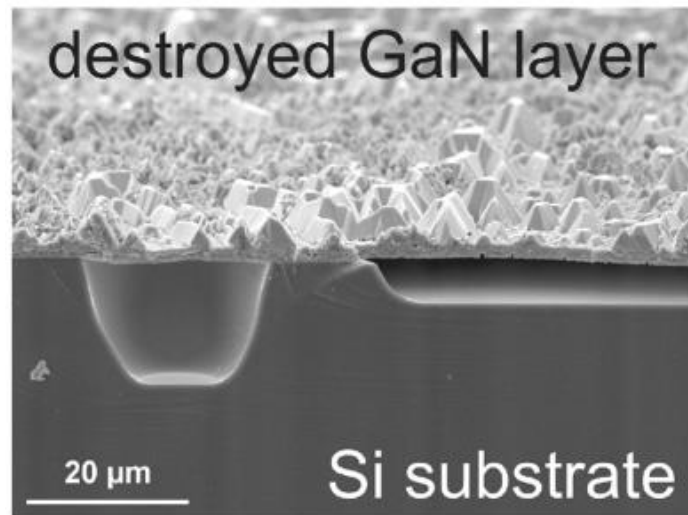


Figure 2-17 Cross-sectional SEM images of melt-back etching between GaN and Si. Reproduced with permission [52].

Reference

- [1] S. M. Sze, Y. Li, and K. K. Ng, *Physics of semiconductor devices*. John Wiley & sons, 2021.
- [2] "Band Gap." PV Education. Available: <https://www.pveducation.org/pvcdrom/pn-junctions/band-gap> (accessed September, 2024).
- [3] "Band Theory of Solids " Hyper Physics. Available: <http://hyperphysics.phy-astr.gsu.edu/hbase/solids/band.html> (accessed September, 2024).
- [4] H. Kashyap. "Here's Everything You Need To Know About Bandgap." inc42. Available: <https://inc42.com/glossary/bandgap/> (accessed September, 2024).
- [5] J. R. Hook and H. E. Hall, *Solid state physics*. John Wiley & Sons, 2013.
- [6] V. E. Laine, *Photonic crystals : fabrication, band structure, and applications*, 1st ed. New York: New York : Nova Science Publishers, c2011, 2011.
- [7] "Introduction to Energy Bands." University of Cambridge. Available: https://www.doitpoms.ac.uk/tlplib/semiconductors/energy_band_intro.php (accessed September, 2024).
- [8] M. Fox, *Optical properties of solids*. Oxford university press, 2010.
- [9] J. Hu, Y. Zhang, M. Sun, D. Piedra, N. Chowdhury, and T. Palacios, "Materials and processing issues in vertical GaN power electronics," *Materials Science in Semiconductor Processing*, vol. 78, pp. 75-84, 2018.
- [10] R. N. Hall, "Electron-hole recombination in germanium," *Physical review*, vol. 87, no. 2, p. 387, 1952.
- [11] W. Shockley and W. Read Jr, "Statistics of the recombinations of holes and electrons," *Physical review*, vol. 87, no. 5, p. 835, 1952.
- [12] H. Morkoç, *Nitride semiconductor devices : fundamentals and applications*, 1st ed. Weinheim: Weinheim : Wiley-VCH, 2013, 2013.
- [13] J. Iveland, L. Martinelli, J. Peretti, J. S. Speck, and C. Weisbuch, "Direct measurement of Auger electrons emitted from a semiconductor light-emitting diode under electrical injection: identification of the dominant mechanism for efficiency droop," *Physical review letters*, vol. 110, no. 17, p. 177406, 2013.
- [14] M. J. Faruki, K. Bera, and N. Karmakar, "Impact of Crystal Orientation on Modulation Bandwidth: Towards GaN LED-Based High-Speed Visible Light Communication," in *Photonics*, 2024, vol. 11, no. 6: MDPI, p. 542.

- [15] T. Wang, "Topical Review: Development of overgrown semi-polar GaN for high efficiency green/yellow emission," *Semiconductor Science and Technology*, vol. 31, no. 9, p. 093003, 2016.
- [16] D. Meyaard, G.-B. Lin, J. Cho, and E. Schubert, "Efficiency droop in gallium indium nitride (GaInN)/gallium nitride (GaN) LEDs," in *Nitride Semiconductor Light-Emitting Diodes (LEDs)*: Elsevier, 2014, pp. 279-300.
- [17] I. Farrer. "Lecture Notes from EEE6212 Semiconductor Materials." University of Sheffield. (accessed September, 2024).
- [18] S. Kasap and P. Capper, *Springer handbook of electronic and photonic materials*. Springer, 2017.
- [19] "Structure - Rock Salt (NaCl)." Libre Texts. Available: [https://chem.libretexts.org/Courses/Kutztown_University_of_Pennsylvania/CHM_320%3A_Advanced_Inorganic_Chemistry_textbook/12%3A_Structures_and_Energetics_of_Metallic_and_Ionic_solids/12.03%3A_Ionic_Lattices/12.3A%3A_Structure_-_Rock_Salt_\(NaCl\)](https://chem.libretexts.org/Courses/Kutztown_University_of_Pennsylvania/CHM_320%3A_Advanced_Inorganic_Chemistry_textbook/12%3A_Structures_and_Energetics_of_Metallic_and_Ionic_solids/12.03%3A_Ionic_Lattices/12.3A%3A_Structure_-_Rock_Salt_(NaCl)) (accessed September, 2024).
- [20] H. Okumura *et al.*, "Growth and characterization of cubic GaN," *Journal of Crystal Growth*, vol. 178, no. 1-2, pp. 113-133, 1997.
- [21] M. Lada, A. Cullis, P. Parbrook, and M. Hopkinson, "Metastable rocksalt phase in epitaxial GaN on sapphire," *Applied Physics Letters*, vol. 83, no. 14, pp. 2808-2810, 2003.
- [22] T. D. Moustakas and R. Paiella, "Optoelectronic device physics and technology of nitride semiconductors from the UV to the terahertz," *Reports on progress in physics*, vol. 80, no. 10, pp. 106501-106501, 2017, doi: 10.1088/1361-6633/aa7bb2.
- [23] P. Rinke, M. Winkelkemper, A. Qteish, D. Bimberg, J. Neugebauer, and M. Scheffler, "Consistent set of band parameters for the group-III nitrides AlN, GaN, and InN," *Physical Review B—Condensed Matter and Materials Physics*, vol. 77, no. 7, p. 075202, 2008.
- [24] J. H. Edgar, "Properties of group III nitrides," 1994.
- [25] F. Bernardini, V. Fiorentini, and D. Vanderbilt, "Spontaneous polarization and piezoelectric constants of III-V nitrides," *Physical Review B*, vol. 56, no. 16, p. R10024, 1997.
- [26] G. R. Desiraju, J. J. Vittal, and A. Ramanan, *Crystal engineering: a textbook*. World scientific, 2011.
- [27] J. Weyher *et al.*, "Morphological and structural characteristics of homoepitaxial GaN grown by metalorganic chemical vapour deposition (MOCVD)," *Journal of Crystal*

- Growth*, vol. 204, no. 4, pp. 419-428, 1999.
- [28] D. C. Look and J. Szelove, "Predicted maximum mobility in bulk GaN," *Applied Physics Letters*, vol. 79, no. 8, pp. 1133-1135, 2001.
- [29] J. Blakemore, "Semiconducting and other major properties of gallium arsenide," *Journal of Applied Physics*, vol. 53, no. 10, pp. R123-R181, 1982.
- [30] S. Porowski, "Growth and properties of single crystalline GaN substrates and homoepitaxial layers," *Materials Science and Engineering: B*, vol. 44, no. 1-3, pp. 407-413, 1997.
- [31] D. R. Lide and G. W. Milne, *Handbook of data on common organic compounds*. CRC press, 1995.
- [32] P. Norton, T. Braggins, and H. Levinstein, "Impurity and lattice scattering parameters as determined from Hall and mobility analysis in n-type silicon," *Physical Review B*, vol. 8, no. 12, p. 5632, 1973.
- [33] A. Kyuregyan and S. Yurkov, "Room-temperature avalanche breakdown voltages of p-n junctions made of Si, Ge, SiC, GaAs, GaP, and InP," *Soviet Physics--Semiconductors(English Translation)*, vol. 23, no. 10, pp. 1126-31, 1989.
- [34] C. J. Glassbrenner and G. A. Slack, "Thermal conductivity of silicon and germanium from 3 K to the melting point," *Physical review*, vol. 134, no. 4A, p. A1058, 1964.
- [35] N. Das, *Advances in Optical Communication*. BoD–Books on Demand, 2014.
- [36] D. Zhuang and J. Edgar, "Wet etching of GaN, AlN, and SiC: a review," *Materials Science and Engineering: R: Reports*, vol. 48, no. 1, pp. 1-46, 2005.
- [37] H. Morkoç, *Handbook of nitride semiconductors and devices, GaN-based optical and electronic devices*. John Wiley & Sons, 2009.
- [38] A. R. Denton and N. W. Ashcroft, "Vegard's law," *Physical review A*, vol. 43, no. 6, p. 3161, 1991.
- [39] F. Bernardini and V. Fiorentini, "Nonlinear macroscopic polarization in III-V nitride alloys," *Physical Review B*, vol. 64, no. 8, p. 085207, 2001.
- [40] F. Bernardini and V. Fiorentini, "Spontaneous versus piezoelectric polarization in III-V nitrides: conceptual aspects and practical consequences," *Physica Status Solidi (b)*, vol. 216, no. 1, pp. 391-398, 1999.
- [41] N. Ikeda *et al.*, "GaN power transistors on Si substrates for switching applications," *Proceedings of the IEEE*, vol. 98, no. 7, pp. 1151-1161, 2010.
- [42] E. Bahat-Treidel, F. Brunner, O. Hilt, E. Cho, J. Wurfl, and G. Trankle,

- "AlGaIn/GaN/GaN:C Back-Barrier HFETs With Breakdown Voltage of Over 1 kV and Low $\text{RON} \times \text{A}$," *IEEE Transactions on Electron Devices*, vol. 57, no. 11, pp. 3050-3058, 2010.
- [43] Y.-F. Wu *et al.*, "Performance and robustness of first generation 600V GaN-on-Si power transistors," in *The 1st IEEE Workshop on Wide Bandgap Power Devices and Applications*, 2013: IEEE, pp. 6-10.
- [44] O. Ambacher *et al.*, "Two-dimensional electron gases induced by spontaneous and piezoelectric polarization charges in N- and Ga-face AlGaIn/GaN heterostructures," *Journal of Applied Physics*, vol. 85, no. 6, pp. 3222-3233, 1999.
- [45] U. K. Mishra, L. Shen, T. E. Kazior, and Y.-F. Wu, "GaN-based RF power devices and amplifiers," *Proceedings of the IEEE*, vol. 96, no. 2, pp. 287-305, 2008.
- [46] J. Ajayan *et al.*, "Challenges in material processing and reliability issues in AlGaIn/GaN HEMTs on silicon wafers for future RF power electronics & switching applications: A critical review," *Materials science in semiconductor processing*, vol. 151, p. 106982, 2022, doi: 10.1016/j.mssp.2022.106982.
- [47] B. J. Baliga, "Semiconductors for high - voltage, vertical channel field - effect transistors," *Journal of applied Physics*, vol. 53, no. 3, pp. 1759-1764, 1982.
- [48] E. O. Johnson, "Physical limitations on frequency and power parameters of transistors," in *Semiconductor Devices: Pioneering Papers*: World Scientific, 1991, pp. 295-302.
- [49] G. Sorrentino, M. Melito, A. Patti, G. Parrino, and A. Raciti, "GaN HEMT devices: Experimental results on normally-on, normally-off and cascode configuration," *IECON 2013 - 39th Annual Conference of the IEEE Industrial Electronics Society*, pp. 816-821, 2013.
- [50] K. Jones *et al.*, "AlGaIn devices and growth of device structures," *Journal of Materials Science*, vol. 50, pp. 3267-3307, 2015.
- [51] D. Zhu, D. Wallis, and C. Humphreys, "Prospects of III-nitride optoelectronics grown on Si," *Reports on Progress in Physics*, vol. 76, no. 10, p. 106501, 2013.
- [52] A. Dadgar *et al.*, "MOVPE growth of GaN on Si (1 1 1) substrates," *Journal of Crystal Growth*, vol. 248, pp. 556-562, 2003.
- [53] H. Ishikawa, K. Yamamoto, T. Egawa, T. Soga, T. Jimbo, and M. Umeno, "Thermal stability of GaN on (111) Si substrate," *Journal of Crystal Growth*, vol. 189, pp. 178-182, 1998.
- [54] R. Ravash *et al.*, "MOVPE growth of semi-polar GaN light-emitting diode structures on planar Si (112) and Si (113) substrates," *Journal of Crystal Growth*, vol. 370, pp. 288-292, 2013.

- [55] N. Suzuki *et al.*, "HVPE growth of semi-polar (112-2) GaN on GaN template (113) Si substrate," *Journal of crystal growth*, vol. 311, no. 10, pp. 2875-2878, 2009.

Chapter 3 Experimental Techniques

3.1 Pre-Growth Treatment

3.1.1 Template Cleaning

Template surface cleaning is a critical step before epitaxial growth, the main objective is to remove any residual dust, particles or contaminants from the wafer surface, any residue may affect the growth process and ultimately the quality of the material. This operation is even more important for patterned templates. The overview of a standard operating procedure for regular templates cleaning/treatment is shown below:

- i. Ultrasonic cleaning:** The templates were cleaned by successively immersing them in solutions of n-butyl acetate (nBA), acetone and isopropyl alcohol (IPA) in an ultrasonic bath. This step effectively removes grease, wax and most organic contaminants. Basically, the immersion time for each solvent is determined by the degree of contamination and the sensitivity of the template. For regular templates, the typical immersion time is 5 minutes for each solution.
- ii. Rinsing:** The wafer is rinsed with flowing deionised water (DI water) to remove residual solvents. This rinsing usually needs to be continued for sufficient time (typically 5 minutes) to ensure that all chemical residues are adequately removed.
- iii. Drying and baking:** The wafers were blown with dry nitrogen gas to remove water droplets from the surface to prevent water staining, and then baked in an oven at 100°C to completely remove adsorbed water. This step is essential to prevent oxidation or other chemical reactions during subsequent growth.

In instances where necessary, oxygen plasma treatment is used to decompose organic contaminants on the wafer surface, such as photoresists and certain recalcitrant polymers. This treatment effectively removes organic layers that cannot be removed by solvent cleaning alone. In specific cases, deep cleaning with acid or alkaline solutions such as KOH, hydrochloric acid (HCl) and aqua regia may be required. These chemicals/solvents are primarily used to remove metal ions, inorganic deposits and other specific contaminants, such as particulate matter and trace heavy metals.

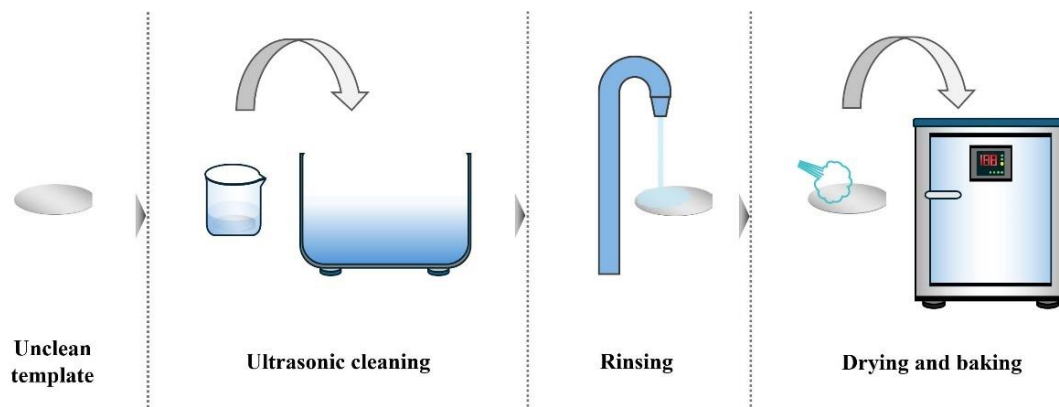


Figure 3-1 Schematic diagram of the regular template cleaning procedure.

3.1.2 Photo-Enhanced Chemical Etching

The ultraviolet (UV) photo-enhanced chemical (PEC) etching process was employed in this project to process the patterned templates with the objective of achieving accurate modulation of the surface properties of the templates prior to overgrowth by MOCVD.

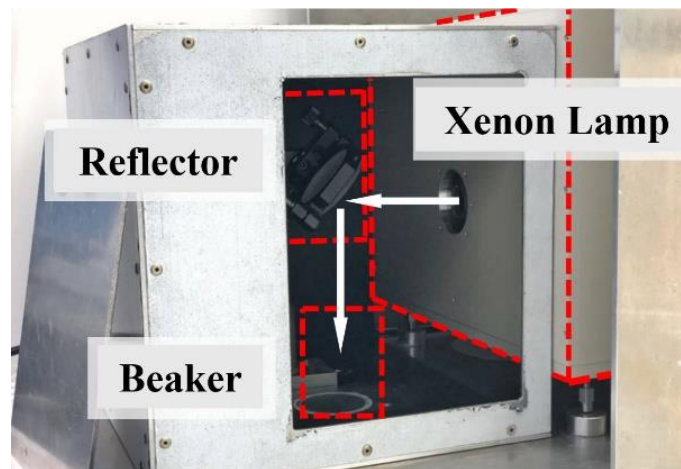


Figure 3-2 the custom PEC etching system employed in this study.

Figure 3-2 illustrates the custom PEC etching system employed in this study. A 450 W Xenon arc lamp with a power density of 1.5 W/cm² was utilized as the UV light source in this system. An aluminium-coated ultraviolet (UV) reflector reflects the UV light and illuminates it vertically onto the sample immersed in a beaker containing a 10% - 20% KOH aqueous electrolyte. This reflector can optimise the efficiency of light utilisation and uniformity of the light. During the etching process, the entire etching system is enclosed within a metal box in order to shield the user from UV radiation.

The ultraviolet photons emitted by a xenon lamp have a higher energy than the band gap of GaN. This results in the excitation of electrons from the valence band to the conduction band, which in turn leads to the formation of electron-hole pairs. The excited electrons can be captured by the oxidant in the electrolyte, participating in the reduction reaction and being consumed, leaving photogenerated holes. These photogenerated holes are highly oxidising and accelerating the etching of GaN. The reaction of GaN with KOH can be generally expressed as [1]:



Where KOH not only acts as a catalyst in this process, accelerating the chemical reaction, but also as a solvent for the reaction product of Ga₂O₃.

3.2 Metal-Organic Chemical Vapour Deposition (MOCVD)

3.2.1 Introduction

Metal-organic chemical vapour deposition (MOCVD), also known as metal-organic vapour phase epitaxy (MOVPE), is one of the fundamental technologies in the semiconductor epitaxial growth. It is a chemical vapour deposition technique in which a metal-organic compound is mixed with a carrier gas and fed into a reaction chamber where it decomposes and reacts at high temperatures, allowing the epi-film to be deposited on the substrate. MOCVD is widely used for producing III-V semiconductors and evolved to meet the requirement for III-V based LEDs and other semiconductor devices. Another common type of epitaxy device is molecular beam epitaxy (MBE), which is based on physical deposition, as opposed to MOCVD, which is based on chemical principles. Compared to MBE, MOCVD has higher growth rates but relatively lower accuracy in terms of film thickness and composition. MBE has lower growth rates but relatively high film quality with good surface uniformity and crystalline quality. MOCVD requires high-temperature and high-pressure reaction conditions, whereas MBE requires a very high vacuum environment. Moreover, the experimental and maintenance costs of MOCVD are lower than MBE. Both technologies have their advantages and disadvantages and will be chosen for different applications in the semiconductor industry [2-5].

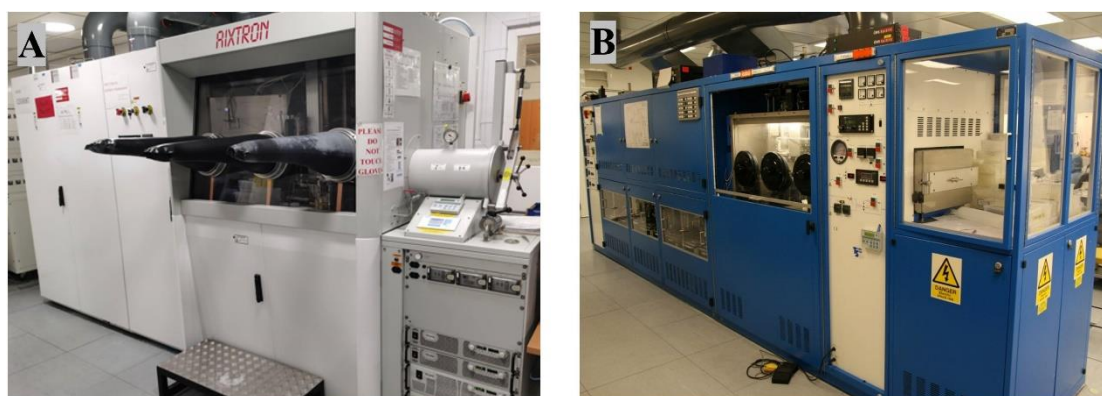


Figure 3-3 Photograph of the (A) Aixtron 3×2” flip-top CCS reactor system; and (B) Thomas-Swan 3×2” vertical CCS reactor system.

The samples described in this thesis were mainly grown using an Aixtron single chamber 3×2” flip-top close-coupled showerhead (CCS) metal organic chemical vapour deposition (MOCVD) system. This instrument was manufactured by AIXTRON Ltd, the flip-top lid structure of its MOCVD

growth chamber is one of the key patented technologies. When sample and substrate loading and unloading are required, the top lid can be flipped over by the swivel arm, allowing sufficient space for easy sample placement and removal. Overall, Aixtron's flip-top growth chamber construction offers benefits such as ease of operation, increased safety, protection of the showerhead and improved stability, contributing to the performance and lifetime of the MOCVD equipment. Figure 3-3A shown the Aixtron 3×2” CCS MOCVD system consists of a reactor cabinet, a load-lock system, a power supply cabinet, an electrical cabinet, a gas delivery/mixing system cabinet and a metal-organic (MO) bubbler cabinet. In addition to the main body, a carrier gas purifier (hydrogen and nitrogen), a cooling water system, a gas phase discharge system and a vacuum system are all essential (not shown). Furthermore, all growth parameter adjustments, and monitoring systems of the Aixtron MOCVD system are operated via the accompanying PC.

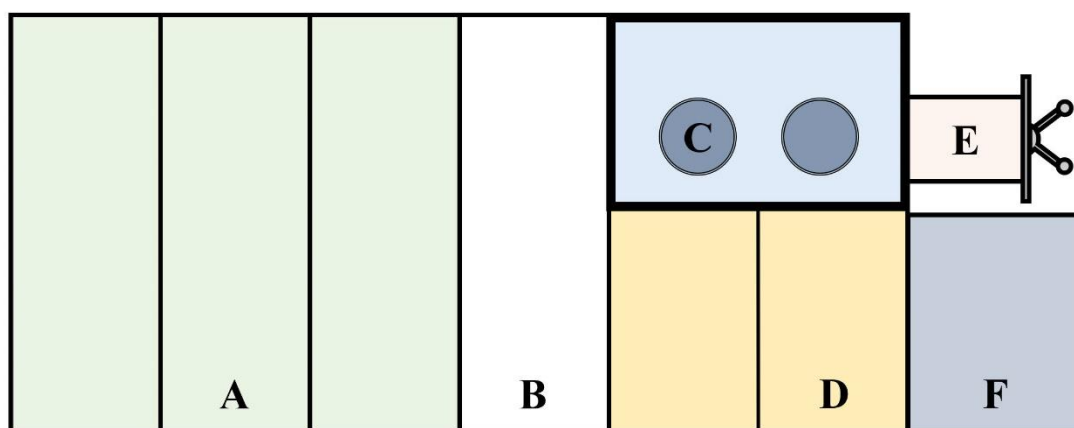


Figure 3-4 The schematic of the Aixtron 3×2” flip-top CCS reactor system; (A) gas mixing cabinet; (B) electrical cabinet; (C) glove box; (D) reactor cabinet; (E) load lock; (F) power supply cabinet.

3.2.2 Basic Principles

In the MOCVD system, the synthesis of compound semiconductors involves using metal-organic (MO) sources. These sources are typically volatile and toxic chemicals. The basic principle of growing III-nitride epitaxial layers in MOCVD is to introduce gaseous III-group and V-group precursors, which consist of metal-organic sources and NH_3 , into the reactor along with the carrier gas through the MOCVD pathway. In the high-temperature and high-pressure reactor, these precursors undergo a controlled chemical reaction to form the desired III-nitride compounds. The MOCVD system employs the internal mass flow controllers (MFCs) to precisely regulate the

injected gases and MO sources. This precise control is crucial for achieving accuracy in important chemical reactions. In practical terms, the epitaxy method is a highly intricate process that consists of multiple stages and reactions. Figure 3-5 illustrates the deposition process and the surface reactions involved.

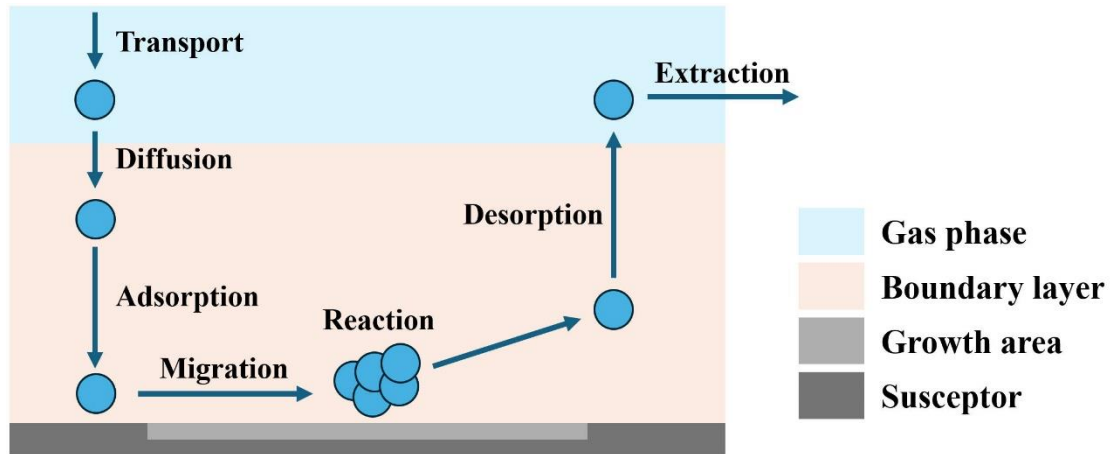


Figure 3-5 Schematic representation of the deposition process and surface reactions occurring during MOCVD growth.

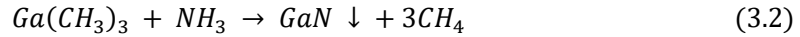
1. **Transport:** Depending on the required growth material, the corresponding group V precursors (NH_3) and group III precursors (TMG, TMA and TMIIn) are supplied in the vicinity of the substrate. Normally, the group III metal-organic sources need to be diluted and delivered by carrier gases, the common carrier gas types are usually either hydrogen (H_2) or nitrogen (N_2).
2. **Diffusion:** Gas molecules, which include metal-organic compounds, carrier gases and reaction gases, have high thermal energy in the high-temperature reactor, which allows them to diffuse freely in the gas phase to transport and interact.
3. **Adsorption:** Interaction between precursor molecules in the gas phase and the substrate surface. When precursor molecules come into contact with the substrate surface, they can interact with active sites on the surface and be adsorbed onto the heated substrate surface.
4. **Migration:** The process of migration of atoms or molecules across the surface of a substrate. Often precursor molecules can move across the surface to locations more favourable to the reaction (called crystallographic regions). The selective area growth of crystals through a masking process is the result of the controlled migration process.

5. **Reaction:** The reaction occurs on the surface of the substrate, resulting in the formation of the anticipated crystals and by-products.
6. **Desorption:** The desorption refers to the process of dissociating adsorbed species (including by-products and saturated precursor molecules) from the surface of the substrate, allowing them to return to the gas phase. Generally, adsorption and desorption occur simultaneously and maintain dynamic equilibrium.
7. **Extraction:** Extraction of the gases, by-products and non-reacting gas molecules is extracted from the reactor by a vacuum system. This process maintains a stable gas phase environment in the reactor.

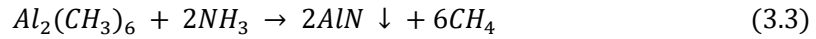
The typically used precursors include metal-organic sources for group-III elements are trimethylgallium (TMG, $\text{Ga}(\text{CH}_3)_3$), trimethylindium (TMIn, $\text{In}(\text{CH}_3)_3$), and trimethylaluminum (TMA, $\text{Al}_2(\text{CH}_3)_6$) were used as the precursors for gallium (Ga), aluminium (Al) and indium (In), while the ammonia (NH_3) was used as the group V element precursor for Nitrogen (N). Furthermore, achieving n-type and p-type doping in III-nitride epitaxial layers can be accomplished by utilizing different types of dopants. Disilane (Si_2H_6) and Bis(cyclopentadienyl) magnesium (Cp_2Mg) are frequently employed for n-type and p-type doping, respectively. Hydrogen (H_2) and nitrogen (N_2) are commonly employed as a carrier gas for the deposition of III-nitride epitaxial layers. The selection of either gas depends on the desired epitaxial layer. H_2 , being the least dense gas found in nature, can be easily purified. Thus, it is a popular choice as a carrier gas for typical metal-organic chemical vapor deposition growth. However, when it comes to InGaN growth, N_2 proves to be a superior option compared to H_2 . This is because indium can be more efficiently incorporated into GaN under N_2 gas conditions. In GaN growth, H_2 is commonly used as a carrier gas due to its positive impact on the crystalline quality and surface flatness of the resulting GaN film [4, 6].

As stated above, the synthesis of the III-Nitride epitaxial layer via MOCVD involves chemical reactions between group III and V precursors on substrate at a high-temperature reactor. In the growth of GaN on a sapphire or silicon substrate, NH_3 and vapourised TMG serve as the V- and III-group precursors. The reaction is conducted in a reaction chamber, with the vapourised TMG carried out of the bubbler by a carrier gas, which is typically pure hydrogen in the case of GaN epitaxial

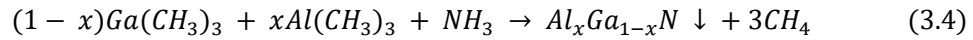
growth. The chemical reaction for GaN epitaxial growth via the following chemical reaction [6-10]:



For AlN epitaxial vapour phase growth via the following:



The growth of an alloy such as AlGaIn necessitates the utilisation of a precursor mixture comprising TMA and TMG. This enables the introduction of TMA into the reactor during the growth of the GaN layer, allowing the co-deposition of aluminium and gallium to form the AlGaIn layer:



3.2.3 Gas System

Purifier

The MOCVD purifier system is a critical component used to provide high-purity purified gases for film growth. Its main function is to remove impurities and moisture from the gases, thus ensuring that the gases meet the requisite purity levels for stable and high-quality film growth. In this study, H₂ or N₂ were used as carrier gases, and NH₃ was used as the group V precursor. Prior to entering the MOCVD gas system, both types of gases have to be purified to enhance stability, reproducibility, and film quality during film growth. The H₂ and N₂ used in this thesis were purified and supplied by a palladium membrane purifier (MegaTorr PS7-PD hydrogen gas purifier) and an in-line purifier (GateKeeper GPU Gas Purifiers), respectively. The NH₃ is directly provided from cylinders outside the purifier system with ultra-pure ammonia of 99.99999% purity [11].

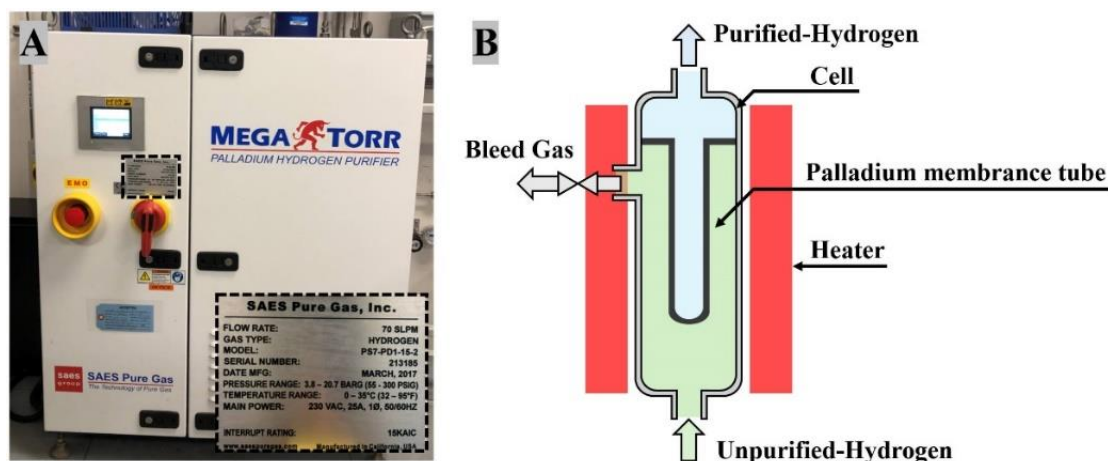


Figure 3-6 MegaTorr PS7-PD hydrogen gas purifier; (A) photograph; (B) schematic diagram.

Palladium membrane purifiers are widely utilised in hydrogen purification to eliminate impurities and harmful elements. This technology is capable of generating hydrogen gas of extremely high purity. These purifiers operate on the principle of selective adsorption and permeability of palladium metal specifically to hydrogen. All purified hydrogen used in this thesis was purified by MegaTorr PS7-PD hydrogen gas purifier. Figure 3-6 shows the hydrogen gas purifier system used in this thesis. Normally, the palladium cell of a the purifier is required to operate at elevated temperatures (the standard operation temperature for this system is 400°C). When the unpurified hydrogen mixture comes into contact with the palladium membrane, the hydrogen molecules (H_2) are adsorbed on the surface of the palladium membrane and decompose into hydrogen atoms. Hydrogen atoms are the smallest known atoms in nature and are the only atoms small enough to diffuse across the palladium membrane driven by the differential H_2 pressure across the membrane. When the hydrogen atoms reach the opposite of the palladium membrane, the hydrogen atoms undergo a recombination process, resulting in the formation of hydrogen molecules and subsequent desorption from the membrane [11].

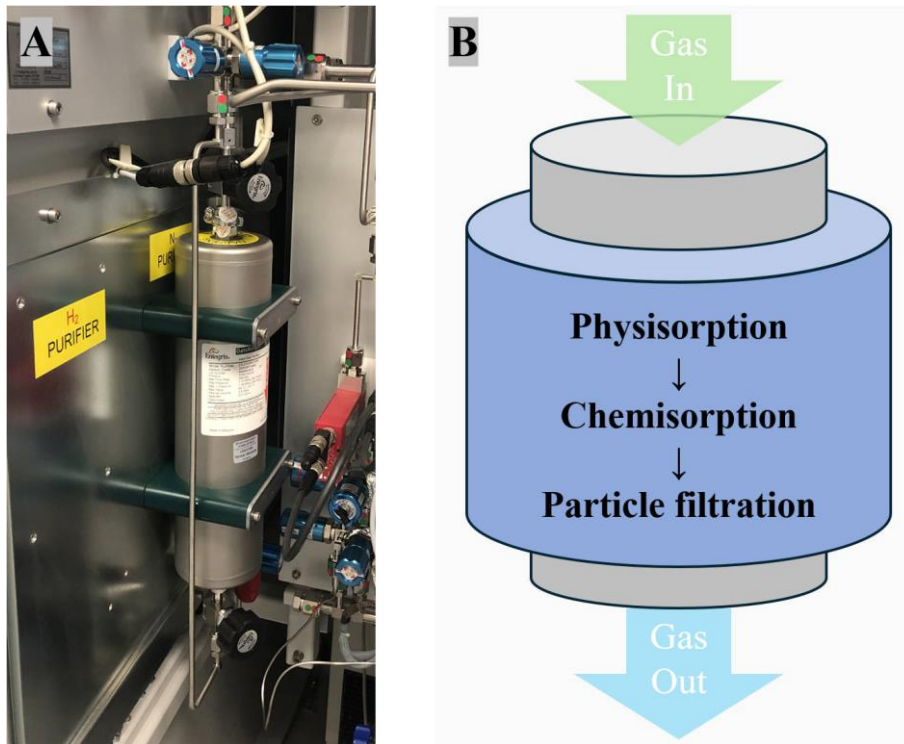


Figure 3-7 The in-line hydrogen gas purifier; (A) photograph; (B) schematic diagram.

In-line purifiers for N_2 purification typically use physical adsorption, chemisorption, and particulate filtration to remove particles and solids from N_2 and to adsorb organics, moisture or other impurities. This kind of purifiers typically do not require additional heating or pressurisation components [12].

Gas delivery system

The gas delivery system is a crucial component within the MOCVD system, ensuring the accurate supply and control of the various gases within the system. In the context of gas delivery systems, gas valves are employed to regulate the opening and closing of gas passages, which are classified as either manual or pneumatic valves. The manual valves are mainly used for the purpose of separating the gas connections of the MOCVD system and the purifier system, ensuring the safety of the system during maintenance and operation. In contrast to manual valves, the pneumatic valves are driven by compressed air or pressurised N_2 , which allows for the easy switching of carrier gases (H_2 or N_2). These pneumatic valves can be controlled by an integrated operating system within the MOCVD system, which increases the flexibility and automation of the gas delivery system. Furthermore, the MFCs are employed to precisely control the molar flow rate of these gases, ensuring that a constant and accurate gas flow rate is maintained during the growth.

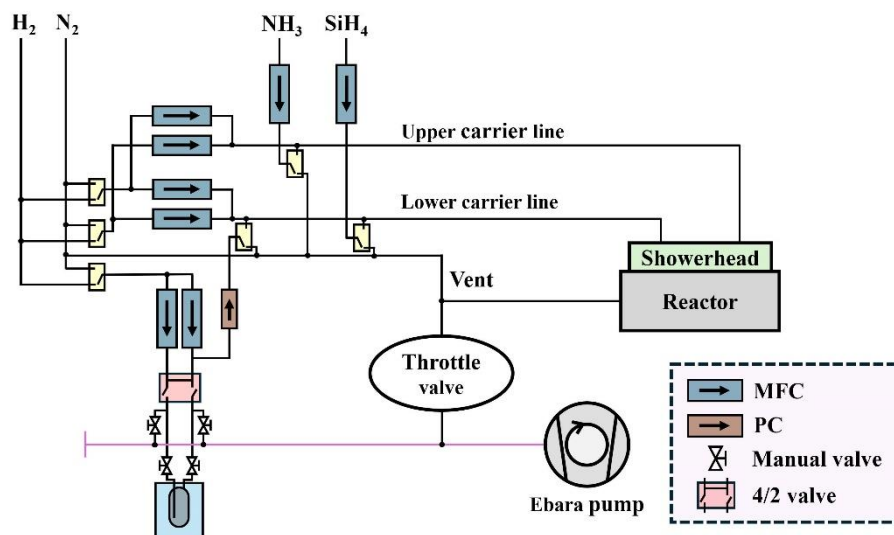


Figure 3-8 Simple schematic diagram of the gas delivery system in an AIXTRON MOCVD system.

Figure 3-8 illustrates the configuration of two separate carrier lines (upper and lower carrier line) connected to the reactor for precursor delivery through the showerhead. The main objective of this design is to provide group V and III precursors in separately, thus avoiding undesirable pre-reactions and allowing precise control of precursor introduction. The upper and lower carrier lines are employed to introduce hydride gases (NH_3) and group III precursors (e.g. TMG, TMA, TMIIn, etc.) respectively into the chamber, respectively. Meanwhile, the n-type and p-type dopant sources (Si_2H_6 and Cp_2Mg) are also injected via the lower carrier line. The reactor is connected to the exhaust system via the main pump, while the reactor pressure can be regulated by a throttle valve located between the reactor and the main pump. The gas delivery system in the MOCVD system achieves precise control of the gas flow rate and the pressure in the reaction chamber through all the components working together, thus ensuring the stability and controllability of the chemical reaction during the growth process.

3.2.4 MO Source System

Bubblers are important components used to store and transport metal-organic precursors, which are typically made of high-purity stainless steel to ensure corrosion resistance and chemical stability. Each bubbler is designed to store a specific MO source, which can be either liquid or solid, depending on the type of precursor used. All of the MO sources employed in this work are liquid, with the exception of TMI and Cp_2Mg , which are solid. In the MOCVD system, each bubbler is

mounted on a thermostatic bath, which maintains a specific temperature in accordance with the type of MO source. The temperature is critical to ensure a steady rate of evaporation of the MO precursor, as the rate of evaporation directly affects the molar flow rate of the precursor into the reactor. The temperatures required of the MO sources covered in this thesis are different, as detailed in *Table 3-1 The Parameters of Common MO Bubblers* [13-16].

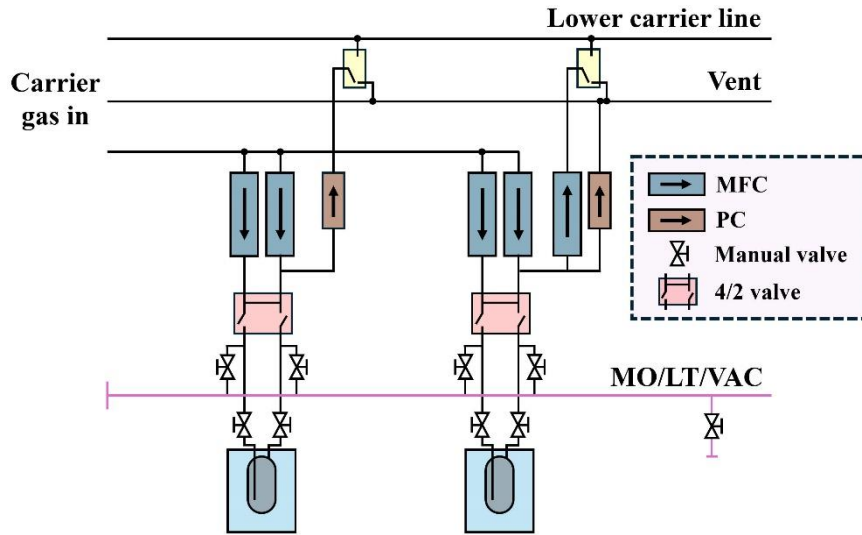


Figure 3-9 The schematic diagram of the MO source system.

The bubbler works by directing the flow of carrier gas through the stored MO source, whereby the MO is extracted by the carrier gas and transported into the chamber. MFCs and valve systems are employed to regulate the delivery of MO sources with precision, as illustrated in Figure 3-9, which is a schematic of the MO system. The valve system comprises manual valves, pneumatic valves and the 4/2 valves. Specifically, the manual valves are employed to manually disconnect the MO source from the MOCVD pipework, which are typically required to manually close the valves during bubbler replacement operations. In addition, several pneumatic valves are employed for the switching of the carrier gas between H₂ and N₂, while a further pneumatic valve is used to regulate the connection between the reactor and the vent line. Of all the valves, the 4/2 valve is the most important, as it enables the switching of the carrier gas flow path during the growth process. Consequently, it allows for the function of carrier gases to pass through or bypass the bubbler.

In MO gas systems, a standard gas system with an additional dilution line can be employed to provide a low-flow carrier gas supply. The left side of Figure 3-9 depicts a standard gas system without dilution lines, which consists of two mass flow controllers (MFCs) and a pressure controller

(PC) for controlling the gas flow rate and the inside pressure of the bubbler, respectively. Another MO gas system with a dilution line is presented on the right side. In order to facilitate precise regulation of the small gas flow, an additional output MFC has been installed on the branch pipeline. The actual injected gas flow rate (f) can be reduced by the introduction of this bypass MFC, and the actual injected gas volume can be calculated by the following equation:

$$f = \frac{f_{source}}{f_{source} + f_{dilute}} \times f_{inject} \quad (3.5)$$

Where the f_{source} is denote the flow rate of bubbler input, f_{dilute} is the flow rate from another input gas line, and the f_{inject} represents the final flow rate of the mixture injected into the reactor.

The vapour partial pressure ($P_{partial}$) of the most group III precursors in each bubbler is dependent on the temperature of the MO source, which is controlled in the thermostatic bath. This relationship between $P_{partial}$ and temperature can be expressed as follows:

$$\log(P_{partial}) = B - \frac{A}{T} \quad (3.6)$$

Where the A and B in this equation are constants depends on the type of the MO source, which list in the *Table 3-1 The Parameters of Common MO Bubblers [13-16]*, and the T is the temperature MO source in Kelvin.

However, for the solid Cp_2Mg source, the equation for the vapour partial pressure is slightly different from the above equation and is expressed as follows:

$$\log(P_{partial}) = B - \frac{A}{T} - 2.18 \ln T \quad (3.7)$$

In accordance with the principles of the ideal gas law, the molar flow rate of the specific MO source (\dot{n}_{MO}) can be determined for a given temperature and pressure. The equation is as follows:

$$\dot{n}_{MO} = \frac{f_{source} \times P_{partial}}{V_m \times (P_{source} - P_{partial})} \quad (3.8)$$

Where f_{source} is the flow rate of the carrier gas into the MO source bubbler, P_{source} presents the partial pressure of the bubbler, $P_{partial}$ is partial pressure of vapourised MO source and V_m expressed as molar volume, the molar volume of an ideal gas is approximately 22,414 cm³/mol at standard temperature and pressure (0 °C and 1 atm).

Table 3-1 The Parameters of Common MO Bubblers [13-16].

Source	Chemical Formula	A	B	Bubbler Temperature (K)	$P_{partial}$ (torr)	$P_{bubbler}$ (torr)
TMG _{1,2}	$Ga(CH_3)_3$	1703	8.07	273	67.91	1300
TMA ₁	$Al(CH_3)_3$	2134	8.22	291	7.70	1500
TMA ₂	$Al(CH_3)_3$	2134	8.22	294	9.15	1500
TMI _{1,2}	$In(CH_3)_3$	3014	10.52	303	2.67	1000
Cp_2Mg	$Mg(C_2H_5)_2$	4198	25.14	303	0.07	900

When the system needs to be supplied with a MO source during the growth, the carrier gas is piped into the bottom of the bubbler, where it comes into contact with the precursor and undergoes gasification. The gasified precursor is then transported through the output pipe at the top of the bubbler to the reaction chamber. The thermal tape will be wrapped around the output pipe of the bubbler for heating the pipe, which functions to prevent condensation of the MO source within the pipe. In addition, it is crucial to highlight that in the case of liquid MO sources, the carrier gas input is situated at the bottom of the bubbler, while the mixture output is located at the top of the bubbler. In contrast, for solid state sources, the aforementioned configuration is reversed.

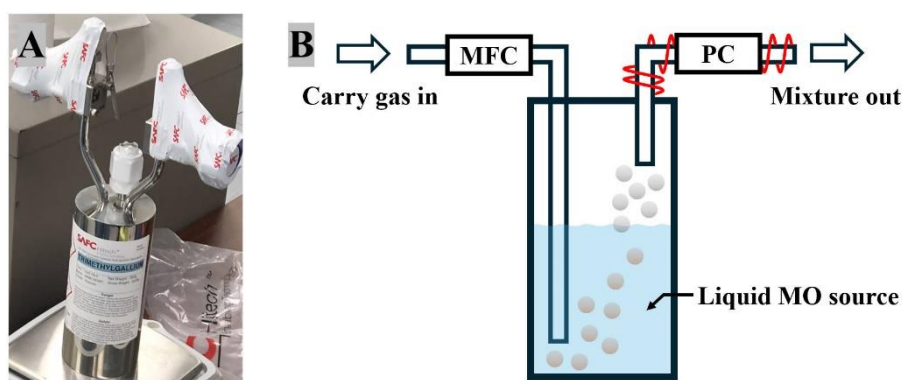


Figure 3-10 (A) Photograph and (B) schematic diagram of the MOCVD bubbler.

3.2.5 Reactor System

The basic configuration of the reactor system is illustrated in Figure 3-11. The reactor body is constructed from stainless steel, which enables it to withstand high pressure and corrosion. When the reactor lid is closed, a double O-ring on the sealing flange allows the chamber to be formed into a completely airtight compartment. A gas line port is situated between the two O-rings and is connected to the main pump, which used to evacuate the pressure between the two O-rings to 0 mbar and monitoring by a pressure sensor. The sample can be placed within the pocket of the susceptor, which is supported by the susceptor support and positioned above the tungsten heater. During the growth, the susceptor will be rotated at 60 rpm (revolutions per minute), thus ensuring a stable and uniform temperature across the sample surface in the pocket [17]. A thermocouple located below the susceptor is employed for real-time monitoring of the temperature data. The quartz liner, which exhibits excellent chemical resistance, is attached to the inner wall of the reactor to protect it from potential damage and contamination. And the exhaust port is connected beneath the chamber via a flange ring and is employed to expel the reacted exhaust gases to the exhaust gas treatment system. The chamber and shower head are both water-cooled, with the cooling water maintained at a constant temperature by a chiller. The showerhead is mounted on the reactor lid, which is located directly above the susceptor when the reactor is closed. And the distance between the shower head and susceptor is designed to be small enough to ensure that the precursor gases can be efficiently directed to the surface of the heated substrate and to prevent parasitic reactions. The distance has been set to 11 mm in accordance with the maintenance manual that accompanied this MOCVD system. The showerhead is equipped with a number of optical ports, which can be used for the installation of an in-situ monitoring system.

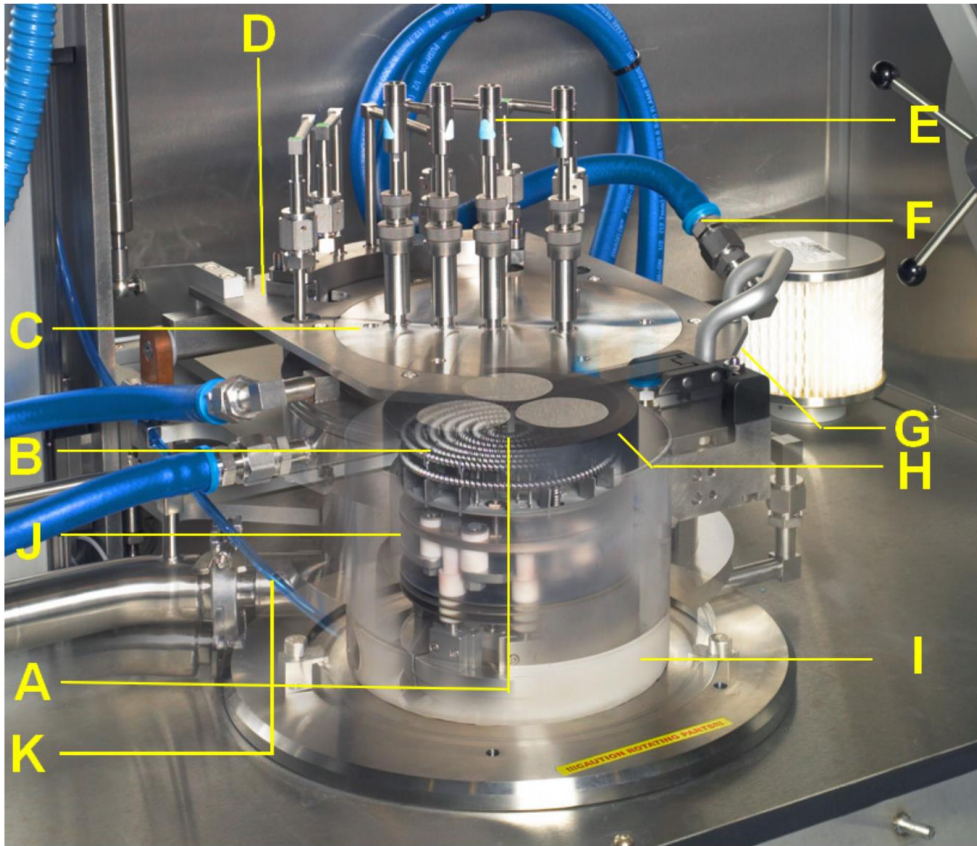


Figure 3-11 The basic configuration of the reactor system; (A) thermocouple; (B) tungsten heater; (C) showerhead; (D) reactor lid; (E) optical probe; (F) Showerhead water cooling; (G) double O-ring seal; (H) susceptor; (I) quartz liner; (J) susceptor support; (K) exhaust.

Showerhead

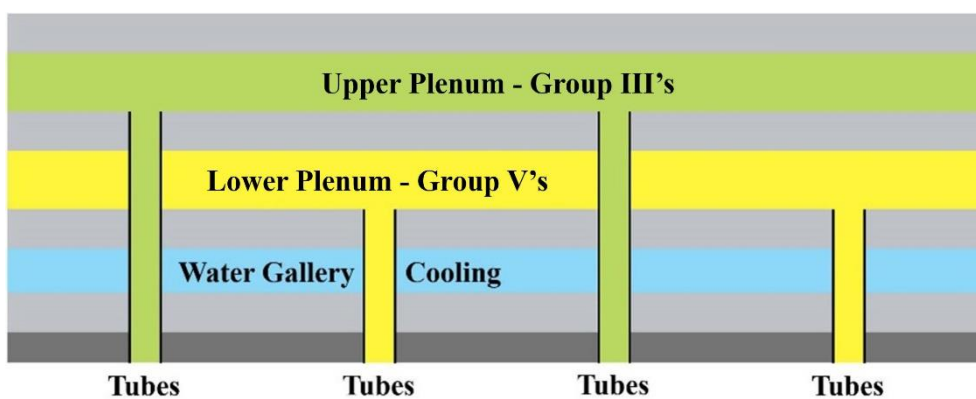


Figure 3-12 Schematic of the cross-sectional configuration of the two-plenums showerhead.

The showerhead is typically designed with two plenums - upper and lower, which allows for the independent introduction of different gases. In this MOCVD system, two plenums are designed to

transport group V and III gases independently of each other into the reactor. This means that the separately transported gases do not mix before passing through the showerhead, thus greatly reducing the likelihood of parasitic reactions and the generation of by-products. Figure 3-12 presents a schematic of the cross-section of the two-plenums showerhead.

Tungsten heater

The tungsten coil heater consists of three tungsten coils and is divided into three heating zones (Figure 3-13B), which are supplied by three separate power supplies. The three independent power supplies can regulate the power output of the three coils separately, with precision temperature control of the zone A, B, and C. This ultimately enables the uniform distribution of the temperature of the entire heater.

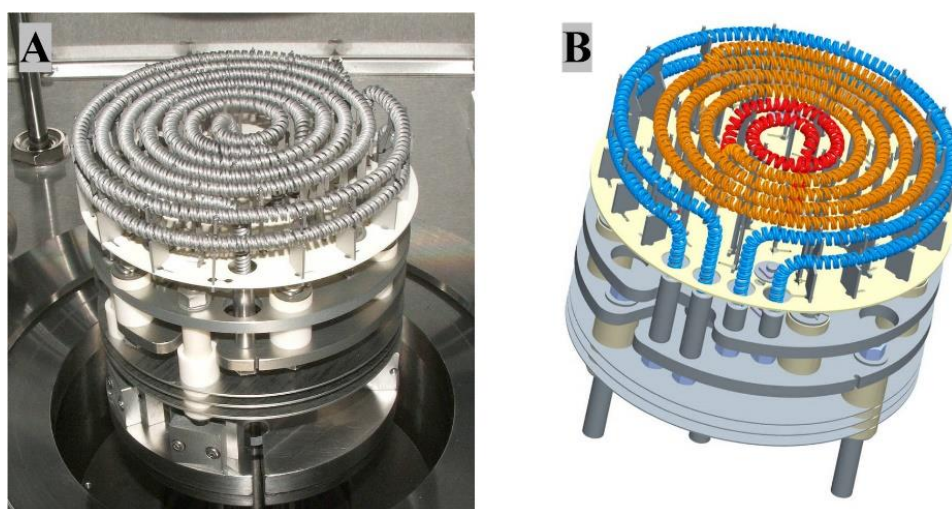


Figure 3-13 Heater unit of the MOCVD system; (A) photo of tungsten heater; (B) heater coil zone schematic - (Red: Zone A; Orange: Zone B; Blue: Zone C).

3.2.6 Reactor Exhaust System

The typical configuration of a reactor exhaust system comprises a pump, filter, and scrubber. The exhaust gases from the reactor are pumped to the two-stage filter system by the main pump through a flexible stainless-steel pipe that is connected to the bottom of the reactor chamber. This two-stage filtration system comprises a mesh filter for the primary filtration of larger particles in the exhaust gases and a 6 μm particle pall filter for the removal of fine particles. It is important to note that the particle-filtered exhaust gases are still harmful to the environment and cannot be vented directly

into the air. Therefore, the exhaust gases are subsequently pumped through stainless steel pipework to a scrubber, where they are decomposed by a heated catalyst into air-friendly gases before being released to the air. The scrubber employed in this MOCVD system is an EDWARDS M150 gas reactor column, comprising a gas reactor column cartridge containing calcium oxide and nickel (II) oxide.



Figure 3-14 The components of the reactor exhaust system; (A) mesh filter; (B) pall filter; (C) overview of EDWARDS M150 gas reactor column; (D) overview of the scrubber heater cell contained a gas reactor column cartridge.

3.2.7 In-situ Monitoring System

The monitoring system allows the operator to monitor crystal growth in the reaction chamber in real time during growth. The growth data acquired through the monitoring technique can be stored and displayed on an accompanying PC, including wafer surface temperature distribution, surface morphology, growth rate and wafer curvature. The three principal in-situ monitoring technologies employed in this work are the ARGUS CCS pyrometric profiling system, interferometer system, and Laytec Epicurve TT system.

Argus

The ARGUS CCS pyrometric profiling system is a multi-channel pyrometer designed to provide precise temperature measurements at discrete points on the susceptor surface within the MOCVD reactor chamber. This measurement technique is based on the principle of black body radiation, which states that when an object is heated, it emits radiation, the level of which is proportional to the temperature. The distribution of radiant energy with respect to the temperature of a blackbody can be described by Planck's law. When combined with Wien's law, the wavelength distribution at any given temperature can be predicted. In reality, no object can be considered an ideal blackbody. Therefore, if the true temperature of an object is to be obtained, its absorptivity and reflectivity must be taken into account. In general, this can be expressed in terms of emissivity (ϵ). For true black body, the $\epsilon = 1$, for real object, the $\epsilon < 1$. Accordingly, the analysis software AIXACT, was developed to obtain both the emissivity corrected temperature and non-emissivity corrected temperature. Figure 3-15 shows the ARGUS monitoring system and 3x2" susceptor.

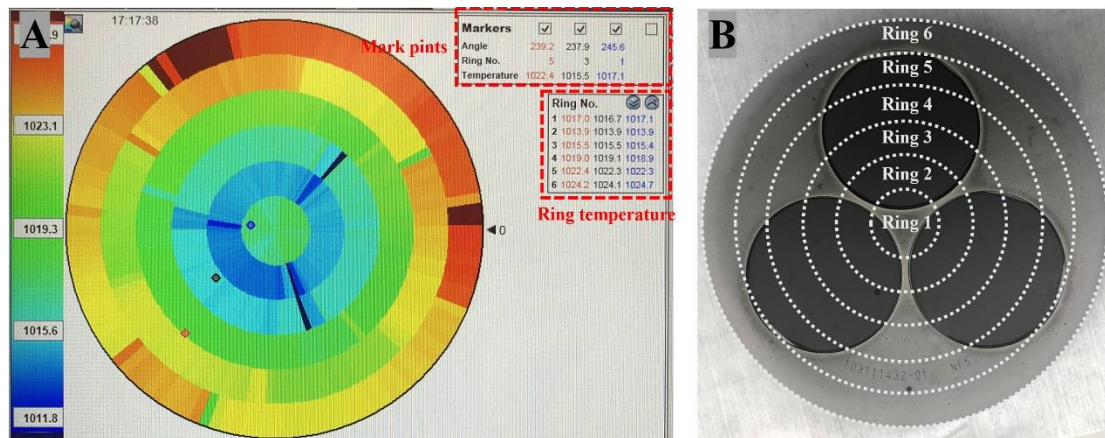


Figure 3-15 (A) The ARGUS CCS system monitoring interface in Aixtron MOCVD system, and (B) the photograph of a 3x2" susceptor with the ring areas are laded.

A number of photodetectors are mounted on the top of the showerhead, as the sample is heated, a small amount of radiation passes through the small holes in the showerhead where it is collected by the photodetectors and converted into an electrical signal that is transmitted to the PC. The number of detectors is dependent on the size of the reactor, in this 3x2" reactor system, the six detectors was used with distributed along the radius of the showerhead from the centre to the edges. During the growth process, the susceptor will rotate at a constant speed, which means that the entire susceptor

is scanned and a temperature map can be displayed by AIXACT. The ARGUS system requires periodic calibration by scanning across all detectors using a blackbody calibrator to ensure the accuracy of the detected data.

Interferometer

The Interferometer is one of the powerful components of the in-situ monitoring system, which uses Fabry-Perot reflectance interferometry to monitor and analyse the behaviour of thin film materials during MOCVD growth. The interferometer measures the reflection light and its interference phenomena of the incident light by emitting a coherent light source (laser) into the surface of the film. This enables the interferometer to obtain the interference pattern of the reflected light, and system then analyses the changes in the interference fringes in real time, ultimate obtain a reflective intensity curve that varies periodically over time. This curve can be used to easily calculate the thickness and growth rate of the film by following equation:

$$d = \frac{\lambda}{2n} \quad (3.9)$$

Where λ presents the wavelength of the incident light source, n denotes the refractive index of the film and d signifies the thickness of the film in single oscillation. The interferometer uses a red laser with a wavelength of 635 nm, and due to its low thin film extinction coefficient ($k < 0.01$), the attenuation of the probe intensity from absorption is negligible. Theoretically, the approximate thickness of a single oscillation in interferometry, d_{GaN} is 133 nm and d_{AlN} is 144nm.

Furthermore, the reflective intensity curve not only calculates the thickness of the film but also indicates the surface roughness of the grown film through the intensity of the reflected signal. In the case of a smooth and uniform film surface, the interference effect of the reflected light can be pronounced, resulting in the formation of clear interference fringes, which are expressed as high reflection intensity and distinct peaks and troughs. Conversely, a rough surface leads to light scattering and multipath interference effects, resulting in a reduction in contrast of the interference fringes and a weaker intensity of the reflected signal. Figure 3-16 shows a typical interferogram recorded for two-step GaN growth in the GaN growth section, from which it is easy to see that the amplitude of the oscillations converges with the growth of the GaN, which means that the surface morphology of the GaN is progressively roughened.

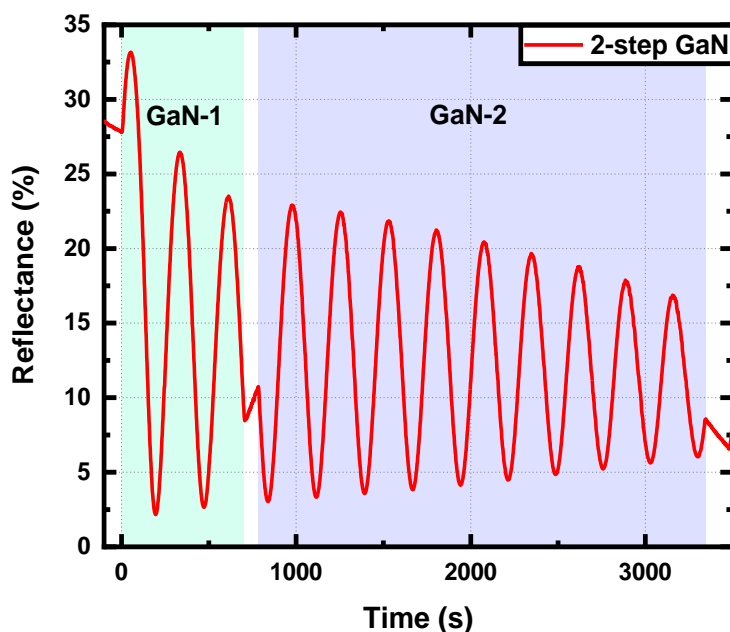


Figure 3-16 Typical interferogram record of the two-Step GaN growth (GaN-1 and GaN-2 part).

Laytec Epicurve

Wafer bending is a common issue in the MOCVD growth process and usually occurs when the lattice mismatch of the grown films between substrate is large. This phenomenon is not solely attributable to the lattice mismatch but is also related by the mismatch in the coefficient of thermal expansion between the film and the substrate. Even in the case of identical materials, the uniform temperature distribution along the direction of the substrate thickness or in the lateral direction can result in differences in thermal expansion, which can lead to wafer bending. Concurrently, wafer bending can result in further uneven temperature distribution, thereby creating a feedback loop that worsens the problem. The issue of wafer bending is of particular concern in the growth of GaN-on-Si, due to the greater difference in the coefficients of thermal expansion and the worse lattice mismatch between Si and GaN. Consequently, an in-situ monitoring system that provides real-time data on wafer curvature, stress and thickness is of particular significance in this context. In this regard, the Laytec Epicurve TT system fulfils an indispensable function.

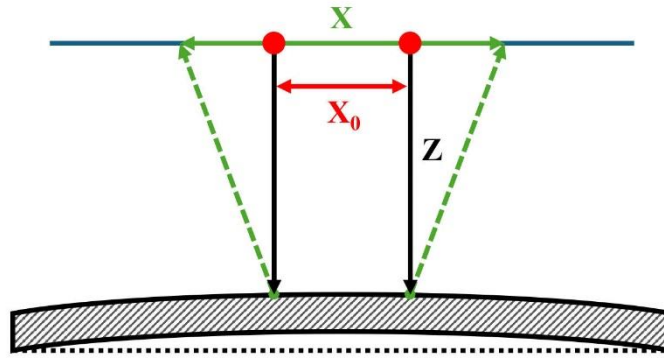


Figure 3-17 The fundamental principle of the Leytec Epicurve.

The Leytec Epicurve system employs two parallel laser beams to irradiate the growing wafer, after which the reflected beams are collected through a detector. If the wafer is ideal flat, the reflected beams will remain parallel. Conversely, if the wafer is curved, the reflected beams will no longer be parallel. This implies that the difference in spacing between the two incident beams and the reflected beams is no longer equal. This difference in spacing directly reflects the degree of bending of the wafer, with greater differences indicating a greater degree of bending. The following equation can be used to quantify the curvature of the wafer (κ):

$$\kappa = -\frac{1}{2Z} \frac{x - x_0}{x_0} \quad (3.10)$$

Where Z is the distance of the laser beam from the optical head to the wafer, x refers to the distance between the reflected laser beams, and the x_0 refers to the distance between two parallel incident laser beams. A positive value of κ indicates a concave bow bending of the wafer, while a negative value indicates a convex bow bending.

3.3 Characterisation Techniques

3.3.1 Nomarski microscopy

The Nomarski microscope, also known as a differential interference contrast (DIC) microscope, is a high-resolution microscope widely used in the field of semiconductor materials and is one of the most effective tools for rapid monitoring of surface morphology. Compared to standard optical microscopes, the DIC system has the function of an optical interferometer in addition to the usual microscope functions, by using optical path differences and polarization phenomena to obtain high contrast imaging. For III-nitride epitaxial layers and substrates (sapphire), which are normally transparent, the DIC system is ideally suited for the characterisation of III-nitrides. Moreover, the DIC system is able to obtain of the additional information other than the topography of the sample surface, such as differences in thickness or variations in refraction index [18, 19]. Figure 3-18 illustrates the mechanisms of a basic DIC system.

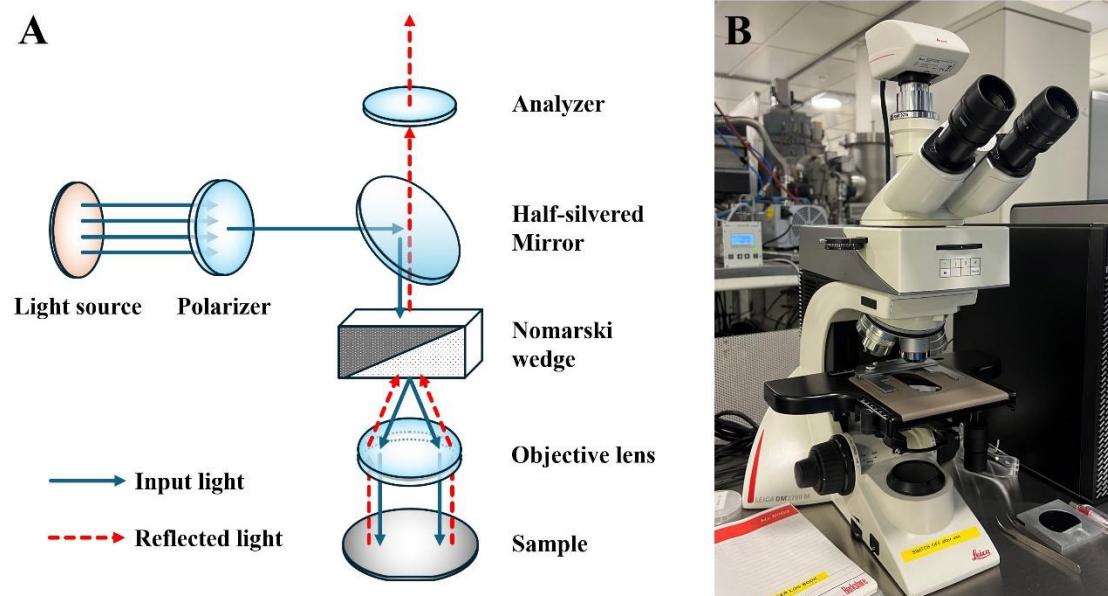


Figure 3-18 (A) Schematic illustration of a basic DIC system, and (B) the photograph of the Leica DMLM microscope system.

A non-polarised light from an incandescent source enters the DIC system is linearly polarised at 45° by a polarizer. A semi-transparent mirror then reflects the linearly polarised light beam into a prism called Wollaston prism and is separated into two orthogonally polarized beams, which are then focused on two adjacent points of a sample surface by a condenser. Due to the difference in

refractive index or thickness of the two points of the sample surface being illuminated, the beams will experience slightly different optical path lengths, and these differences will be carried by the phase of the two beams, which will then be reflected into the Nomarski prism, and these two beams will be recombined into a single ray of light with a combined path length before reaching the analyser. The analyser is a second polarizer, which makes the vibrations of the beam into the same plane and axis, causing interference to occur between the two wavefronts and become one ray of light with linear polarization and then travels to the eyepiece or camera. As optical interference is sensitive to the difference in optical path length, any difference in refractive index or thickness of the sample surface can brighten or darken the image, thus improving the contrast of the DIC image and providing a three-dimensional appearance of the sample surface [19]. Figure 3-18B shows the Leica DMLM microscope that employed in this work.

3.3.2 X-ray Diffraction (XRD)

X-ray diffraction (XRD) is a non-destructive characterization method. It is widely used to investigate crystalline materials to obtain characterization information including lattice parameters, chemical composition, strain state of epi-layers, defect information, and layer thicknesses of thin films and superlattice or quantum wells. Moreover, XRD can be employed for a multitude of measurements by modifying the experimental configuration to align with the particular research objectives. The Bragg's diffraction is the physical foundation of the XRD measurement, as depicted in the illustration below [20].

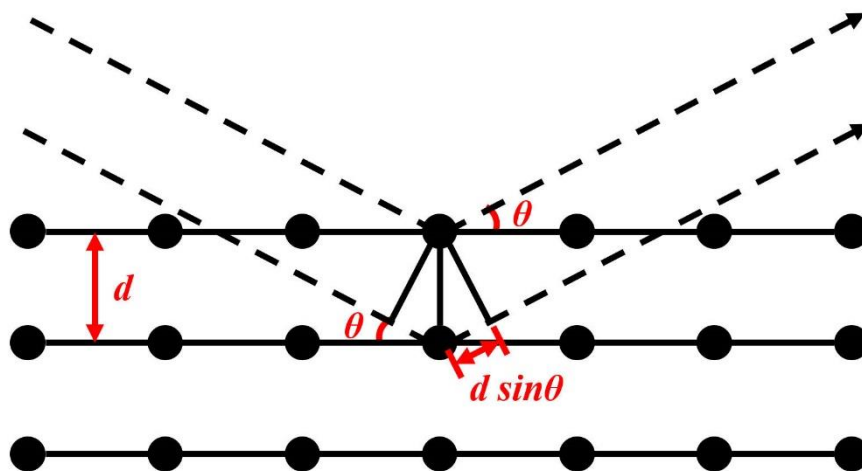


Figure 3-19 Schematic illustration of the X-ray diffraction with Bragg's law.

The periodic structure of a crystal looks like a grating, the incident X-ray into the crystalline structures and diffracted by the crystal. Generate constructive interference at certain incident angles which meet Bragg's law. The incident angles can be determined using the equation below [21, 22]:

$$n\lambda = 2d\sin(\theta) \quad (3.11)$$

where n is an integer as called order of diffraction; λ is the wavelength of the X-ray; d is the spacing between two adjacent atomic planes of the measured sample; and θ is the angle of the incident X-ray beam; 2θ is the angle of the diffracted X-ray beam relative to the incident beam.

Bruker D8 X-ray diffractometer was used main characterization devices in this project, which consists of an X-ray tube, an incident X-ray optics unit, a sample stage with vacuum fix system, a secondary optics unit and a detector to receive X-ray diffraction. In this project the XRD is mainly used to evaluate the crystal quality, calculation of the different molecular components, and the observation of internal stresses within the material. Figure 3-20 shows the Bruker D8 X-ray diffractometer and the key components are marked.

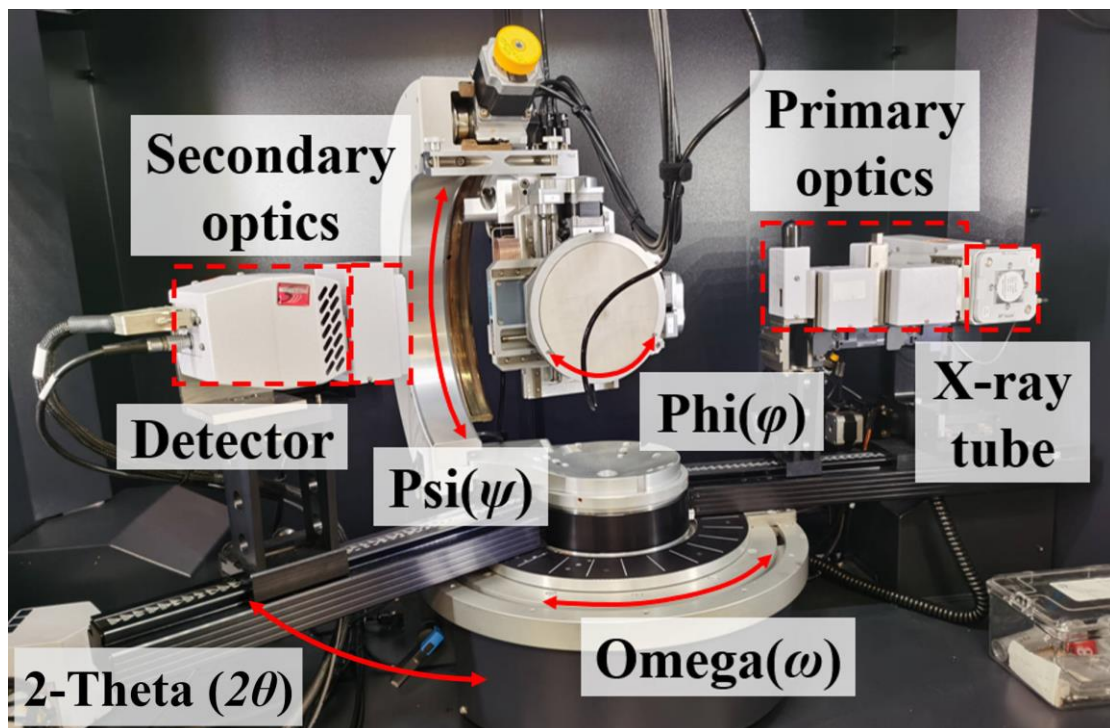


Figure 3-20 Photo of the Bruker D8 X-ray diffractometer.

3.3.3 Scanning Electron Microscopy (SEM)

Scanning electron microscopy (SEM) is one of the powerful characterization techniques employed in semiconductor study to investigate sub-micron structures and nanoscale information about the sample. Since SEM uses an electron beam as the illumination source, it can produce images with higher magnification and resolution than conventional optical microscopes that use visible light. In addition, as the sample is placed on an angle-adjustable sample stage, the SEM can obtain images of the sample from different angles by tilting the sample stage to meet experimental requirements. The Raith 150 EBL series SEM system used in this work shown in Figure 3-21B.

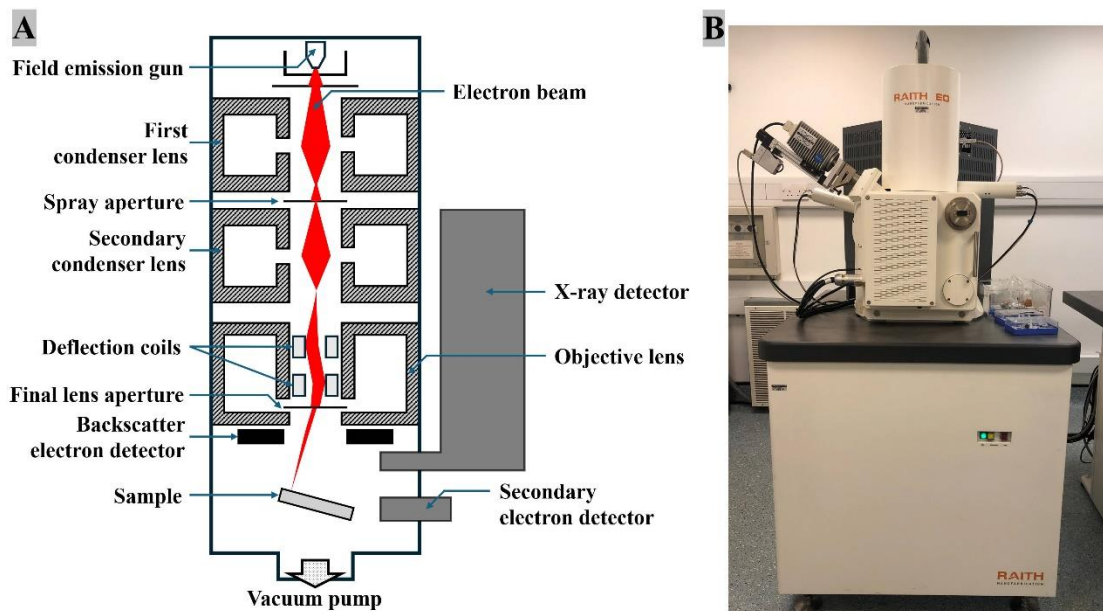


Figure 3-21 (A) Schematic structure of an EBL-SEM system and (B) the photograph of a Raith 150 EBL series SEM system which used in this project. Adapted with permission [23].

Figure 3-21A illustrates the basic structure of the typical EBL-SEM system, which including a field emission gun (FEG), a series of magnetic condenser lens, a set of deflection coils, a various of detectors and an angle-adjustable sample stage. Furthermore, the SEM must operate under a high vacuum environment to reduce the interaction of the electron beam with molecules in the air and improves image quality. A high energy electron beam is generated from a field emission gun then collimated and focused by a magnetic condenser lens. The collimated electron beam can be narrowed using a lens aperture and the well-focused beam are then shone onto the sample. The high-energy electron beam excites the atoms within the sample, resulting in the release of particles or

waves due to the matter interaction of the electrons. These released particles are collected by specific detectors, which convert them into electrical signals to the computer, providing the necessary information and images [24].

When the primary electron beam from the SEM interacts with the surface of the sample, it releases particles and waves through various signal excitation mechanisms. These signals carry information about the characterisation of the sample. Four types of signals are commonly collected by detectors and used to assess the characteristics of the sample, which are:

- i. Backscattered electrons (BSE).** Backscattered electrons are electrons that are reflected back from the sample by elastic scattering due to the interaction of the electron beam with the nucleus of the sample, which has high energy and high penetrating power. As the electron beam interacts with the electron cloud of the atom, the degree of elastic scattering is influenced by the atomic number of the sample. This makes BSE highly sensitive to the atomic number, and it is often used to provide information about the chemical composition and density distribution of the sample.
- ii. Secondary electrons (SEs).** Secondary electrons are the most common signal used in SEM imaging, which is emitted by bombarding the surface of a sample with the primary electron beam. The SEs are therefore highly sensitive to the morphology and topography of the sample surface and provide high-resolution and contrast images of the sample surface.
- iii. X-ray emission.** When the electron beam interacts with the sample atoms, the part of the primary electrons produced is from the inner shell of the atom. As the electrons escape their original position, holes are created and are quickly filled with other electrons from the higher energy shell and unleash the energy. These energies are emitted in the form of X-rays with different characteristics, each with its own specific energy level and characteristic X-rays, so that by detecting these X-rays and analysing their energy, the elemental species and relative content of the sample can be determined. Therefore, the elemental composition of the sample can be determined by energy dispersive X-ray (EDX) analysis.
- iv. Light emission.** When an electron beam interacts with the surface of a sample and released energy can manifest in different forms, one of which is light, containing both visible and

ultraviolet light. It can be used to analyse the surface properties of materials, thus providing in-depth analysis and characterisation of materials.

3.3.4 Atomic Force Microscopy (AFM)

Atomic Force Microscopy (AFM) is a high-resolution surface scanning probe microscopy technique that uses a nano-scale tip to scan the surface of a sample and generates a high-resolution surface topography image by measuring the force of interaction between the probe and the sample. Unlike other high-resolution microscopy techniques, AFM does not require special preparation of the sample and can image a variety of materials directly, therefore this technique is often used to characterise the surface roughness of a material. Figure 3-22A shows a fundamental illustration of the AFM mechanism. A sharp nanoscale probe is mounted on a cantilever and a laser beam is directed at the cantilever and reflected onto the detector unit. As the tip of the probe comes very close to contact with the sample surface, repulsive forces gradually make the cantilever away from the sample surface and the reflected laser light is deflected. During the scanning process, the cantilever is deflected (away from the sample surface) by the topography of the sample surface and the direction of reflection of the beam changes, which is captured by the detector and transmitted to the computer control unit and imaged by the software.

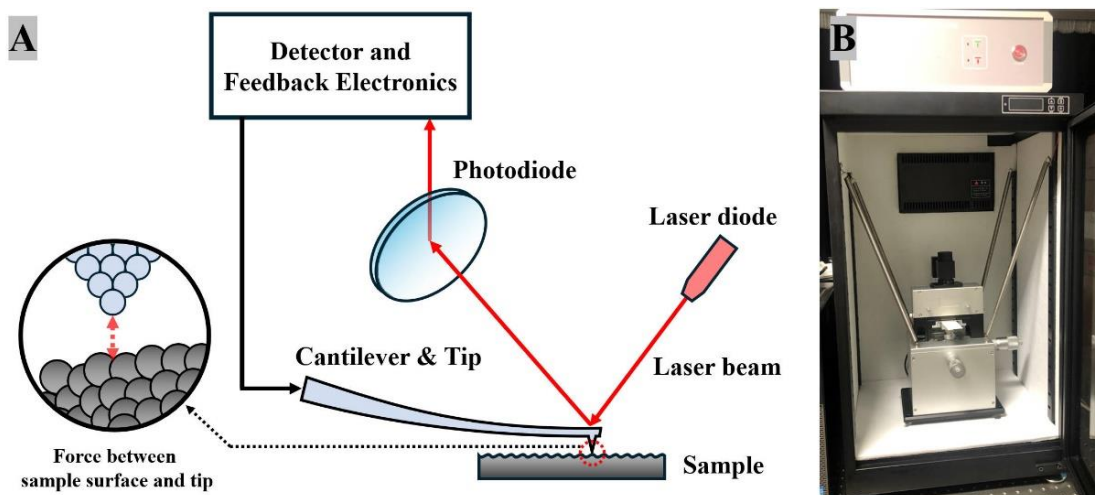


Figure 3-22 (A) Schematic diagram of an AFM system and (B) the AFM system used in this project.

Depending on the differences in the interaction forces generated between the tip and the sample surface, the AFM has three basic modes of operation: contact mode, non-contact mode and tapping mode. Contact mode and non-contact mode are the two most commonly used modes and can be

used in various scenarios. Contact mode is the most direct imaging mode of AFM, it allows to obtain of high-resolution imaging. Through the scanning process, the probe tip remains in contact with the sample surface and the tip deflects according to the roughness of the sample surface. The interaction forces are measured by the bending situation of the tip and generated an image of the surface topography by software. The deformation of the tip is driven by the repulsive forces generated between the tip and the sample surface atoms. However, as the probe tip is in direct contact with the sample surface, the force exerted on the tip by the cantilever during scanning typically in the range of 10^{-10} to 10^{-6} N. This may cause damage to the sample surface and therefore the contact mode is not suitable for measuring samples with soft surfaces. The non-contact mode allows for imaging the sample with soft surface. Through the scanning process, the probe tip does not touch the sample surface, the probe is oscillating at a distance of 5 to 10 nm above the sample surface and the interaction between the sample and the tip is controlled by van der Waals forces, typically 10^{-12} N, which reduces the damage to the sample surface. However, the experimental environment in this mode is demanding because of the inevitable accumulation of airborne moisture on the sample surface, which can affect the imaging results.

3.3.5 Photoluminescence (PL)

PL is a phenomenon where semiconductor materials absorb photons, exciting electrons to higher energy levels, and then emit photons as these electrons return to a lower energy state. When a laser with photon energy higher than the semiconductor's band gap is used as the excitation source, electrons in the valence band are excited to the conduction band with higher energy level, creating holes. These excited electrons eventually recombine with the holes, emitting photons in the process. The presence of defects in a detected semiconductor has the potential to influence the optical properties, as these defects may act as non-radiative recombination centres. Photoluminescence (PL) spectroscopy is a non-destructive and non-contact method that is widely employed for the characterisation of semiconductors. It can be used to investigate a range of optical properties, including band gaps, alloy composition, crystal defects, the quantum-confined Stark effect (QCSE), and strain. Furthermore, PL is capable of detecting specific impurities, with doping density inferred from emission intensity and impurity energy levels calculated from PL peak positions. However, PL is limited in its ability to provide accurate impurity concentration data [25-28].

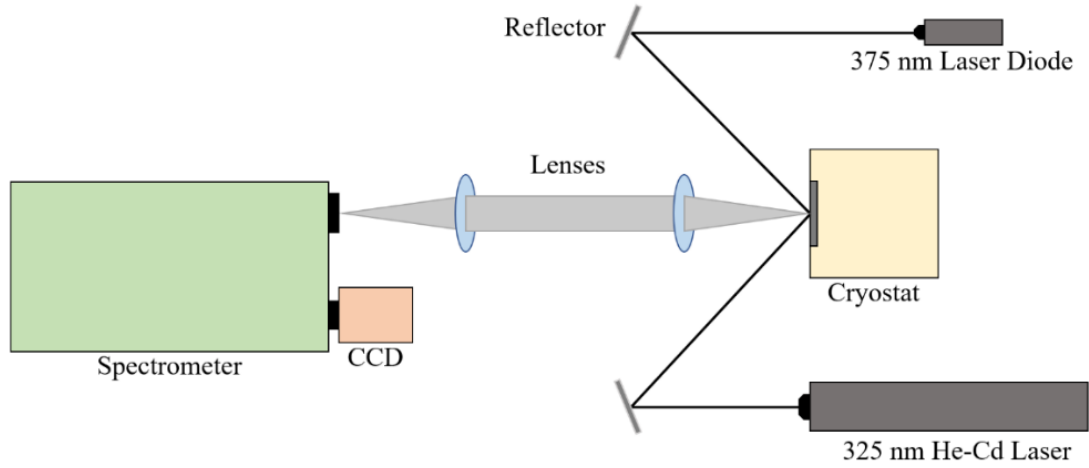


Figure 3-23 Schematic diagram of a custom-built PL system.

The PL system employed in this thesis is a custom-built PL system utilising a 325 nm He-Cd laser or a 375 nm laser as the emission source. The laser is reflected by a specially processed aluminium-coated mirror with an extremely high reflectivity of 99% at the wavelengths between 300 nm to 500 nm laser sources, then focused onto the sample surface. The sample is placed on a stage inside a helium (He) closed-cycle cryostat, allowing temperature adjustment from 10K to 300K for PL measurements at different temperatures. Then a pair of 2-inch lenses is employed to collect and collimate the luminescence from sample into a spectrometer and dispersed onto a charge-coupled device (CCD) detector. The different materials can detect by the specific laser wavelength such as the 244 nm laser, which is typically used to detect AlGaIn, the 325 nm laser, which is used to detect GaN and InGaIn, and the 375 nm laser is for InGaIn to meet different measurement requirements.

3.3.6 Confocal Microscopy

Confocal microscopy is a high-resolution imaging technique widely used in semiconductor and material research. It is a type of fluorescence microscopy that uses a focused laser beam to illuminate a specific area of the sample and then collects the emitted light from that area. By focusing the laser at different depths in the sample and collecting the emitted light at these depths, a series of optical cross-sections can be generated which can be used to reconstruct a three-dimensional image.

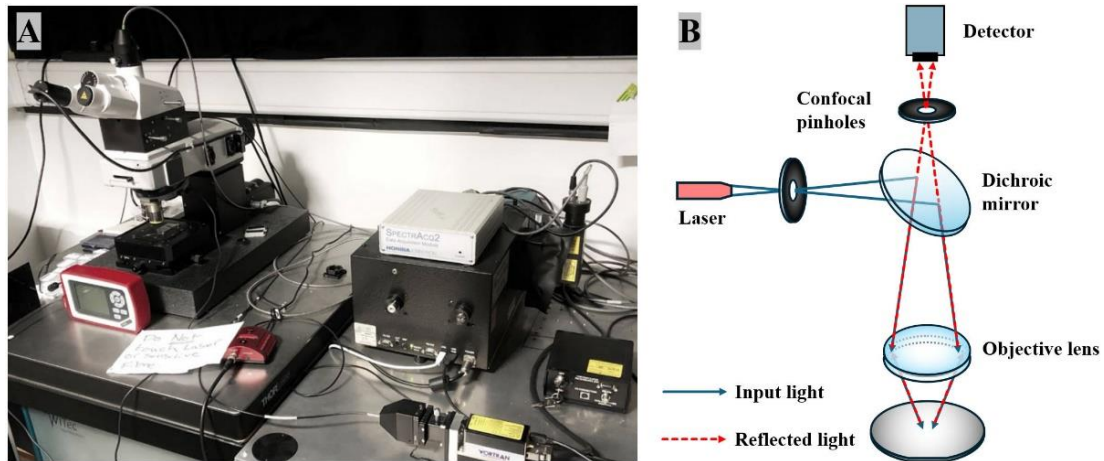


Figure 3-24 (A) Photograph of confocal microscopy system (WITec 300R) and (B) the schematic illustration of a confocal microscopy system.

Figure 3-24B shows the schematic illustration of a basic confocal microscope. A laser is used as a light source and is focused by a light source pinhole aperture to produce a diffraction-limited spot. The light spot is then reflected by a dichroic mirror to an objective lens and focused onto a small area on the surface of the sample. By adjusting the position and direction of the laser beam, the illuminated position can be changed. The fluorescent signals emitted from the sample are then gathered by the same objective lens, passed through a dichroic mirror and finally focused onto a pinhole aperture to be collected by the detector and converted into electrical signals. The converted electrical signals are then sent to a computer to re-organise and process the signals reflected from the sample at different depths, finally generating a series of optical slices to create a three-dimensional image. Confocal microscopy is therefore a powerful tool for better study of the optical of nanostructured materials which allowed to provide high spatial resolution and depth resolution images of the sample.

3.4 Fabrication Techniques

This section presents the fabrication equipment and key techniques employed in this project, including plasma-enhanced chemical vapour deposition (PECVD) for thin film deposition, photolithography techniques, and finally, reactive-ion etching (RIE) and inductively coupled plasma-RIE (ICP-RIE) systems for dry etching processes.

3.4.1 Thin-Film Deposition

Plasma Enhanced Chemical Vapour Deposition

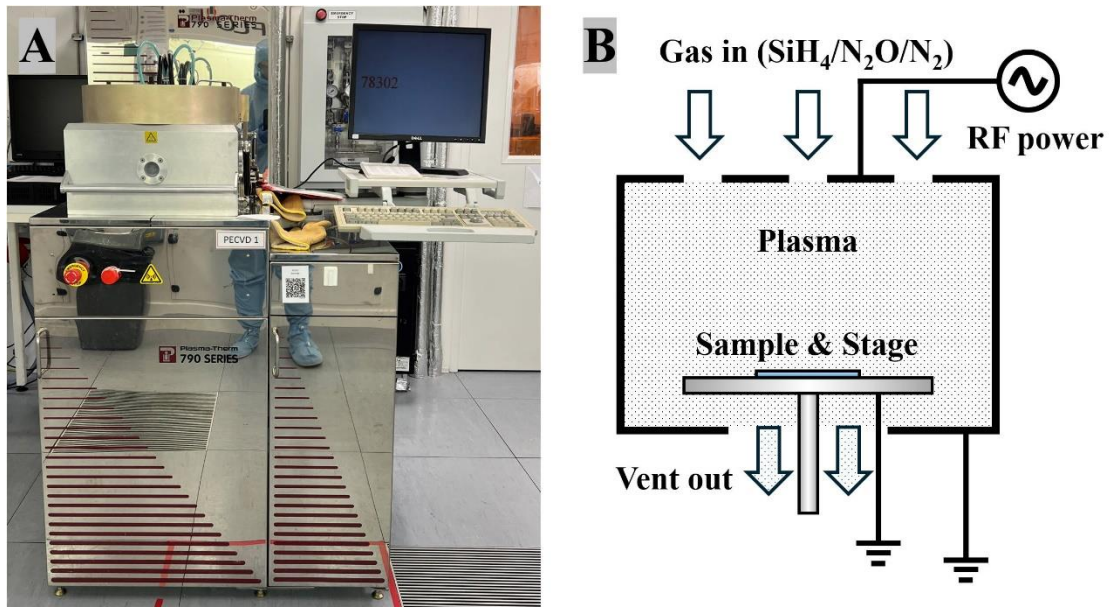


Figure 3-25 (A) The photograph of Plasma-Therm 790 series PECVD system and (B) the schematic illustration of a PECVD system.

PECVD is a common technique for the deposition of dielectric films, such as silicon dioxide (SiO₂) or silicon nitride (Si₃N₄), on a substrate by a plasma-excited chemical reaction. PECVD can be performed at a lower temperature than conventional CVD techniques, while simultaneously increasing deposition rates and improving film quality. Figure 3-25B depicts a schematic illustration of PECVD system. During the deposition process, a variety of reactive gases are introduced into the reaction chamber while the sample is heated to the required temperature. A radio frequency (RF) bias is applied between two parallel electrodes near the sample, with the objective of ionising the reactive gases and generating plasmas. When activated substances in the gas mixture contact with

the sample surface, precursors are generated. These precursors then form the desired thin film structure on the sample surface by diffusion and surface reactions.

In this study, a Plasma-Therm 790 series PECVD system was employed to deposit SiO₂ on GaN-Si/Sapphire templates with the objective of creating patterned templates for subsequent overgrowth. In this system, the reaction gases of silane (SiH₄), nitrous oxide (N₂O), and nitrogen (N₂) are used to deposit SiO₂, with the respective flow rates of 160 sccm, 900 sccm, and 240 sccm. This reaction occurs in the chamber of the pressure is 900 mTorr and at a temperature of 300°C. The typical thickness of the SiO₂ deposit layer required to create the pattern templates for this project ranged from 300 to 400 nm.

3.4.2 Photolithography

Photolithography is a fundamental technology in semiconductor manufacturing, used to precise transfer of micro-patterns from a photomask to a silicon wafer or substrate. The process typically involves the utilisation of ultraviolet (UV) or short-wavelength light to facilitate the transfer of a pre-designed pattern onto a photosensitive medium (photoresist). Given the high sensitivity of the photoresist, the process is conducted in a yellow room to prevent inadvertent exposure to short-wavelength light, which could precipitate unintentional chemical reactions. The photolithography operation is comprised of three principal phases: coating, exposure and developing.

Coating

Before the photolithography process begins, the substrate must be thoroughly cleaned to remove all dust, oils, and other impurities that may affect the adhesion of the photoresist or the accuracy of the pattern, the cleaning procedure is described in section of *Template Cleaning*. In order to obtain a thin, uniform photoresist-coated sample, the sample is positioned on a sample stage and fixed by means of a vacuum device in the spinner. A small amount of photoresist is then dotted in the centre of the sample. Subsequently, the stage in the spinner is activated to rotate at a high speed, typically at 4,000 rpm for 30 seconds. This process ensures that the photoresist is evenly distributed and forms a thin uniform coating layer of photoresist. Finally, the photoresist-coated sample is followed by baking at 100°C for 60 seconds on a hot plate, with the objective of solidifying the photoresist and removing any excess solvents. Figure 3-26 shows spin coater used in this study.

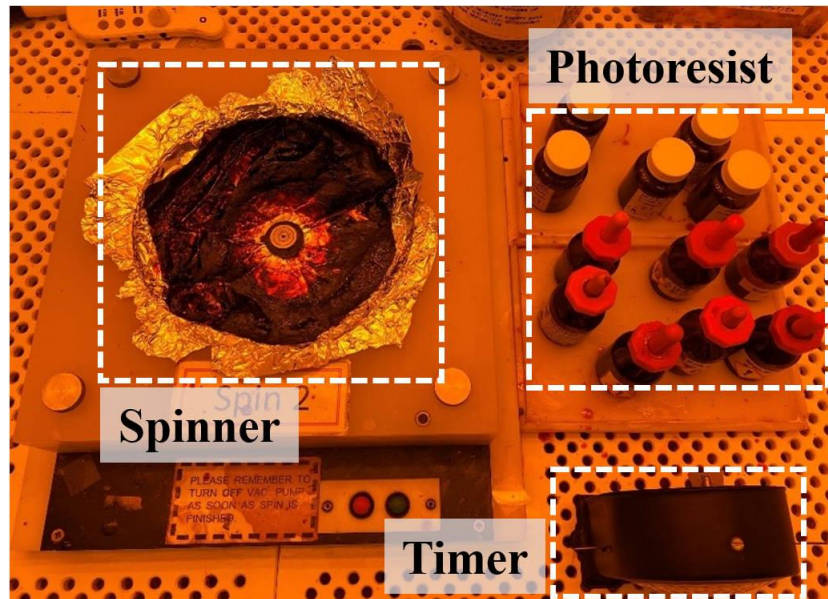


Figure 3-26 The equipment of the coating process; includes the spinner, timer and photoresist.

Exposure

Once a sample with a photoresist-coated layer has been obtained, the subsequent stage of the photolithography process is to use a mask aligner to precisely transfer the pattern from the photomask to the photoresist. The photomask employed in photolithography is a quartz plate coated with a patterned chrome layer, the pattern of which can be customised to suit the desired purpose. In the exposure operation, the photoresist-coated sample is first aligned with the photomask. The photomask is fixed to a non-movable holder, and the sample is fixed to an adjustable sample stage by vacuum, allowing for the precise manual adjustment of the position of the sample stage and the photomask. After alignment, a light source of a specific wavelength is used to illuminate the photoresist. The UV light source illuminates pass through the transparent regions of the photomask to the photoresist, while the opaque regions block the light, thereby transferring the pattern to the photoresist. The photosensitiser in the photoresist undergoes a chemical reaction to form a polymer when exposed to UV light. In positive photoresists, the photoresist in the exposed area becomes soluble, whereas in negative photoresists, the exposed area becomes insoluble. Figure 3-27 illustrates a Karl Suss MJB3 UV400 series mask aligner with a light wavelength of 350-450nm is employed in this work.

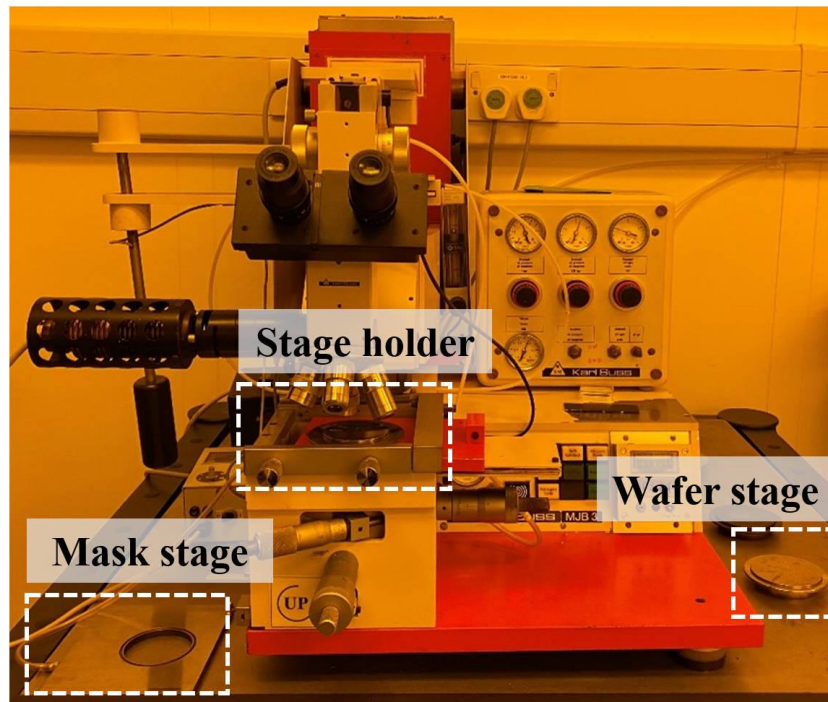


Figure 3-27 The Karl Suss MJB3 UV400 series mask aligner in yellow room.

Developing

The final stage of the photolithography process is the development, the exposed-sample is immersed in a beaker containing a prepared developer solution for approximately 60 seconds, during which the photoresist is locally removed by the developer. The final patterned area that is left behind as a result of the development process which depends on the type of photoresist that is used. If a positive photoresist is used, the exposed portion is dissolved by the developer during the development process, leaving an unexposed area. Conversely, if a negative photoresist is used, the unexposed photoresist is dissolved, and the exposed portion is retained to form the final pattern. Following the completion of the development, the samples were placed on a hot plate for a bake treatment. This process served to further solidify the residual photoresist and to remove any excess developer.

3.4.3 Dry Etching

Reactive-Ion Etching

RIE is a dry etching technique widely used in semiconductor fabrication that utilises reactive ions in a plasma to directionally etch a specific material to achieve high precision pattern transfer. RIE is similar to PECVD in that it involves the generation of a plasma through the application of a RF

bias between two parallel electrodes to excite a reactive gas. In contrast to PEVCD, the plasma generated by RIE is employed to chemically etch away material from the surface of the sample, rather than forming a thin film on its surface.

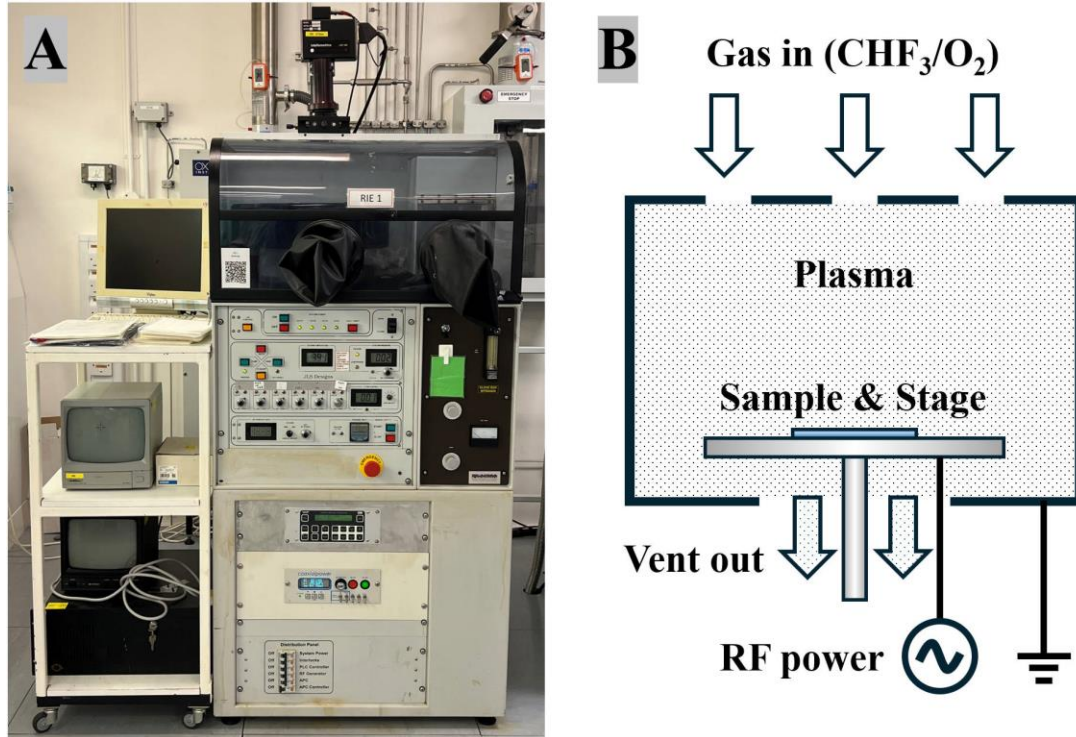


Figure 3-28 (A) The photograph of Plasma-Therm Shuttlelock RIE system and (B) the schematic illustration of a RIE system.

In an RIE system, the walls of the reaction chamber are grounded, and the sample stage is electrically isolated from it. This design allows the establishment of a strong electric field between the two electrodes, which is capable of vertically accelerating the electrons. As the electrons move at high speeds, they collide with the molecules of reactive gas and forming a plasma. In addition, these electrons are not only accelerated by the electric field, but also produce a charge build-up on the sample stage. These accumulated charges provide the driving force for the reactive ions to move towards the sample, thus facilitating chemical reactions and ion bombardment. this combination of ion bombardment and chemical reaction provides the high precision and directionality characteristics of RIE, enabling the precise transfer of patterns and the removal of materials. RIE technology offers a more precise and less damaging sidewall profile than traditional wet etching techniques. In this study, the Plasma-Therm Shuttlelock RIE system was employed to etch a SiO₂ deposit layer, thereby fabricating a dielectric mask-based pattern template.

Inductively Coupled Plasma

ICP-RIE represents an advanced dry etching technology that is an enhanced version based on RIE technology. It offers higher plasma density and lower ion energy, thus enabling a more efficient and precise etching process. In ICP technology, plasma is generated using a different method than traditional RIE, which uses a separate RF coil located above the reaction chamber, through which RF power is applied to generate a time-varying electromagnetic field. This electromagnetic field excites the reactive gas through inductive coupling, thereby facilitating the efficient generation of plasma. Furthermore, RF power is still applied to the lower electrode of the reaction chamber, which serves to attract and accelerate reactive ions in the plasma, causing them to move towards the sample surface with higher energy. By adjusting the RF power of the upper coil and the lower electrode separately, it is possible to achieve independent control of the plasma density and ion energy, thus enabling accurate control during the etching process.

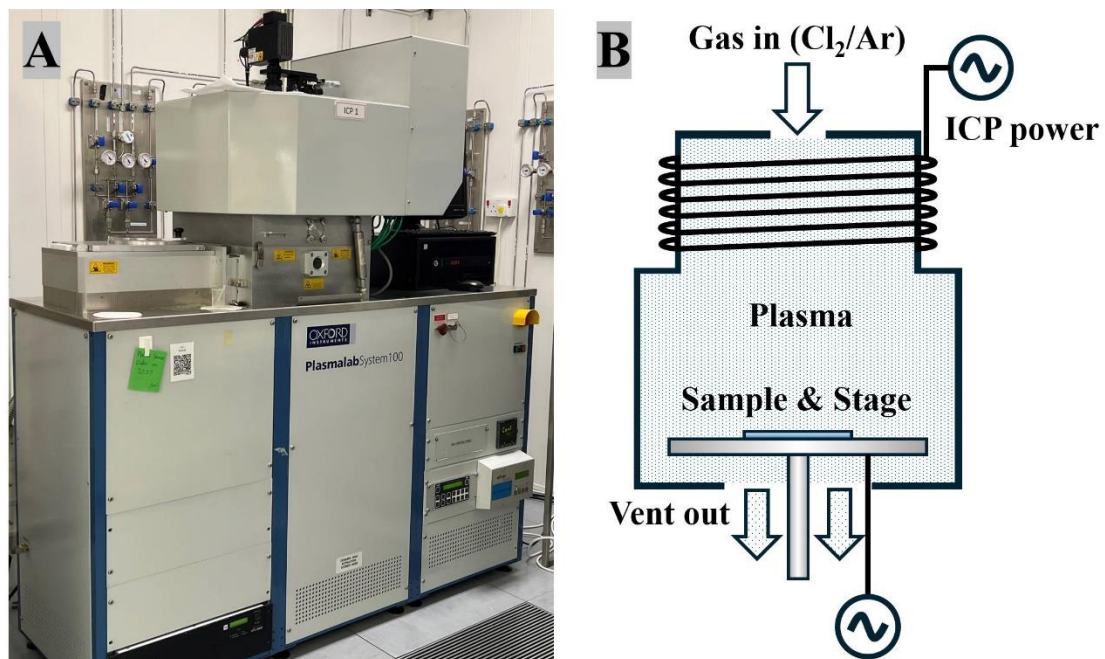


Figure 3-29 (A) The photograph of Oxford Instruments Plasmalab System 100 which used in this project and (B) the schematic illustration of a ICP system.

The ICP system employed in this project, a Plasmalab System 100 from Oxford Instruments is shown in Figure 3-29. The ICP is fitted with an interferometric endpoint system to monitor the depth and rate of etching of the sample. In a monitoring system, when a laser beam is directed towards the surface of an etched sample, a portion of the beam is reflected back onto the detector. As the sample

surface undergoes a gradual change due to the etching process, the reflected light exhibits a corresponding change in phase and displays interference phenomena. Due to interference effects, the intensity of the detected light varies as the surface is etched due to changes in optical path length. The depth of etching can be determined by analysing the periodic variations in the light signal, while the rate of etching can also be calculated by knowing the depth and etching time. A theoretical model for such periodic oscillations can be calculated by knowing the laser wavelength, refractive index and reflectivity.

Reference

- [1] D. Zhuang and J. Edgar, "Wet etching of GaN, AlN, and SiC: a review," *Materials Science and Engineering: R: Reports*, vol. 48, no. 1, pp. 1-46, 2005.
- [2] A. Tan, N. Hamzah, M. Ahmad, S. Ng, and Z. Hassan, "Recent advances and challenges in the MOCVD growth of indium gallium nitride: A brief review," *Materials Science in Semiconductor Processing*, vol. 143, p. 106545, 2022.
- [3] R. Chen *et al.*, "Comparison of CVD-and MBE-grown GaN nanowires: crystallinity, photoluminescence, and photoconductivity," *Journal of Electronic Materials*, vol. 44, pp. 177-187, 2015.
- [4] A. G. Thompson, "MOCVD technology for semiconductors," *Materials Letters*, vol. 30, no. 4, pp. 255-263, 1997.
- [5] A. C. Jones and M. L. Hitchman, "Overview of chemical vapour deposition," *Chemical vapour deposition: precursors, processes and applications*, vol. 1, pp. 1-36, 2009.
- [6] Z. Zhang, H. Fang, Q. Yao, H. Yan, and Z. Gan, "Species transport and chemical reaction in a MOCVD reactor and their influence on the GaN growth uniformity," *Journal of Crystal Growth*, vol. 454, pp. 87-95, 2016.
- [7] J. Sun, J. Redwing, and T. Kuech, "Model development of GaN MOVPE growth chemistry for reactor design," *Journal of Electronic Materials*, vol. 29, pp. 2-9, 2000.
- [8] R. Zuo, H. Yu, N. Xu, and X. He, "Influence of gas mixing and heating on gas-phase reactions in GaN MOCVD growth," *ECS Journal of Solid State Science and Technology*, vol. 1, no. 1, p. P46, 2012.
- [9] H. Fang, Z. Zhang, Y. Pan, R. Ma, S. Liu, and M. Wang, "Systematic study of epitaxy growth uniformity in a specific MOCVD reactor," *Crystal Research and Technology*, vol. 49, no. 11, pp. 907-918, 2014.
- [10] G. Solomon, D. Miller, M. Ramsteiner, A. Trampert, O. Brandt, and K. Ploog, "Combined hydride and metal organic vapor-phase epitaxy of GaN on sapphire," *Applied Physics Letters*, vol. 87, no. 18, 2005.
- [11] "MegaTorr® PS7-PD Hydrogen Gas Purifiers." Entegris. Available: <https://www.entegris.com/shop/en/USD/products/gas-filtration-and-purification/gas-purifiers/MegaTorr-PS7-PD-Hydrogen-Gas-Purifiers/p/GateKeeperMGTPalladiumHydrogenGasPurifiers> (accessed September, 2024).
- [12] "GateKeeper® GPU Gas Purifiers." Entegris. Available: <https://www.entegris.com/shop/en/USD/products/gas-filtration-and-purification/gas->

- [purifiers/GateKeeper-GPU-Gas-Purifiers/p/GateKeeperGPUGasPurifiers](#) (accessed September, 2024).
- [13] Nouryon. "Product Data Sheet TMGa SSG." Available: <https://www.nouryon.com/globalassets/inriver/resources/pds-tmga-ssg-electronics-glo-en.pdf> (accessed September, 2024).
- [14] Nouryon. "Product Data Sheet TMAI SSG." Available: <https://www.nouryon.com/globalassets/inriver/resources/pds-tmai-ssg-electronics-glo-en.pdf> (accessed September, 2024).
- [15] Nouryon. "Product Data Sheet TMIn SSG." Available: <https://www.nouryon.com/globalassets/inriver/resources/pds-tmin-ssg-electronics-glo-en.pdf> (accessed September, 2024).
- [16] Nouryon. "Product Data Sheet Cp2Mg SSG." Available: <https://www.nouryon.com/globalassets/inriver/resources/pds-cp2mg-ssg-electronics-glo-en.pdf> (accessed September, 2024).
- [17] R. C. Walker, A. G. Thompson, G. S. Tompa, P. A. Zawadzki, and A. Gurary, "Vertical high-speed rotating disk reactors for production scale MOVPE of compound semiconductors," in *Second International Conference on Thin Film Physics and Applications*, 1994, vol. 2364: SPIE, pp. 484-489.
- [18] D. L. Lessor, J. S. Hartman, and R. L. Gordon, "Quantitative surface topography determination by Nomarski reflection microscopy. I. Theory," *Journal of the Optical Society of America*, vol. 69, no. 2, pp. 357-366, 1979.
- [19] J. S. Hartman, R. L. Gordon, and D. L. Lessor, "Quantitative surface topography determination by Nomarski reflection microscopy. 2: Microscope modification, calibration, and planar sample experiments," *Applied Optics*, vol. 19, no. 17, pp. 2998-3009, 1980.
- [20] M. Moram and M. Vickers, "X-ray diffraction of III-nitrides," *Reports on Progress in Physics*, vol. 72, no. 3, p. 036502, 2009.
- [21] F. Rustichelli, "On the deviation from the Bragg law and the widths of diffraction patterns in perfect crystals," *Philosophical Magazine*, vol. 31, no. 1, pp. 1-12, 1975.
- [22] J. C. Spence, "Lawrence Bragg, microdiffraction and X-ray lasers," *Acta Crystallographica Section A: Foundations of Crystallography*, vol. 69, no. 1, pp. 25-33, 2013.
- [23] MarcoTolo. "File: Schema MEB (en).svg." Available: [https://commons.wikimedia.org/wiki/File:Schema_MEB_\(en\).svg](https://commons.wikimedia.org/wiki/File:Schema_MEB_(en).svg). (accessed September, 2024).

- [24] B. J. Inkson, "Scanning electron microscopy (SEM) and transmission electron microscopy (TEM) for materials characterization," in *Materials characterization using nondestructive evaluation (NDE) methods*: Elsevier, 2016, pp. 17-43.
- [25] H. B. Bebb and E. Williams, "Photoluminescence I: theory," in *Semiconductors and semimetals*, vol. 8: Elsevier, 1972, pp. 181-320.
- [26] E. Williams and H. B. Bebb, "Photoluminescence II: gallium arsenide," *Semiconductors and Semimetals*, vol. 8, pp. 321-392, 1972.
- [27] I. Buyanova *et al.*, "Photoluminescence of GaN: Effect of electron irradiation," *Applied physics letters*, vol. 73, no. 20, pp. 2968-2970, 1998.
- [28] M. A. Reshchikov, "Measurement and analysis of photoluminescence in GaN," *Journal of applied physics*, vol. 129, no. 12, 2021.

Chapter 4 Optimisation of c-plane GaN Growth on (111) Silicon

Achieving high quality and crack-free C-plane GaN films on (111) silicon is a fundamental requirement in the study of GaN-on-silicon. In this chapter, the growth mechanism of C-plane GaN growth on (111) Si substrates is investigated in detail and the growth process is optimised in several aspects to achieve the high quality and crack-free GaN on Si templates for subsequent device studies. Firstly, the effect of different substrate pre-treatments on growth was investigated in order to select the most appropriate pre-treatment process was investigated. Next, the AlN buffer layer was optimised by studying the growth conditions. Subsequently, the optimisation of internal stress is investigated. Finally, the growth conditions for GaN were optimised. The experimental design and objectives are presented in each subsection and the optimal optimisation conditions are summarised at the end of each subsection. The experimental results are supported by various characterisation measurements including optical microscopy, X-ray diffraction, scanning electron microscopy and the LayTec TT Epicurve system. The optimised GaN-on-Si template paves the way for subsequent device structure investigations.

4.1 Introduction

In the field of epitaxial crystal growth, the reduction of heterogeneous lattice mismatches is a fundamental method for improving the properties of epitaxial materials. Larger lattice mismatches can exacerbate the formation of stresses and defects, thus significantly affecting the structural and electronic properties of epitaxial materials. In principle, the ideal substrate for epitaxial growth of GaN materials is a homogeneous bulk GaN substrate, as the homoepitaxial substrate does not present lattice mismatch issues and therefore relatively high-quality epitaxial crystals can be obtained. However, the difficulty of obtaining large GaN crystals directly by conventional methods has resulted in very expensive GaN homogeneous substrates with size limitations. Currently, the native GaN substrates are fabricated by growing thick GaN films on sapphire substrates and then separating the GaN films from the sapphire by separation techniques. However, the complexity of the process significantly increases the cost of native GaN substrates. As a result, most research into

GaN-based semiconductors has focused on relatively inexpensive heterogeneous substrates to achieve better economics. In general, the three main substrates for modern heterogeneous epitaxial studies of GaN-based semiconductors are silicon carbide, sapphire and silicon. It is therefore a major challenge in modern III-nitride research to obtain GaN of reasonable crystal quality to meet device requirements on heterogeneous substrates.

Among the heterogeneous substrates available for GaN growth, silicon substrates have attracted much attention in recent years as a promising substrate due to their low production cost and availability in large wafer sizes. Nowadays, with the development of GaN applications, most GaN optoelectronic devices have higher requirements for heat dissipation and electrical conductivity. Compared to sapphire, silicon has better thermal and electrical conductivity and can therefore better meet the requirements of high-performance GaN-based devices. In addition, removal of the device substrate may be required for different requirements. Silicon substrates, due to their chemically active nature, can be easily stripped from the device by wet etching processes, whereas chemically stable sapphire substrates require more expensive and complex stripping processes. The main challenges in growing of GaN on Si are due to the large mismatch in lattice constants and thermal expansion coefficients between GaN and Si, where the large lattice mismatch can introduce large dislocations and the thermal expansion coefficient mismatch can lead to severe cracking issues due to the tensile stress introduced by the cooling process. In addition, gallium will easily react with silicon at high temperatures to form a Ga-Si alloy (melt-back etching), which means that the traditional two-step growth technique used to obtain GaN film on sapphire cannot be applied to silicon substrates. Therefore, GaN growth on Si needs to be considered as a separate technique that takes into account melt-back etching while optimising internal stresses [1-4]

So far, several techniques for the growth of GaN epi-film on silicon have been investigated and optimised approaches have been proposed, such as selective epitaxial growth in patterned Si, AlN/GaN superlattice buffer layer, low temperature AlN interlayer, $\text{Al}_x\text{Ga}_{1-x}\text{N}$ interlayer and the graded $\text{Al}_x\text{Ga}_{1-x}\text{N}$ strain-relief buffer layers [5-8]. Specifically, the AlN buffer layer technology is heavily used in GaN-on-Si and effectively avoids the melt-back etching, providing a good crystalline foundation for the subsequent stress control engineering structure. Meanwhile, for stress relief engineering, the large number of works using the graded $\text{Al}_x\text{Ga}_{1-x}\text{N}$ strain-relief layer to

compensate for the stress from GaN during the cooling process have been extensively reported. There are two main schemes of grading: linear and step. The linear-graded is mainly to change from a high Al component to a low Al component according to a certain linear relationship as the thickness of the grown $\text{Al}_x\text{Ga}_{1-x}\text{N}$ layer increases. The step-graded composed of multiple layers (three or more layers) of $\text{Al}_x\text{Ga}_{1-x}\text{N}$ with different compositions to form a stress-regulated layer, and the combination of Al compositions is usually 0.75, 0.5, 0.25 or more combinations. However, the complexity of the growth process and the extended growth time increase production costs, while also contributing to the overall thickness of the epitaxial layer and potentially introducing interface defects, all of which are critical factors to consider [5, 8-16].

In this work, we present a detailed study and optimisation of each growth step based on a growth process for growing c-plane GaN on (111) silicon. First, in the silicon substrate pre-treatment, different pre-treatment processes were applied to 430 μm silicon substrate. For comparison, an AlN buffer layer was grown on the treated substrate under the same growth conditions, the surface morphology was observed by optical microscopy and the crystal quality of the AlN was determined by XRD rocking curve measurements. The AlN buffer layer was investigated with a focus on the effect of Al pre-flow and nitridation on the quality of the AlN layer. In addition, the growth conditions for LT-AlN and HT-AlN growth techniques were also optimised. XRD rocking curve measurements were used to measure the AlN crystal quality, optical microscopy provided a surface morphological image of the sample and SEM provided the high-resolution top-view and cross-sectional image. To optimise the internal stresses, the AlGaIn stress relief layer has been investigated, and the degree of wafer cracking is observed by optical microscopy. At the end of this chapter, the growth conditions of GaN layers have been optimised by investigating GaN growth conditions to improve the surface morphology and crystal quality of GaN. The surface morphological image of the GaN layer was measured by optical microscopy and XRD rocking curve measurements determined the crystal quality of the GaN.

4.2 Pre-growth Treatment of (111) Silicon

Due to the high chemical activity of silicon, when silicon wafers are exposed to air for long periods of time, the silicon reacts with oxygen to form a layer of silicon dioxide (SiO_2) on the surface. This natural oxide layer is typically a few nanometres thick and can be further thickened with exposure time or under high temperature conditions. SiO_2 is chemically inert, and during epitaxial growth, the oxide layer impedes the adsorption and diffusion of III-V atoms on the wafer surface, thereby influencing the initial nucleation process of epitaxial growth. Consequently, the epitaxial layer is challenging to grow directly on the oxidised silicon substrate. Furthermore, the presence of the oxide layer at the interface between Si and the epitaxial layer will result in a further increase in the defect density of the epitaxial layer. It is therefore of the utmost importance to undertake a pre-treatment process on the Si substrate before growth in order to overcome the natural oxidation properties of Si and to obtain high-quality epitaxial layers.

This section presents a comparison of two Si substrate pre-treatment methods: chemical cleaning and high-temperature annealing. In detail, an AlN buffer layer is grown on the treated silicon substrate with the same growth conditions, and the surface morphology is observed using an optical microscope and a scanning electron microscope in order to determine the most appropriate pre-treatment method.

4.2.1 Chemical Treatment vs. High Temperature Annealing

The first approach of pre-treatment of Si substrates is chemical cleaning, which involves the use of chemical solvents, acid oxidation, and hydrofluoric acid (HF) etching. In order to ensure the complete removal of residual contaminants and moisture from the surface, the chemically treated samples must be rinsed at the end with flowing deionised water and dried with a nitrogen gun and placed in an oven. Only Si substrates that have completed the above cleaning procedures can be used for epitaxial growth and will be placed in the MOCVD glove box within a nitrogen environment. The glove box is equipped with an oxygen and moisture sensor, which is responsible for monitoring the internal environment of the glove box. The oxygen content of the glove box is typically maintained at approximately 10 ppm, while the moisture content is kept below 0.5 ppm.

The second method of Si substrate pre-treatment is to place the silicon substrate directly in the Aixtron MOCVD reactor for high temperature annealing with no chemical treatment. In the majority of cases, the ambient gas employed in the high-temperature annealing treatment of MOCVD is hydrogen, and the annealing temperature is usually higher than 1200 °C. The high-temperature annealing can be performed as a separate processing step, or annealing can be performed and followed by epitaxial growth. Since doing it separately requires substrate transfer process and additional time, performing the high temperature annealing directly in the MOCVD system and following epitaxial growth helps to increase efficiency and reduce contamination.

Experiment Design

For the first approaches of pre-treatment, the standard operating procedures are listed below:

- i. Chemical solvent cleaning:** The silicon substrate was sequentially immersed successively in n-butyl acetate, acetone, and isopropanol (IPA) for 5 min each, after which it was rinsed with ionized (DI) water to remove residual solvent.
- ii. Acid Oxidation Cleaning:** The silicon substrate was immersed in a solution (as known as Piranha solution) comprising concentrated sulfuric acid (H₂SO₄), hydrogen peroxide (H₂O₂) and DI water in a ratio of 1:1:2 for a period of five minutes, and after rinsed with DI water.
- iii. Hydrofluoric acid immersion:** The silicon substrate was immersed in a 40% hydrofluoric acid solution for 5 minutes, followed by rinsing with DI water to remove residues.
- iv. Drying:** The water droplets were blown off from the Si substrate by a dry nitrogen spray gun, and then baked in an oven at 100°C for one minute to remove any residual moisture.

With regard to the second pre-treatment method, the untreated Si substrate will be removed from the original packaging provided by the manufacturer and directly placed into the MOCVD for high-temperature annealing.

In order to assess the impact of substrate pre-treatment on subsequent growth, an AlN buffer layer will be grown directly on the treated substrate under identical growth conditions and the surface morphology of AlN will be evaluated. The experimental set was designed with four samples (A, B, C, D) with the different conditions and listed in the Table 4-1. Both samples A and B were subjected

to the aforementioned chemical treatment, whereas samples C and D were not. Samples A and C were subjected to annealing at 1280 °C prior to the growth of an AlN buffer layer, whereas samples B and D were annealed at 1340 °C. The atmosphere gas used in the annealing was H₂ with a flow rate of 1000 sccm, a reactor pressure of 86 mbar and annealing for 900 seconds.

Table 4-1 the annealing parameters of Samples A, B, C and D.

Sample	Chemical treatment	Annealing temperature (°C)
A	Yes	1280
B	Yes	1340
C	No	1280
D	No	1340

Results

The various samples were investigated using optical microscopy with representative images shown in Figure 4-1. The obtained images indicate that, under the conditions of annealing temperature at 1280 °C, the chemically cleaned sample A exhibits a uniform surface, although it contains some small particles or defects. In contrast, the non-chemically cleaned sample C displays a non-uniform surface with a higher concentration of particles and pits. Meanwhile, at an annealing temperature of 1340 °C, the chemically cleaned sample B exhibited clear particles and defects on the surface, as well as a lower surface quality. In contrast, sample D, which had not undergone chemical cleaning, displayed a uniform surface with no visible particles or defects.

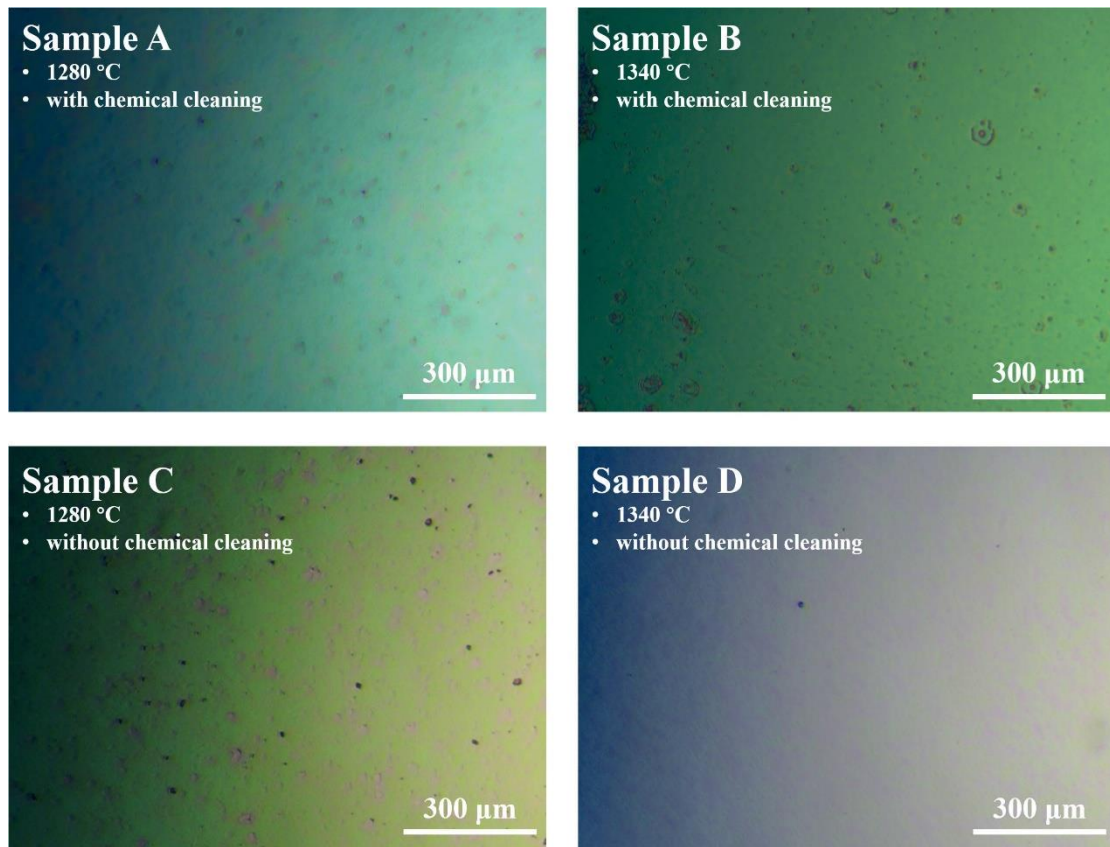


Figure 4-1 the optical microscope images of four samples (A, B, C, D) with different pre-treatment methods under two different annealing temperatures.

A comparison of samples A and C reveals that chemical cleaning has a markedly positive effect on the surface topography at the lower annealing temperature of 1280 °C. A comparison of samples B and D reveals that the chemically cleaned samples exhibit a greater number of particles and defects at the higher annealing temperature (1340 °C). This indicates that chemical cleaning has a significant positive effect on surface cleanliness at their lower annealing temperatures. However, the condition of the surface of the samples deteriorates at the higher annealing temperatures. Comparing the surface morphology of chemically cleaned samples at different annealing temperatures (A and B) reveals a significant increase in surface particles and defects at an annealing temperature of 1340 °C relative to those annealed at a temperature of 1280 °C. And a comparison of the surface morphology of the uncleaned samples at different temperatures (C and D) reveals that the high-temperature annealing (1340 °C) results in a more uniform surface with fewer defects.

Summary

The impact of changes in annealing temperature on surface morphology was found to be more significant than that of chemical cleaning. It was observed that chemical cleaning resulted in enhanced surface quality when annealed at 1280 °C. However, the quality of the non-chemically cleaned surface was found to be better when annealed at 1340 °C. This indicates that the annealing temperature plays important in determining surface cleanliness and quality. Nevertheless, it cannot be denied that chemical cleaning is an effective method for improving surface quality and for the removal of contaminants from the substrate surface. However, due to the cumbersome steps of chemical cleaning, it often takes several hours to prepare a substrate, and once a mistake occurs in the middle of the process, it needs to be cleaned from the beginning, which significantly increases the overall preparation cost and introduces additional sources of variability and potential errors. For instance, if the drying step is not properly controlled, watermarks may form on the surface of the grown sample, which could lead to a significant degradation in the quality of the epitaxial layer, due to the residual chemical. Consequently, the high temperature annealing method is more advantageous in terms of simplicity and performance when implemented directly prior to epitaxial growth. For all of the aforementioned reasons, all Si-based samples grown in this study were subjected to the high temperature annealing method under the H₂ ambient and then continued directly to epitaxial growth.

4.2.2 Optimisation of High Temperature Annealing

High-temperature annealing represents a crucial pre-treatment process before the epitaxial growth. It can effectively improve the surface cleanliness and flatness of the substrate, which are of paramount importance in ensuring the quality of the epitaxial layer for subsequent growth. Therefore, the further research is required on the subject of the silicon substrate annealing process with a view to optimising the annealing conditions. The objective of this section is to investigate the effect of different annealing times on the quality of subsequent epitaxial growth layers on Si substrates to determining the optimal annealing time.

Experiment Design

In order to compare the influence of different annealing times on the quality of subsequent epitaxial

layers, a new experimental group will be designed comprising five samples (A-E). These samples will be subjected to different annealing durations, as shown in Table 4-2. The annealing will be conducted under an H₂ ambient with a flow rate of 1000 sccm and a reactor pressure of 86 mbar. Following annealing, an AlN buffer layer will continue to grow using the LT&HT AlN growth method. For the growth of LT-AlN, the growth temperature was 1150 °C, the flow rate of NH₃ was 300 scc. And for HT-AlN growth, the growth temperature was 1310 °C, flow rate of NH₃ was 100 sccm. The reactor pressure and TMA flow rate for both LT-AlN and HT-AlN were 86 mbar and 20 sccm, respectively. The X-ray diffraction rocking curve measurements will be used to determine the FWHM values of (002) AlN from the five samples, with a view to facilitating a visual comparison of crystal quality.

Table 4-2 The annealing parameters of samples A, B, C, D and E, under the reactor pressure of 86 mbar and annealing temperature of 1340 °C.

Sample label	Annealing time (s)
A	600
B	900
C	1800
D	2700
E	3600

Results and discussion

Figure 4-2 shows the FWHM values of the AlN layer at different annealing times obtained from X-ray diffraction measurements of the (002) AlN peak widths to assess crystal quality. The value of the FWHM of the symmetrical (002) plane rocking curve corresponds to the density of screw dislocations, with smaller values indicating higher crystal quality and lower defect density [17, 18].

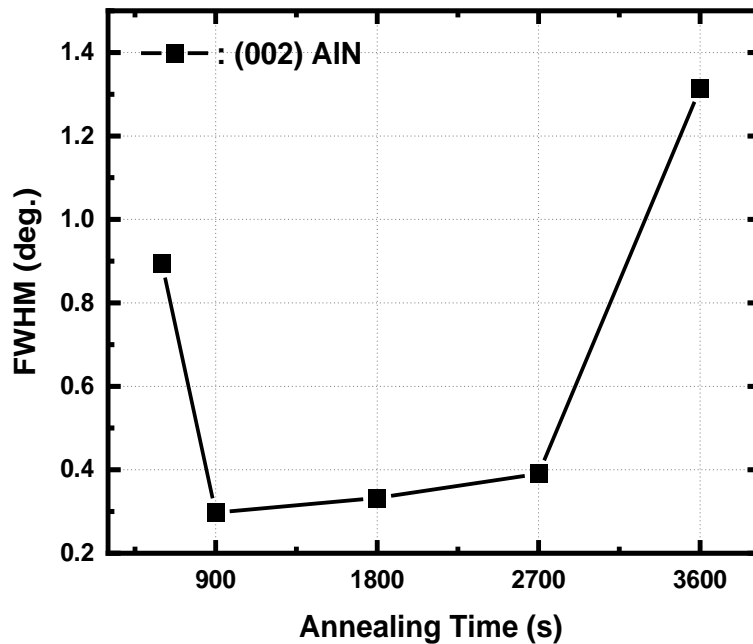


Figure 4-2 the Full-Width Half-Maximum (FWHM) values for (002) AlN vs. surface preparing annealing Time, which determined by Bruker X-ray diffraction rocking curve measurements.

The annealing time of 600 seconds was insufficient to significantly enhance the quality of the AlN layer. This may be attributed to the fact that the high-temperature annealing time was insufficient to adequately remove the surface contaminants and oxides. The AlN crystal quality was significantly superior to that of the other experimental groups when the annealing time was 900 seconds. In contrast, there was no discernible deterioration in the crystal quality when the annealing time was 1800 seconds and 2700 seconds. When the annealing time was 3600 seconds, the AlN crystal quality deteriorated significantly with the worst FWHM value. The observed deterioration in crystal quality is likely attributable to the long annealing time, which has resulted in the deterioration of the silicon substrate surface topography and the formation of defects.

Based on the above, it can be concluded that the shorter annealing times may not be sufficient for the surface cleanliness of the substrate, while prolonged annealing times may introduce new defect problems to the substrate. Therefore, the annealing time between 900 and 1800 seconds can have a positive effect on the substrate. Furthermore, based on the optimisation of the overall growth time, the ideal annealing time for the Si substrate is 900 seconds.

4.3 Optimisation of AlN Buffer Layer Growth

In the GaN-on-Si technology, the AlN buffer layer plays a crucial role as the initial step in the epitaxial growth process. In addition to improving lattice mismatch and buffering thermal stress, the high quality AlN layer with a smooth surface also provides an ideal substrate for the subsequent epitaxial growth, which plays a decisive role in the quality of the final epitaxial layer. Therefore, it is necessary to optimise the growth conditions of AlN in order to obtain a higher quality AlN buffer layer on the Si substrate.

4.3.1 The Initial Growth Process of AlN Layer

In the existing technique of growing AlN layers on Si substrates by MOCVD, there are two common methods for the initial growth process, namely NH₃ nitridation and TMA pre-deposition flow (also called TMA pre-flow). Specifically, the NH₃ nitridation process means that NH₃ is introduced to nitride the silicon surface to form a very thin layer of silicon nitride on prior to the growth of AlN. i.e. the NH₃ is preferentially fed into the reactor before the TMA precursor. Meanwhile, the TMA pre-flow refers to the preferential introduction of TMA precursors before the growth of the AlN layer, i.e. the TMA precursors are preferentially introduced into the reactor before the passage of NH₃. This can form a very thin layer of aluminium oxide (Al₂O₃) or Al-Si compounds on the surface of the Si substrate. In this section, the effect of two different initial processes on the quality of AlN crystals is investigated and the experimental results are corroborated by obtaining FWHM values of (002) AlN from XRD rocking curve measurements.

Experiment Design

In this section, the growth of AlN on Si substrates is carried out using two different initial processes and the grown samples are divided into two categories. The AlN layer is grown by the LT&HT AlN growth method. As described in Section 4.2, all Si substrates which used to growth were subjected to high temperature annealing in a H₂ atmosphere and then immediately growth of AlN layer.

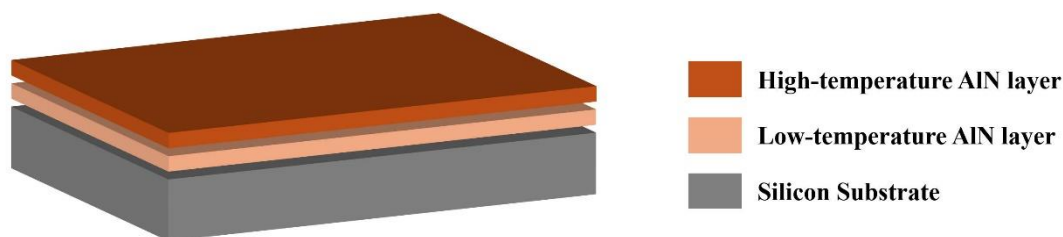


Figure 4-3 Structure of AlN buffer layer on Si substrate.

For the AlN growth with the NH_3 nitridation, after the annealing, the temperature of the reactor was reduced to 1150 °C, the NH_3 was then introduced into the reactor chamber at a flow rate of 90 sccm. After nitridation, the NH_3 flow rate was then increased to the 300 sccm and the TMA was introduced at a flow rate of 20 sccm to facilitate the growth of the LT-AlN layer. The HT-AlN layer was then grown at the 1310 °C with the same TMA flow rate, and the NH_3 flow rate of 100 sccm.

For AlN growth with TMA pre-flow, after annealing, the TMA source was injected into the reactor chamber at a flow rate of 20 sccm for pre-flow process at a reactor temperature of 1150 °C. Once the pre-flow process was completed, the NH_3 was directly fed into the reactor at a flow rate of 300 sccm to start the growth of LT-AlN layer, followed by the growth of HT-AlN layer at 1310 °C with an NH_3 flow rate of 100 sccm. The reactor pressure for both initial process and AlN growth remained constant at 86 mbar. Figure 4-4 illustrates the simple gas flow schemes used for TMA and NH_3 for the AlN growth with (A) NH_3 nitridation and (B) TMA pre-flow.

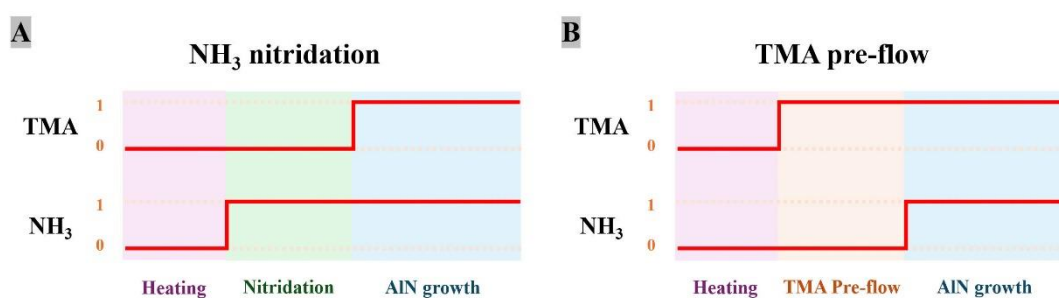


Figure 4-4 The gas flow used for TMA and NH_3 for the (A) NH_3 nitridation and (B) TMA pre-flow method.

For purpose of compare, several AlN on Si samples were grown by two initial processes. And the AlN crystal quality of all samples was determined by obtaining FWHM values of (002) AlN from XRD rocking curve measurements.

Results and discussion

Table 4-3 the (002) AlN FWHM values, mean values and standard deviation of samples by two different initial processes, group A: NH₃ nitridation; group B: TMA pre-flow.

Sample group	Initial processes	Sample label	(002) AlN FWHM (°)	Mean value \bar{x}	Standard deviation σ
A	NH ₃ nitridation	A ₁ (N079)	0.3201	0.2999	0.0144
		A ₂ (N080)	0.2876		
		A ₃ (N081)	0.2919		
B	TMA pre-flow	B ₁ (N113)	0.2162	0.2406	0.0210
		B ₂ (N132)	0.2381		
		B ₃ (N134)	0.2674		

Table 4-3 shows the FWHM values, mean values and standard deviation for (002) AlN grown under different initial treatment procedures: (Group A) NH₃ nitridation and (Group B) TMA pre-flow. The tabular data indicates that the FWHM values of the TMA pre-flow treated sample group B are generally lower than those of the NH₃ nitridation treated sample group A, which suggests that the TMA pre-flow initial treatment can enhance the crystal quality of the AlN layer to a greater extent than the NH₃ nitridation. In the meantime, the standard deviation of the two groups indicates that the FWHM values of the samples obtained by the NH₃ nitridation exhibit less fluctuation and greater stability, whereas the TMA pre-flow, despite its effectiveness in improving AlN crystal quality, but displays larger fluctuations in its FWHM values and is slightly less stable. In order to obtain a better quality of AlN crystals, the initial growth process of TMA-pre flow will be employed as the standard process for AlN growth in this job.

4.3.2 Optimisation of LT&HT-AIN Growth Temperature

The AlN layer grown at low temperatures provides high-quality nucleation sites, while enhancing the lattice relaxation of the aluminium nitride interlayers. In contrast, the growth of an AlN layer at high temperatures results in a surface that is more atomically flat. Consequently, this AlN growth method can optimise stress management, improve surface flatness and enhance crystal quality. However, low and high temperatures are a vague relative concept, based on this idea, in order to better investigate the effect of the temperature difference between the two on the quality of the AlN crystals, this section will growth of AlN layers by using the different temperature differences (ΔT).

In this section, the effect of different temperature differences (ΔT) on the quality of AlN grown using the LT&HT method will be investigated and analysed by obtaining FWHM values of (002) AlN from XRD rocking curve measurements.

Experiment Design

In this experiment, a series of samples was designed to investigate the effect of temperature difference on the quality of an AlN layer. The samples were grown LT&HT AlN layer by using different temperature differences (ΔT). All samples were subjected to high-temperature annealing of the Si substrate under H_2 ambient, followed by a TMA pre-flow process at 1150 °C and then growth of a low-temperature AlN layer at the same temperature. Subsequently, a second AlN layer was grown under the specified temperature which was ramped up by a ΔT based on the 1150 °C. The growth parameters of AlN layer are shown in the Table 4-4.

Table 4-4 The growth conditions of AlN layer by LT&HT method.

Step	Temperature (°C)	Pressure (mbar)	MO source (sccm)	NH ₃ (sccm)
TMA-pre	1150	86	Al: 20	/
LT-AIN	1150	86	Al: 20	300
HT-AIN	1150 + ΔT	86	Al: 20	100

Results and discussion

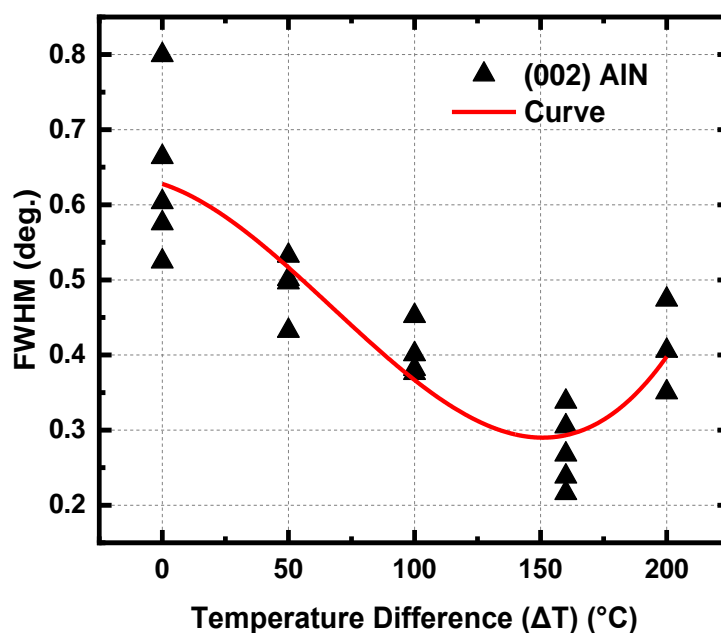


Figure 4-5 Relation between the 002 AlN FWHM values and the different growth temperature differences for the HT-AlN layers relative to the LT-AlN.

The Figure 4-4 illustrates the variation in 002 AlN FWHM values for AlN layers grown at different low temperature and high temperature growth temperature differences (ΔT). It is evident that when there is no temperature differential ($\Delta T = 0^\circ\text{C}$), the highest FWHM values are obtained, between 0.5 and 0.8. As the ΔT increases to 50 °C and 100 °C, a corresponding decrease in FWHM can be observed. With the lowest FWHM for ΔT was 160°C, indicating that the quality of the AlN layer was optimal within this temperature differential. When ΔT continues to increase, the FWHM of the obtained samples once again demonstrates an upward trend. The trend of FWHM values can also be clearly observed based on the red fitting curve in the figure. It can be demonstrated that a ΔT of 160°C represents an optimal compromise. A ΔT that is either too small or too large can result in a deterioration in the quality of the crystals.

4.3.3 Optimisation of HT-AlN Growth

Furthermore, based on the LT&HT AlN growth method, in order to further improve the crystal quality of AlN, the growth conditions of high-temperature AlN layers were investigated. Therefore,

two growth method for HT-AlN growth has been designed: (i) Single HT-AlN layer; and (ii) Two HT-AlN layer. In the second method, the V/III ratios AlN layer modified by modifying the flow rate of Al, resulting in the division of HT-AlN into two parts: HT-AlN-1 and HT-AlN-2.

The main objective of this section is to enhance the crystalline quality of the final AlN layer by optimising the growth conditions of HT-AlN. The (002) AlN FWHM value has been obtained from the XRD measurement.

Experiment Design

After the high-temperature annealing of the Si substrate under a H₂ environment, the temperature in the reactor was reduced to 1150 °C for the TMA pre-flow treatment, the low-temperature AlN layer was then grown at the same temperature. The growth conditions of LT-AlN are identical to those described in Table 4-5. For growth for HT-AlN layer, the first growth method is same as previously described, with a growth temperature of 1310°C. TMA and NH₃ were introduced into the reactor at a flow rate of 20 sccm and 100 sccm, respectively, while maintaining a reactor pressure of 86 mbar. The second growth method is derived HT-AlN into the two parts by different TMA flow rate, with the flow rate of HT-AlN-1 is 20 sccm, while the HT-AlN-2 is 45 sccm. The remaining growth conditions were kept constant as shown in Table 4-5. Concurrently, the growth time of the AlN layer will be regulated in accordance with the growth rate calculated during the growth process, in order to ensure that the thickness of the AlN layer obtained by the two methods is identical.

Table 4-5 the growth parameters of two different HT-AlN growth methods.

Method	Growth step	Temperature (°C)	Pressure (mbar)	MO source (sccm)	NH ₃ (sccm)
Single HT-AlN	HT-AlN	1310	86	Al: 20	100
Two HT-AlN	HT-AlN-1	1310	86	Al: 20	100
	HT-AlN-2	1310		Al: 45	

Results and discussion

Table 4-6 the (002) AlN FWHM values of samples by two different HT-AlN growth methods.

Sample group	Growth method	Sample label	(002) AlN FWHM (°)	Mean value \bar{x}	Standard deviation σ
A	Single HT-AlN	A ₁ (N415)	0.2162	0.2406	0.0210
		A ₂ (N420)	0.2381		
		A ₃ (N434)	0.2674		
B	HT-AlN 1&2	B ₁ (N524)	0.1479	0.1518	0.0065
		B ₂ (N526)	0.1465		
		B ₃ (N530)	0.1609		

Table 4-6 presents the FWHM values, mean values and standard deviation for (002) AlN of the samples obtained through two different growth methods of HT-AlN: (Group A) single HT-AlN method and (Group B) HT-AlN 1&2 method. The tabular data indicates that, the samples obtained by using the two-stage high-temperature AlN growth method (Group B) are significantly better than the samples using the single high-temperature AlN growth method (Group A) in terms of both crystal quality and consistency. The lower FWHM values and smaller data variability indicate that the two-step high-temperature AlN growth method is more effective in improving the crystal quality of AlN layers and reducing the defect density.

4.4 Optimisation of AlGaN Buffer Layer

One of the most significant challenges currently facing the field of silicon-based III-nitride semiconductors is to achieve crack-free GaN, which is fundamentally due to the effective management of internal stresses. The significant disparity in thermal expansion coefficients between silicon and GaN results in the generation of tensile stresses during the post-growth GaN cooling process, which subsequently leads to the formation of surface cracks in the GaN. The objective of managing internal stresses is to mitigate cracking issues by introducing additional compressive strains to compensate for the eventual tensile strains generated during cooling. Additional internal stress can affect the performance of the final light-emitting device through a variety of mechanisms, such as lowering the light output efficiency and causing light-emitting wavelength drift. Therefore, optimising the management of internal stress in GaN-on-Si technology is a crucial point to develop high-performance light-emitting devices.

This section investigates AlGaN buffer layers grown on optimized AlN layers. Recent studies have demonstrated that a graded AlGaN buffer layer is an effective method for controlling stress in GaN-on-Si. This is achieved by introducing compressive stress prior to GaN growth, which compensates for the tensile stress that occurs during cooling. The graded AlGaN buffer layer is typically composed of a series of AlGaN layers with a graded Al content. This structure serves to prevent the formation of cracks in the subsequent GaN layer by adjusting the Al content and thickness layer by layer [14, 19-22]. However, the growth process of multilayer structures is not only more complex and time-consuming but also results in an increased overall thickness of the epitaxial layer and the potential introduction of additional defects. Therefore, it is necessary to optimise the AlGaN buffer layer in order to achieve an effective single AlGaN stress-release layer.

In order to achieve a crack-free GaN epitaxial layer, the key growth factors of the AlGaN buffer layer will be systematically optimised in this section. The factors include the thickness and Al content. Furthermore, in the case of GaN on Si, the incomplete release of internal stresses will manifest itself directly in the degree of cracking on the surface, which can be easily observed by the naked eye. Meanwhile, the optical microscopy will be employed as a standard characterisation technique to examine the surface morphology and the presence of cracks.

Experiment Design

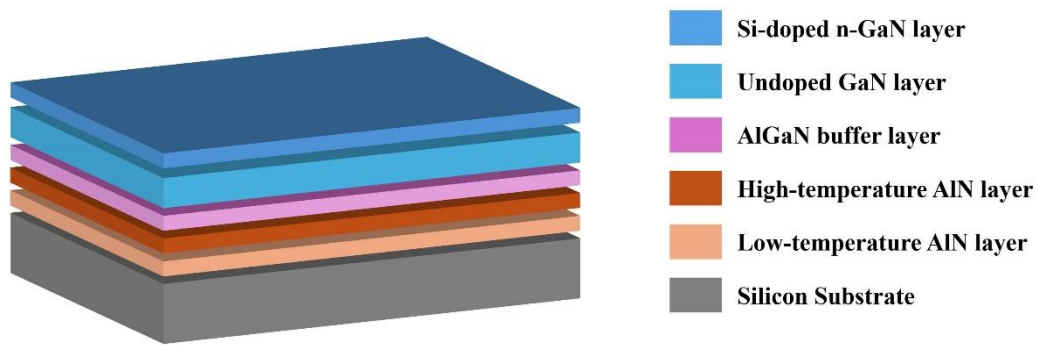


Figure 4-6 Structure of GaN on Si.

In this section, three experimental groups (A, B and C) were designed and growth of AlGaN layers. The corresponding growth conditions were adjusted according to different comparison purposes in order to identify the optimal growth conditions. As previously discussed in the experimental sections, all experimental groups performed a high-temperature annealing of the Si substrate in H_2 ambient followed by a TMA pre-flow process at $1150\text{ }^\circ\text{C}$ and growth of low-temperature AlN layers at the same temperature. Subsequently, the high-temperature AlN layer growth was carried out after the reaction chamber temperature was raised to $1310\text{ }^\circ\text{C}$ to obtain a high-quality AlN layer. Following this, the AlGaN buffer layers with different thicknesses and Al contents will continue to grow on top of the AlN layer. The Al content of the AlGaN layer can be modified by varying the flow rate of the TMA or TMG sources. Finally, in order to better observe the surface cracks, a total thickness of $2.5\text{ }\mu\text{m}$ GaN layers was grown, comprising $2.3\text{ }\mu\text{m}$ of undoped GaN and $0.3\text{ }\mu\text{m}$ of n-GaN layer.

The specific parameters of grown AlGaN layer will be presented in Table 4-7. The experimental Group A was designed to investigate the effect of varying thicknesses of AlGaN layers on subsequent GaN surfaces at a similar Al content. The objective of Group B is to investigate the influence of Al content on the subsequent GaN surface under the same AlGaN thickness. And the experimental group C comprised four samples (C_1 , C_2 , C_3 and C_4), which were employed to investigate the effect of different combinations of AlGaN buffer layer thicknesses and Al content on the subsequent GaN layer cracking. The Al content and AlGaN thickness of all samples can be determined by XRD ω - 2θ curve and growth rate.

Table 4-7 Growth Conditions of AlGaIn Buffer Layer in Different Groups.

Sample Group	Sample Label	Thickness (nm)	Al Content (%)
A	A ₁ (N688)	500	26
	A ₂ (N685)	700	26
	A ₃ (N689)	800	26.8
B	B ₁ (N684)	700	29
	B ₂ (N685)	700	26
	B ₃ (N686)	700	22.5
C	C ₁ (GN4326)	500	29.5
	C ₂ (GN4328)	700	30
	C ₃ (GN4327)	500	26
	C ₄ (GN4325)	700	26

Results

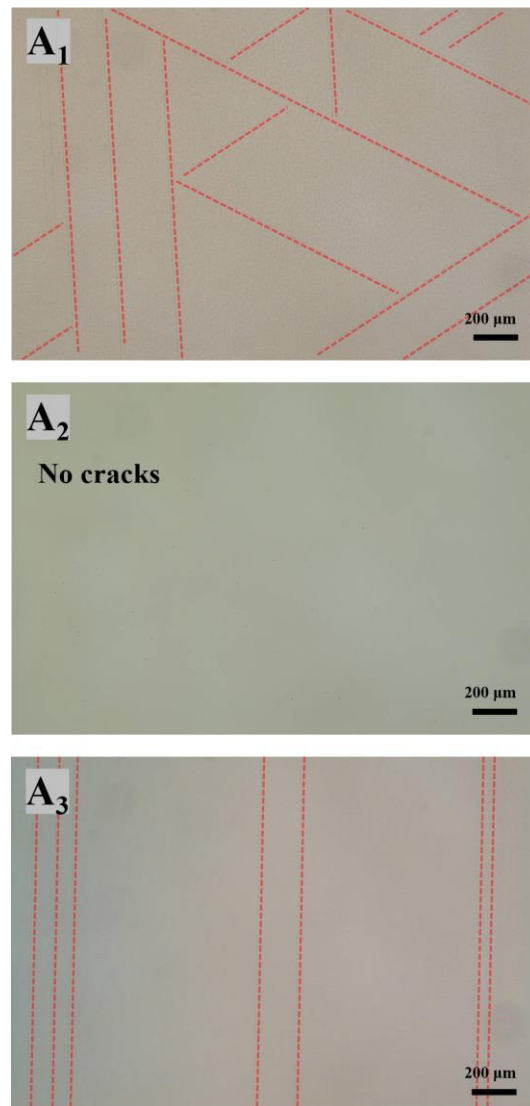


Figure 4-7 Optical microscopy images of Group A; (A₁) 500nm AlGaIn; (A₂) 700nm AlGaIn and (A₃) 800nm AlGaIn. The red line serves to highlight the cracks.

As illustrated in Figure 4-7, the optical microscopy images demonstrate that samples A₁ and A₃ exhibit clearly visible cracks on their surfaces, with A₁ displays the most severe cracks, intersecting cracks forming triangles, while A₃ displays mostly parallel strip cracks; and sample A₂ had no cracks observed. Furthermore, the surface of A₁ appears to be rougher and more uneven than that of A₂ and A₃. Given that all three samples were subjected to identical growth conditions, with the exception of the thickness of the AlGaIn layer, it can be concluded that the thickness of the AlGaIn layer has an effect on the generation of cracks.

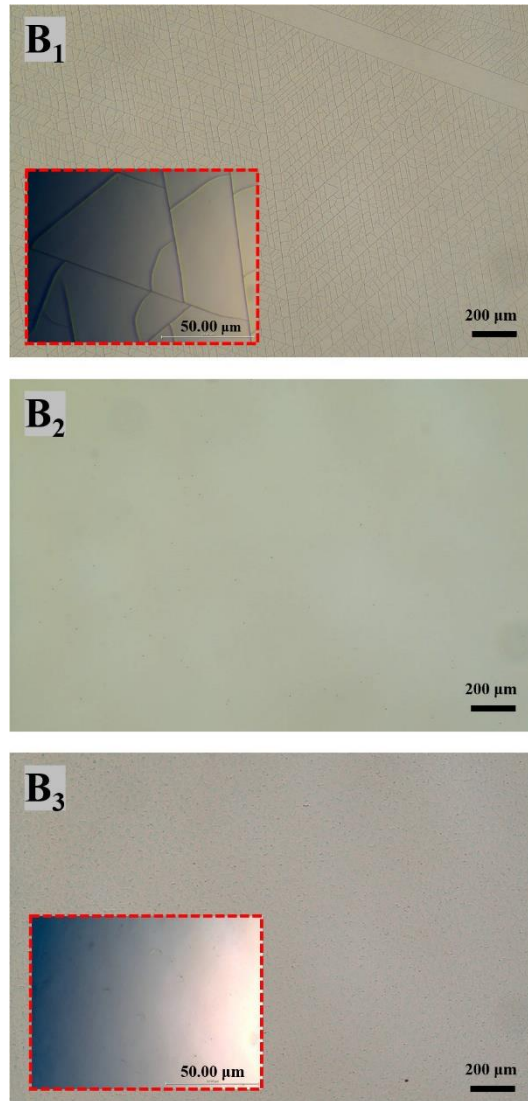


Figure 4-8 Optical microscopy images of Group B; AlGaIn layer with (B₁) 29% Al content; (B₂) 26% Al content and (B₃) 22.5% Al content.

Figure 4-8 presents the optical microscopy images of Group B. Sample B₁ exhibited severe and dense cracking on the surface, while samples B₂ and B₃ demonstrated no observed cracking. Meanwhile, the surface of sample B₃ exhibited a high density of pits with the lowest Al content, which were considerably more than those observed in samples B₁ and B₂. It can be demonstrated that the Al content exerts a significant influence on the formation of surface cracks and pits when the remaining growth conditions are held constant. Figure 4-9 illustrates the ω -2 θ curve, which is aligned with the AlN peak of samples B₁, B₂, and B₃. It can be clearly observed that as the Al content in AlGaIn decreases, the peak position of AlGaIn gradually moves closer to the GaN peak.

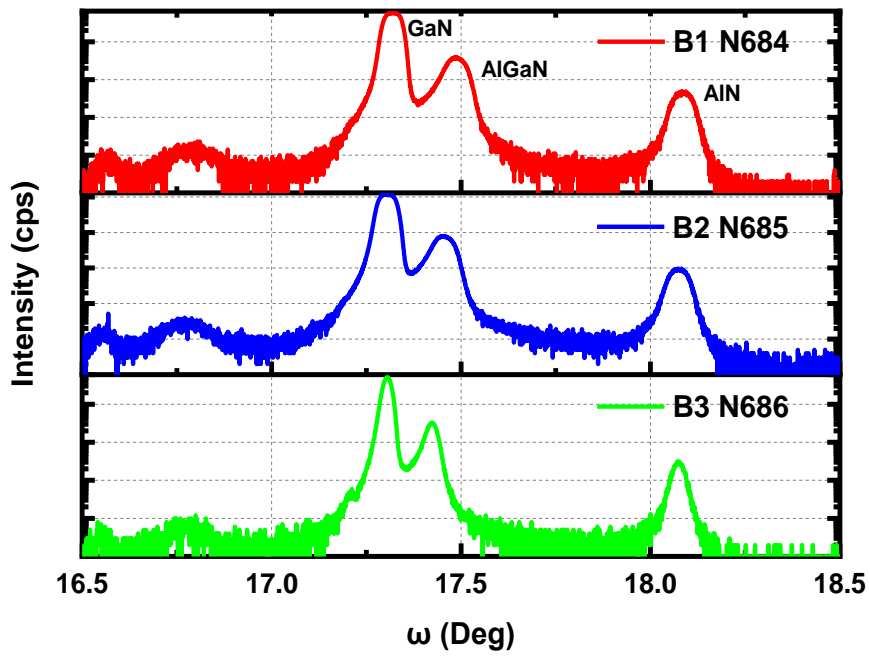


Figure 4-9 XRD ω - 2θ scan aligned on AlN of Sample B₁ (red), B₂ (blue) and B₃ (green).

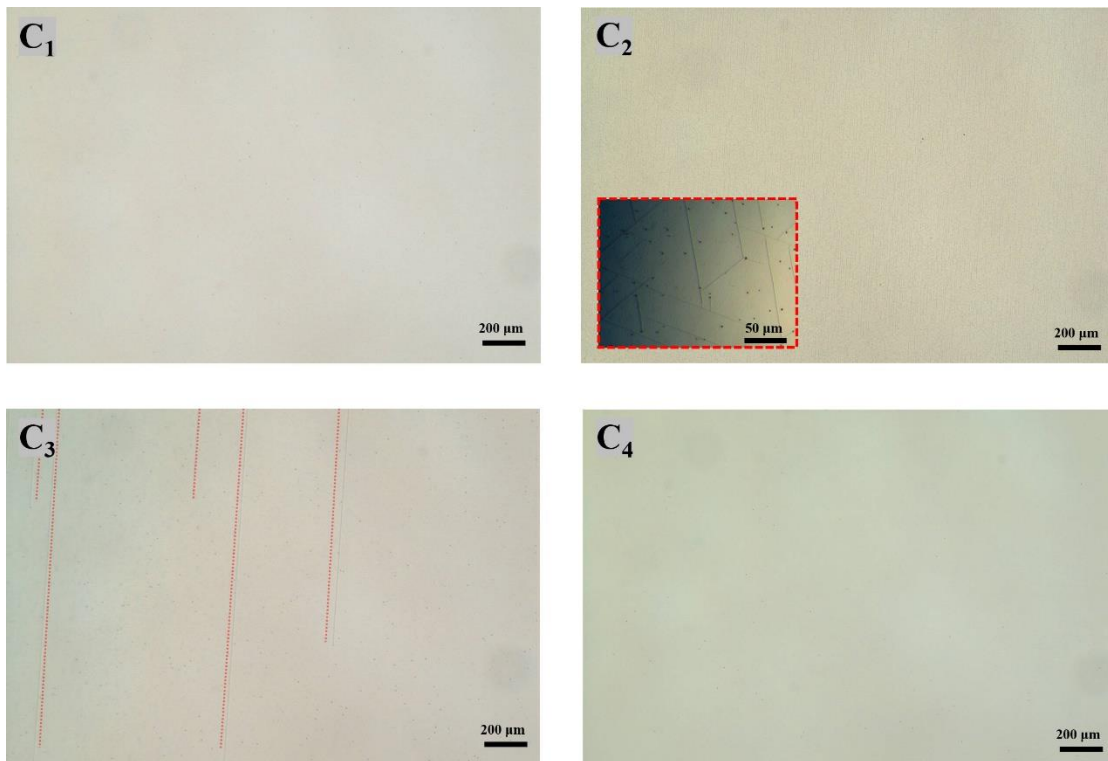


Figure 4-10 Optical microscopy images of Group C; (C₁) 500nm AlGaN with 29.5% Al; (C₂) 700nm AlGaN with 30% Al; (C₃) 500nm AlGaN with 26% Al; and (C₄) 700nm AlGaN with 26% Al.

As illustrated in Figure 4-10, the samples C₁ and C₄ display a crack-free surface, whereas the sample C₂ exhibits a high degree of cracking and C₃ exhibits a slight degree of streak cracking on surface. This suggests that the different thickness of AlGa_xN combinations with different Al content can also achieve the purpose of reducing crack generation. In case of this, the thinner AlGa_xN with a high Al content or thicker AlGa_xN with a lower Al content can both provide sufficient counteracting stress to improve surface from cracking.

Summary

From the results of the experimental group A, it can be concluded that under the same growth conditions, thicker AlGa_xN can mitigate the generation of cracks, but excessive thickness can also result in the formation of cracks. At a 26% Al content, a 700 nm thickness of AlGa_xN is optimal.

The results of the experimental group B indicate that the Al content has an effect on the generation of cracks and pits. At an AlGa_xN thickness of 700 nm, an Al content below 29% is beneficial in reducing cracking, but a too-low Al content increases the density of pits. The AlGa_xN with 26% Al content is the most suitable when the thickness of AlGa_xN is 700 nm.

The experimental group C demonstrate that when the Al component reaches 30%, the thinner AlGa_xN can prevent surface cracking, with an optimal thickness of 500 nm. Conversely, when the Al content is low (26%), thicker AlN can also mitigate the cracking problem, with an optimal thickness of 700 nm. Furthermore, the more severe cracking issue will occur when the Al content is too high (over the 29%), as evidenced by samples B₁ and C₂.

4.5 Optimisation of GaN Growth

The aforementioned section describes the completion of optimisation processes related to the pre-treatment process, the growth of the AlN layer, and the growth of the AlGaN layer. The objective of optimising the pre-treatment method was to develop a more convenient and stable pre-processing method for GaN on Si. The optimisation of the AlN layer was aimed at obtaining higher quality AlN crystals and improved interfacial flatness. The development of a single AlGaN buffer layer allows the GaN layer to be grown with sufficient compressive strain before growth and compensating for the tensile strain generated during cooling, while optimising the overall growth process. On this basis, thus allowing the ultimate goal of this chapter: the growth of c-plane GaN on (111) silicon substrates with a crack-free surface and excellent crystal quality.

In this section, the GaN layer was grown on a Si substrate with a single AlGaN/HT<-AlN/Si structure. Meanwhile, in this work, the growth procedure of GaN layer is divided into two distinct steps, designated as GaN-1 and GaN-2, which are distinguished by the differing growth conditions employed. The difference growth conditions for the GaN-1 and GaN-2 included the reactor pressure, MO source flow rate, and NH₃ flow rate. This growth procedure for GaN has been designed to first perform a three-dimensional growth mode, then followed by a two-dimensional growth mode. The formation of three-dimensional island-like structures at the initial stage of epitaxial growth serves to reduce stress and defect density, and then the flat and continuous two-dimensional films are formed. This combined growth mode can significantly improve the quality and form smooth surface of GaN epitaxial layers.

The in-situ reflectance monitoring system was employed to track any changes in reflectance of the sample surface throughout the growth process. The results were assessed using optical microscopy images and (002) XRD rocking curves.

Experiment Design

For the purpose of optimising of growth conditions for the GaN, all AlGaN/AlN/Si structures will be grown using the optimised conditions set out in the above section, followed by continuous growth of the GaN layer. All silicon substrates were subjected to high-temperature annealing, followed by a TMA pre-flow treatment, prior to the growth of an AlN layer using the LT&HT method. The single

AlGaIn buffer layer was deposited with a thickness of approximately 700 nm and an Al content of 26%. Subsequently, GaN layers with a total thickness of approximately 1.5 μm are deposited on top of an AlGaIn layer containing GaN-1 and -2 layers. Finally, a 300 nm thick Si-doped n-GaN layer is grown. Figure 4-11 illustrates the structure of GaN on Si with the GaN-1 and GaN-2 layer.

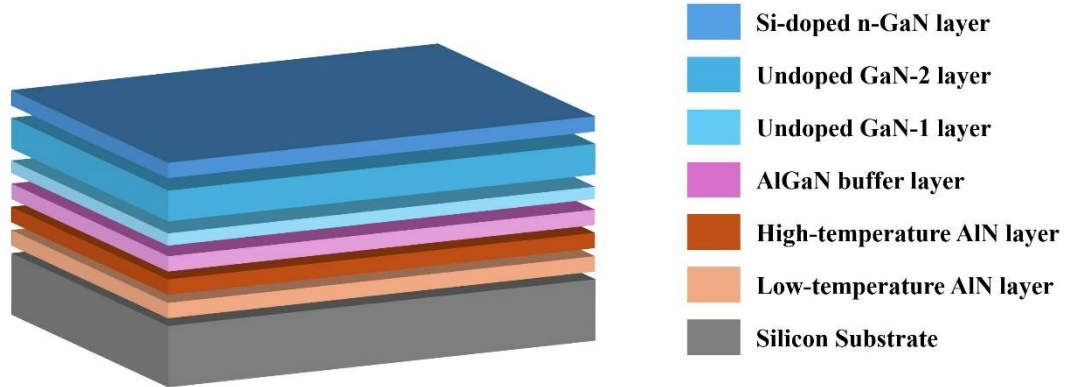


Figure 4-11 the structure of GaN on Si with single AlGaIn layer and two-step undoped GaN layer.

Table 4-8 Growth conditions of GaN-1 and GaN-2 layer.

Sample	Step	Temperature ($^{\circ}\text{C}$)	Pressure (mbar)	MO source (sccm)	NH_3 (sccm)
A (N693)	GaN-1	1215	600	Ga: 49	3100
	GaN-2		300	Ga: 38	2100
B (N695)	GaN-1	1215	600	Ga: 45	3100
	GaN-2		300	Ga: 38	2100
C (N696)	GaN-1	1215	600	Ga: 45	3100
	GaN-2		300	Ga: 38	1600

Table 4-8 lists the details growth conditions of GaN-1 and GaN-2 layer for three samples, which labelled as A (N693), B (N695) and C (N696).

Results

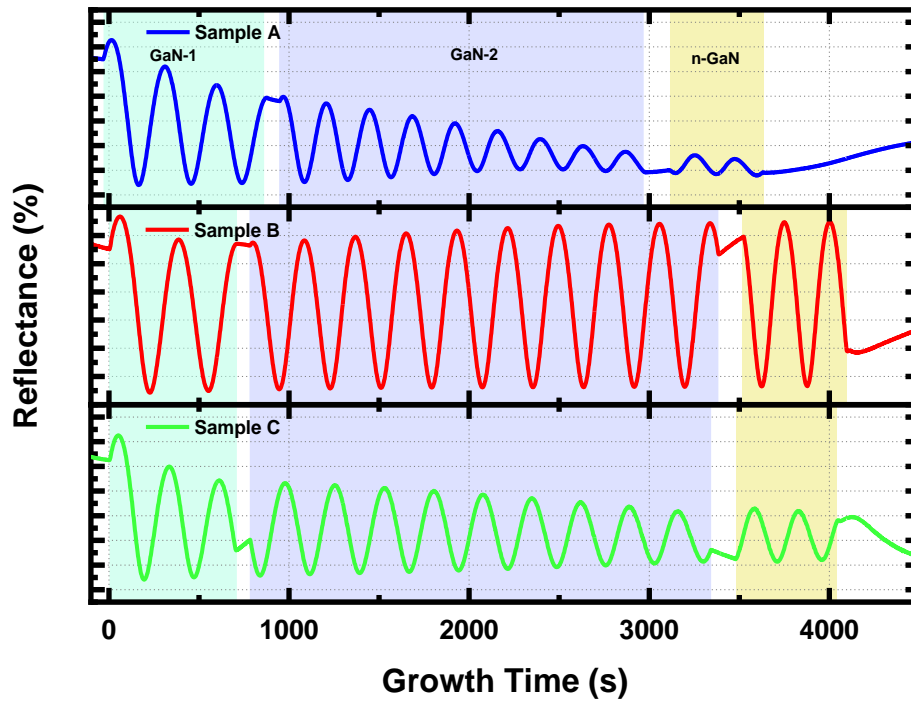


Figure 4-12 the in-situ reflectance curve for the GaN growth part of Samples A (blue curve), B (red curve) and C (green curve).

Figure 4-12 illustrates the reflectance curve for the three samples during the GaN growth phase. The Samples A (blue) and C (green) demonstrate a consistent decrease in average reflectance as the growth progresses. This consistent decline in reflectivity is indicative of surface degradation, resulting in a reduction in reflective intensity and ultimately leading to a roughened sample surface. Meanwhile, the downward trend in curve of Sample A is even more dramatic. In contrast, the curve of Sample B (red) demonstrates reflectance without degradation and with an upward trend, which means that the surface of the GaN gradually improves and becomes smoother, thus increasing the reflectivity.

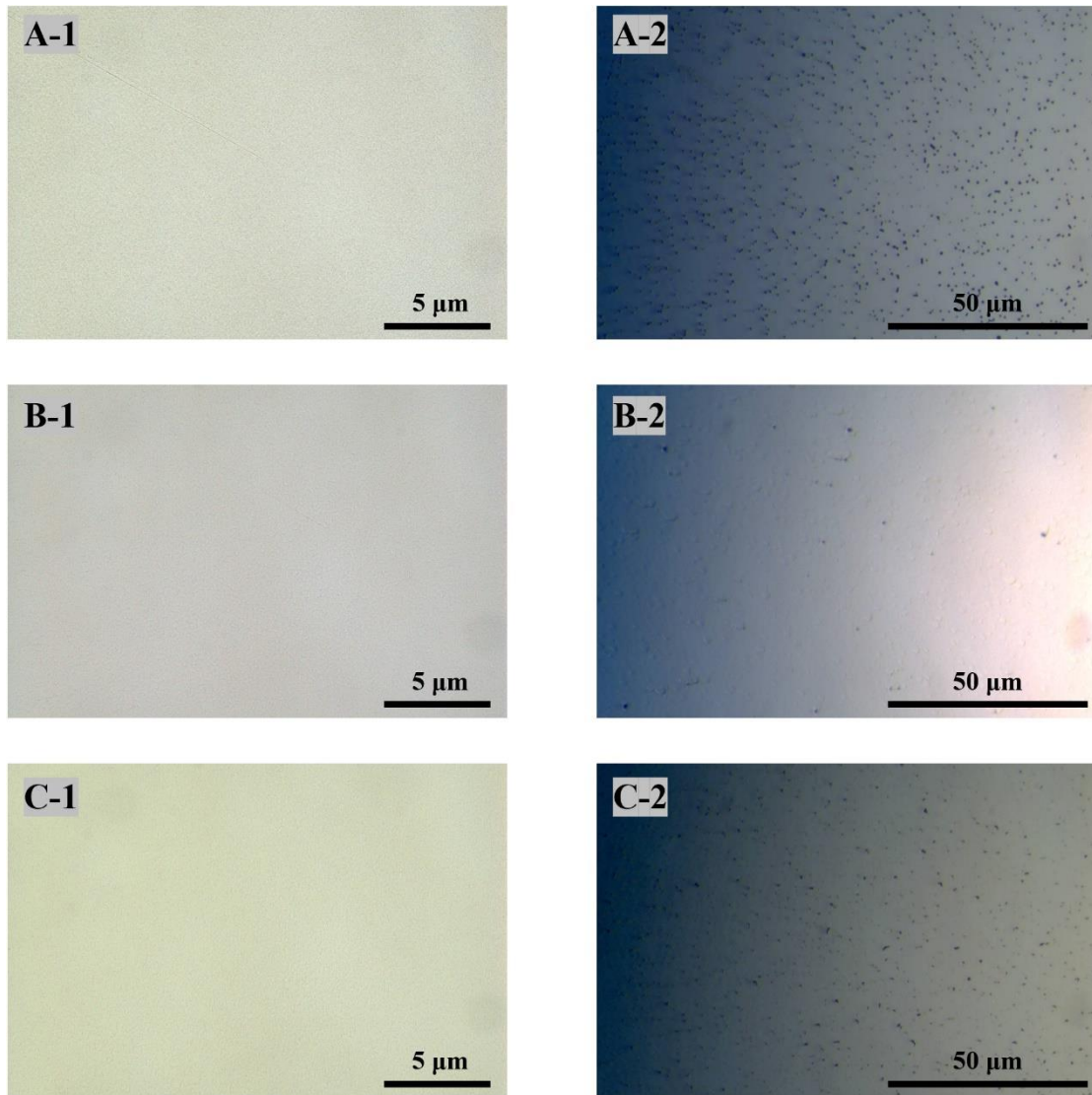


Figure 4-13 Optical microscopy images at two magnifications of Samples A (A-1 & -2) , B (B-1 & -2) and C (C-1 & -2).

As illustrated in Figure 4-13, the surfaces of Samples A and C exhibit a high density of pits, with Sample A displaying a greater density of pits than Sample C. Conversely, Sample B shows a relatively smooth GaN surface with a low density of pits. The observed surface condition of GaN correlates with the trend of its reflectivity curve. A decreasing trend in the reflectance curve corresponds with poor surface morphology, while a reflectance that remains at a large amplitude indicates relatively good surface morphology.

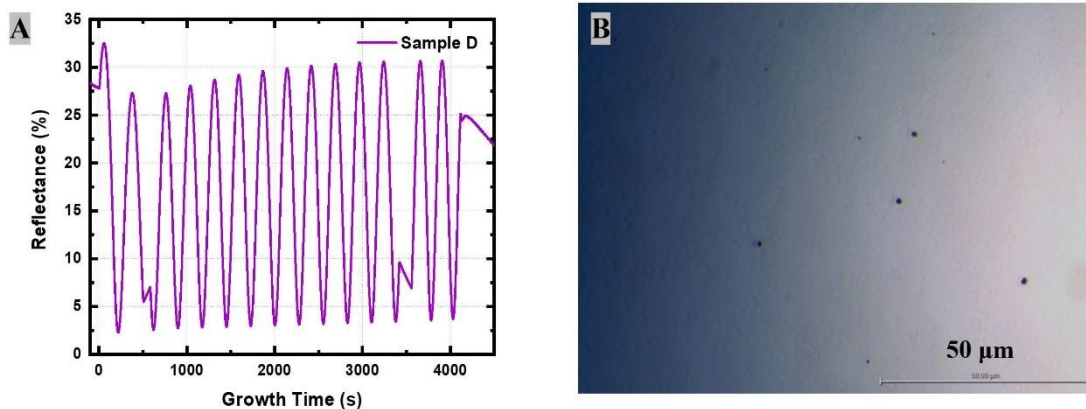


Figure 4-14 (A) the in-situ reflectance for the GaN growth phase; and (B) the optical microscopy image of Sample D.

In order to demonstrate the reproducibility of the growth conditions of Sample B, Sample D was grown under the same conditions. Figure 4-14A illustrates the reflectivity curve of sample D, which does not exhibit a discernible drop trend. Figure 4-14B depicts the GaN surface with the presence of a small density of pits.

Summary

Firstly, an examination of the reflectance in Figure 4-12 and the GaN surface microscope images in Figure 4-14 reveals a strong relationship between the reflectivity curves and the surface morphology of the epitaxial layer. In the event that the reflectivity curves demonstrate a decreasing tendency, this indicates that the surface morphology of the epitaxial layer is characterised by a rough surface.

A comparison of Samples A and B, the GaN surface of Sample B is better, which may be due to the higher V/III ratio of the GaN-1 layer of Sample B than that of Sample A. The higher V/III ratio in the GaN-1 phase may facilitate the initial 3D growth and finally improves the growth of the subsequent GaN layers. Comparing Sample B and Sample C, the GaN-2 layer of Sample C has a lower V/III ratio than that of sample B, and the surface morphology of Sample C is relatively poor. This may be attributed to the V/III ratio of Sample B in the GaN-2 layer is too low, which leads to the insufficient supply of the group V elements, and subsequent impact on the epitaxial layer surface. Concurrently, among the three samples, Sample B has the best surface morphology, followed by Sample C, with Sample A having the worst. This suggests that the GaN-1 layer has a significant influence on the subsequent GaN growth. Finally, since samples B and D were grown under the

same conditions and exhibited comparable surface morphologies, it demonstrates that the GaN on Si obtained under these conditions is reproducible. Figure 4-15 shows the full reflectance and curvature curve of the GaN on (111) Si growth process with optimised growth conditions.

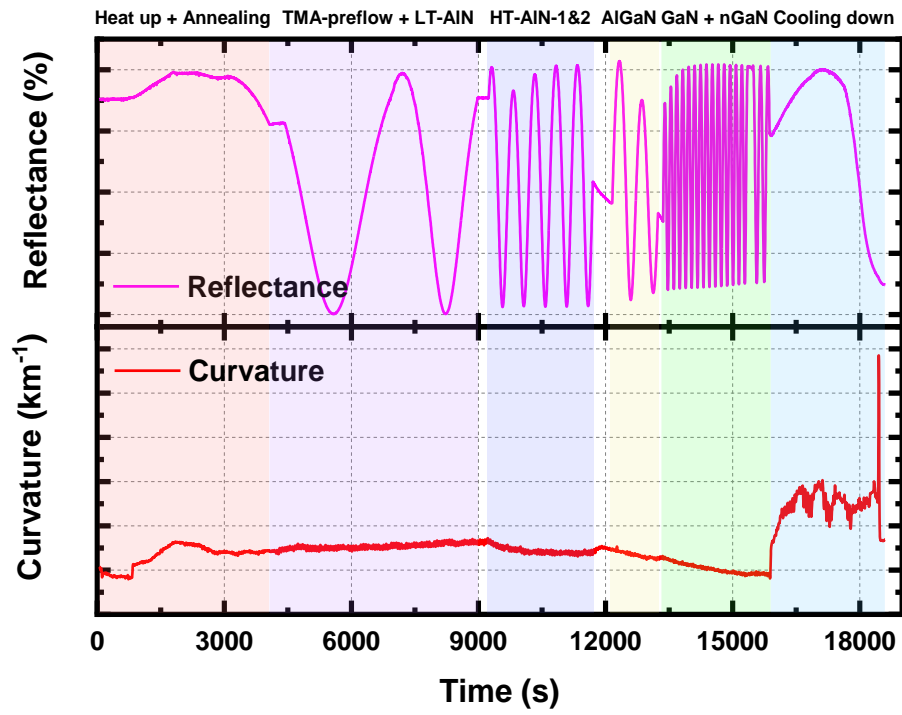


Figure 4-15 Reflectance and curvature for the optimized growth process for GaN on Si(111).

4.6 Conclusions

In conclusion, the growth of crack-free c-plane GaN films on typical (111) Si substrates has been successfully achieved by a series of optimisation techniques applied to the growth process. To address the issue of oxidised layers that tend to form on Si surface, both high-temperature annealing and chemical treatment methods have been demonstrated to be equally effective in treating Si substrate. However, the direct application of high-temperature annealing for Si treatment, without prior chemical treatment, can streamline the process while circumventing the consequences of residual chemical substances. The high-quality and smooth surface of the AlN layer can provide an excellent foundation for the subsequent growth of epitaxial layers and also effectively avoids melt-back etching. The utilisation of the TMA-pre flow initial process, coupled with the optimisation of the growth temperature of the two-step AlN method and the HT-AlN growth, has resulted in the achievement of AlN layers with a good crystalline quality and a smooth surface on Si substrates. Meanwhile, by investigating the growth conditions of the AlGaN buffer layer, a specific single AlGaN buffer layer was developed to achieve crack-free GaN growth. Finally, the GaN growth, which is based on a two-step GaN growth method has been investigated. The MO source and ammonia flow rate for each step was investigated and a GaN layer with a smooth surface was obtained. Furthermore, it was found that the GaN-1 layer (with the higher growth pressure and V/III ratio) exerts a dominant influence on the subsequent growth of GaN.

Reference

- [1] H. Ishikawa, G. Y. Zhao, N. Nakada, T. Egawa, T. Jimbo, and M. Umeno, "GaN on Si Substrate with AlGaN/AlN Intermediate Layer," *Japanese Journal of Applied Physics*, vol. 38, no. 5, pp. 492-494, 1999, doi: 10.1143/jjap.38.1492.
- [2] J. Chung, K. Ryu, B. Lu, and T. Palacios, "GaN-on-Si technology, a new approach for advanced devices in energy and communications," in *2010 Proceedings of the European Solid State Device Research Conference*, 2010: IEEE, pp. 52-56.
- [3] E. P. Conversion, "Gallium nitride (GaN) technology overview," *Power*, vol. 3, no. 2, p. 1, 2012.
- [4] A. Dadgar, "Sixteen years GaN on Si," *physica status solidi (b)*, vol. 252, no. 5, pp. 1063-1068, 2015.
- [5] M. Jamil, J. Grandusky, V. Jindal, F. Shahedipour-Sandvik, S. Guha, and M. Arif, "Development of strain reduced GaN on Si (111) by substrate engineering," *Applied Physics Letters*, vol. 87, no. 8, 2005.
- [6] S. Raghavan, X. Weng, E. Dickey, and J. M. Redwing, "Effect of AlN interlayers on growth stress in GaN layers deposited on (111) Si," *Applied Physics Letters*, vol. 87, no. 14, 2005.
- [7] J. Leathersich, *Design and Development of Stress Engineering Techniques for III-Nitride Epitaxy on Si*. State University of New York at Albany, 2015.
- [8] B. Zhang and Y. Liu, "III-Nitride Semiconductor LEDs Grown on Silicon and Stress Control of GaN Epitaxial Layers," *Handbook of Solid-State Lighting and LEDs*, pp. 517-556, 2017.
- [9] T. Wang, "Topical Review: Development of overgrown semi-polar GaN for high efficiency green/yellow emission," *Semiconductor Science and Technology*, vol. 31, no. 9, p. 093003, 2016.
- [10] A. Dadgar, C. Hums, A. Diez, J. Bläsing, and A. Krost, "Growth of blue GaN LED structures on 150-mm Si (1 1 1)," *Journal of Crystal Growth*, vol. 297, no. 2, pp. 279-282, 2006.
- [11] S. B. Dolmanan *et al.*, "Thin-film InGaN/GaN vertical light emitting diodes using GaN on silicon-on-insulator substrates," *Electrochemical and Solid-State Letters*, vol. 14, no. 11, p. H460, 2011.
- [12] J. Perozek *et al.*, "Investigation of structural, optical, and electrical characteristics of an AlGaIn/GaN high electron mobility transistor structure across a 200 mm Si (1 1 1) substrate," *Journal of Physics D: Applied Physics*, vol. 50, no. 5, p. 055103, 2017.

- [13] K. Cheng *et al.*, "Flat GaN epitaxial layers grown on Si (111) by metalorganic vapor phase epitaxy using step-graded AlGa_N intermediate layers," *Journal of Electronic Materials*, vol. 35, pp. 592-598, 2006.
- [14] B. Leung, J. Han, and Q. Sun, "Strain relaxation and dislocation reduction in AlGa_N step-graded buffer for crack-free GaN on Si (111)," *physica status solidi (c)*, vol. 11, no. 3-4, pp. 437-441, 2014.
- [15] E. Feltin *et al.*, "Crack-free thick GaN layers on silicon (111) by metalorganic vapor phase epitaxy," *Physica Status Solidi (a)*, vol. 188, no. 2, pp. 531-535, 2001.
- [16] S.-H. Jang and C.-R. Lee, "High-quality GaN/Si (111) epitaxial layers grown with various Al_{0.3}Ga_{0.7}N/GaN superlattices as intermediate layer by MOCVD," *Journal of Crystal Growth*, vol. 253, no. 1-4, pp. 64-70, 2003.
- [17] B. Heying *et al.*, "Role of threading dislocation structure on the x-ray diffraction peak widths in epitaxial GaN films," *Applied Physics Letters*, vol. 68, no. 5, pp. 643-645, 1996.
- [18] M. Vickers *et al.*, "In-plane imperfections in GaN studied by x-ray diffraction," *Journal of Physics D: Applied Physics*, vol. 38, no. 10A, p. A99, 2005.
- [19] S. Raghavan and J. Redwing, "Growth stresses and cracking in GaN films on (111) Si grown by metalorganic chemical vapor deposition. II. Graded AlGa_N buffer layers," *Journal of Applied Physics*, vol. 98, no. 2, 2005.
- [20] P.-Q. Xu *et al.*, "The influence of graded AlGa_N buffer thickness for crack-free GaN on Si (111) substrates by using MOCVD," *Chinese Physics Letters*, vol. 30, no. 2, p. 028101, 2013.
- [21] Y. Yang *et al.*, "Effect of compositionally graded AlGa_N buffer layer grown by different functions of trimethylaluminum flow rates on the properties of GaN on Si (111) substrates," *Journal of Crystal Growth*, vol. 376, pp. 23-27, 2013.
- [22] S. Ghosh, A. M. Hinz, M. Frentrup, S. Alam, D. J. Wallis, and R. A. Oliver, "Design of step-graded AlGa_N buffers for GaN-on-Si heterostructures grown by MOCVD," *Semiconductor Science and Technology*, vol. 38, no. 4, p. 044001, 2023.

Chapter 5 Comparative Study of GaN-Based Optical and Electrical Devices on Sapphire and Silicon

This chapter presents a comparative analysis of GaN-based optical and electrical structures grown on (111) Si and (0001) sapphire substrates. In particular, the optical devices concentrate on c-planar LED structures with InGaN/GaN multi-quantum wells (MQWs) as the active region, whereas the electrical devices focus on high electron mobility transistors (HEMTs). The main objective of this chapter is to investigate and compare the performance of optoelectronic devices on two different substrates, with a view to paving the way for the future migration of optoelectronic devices from the traditional sapphire substrate to the more cost-effective Si substrate.

5.1 Introduction

III-nitrides materials, including GaN, AlN, InN and its alloys, are regarded as the pivotal materials in the domains of modern optoelectronics and power electronics, due to their wide bandgap, high breakdown voltage and high electron mobility. Consequently, III-nitrides materials are widely used in optoelectronics, power electronics and RF devices [1-6]. In recent decades, a variety of substrates have been employed for the growth of GaN materials, including homogeneous GaN, SiC, sapphire, and Si. Among these, sapphire is the principal substrate for recent GaN epitaxial growth due to the maturity of the GaN growth technology on sapphire. However, the low thermal conductivity efficiency and difficulty in compatibility with Si-based manufacture of sapphire limit their popularity in large-scale commercial applications. In contrast, Si is an attractive alternative substrate for GaN-based devices due to its low cost, large size, good thermal conductivity, and compatibility with existing silicon-based manufacture. In particular, (111)-oriented Si substrates for GaN-based device growth show potential advantages in terms of lattice matching and defect control [7, 8].

Nevertheless, the integration of GaN-based optical and electrical devices on Si substrates is confronted with a multitude of challenges. In terms of optical devices, the majority of III-nitride based LEDs grown on Si substrates employ the InGaN/GaN MQW structures as the active regions.

Due to the significant lattice mismatch between GaN and Si, which results in an increased defect density in the GaN film, particularly in the form of dislocations. These dislocations act as non-radiative recombination centres, reducing the internal quantum efficiency (IQE) of the LEDs [9-11]. Concurrently, the doping rate of indium in the InGaN/GaN MQWs is directly correlated with the emission wavelength. The high indium content in InGaN is a critical factor in the development of green, yellow or higher wavelength III-nitrides based emitters. Furthermore, the doping of In into GaN is also influenced by stress. In theory, stress facilitates the convergence of the InGaN layer towards lattice-matched conditions by influencing the vapour-solid thermodynamic equilibrium. This implies that the lattice mismatch is reduced by the spontaneous reduction of the amount of indium doping during epitaxial growth, thereby improving the stress and defect density [12-14]. The GaN-based LED devices grown on Si substrates are typically dominated by tensile stress, whereas GaN grown on sapphire substrates are subject to compressive stress. Typically, tensile stress increases the amount of indium doping in GaN, resulting in a red-shift in the emission wavelength, whereas compressive stress usually leads to a decrease in the amount of indium doping, resulting in a blue shift [15]. Therefore, even InGaN/GaN MQWs grown under the identical conditions should emit at different wavelengths on different substrates. It is reasonable to assume that in the case of InGaN/GaN MQWs-based LEDs on Si substrate, the indium incorporation rate in GaN may be higher due to tensile stress, thus contributing to long wavelength emission. Therefore, the transfer of mature growth technology for InGaN MQW-based LEDs from sapphire to Si represents a topic that requires further investigation, particularly in regard to manufacturing compatibility and cost-efficiency. For GaN-based electronic devices, the GaN-based HEMT devices on a Si substrate is face a number of challenges, due to the presence of significant lattice and thermal mismatches between GaN and Si, which increase the defect density of the GaN crystals and introduce additional stresses leading to cracking problems. This ultimately leads to increased current collapse effects and limits the performance of the HEMT devices [16-20].

In this chapter, the InGaN/GaN MQWs-based LEDs structure and a simple HEMT structures are grown on Si and sapphire, respectively, and the differences in their performance on different substrates are comparative studied. For the study of the MQWs structure, the InGaN/GaN MQWs-based LEDs were grown on a GaN on Si template. At the same time, a GaN on sapphire template

was included in the same growth run with the objective of obtaining a control sample, which means that the structures were grown on GaN/Si and GaN/sapphire under identical conditions. The samples grown on both Si and sapphire substrates were subjected to PL and XRD measurements, and their optical characteristics were investigated. For the study of HEMT structures, basic HEMT structures were grown on Ga-polar GaN on Si substrate, and the device performance was demonstrated.

5.2 Comparison Study of C-planar LED with InGaN/GaN MQWs on (0001) Sapphire and (111) Si Substrates

In light of the advancement of III-nitride optoelectronics and the increasing demand for a range of substrate applications, it has become imperative to investigate the influence of different substrates on the characteristics of the grown III-nitride materials. Sapphire and Si are two substrates that are commonly used in epitaxial growth, each with unique advantages. However, the significant lattice mismatch and difference in coefficients of thermal expansion between GaN and Si result in the tendency to generate defects and stresses during the growth process. The discrepancy in thermal expansion coefficients gives rise to the phenomenon of tensile strain in the case of GaN on Si and compressive strain of GaN on sapphire. This discrepancy in strain states has an influence on the indium incorporation rate into GaN throughout the growth process, which in turn affects the growth process and optical characteristics of InGaN/GaN MQWs [15, 21]. This section presents a comparative analysis of InGaN/GaN MQW-based LEDs grown on both Si and sapphire substrates under identical growth condition. The standard PL measurement revealed a significant difference in the emission wavelengths of InGaN/GaN MQWs on GaN-on-Si and GaN-on-Sapphire templates, which shows that the different indium incorporation ratio in two kinds of templates. Furthermore, additional XRD ω - 2θ measurements substantiate the assertion that the indium content in the InGaN MQWs grown on two different GaN templates differ. The findings presented in this section provide crucial guidance for the optimisation of GaN-based optoelectronic device growth on Si substrates, as well as for the transfer of the proven experience of GaN LED growth on sapphire to Si substrates.

Experiment design

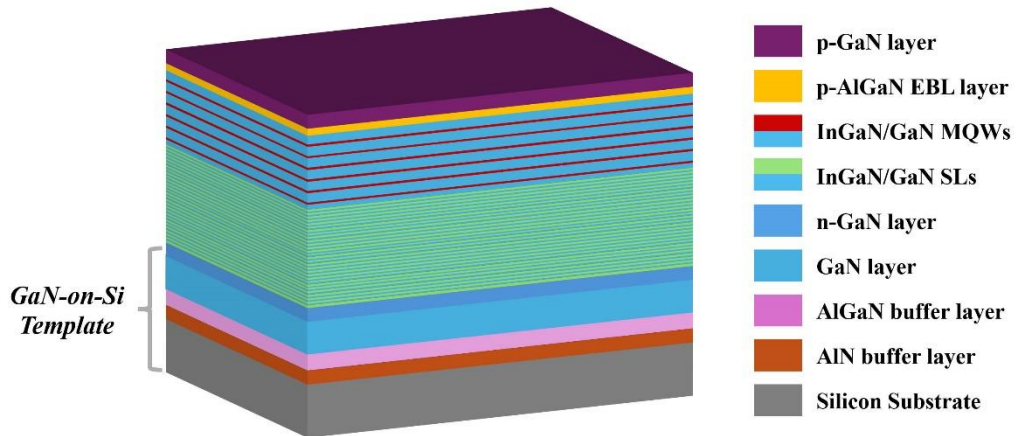
In this section, the InGaN/GaN MQWs structure is overgrown on the top of the GaN-on-Si and GaN-on-Sapphire templates. Both two kinds of templates are prepared by the standard growth method of GaN-on-Si and GaN-on-Sapphire by MOCVD. In detail, for growth of the GaN-on-Sapphire template, the standard single-side polished c-plane (0001) sapphire substrate was initially subjected to a high-temperature annealing process in a hydrogen atmosphere at 1220°C. The reaction chamber was then cooled down to 620°C and NH₃ was introduced into the chamber without any MO source for the nitridation process, which was maintained for 180 seconds. Subsequently, a

TMG source was introduced directly into the chamber to facilitate the growth of a 20 nm thin low-temperature nucleation layer, which plays a pivotal role in the subsequent growth of high-quality GaN layers. Following the growth of the low-temperature nucleation layer, the temperature of the reaction chamber was increased to 1275°C in order to facilitate the growth of an undoped GaN layer with a thickness of 1.5 μm, and a 300 nm n-GaN layer was grown in the end.

And for growth of the GaN-on-Si template, the standard single-side polished c-plane (001) Si substrate was initially annealed at 1340 °C for 600 seconds. Subsequently, the reactor temperature was decreased to 1150 °C, and the TMA pre-flow process was carried out by directly introducing TMA into the reaction chamber in the absence of NH₃. Next, a thin layer of low-temperature AlN (LT-AlN) was deposited at 1150 °C through the additional introduction of NH₃, followed by the growth of a layer of high-temperature AlN (HT-AlN) at 1310 °C. To address the crack issue that occurs during the cooling down process, a stress-relief layer of step-graded Al_xGa_{1-x}N will be grown and used to generate additional compressive strain to compensate for the tensile strain generated during the cooling process after deposition of the GaN layer. The AlGa_xN buffer layer has a total thickness of 700 nm, comprising a 260 nm Al_{0.35}Ga_{0.65}N-1 layer and a 440 nm Al_{0.17}Ga_{0.83}N-2 layer. Finally, a 1.5 μm undoped GaN layer and a 300 nm n-GaN layer were grown at 1315 °C.

In the MQWs growth process, the two standard templates will initially undergo the standard cleaning treatment and then be placed simultaneously in the 3×2" pockets susceptor in the MOCVD reaction chamber for the next MQWs overgrowth process. Once the requisite temperature had been reached within the reactor, a thin layer of n-GaN was initially deposited on the upper surface of the template. Subsequently, the 30 pairs of InGa_xN/GaN superlattice layers (SLs) were grown as a transition layer with a preset thickness of InGa_xN:4.2 nm/GaN:2.4 nm. Following the deposition of the SLs layer, the 5 periods of InGa_xN/GaN MQWs are grown as the active region. It is important to note that the indium content in the SLs is significantly lower than that in the MQWs. Next, a thin p-AlGa_xN layer is deposited as an electron-blocking layer (EBL), and finally, a p-GaN layer of approximately 200 nm are grown.

A) MQWs on GaN-on-Si Template



B) MQWs on GaN-on-Sapphire Template

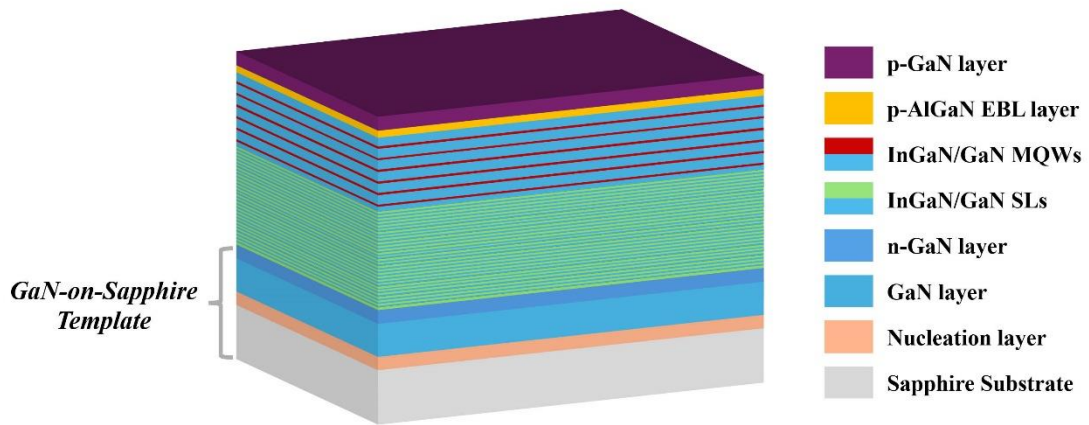


Figure 5-1 Schematic diagram of InGaN/GaN MQWs structure with InGaN/GaN SLs on (A) GaN-on-Si template and (B) GaN-on-Sapphire template.

Figure 5-1 shows the schematic diagram of the MQWs structure grown on the two kinds of GaN templates. As both templates were grown in the same growth run, this ensures that the obtained LED structure was grown under identical conditions. The growth recipe used in this study is for growing InGaN/GaN MQWs structures on sapphire substrate are optimised. Consequently, this comparative study provides valuable insights for the future optimisation of InGaN/GaN MQWs on a Si substrate. Furthermore, the obtained samples were subjected to standard photoluminescence and X-ray diffraction measurements to analyse the differences in optical properties and structure. These two kinds of samples will be named as Sample A (MQWs on Si template) and Sample B (MQWs on Sapphire template) in order to easily describe.

Results and Discussion

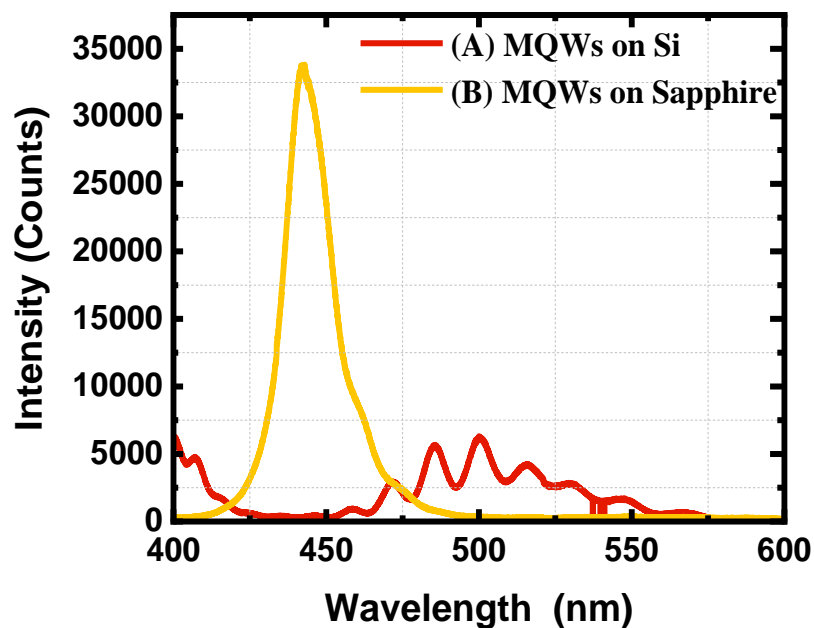
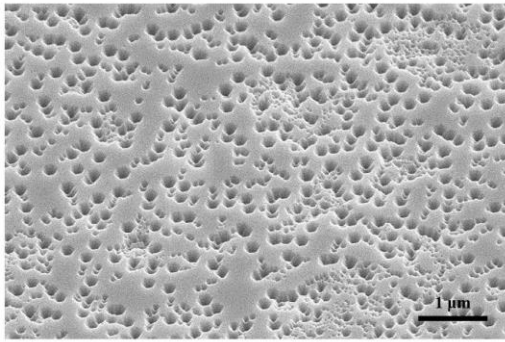


Figure 5-2 RT-PL spectra of MQWs on Si (sample A) and MQWs on sapphire (sample B).

Figure 5-2 illustrates the standard RT-PL spectra of MQWs on both Si and Sapphire substrates, which were subjected to identical growth conditions and the measurement point are both in the centre of the samples. The spectra demonstrate that the Si sample displays a green emission peak at a wavelength of 509 nm, while a relatively strong blue emission wavelength peak at 443nm is observed in the sapphire sample. Furthermore, the PL spectra obtained from MQWs on sapphire substrate exhibit a narrower spectral width, indicative of a higher concentration of luminescence wavelengths and relatively higher luminescence efficiencies. In contrast, the spectra of MQWs on Si substrate display a broader spectral width, suggestive of a wider distribution of luminescence wavelengths and lower luminescence efficiencies. It can be inferred that the discrepancy in emission wavelength is attributable to the different stress states that are induced by two substrates, which in turn influence the indium content in the InGaN and consequently result in a shift in the emission wavelength. Meanwhile, the MQW on GaN-on-sapphire exhibits higher luminescence intensity, which can be attributed to their better lattice matching and a lower defect density in comparison to that of a GaN-on-Si. The SEM images presented in Figure 5-3 demonstrate the surface morphology of the two samples, with sample A exhibits a large surface pits density than sample B.

A) MQWs on GaN-on-Si Template



B) MQWs on GaN-on-Sapphire Template

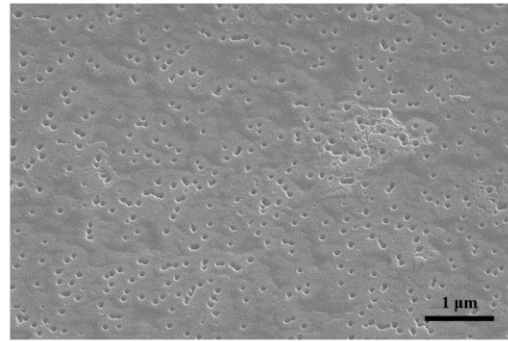


Figure 5-3 the SEM images of (A) MQWs on Si template and (B) MQWs on sapphire template.

In conclusion, the presented PL spectra demonstrate that there are significant differences in the luminescence properties of InGaN/GaN MQW structures grown on GaN-on-Si and GaN-on-Sapphire templates, even when subjected to identical growth conditions. To avoid the potential impact of uncontrollable factors on the reproducibility of experimental outcomes, an experimental control set of InGaN/GaN MQW structures, designated as Sample C and Sample D, were grown on GaN-on-Si and GaN-on-Sapphire templates using identical growth recipes.

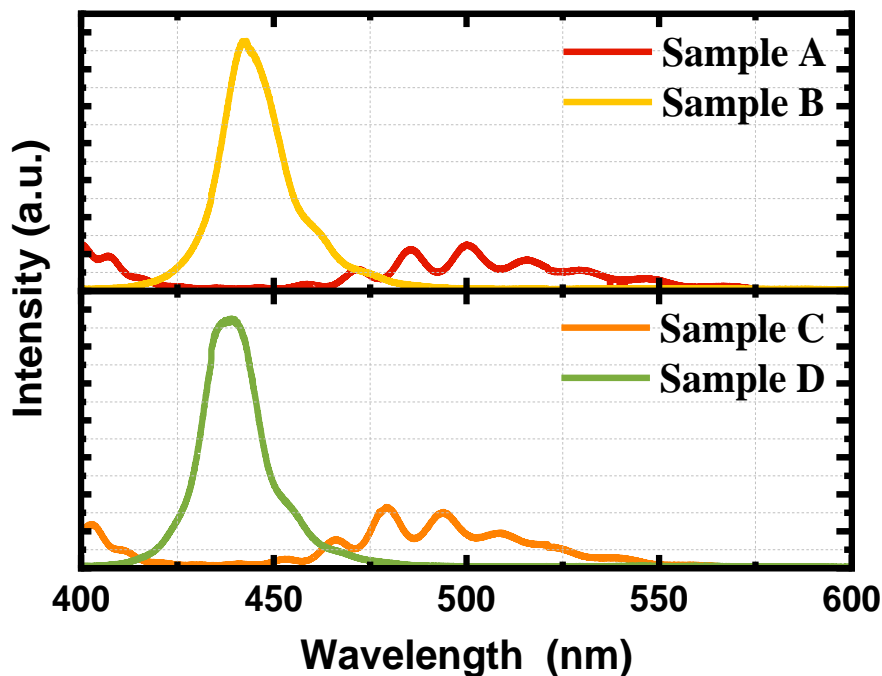


Figure 5-4 The RT-PL spectra of four samples (A-D).

Figure 5-4 illustrates that the RT-PL spectra obtained for samples C and D are a highly comparable to those of samples A and B. The InGaN/GaN MQW samples grown on sapphire-based GaN

templates exhibit shorter emission wavelengths and narrower spectral widths obtained than the those grown on GaN-on-silicon templates. Consequently, it can be seen that the outcomes of this experiment are reproducible. Table 5-1 presents the template type, emission wavelengths and half-height widths (FWHM) of the PL spectra of the MQWs for the four samples.

Table 5-1 the MQWs emission wavelength and FWHM of four samples A, B, C and D.

Sample Label	Template	MQWs Emission wavelength (nm)	FWHM (nm)
A (GN4251A)	GaN on Si	503	39.7
B (GN4251B)	GaN on Sapphire	443	17.5
C (GN4252A)	GaN on Si	495	38.4
D (GN4252B)	GaN on Sapphire	439	16.7

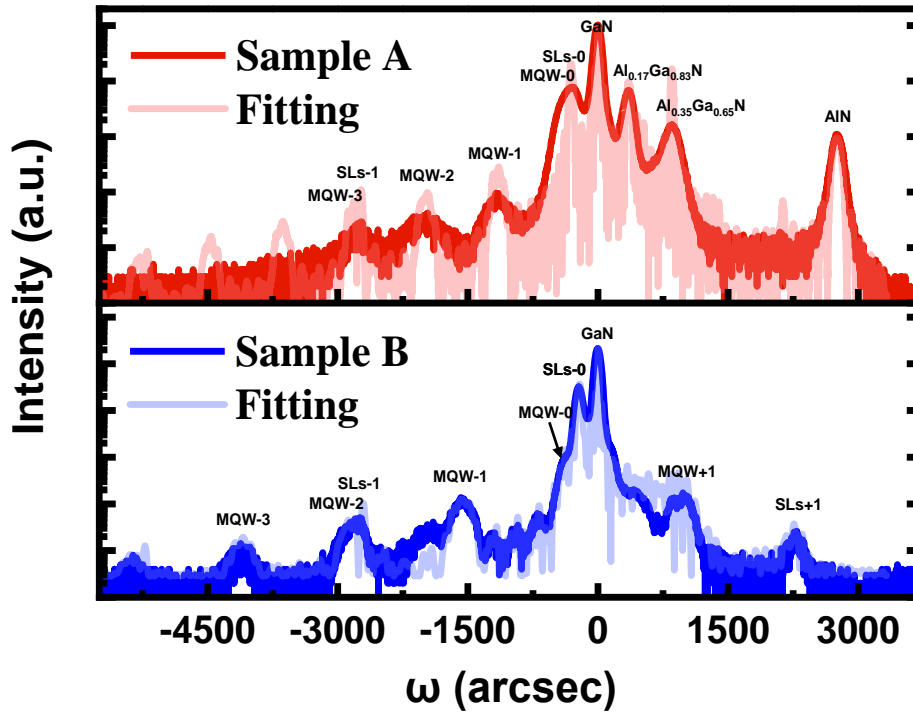


Figure 5-5 The XRD ω - 2θ spectra and corresponding fitting curves for samples A (red) and B (blue).

The satellite peaks of both SLs and MQWs are labelled in the figure.

The XRD measurement curves and corresponding fitting curves for samples A and B are presented in Figure 5-5, the curves are aligned according to the GaN peaks. The former was obtained using an omega-2theta scan mode on a Bruker D8 X-ray diffraction system, whereas the latter were determined by employing the LV-RADS simulation software. For the sample A, the diffraction patterns have shown two distinct peaks between the GaN and AlN peak, which corresponded to the AlGaN-1 and AlGaN-2 layers with Al contents of 35% and 17%, respectively. Meanwhile, the diffraction patterns of the two samples have revealed the presence of satellite peaks associated with both of InGaN/GaN SLs and 5 periods of InGaN/GaN MQWs. These observed satellite peaks have been labelled in the figure with different orders of occurrence.

Table 5-2 presents a various parameter for Sample A and Sample B, including indium content, InGaN well thickness, and GaN barrier thickness of both InGaN/GaN SLs and MQWs and the emission wavelength of MQWs. These data were obtained through the combination of simulation curves generated by Bruker LV-RADS simulation software and XRD measurement curves. Based on the data presented in the Table 5-2, sample B, which is grown on the GaN-sapphire template,

exhibits an SLs structure with an InGaN well having an indium content of 3.2%, a well thickness of 4.3 nm, and a GaN barrier thickness of 2.2 nm. The MQWs of sample B demonstrates an indium content of 12.8% in the InGaN quantum well, with the well thickness of 2.6 nm, and a GaN barrier thickness of 10.2 nm. In contrast, the Si template-based sample A which exhibits significantly different parameters. Sample A has an SLs with an InGaN thickness of 4.2 nm, comprising 4.5% indium, and a GaN barrier thickness of 2.4 nm. The MQWs of sample A shows a 3 nm thick InGaN quantum well with 16% indium content, and a GaN barrier thickness of 14.4 nm.

Table 5-2 the parameters of Samples A and B, inclusive of the Indium content, InGaN quantum well thickness and GaN barrier thickness of both SLs and MQWs.

Sample Label	Emission wavelength (nm)	SLs			MQWs		
		Indium content (%)	Well thickness (nm)	Barrier thickness (nm)	Indium content (%)	Well thickness (nm)	Barrier thickness (nm)
A	509	4.5	4.3	2.4	16	3	14.4
B	443	3.2	4.2	2.2	12.8	2.6	10.2

The aforementioned results have demonstrated that the indium content of InGaN in LED structures grown on a silicon template (Sample A) is significantly higher than that of LEDs grown on a sapphire template (Sample B). Furthermore, as both samples A and B were grown under identical conditions, the MQW of Sample A was deposited in a thicker layer compared to that deposited by Sample B. Consequently, it can be demonstrated that the MQW of Sample A was deposited at a faster growth rate. It is demonstrated once again that in the case of GaN-on-Si templates, tensile strain is responsible for the enhancement of both the indium doping rate and the growth rate of GaN. This is due to the variation in vapour-solid thermodynamic equilibrium resulting from the discrepancy in strain states [12-14, 22].

Summary

This section presents a comparative investigation into the effect of different substrates on the optical properties of c-plane InGaN/GaN MQWs-based LED structures grown on GaN-on-(0001) sapphire and GaN-on-(111) silicon substrates. The study reveals significant discrepancies in the growth and optical properties of the LED structures grown on the two different substrates. In detail, the MQW grown on the GaN-on-Si template displays a significantly longer emission wavelength than that of the MQW grown on the GaN-on-Sapphire template. However, the former exhibits a broader FWHM of the PL spectra and lower emission intensity than that of the MQW grown on the GaN-on-Sapphire template. The XRD ω - 2θ measurements and the corresponding simulation curves demonstrate that InGaN/GaN MQWs grown on GaN-on-Si templates show a higher indium content and faster growth rates than it grown on GaN-on-Sapphire templates under identical growth conditions. The above differences that occur on the two different substrates can be attributed to changes in the vapour-solid thermodynamic equilibrium, which are a consequence of the disparate strain states to which GaN on silicon and GaN on sapphire are subjected. In general, the GaN-on-Si template is predominantly subjected to tensile strains. Finally, as the growth recipe employed in this experiment was optimised for the growth on sapphire templates, further optimisation is necessary to facilitate the transfer of the growth technology of LEDs from sapphire to a silicon substrate.

5.3 Investigating the Effect of NH₃ Ambient Gas in Cooling on the Optical Properties of InGaN/GaN MQWs-based LEDs

Ammonia (NH₃) is a crucial gas used to provide the group V element when depositing III-nitrides using a MOCVD system. As a precursor for the group V element, ammonia provides a continuous supply of nitrogen in the ambient gas, preventing the decomposition of the nitride layer at high growth temperature. During the cooling phase at the end of the growth process, a certain proportion of NH₃ is introduced into the ambient gas to stabilize the surface, thereby preventing the decomposition of the epi-layer at the high temperatures present during the initial cooling period.

Experiment design

In order to investigate whether the NH₃ ambient gas during the cooling phase exerts an effect on the optical properties of the final InGaN/GaN MQWs-based LED structures, a new experimental group was designed based on samples A and B in Section 5.2, named samples E and F, which were grown on a GaN-on-Si template and a GaN-on-Sapphire template, respectively, and were prepared in the same growth run. Furthermore, the complete material stacks of samples E and F were prepared using the same recipes as samples A and B, with the only difference that N₂ was employed as the ambient gas exclusively during the cooling phase, in place of NH₃. The objective of this experimental group is to evaluate the effect of NH₃ on the optical performance of GaN-based LEDs during the cooling down process.

Results and Discussion

Figure 5-6 depicts the standard RT-PL spectra from the centre of samples A, B, E and F. The PL spectra indicate a slight difference in MQWs emission wavelengths between sample E (GaN-on-Si template, cooled without NH₃) and sample A (GaN-on-Si template, cooled with NH₃), with the former exhibiting a longer wavelength at 520 nm compared to the latter's 502 nm. In contrast, samples B (GaN-on-Sapphire template, cooled with NH₃) and F (GaN-on-Sapphire template, cooled without NH₃) exhibit comparable emission wavelengths at 443 nm and 439 nm, respectively. Notably, the emission wavelength of the SLs in sample E is longer than that in sample A, which

could be another contributing factor to the observed wavelength difference. Table 5-3 provides detailed specifications regarding the substrate type, cooling ambient gas, emission wavelengths of MQWs, and FWHM of the MQWs for samples A, B, E, and F.

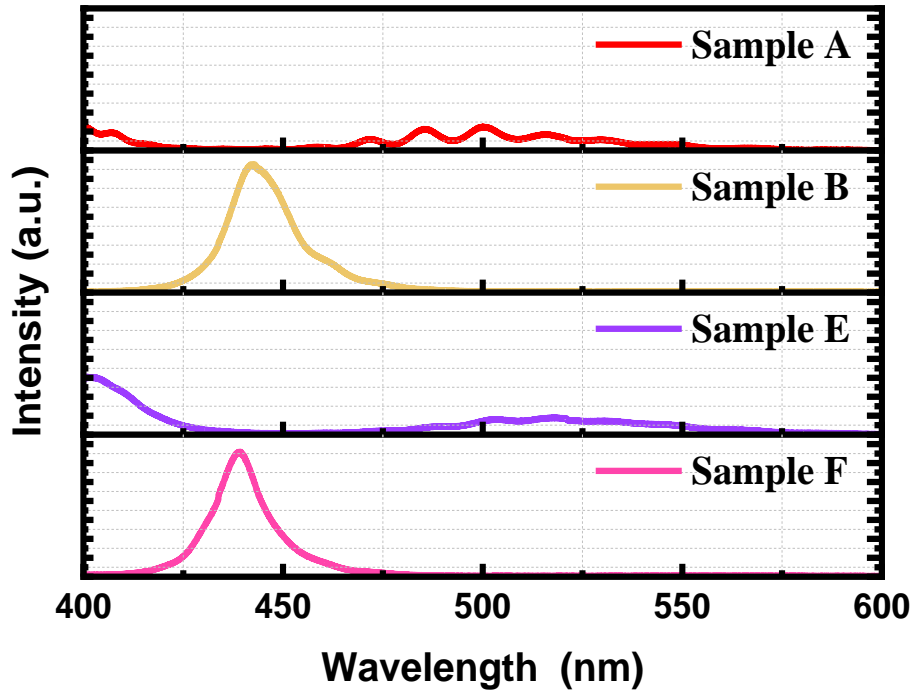


Figure 5-6 RT-PL spectra of Samples A, B, E and F, under the same the intensity scale.

Table 5-3 the template type, cooling ambient, MQWs emission wavelength, and FWHM of Samples A, B, E and F.

Sample Label	Template	Cooling ambient	MQWs Emission wavelength (nm)	PL FWHM (nm)
A	GaN on Si	NH ₃	503	39.7
B	GaN on Sapphire	NH ₃	443	17.5
E	GaN on Si	N ₂	520	56.7
F	GaN on Sapphire	N ₂	439	14.2

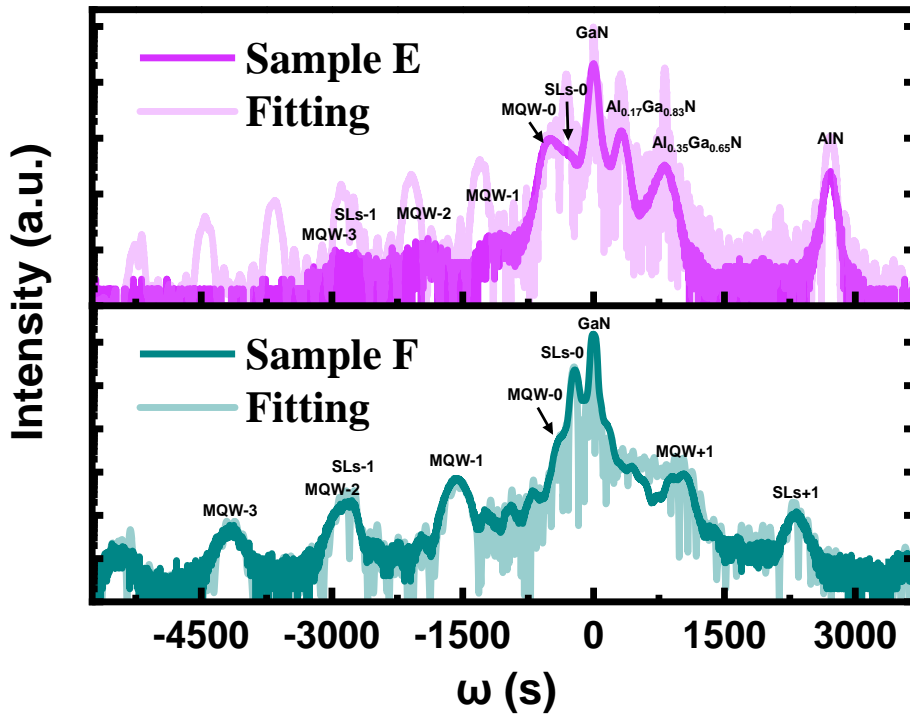


Figure 5-7 The XRD ω - 2θ spectra and corresponding fitting curves for samples E and F. The satellite peaks of both SLs and MQWs are labelled in the figure.

Figure 5-7 shows the XRD measurement spectra by the ω - 2θ scan mode and the corresponding fitting curves for both sample E and F. The satellite peaks from the InGaN/GaN SLs and InGaN/GaN MQWs of both samples can be observed in the figure, which have been labelled for clarity. A comparative analysis of Figure 5-5 and Figure 5-7 reveals that the satellite peaks exhibited by sample E are less pronounced (rougher) than those observed in the XRD curve of sample A. Moreover, an anomalous peak is discernible at the location of the SLS-0 and MQW-0 peaks, but is not observed in sample A. This phenomenon may be attributed to the relatively weak intensity of the satellite peaks exhibited by SLs, which is likely a consequence of the suboptimal quality of the SLs layer. In contrast, samples B and F, which were both grown on the GaN-on-Sapphire template, exhibited similar XRD spectra, with no significant difference between them.

Table 5-4 the parameters of Samples A, B, E and F, inclusive of the Indium content, InGaN quantum well thickness and GaN barrier thickness of both SLs and MQWs.

Sample Label	Emission wavelength (nm)	SLs			MQWs		
		Indium content (%)	Well thickness (nm)	Barrier thickness (nm)	Indium content (%)	Well thickness (nm)	Barrier thickness (nm)
A	509	4.5	4.3	2.4	16	3	14.4
B	443	3.2	4.2	2.2	12.8	2.6	10.2
E	520	7	4.5	2.4	18	3	15.5
F	439	3.3	4.3	2.2	12.5	2.5	10.3

Table 5-4 presents the layer parameters of both SLs and MQWs for four samples. The presented parameters illustrate that the indium content of the InGaN layer in both SLs and MQWs of sample E is significantly higher than that of sample A, which is 7% and 18%, respectively. Conversely, the various parameters of samples B and F are approximately similar with no significant difference. This also serves to confirm that the different wavelengths observed in the PL spectra for samples A and E are a consequence of the difference in indium contents present in the InGaN layers [23, 24].

Summary

This section presents a comparative investigation into the effect of NH₃ ambient gas in the cooling phase on the optical properties of InGaN/GaN MQWs-based LED structures grown on (111) silicon and (0001) sapphire. It was demonstrated that InGaN/GaN MQWs-based LED structures grown on a GaN-on-Si template in the absence of ammonia ambient gas cooling exhibited longer wavelengths and higher In content than samples subjected to ammonia ambient gas cooling, but this phenomenon was not observed in the sample grown on a GaN-on-Sapphire template. Furthermore, the spectra of PL and XRD exhibited no discernible difference in the samples on the sapphire template, indicating that no unanticipated variables were present during this growth process and that this growth recipe

is still reproducible. Therefore, the differences observed in the samples grown on the Si template may be attributed to the fact that the samples grown on the Si template are more susceptible to the ambient gases of the cooling process. It is therefore debatable whether the removal of ammonia during the cooling process has an effect on the optical performance of InGaN/GaN MQWs-based LEDs, and further experimental proof is required.

5.4 Growth of AlGa_N/Ga_N HEMTs on (111) Si

With the in-depth research on GaN materials, GaN-based power electronic devices, such as high electron mobility transistors (HEMTs), have demonstrated excellent performance at high frequencies, high power, and high temperatures. This exceptional performance makes them highly promising for a wide range of applications in wireless communications, power electronics, radar, and other fields [25, 26]. The wide bandgap (3.4 eV), high breakdown electric field (>106 V/cm), electron mobility (2×10^7 cm/s) and thermochemical stability of GaN materials render them a novel and optimal alternative material to conventional electronic devices [27]. At the present time, HEMTs comprising AlGa_N/Ga_N structures grown on silicon carbide (SiC) substrates represent one of the most promising technologies for power applications, as evidenced by numerous publications demonstrating their excellent performance [28]. Despite the impressive electrical performance and high-frequency characteristics observed in AlGa_N/Ga_N HEMTs on SiC substrates, there remain significant challenges pertaining to cost and fabrication process complexity that require further investigation. Furthermore, HEMTs on sapphire substrates have also undergone considerable development, largely due to their exceptional thermal stability and electrical insulating properties, which render them significantly competitive in the domain of RF, microwave, and low-power electronic devices. Consequently, sapphire substrates also occupy a crucial role in the development of GaN-based HEMTs, offering benefits over SiC substrates in terms of cost and process maturity [29, 30]. In recent years, there has been a great deal of interest in GaN-based electrical devices using Si as a substrate. This is a crucial field of study, as it has the potential to significantly reduce the cost of individual devices and increase the possibilities for integrating semiconductor devices. This is due to the large-scale availability of silicon substrates and the feasibility of integrating them with existing metal-oxide-semiconductor (MOS) technologies [31, 32]. However, the significant lattice mismatch and thermal expansion coefficient difference between Si and GaN can easily lead to the formation of high defect densities and additional stresses, which in turn can affect the functionality and reliability of the device. This poses a significant challenge to the development of GaN-based HEMTs on Si substrates.

In this section, a basic AlGa_N/Ga_N-based HEMT structure with an AlN interlayer will be grown on a (111) Si substrate. This section will perform the XRD and electron channelling contrast imaging

(ECCI) characterisation to determine the quality of the epitaxial layers and to observe the dislocation density on the sample. Additionally, the electrical characteristics of the fabricated HEMT devices will be measured.

Experiment design

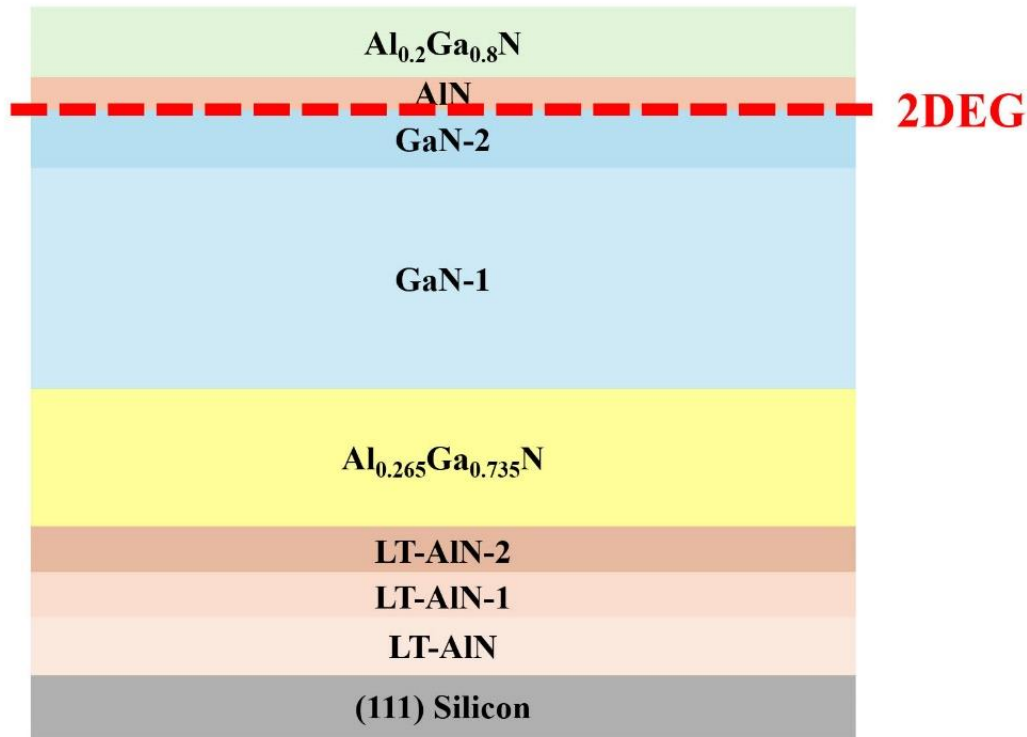


Figure 5-8 Schematic of an AlGaIn/GaN HEMT structure on (111) Si substrate with an AlN interlayer.

In this section, a basic AlGaIn/GaN HEMT structure with a thin AlN interlayer was grown on (111) Si and is labelled as GN4337. Initially, a standard 2-inch single-polished (111) Si wafer was placed on the susceptor within an MOCVD reactor and subjected to high-temperature annealing in a H_2 ambient to remove surface impurities and oxides. Subsequently, the reactor temperature was reduced to 1007°C , and a 177-second TMA pre-flow was performed without any NH_3 flow. Following this, an LT-AlN layer was grown at the same temperature with the introduction of NH_3 . The temperature was then increased to 1135°C to sequentially grow HT-AlN-1 and HT-AlN-2 layers by the different TMA flow rates. Next, an approximately 650 nm thick $\text{Al}_{0.265}\text{Ga}_{0.735}\text{N}$ stress-compensating layer was deposited. Subsequently, the reactor temperature was reduced to 1050°C for the growth of a 1.5 μm GaN-1 layer, followed by a 300 nm GaN-2 layer. Immediately thereafter, a very thin AlN interlayer was grown at the same temperature, followed by the deposition of a 25

nm $\text{Al}_{0.2}\text{Ga}_{0.8}\text{N}$ barrier layer. Figure 5-8 provides a schematic representation of a basic AlGaN/GaN HEMTs structure grown on (111) Si with a thin AlN interlayer.

Results and Discussion

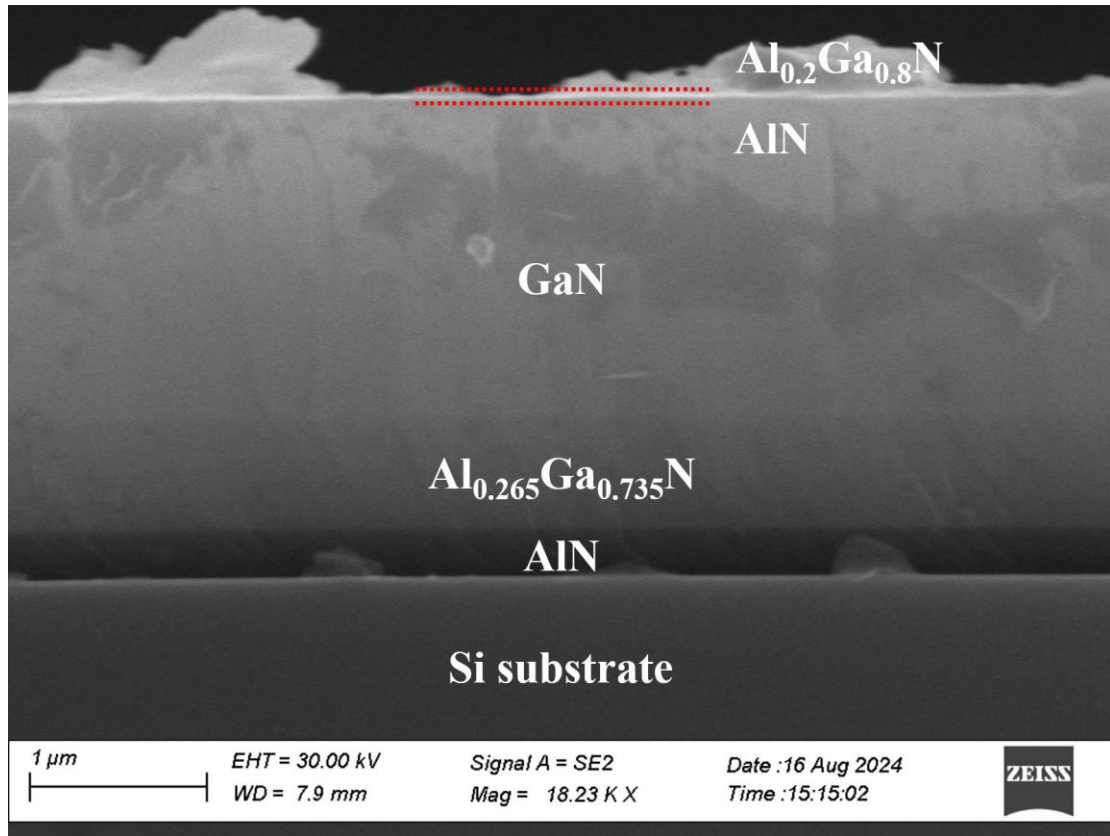


Figure 5-9 Cross-sectional SEM image of an AlGaN/GaN HEMT on (111) Si with an AlN interlayer.

Figure 5-9 shows the cross-sectional SEM image of sample GN4337, a basic AlGaN/GaN HEMT on (111) Si substrate with a thin AlN interlayer, and all layers are labelled in this image. Furthermore, the interface of each layers is clearly visible without any apparent irregularities.

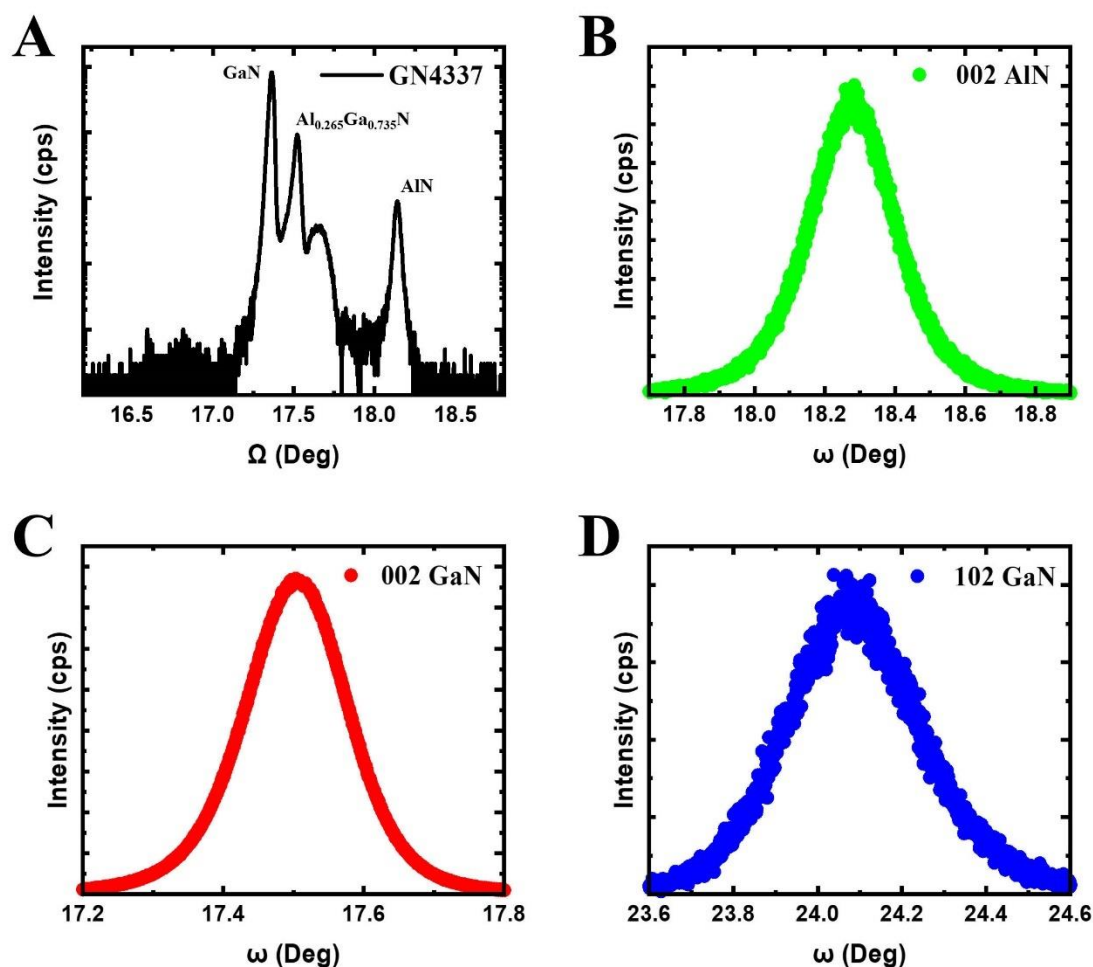


Figure 5-10 XRD results of sample GN4337: (A) ω - 2θ scan, the important peaks are labelled; XRD rocking curves of (B) (002) AlN, (C) (002) GaN, and (D) (102) GaN.

Figure 5-10 illustrates the XRD characterisation results of sample GN4337. The ω - 2θ scan (Figure 5-10A) clearly displays distinct peaks corresponding to GaN, AlN, and AlGa_N, all of which have been appropriately labelled. Notably, the peak observed between the $\text{Al}_{0.265}\text{Ga}_{0.735}\text{N}$ and AlN peaks corresponds to the $\text{Al}_{0.2}\text{Ga}_{0.8}\text{N}$ barrier layer. Additionally, Figure 5-10B-D presents the XRD rocking curves for (002) AlN, (002) GaN, and (102) GaN, with the corresponding measured FWHM values being 0.2865, 0.1718, and 0.3330, respectively.

Table 5-5 FWHM Values of Sample GN4337; Including (102) AlN, (002) GaN and (102) GaN.

Sample	002 AlN FWHM (deg)	002 GaN FWHM (deg)	102 GaN FWHM (deg)
GN4337	0.2865	0.1718	0.3330

The screw dislocation density (D_{screw}) and edge dislocation density (D_{edge}) in the GaN layer can be approximately calculated based on the FWHM values of (002) and (102) GaN, according to the following equations [33, 34]:

$$D_{screw} = \frac{\beta_{(0002)}^2}{4.35b_{screw}^2} \quad (5.1)$$

$$D_{edge} = \frac{\beta_{(10\bar{1}2)}^2 - \beta_{(0002)}^2}{4.35b_{edge}^2} \quad (5.2)$$

In both equations, the $\beta_{(0002)}$ and $\beta_{(10\bar{1}2)}$ denote the FWHM values in radians for the symmetric (0002) and asymmetric (10 $\bar{1}$ 2) scans, respectively. The lengths of the Burgers vectors for screw dislocations b_{screw} and edge dislocations b_{edge} are 0.5185 nm and 0.3189 nm, respectively.

Therefore, the screw and edge dislocation densities for sample GN4337 can be calculated:

$$D_{GN4337\ screw} = \frac{\left(\frac{0.1718\pi}{180}\right)^2}{4.35(0.5185nm)^2} = 7.7 \times 10^8 cm^{-2}$$

$$D_{GN4337\ edge} = \frac{\left(\frac{0.333\pi}{180}\right)^2}{4.35(0.3189nm)^2} = 7.6 \times 10^9 cm^{-2}$$

Table 5-6 FWHM values and corresponding calculated screw and edge dislocation densities for the (002) and (102) GaN reflections in samples GN4337.

Sample	Substrate	002 GaN FWHM (deg)	102 GaN FWHM (deg)	Screw Defects (cm ⁻²)	Edge Defects (cm ⁻²)
GN4337	Silicon	0.1718	0.3330	7.7×10 ⁸	7.6×10 ⁹

To better determine and observe the extent of dislocations present in the sample, the SEM Electron Channelling Contrast Imaging (ECCI) analysis was conducted [35, 36]. Figure 5-11 illustrates the electron channelling contrast image of the surface of sample GN4377.

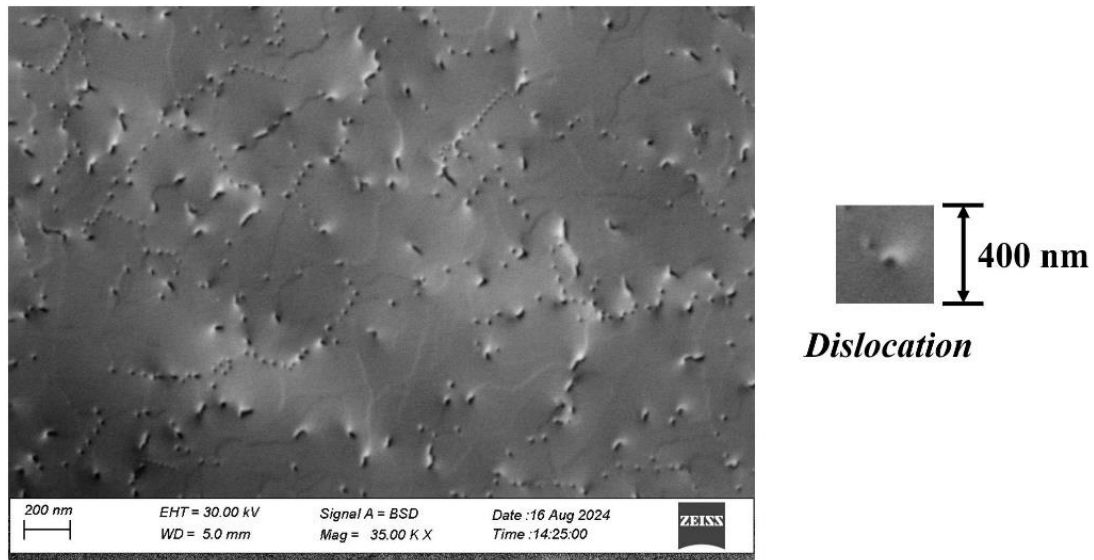


Figure 5-11 Electron channelling contrast image of GN4337. The image shows dislocations (spots with black-white contrast) and atomic steps (lines).

The ECCI image demonstrates a high density of dislocations and prominent step structures on the sample surface, which is consistent with the relatively poor FWHM values determined by the XRD rocking curve. The counted threading dislocation density (TD density) according to the ECCI image is $6.13 \times 10^9 \text{ cm}^{-2}$, which indicates that the crystal quality of the sample is not ideal.

To further assess the overall quality of the HEMT structure, a standard fabrication process for GaN-HEMT was carried out on the sample GN4337. The process as shown in the Figure 5-12. First, the active region of the HEMT will be defined by ICP etching. Subsequently, a metal stack of Ti/Al/Ti/Au was deposited, followed by annealing in a N_2 ambient to form Ohmic contacts for the source and drain. Finally, the Schottky gate of the HEMT was formed by the deposition of Ni/Au.

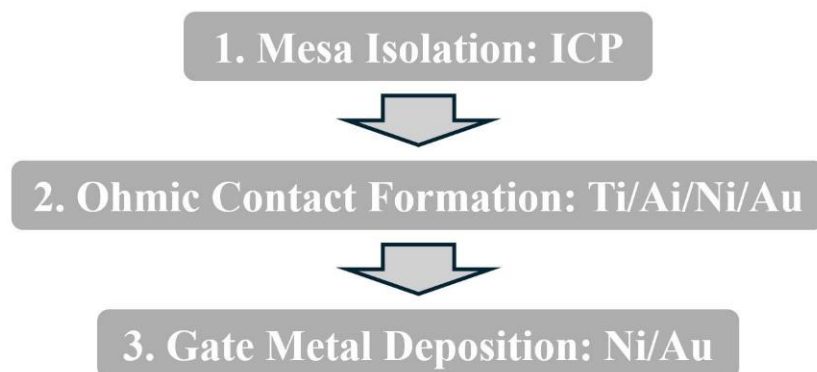


Figure 5-12 Flow chart of standard fabrication process for GaN-HEMT.

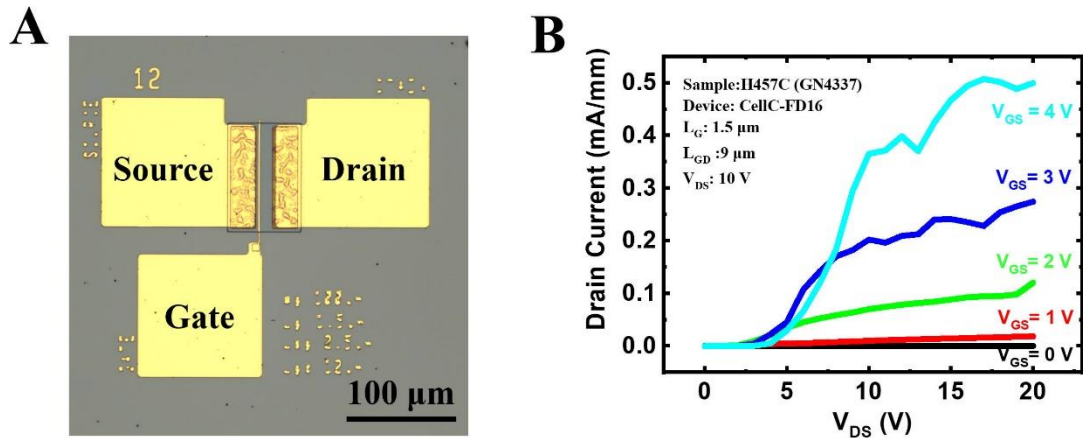


Figure 5-13 (A) Optical image of the HEMT device H457C - (GN4337 after device); (B) Current-voltage (I-V) characteristics as a function of gate voltage.

Figure 5-13 shows the schematic configuration of the HEMT device and the corresponding current-voltage (I-V) curves as a function of drain-source voltage (V_{DS}) under the different gate-source voltages ($V_{GS} = 0-4$ V). The fabricated HEMT device with a gate length (L_G) of 1.5 μm and a gate-to-drain distance (L_{GD}) of 9 μm , the maximum current density observed at $V_{GS} = 4$ V and $V_{DS} = 17$ V was approximately 0.5 mA/mm. This result is significantly lower than the reported results for current HEMTs on Si research [20, 37]. This extremely poor HEMT performance can be attributed to the high dislocation density in the HEMT epi-structure, which exerts a considerable impact on the functionality of the HEMT.

Summary

This section presents a basic AlGaIn/GaN HEMT structure with an AlN interlayer on a (111) Si substrate and provides an analysis of the epitaxial layer quality and device performance. The cross-sectional SEM images of the sample demonstrate the presence of distinct epitaxial layer structures with smooth interfaces. However, XRD analysis shows high FWHM values, which suggest poor crystal quality and a high dislocation density. This finding is corroborated by the ECCI images, which display a high density of dislocations and step structures. The I-V characteristics of the fabricated HEMT also demonstrate suboptimal performance, falling short of the performance reported for Si-based HEMTs. This discrepancy is likely linked to the high dislocation density within the sample, which highlights the necessity for further optimisation of the growth process to improve device quality.

5.5 Conclusions

In this chapter, both InGaN/GaN MQW-based LEDs and AlGaIn/GaN-based HEMTs were grown on crack-free GaN-on-Si templates. For the LED structure, planar InGaN/GaN MQW LEDs were grown under identical conditions on both sapphire and (111) Si substrates, and the differences in epitaxial growth and optical properties due to the different substrates were comparatively analysed. The study revealed that the emission wavelength of MQWs grown on GaN-on-Si templates was significantly longer than that of MQWs grown on GaN-on-sapphire templates. Additionally, the corresponding XRD ω - 2θ measurements and simulated fitting curves confirmed that, under the same growth conditions, the InGaN/GaN MQWs grown on Si substrates exhibited a higher indium content and faster growth rates compared to those grown on sapphire substrates.

Furthermore, the influence of utilising N₂ instead of NH₃ as the ambient gas during the final cooling stage on the optical properties of InGaN/GaN MQWs was investigated. The results showed that under N₂ cooling conditions, the InGaN/GaN MQWs grown on Si substrates exhibited a higher indium content and longer emission wavelengths than those cooled in an NH₃ atmosphere. However, this phenomenon was not observed in MQWs grown on sapphire substrates.

Finally, an AlGaIn/GaN HEMT structure grown on (111) Si was also fabricated and characterised. The results indicated that the performance of this HEMT was significantly inferior to that of previously reported HEMTs on silicon, which is likely due to the poor overall crystal quality and high dislocation density in the epitaxial layers of the HEMT.

Reference

- [1] U. K. Mishra, L. Shen, T. E. Kazior, and Y.-F. Wu, "GaN-based RF power devices and amplifiers," *Proceedings of the IEEE*, vol. 96, no. 2, pp. 287-305, 2008.
- [2] M. Ishida, T. Ueda, T. Tanaka, and D. Ueda, "GaN on Si technologies for power switching devices," *IEEE Transactions on Electron Devices*, vol. 60, no. 10, pp. 3053-3059, 2013.
- [3] J. Millan, P. Godignon, X. Perpiñà, A. Pérez-Tomás, and J. Rebollo, "A survey of wide bandgap power semiconductor devices," *IEEE transactions on Power Electronics*, vol. 29, no. 5, pp. 2155-2163, 2013.
- [4] M. Kuzuhara and H. Tokuda, "Low-loss and high-voltage III-nitride transistors for power switching applications," *IEEE Transactions on Electron Devices*, vol. 62, no. 2, pp. 405-413, 2014.
- [5] S. Nakamura and M. R. Krames, "History of gallium–nitride-based light-emitting diodes for illumination," *Proceedings of the IEEE*, vol. 101, no. 10, pp. 2211-2220, 2013.
- [6] E. Bahat-Treidel, *GaN-based HEMTs for high voltage operation: design, technology and characterization*. Cuvillier Verlag, 2012.
- [7] S. Chowdhury, B. L. Swenson, M. H. Wong, and U. K. Mishra, "Current status and scope of gallium nitride-based vertical transistors for high-power electronics application," *Semiconductor Science and Technology*, vol. 28, no. 7, p. 074014, 2013.
- [8] D. Kahng, *Silicon integrated circuits*. Academic press, 2013.
- [9] S. Watanabe *et al.*, "Internal quantum efficiency of highly-efficient In_xGa_{1-x}N-based near-ultraviolet light-emitting diodes," *Applied Physics Letters*, vol. 83, no. 24, pp. 4906-4908, 2003.
- [10] H. Zhao, G. Liu, J. Zhang, J. D. Poplawsky, V. Dierolf, and N. Tansu, "Approaches for high internal quantum efficiency green InGa_N light-emitting diodes with large overlap quantum wells," *Optics Express*, vol. 19, no. 104, pp. A991-A1007, 2011.
- [11] H. Zhao, G. Liu, J. Zhang, R. A. Arif, and N. Tansu, "Analysis of internal quantum efficiency and current injection efficiency in III-nitride light-emitting diodes," *Journal of Display Technology*, vol. 9, no. 4, pp. 212-225, 2013.
- [12] M. Aumer, S. LeBoeuf, S. Bedair, M. Smith, J. Lin, and H. Jiang, "Effects of tensile and compressive strain on the luminescence properties of AlInGa_N/InGa_N quantum well structures," *Applied Physics Letters*, vol. 77, no. 6, pp. 821-823, 2000.
- [13] S. Pereira *et al.*, "Strain and composition distributions in wurtzite InGa_N/Ga_N layers

- extracted from x-ray reciprocal space mapping," *Applied Physics Letters*, vol. 80, no. 21, pp. 3913-3915, 2002.
- [14] D. Iida, Z. Zhuang, P. Kirilenko, M. Velazquez-Rizo, M. A. Najmi, and K. Ohkawa, "633-nm InGaN-based red LEDs grown on thick underlying GaN layers with reduced in-plane residual stress," *Applied Physics Letters*, vol. 116, no. 16, 2020.
- [15] W. Paszkowicz, "X-ray powder diffraction data for indium nitride," *Powder Diffraction*, vol. 14, no. 4, pp. 258-260, 1999.
- [16] A. Dadgar *et al.*, "Anisotropic bow and plastic deformation of GaN on silicon," *Journal of Crystal Growth*, vol. 370, pp. 278-281, 2013.
- [17] F. Semond, "Epitaxial challenges of GaN on silicon," *Mrs Bulletin*, vol. 40, no. 5, pp. 412-417, 2015.
- [18] S. Chang, L. Lung Wei, T. Tung Luong, C. Chang, and L. Chang, "Threading dislocation reduction in three-dimensionally grown GaN islands on Si (111) substrate with AlN/AlGaIn buffer layers," *Journal of Applied Physics*, vol. 122, no. 10, 2017.
- [19] P. Kharei, A. Baidya, N. P. Maity, and R. Maity, "An insight to current collapse in GaN HEMT and suppressing techniques," *Engineering Research Express*, vol. 5, no. 1, p. 012001, 2023.
- [20] Y. Cai *et al.*, "Strain Analysis of GaN HEMTs on (111) Silicon with Two Transitional Al(x)Ga(1-x)N Layers," (in eng), *Materials (Basel)*, vol. 11, no. 10, Oct 13 2018, doi: 10.3390/ma11101968.
- [21] M. Moram and M. Vickers, "X-ray diffraction of III-nitrides," *Reports on Progress in Physics*, vol. 72, no. 3, p. 036502, 2009.
- [22] T. Lan *et al.*, "Effect of strain modification on crystallinity and luminescence of InGaIn/GaN multiple quantum wells grown by MOCVD," *Applied Physics A*, vol. 124, pp. 1-8, 2018.
- [23] J. Allegre *et al.*, "Optical properties of InGaIn/GaN multiple quantum wells," in *Materials Science Forum*, 1998, vol. 264.
- [24] Y. Tong-Jun *et al.*, "Strain effect on photoluminescences from InGaIn MQWs with different barriers grown by MOCVD," *Chinese Physics Letters*, vol. 24, no. 5, p. 1365, 2007.
- [25] F. Zeng *et al.*, "A comprehensive review of recent progress on GaN high electron mobility transistors: Devices, fabrication and reliability," *Electronics*, vol. 7, no. 12, p. 377, 2018.
- [26] R. Yan, J. Xi, and L. He, "A 2–10 MHz GaN HEMTs half-bridge driver with bandgap

- reference comparator clamping and dual level shifters for automotive applications," *IEEE Transactions on Industrial Electronics*, vol. 67, no. 2, pp. 1446-1454, 2019.
- [27] M. Mohd Razip Wee, M. M. Jaafar, M. S. Faiz, C. F. Dee, and B. Yeop Majlis, "A Theoretical Study of Surface Mode Propagation with a Guiding Layer of GaN/Sapphire Hetero-Structure in Liquid Medium," *Biosensors*, vol. 8, no. 4, p. 124, 2018.
- [28] Y.-F. Wu *et al.*, "30-W/mm GaN HEMTs by field plate optimization," *IEEE Electron Device Letters*, vol. 25, no. 3, pp. 117-119, 2004.
- [29] S. Çörekçi, M. Öztürk, A. Bengi, M. Çakmak, S. Özçelik, and E. Özbay, "Characterization of an AlN buffer layer and a thick-GaN layer grown on sapphire substrate by MOCVD," *Journal of materials science*, vol. 46, pp. 1606-1612, 2011.
- [30] L. Zhang *et al.*, "AlGaN/GaN/InGaN/GaN DH-HEMTs with GaN channel layer grown at high temperature," *The European Physical Journal-Applied Physics*, vol. 62, no. 2, p. 20105, 2013.
- [31] S. Joblot, Y. Cordier, F. Semond, P. Lorenzini, S. Chenot, and J. Massies, "AlGaN/GaN HEMTs on (001) silicon substrates," *Electronics Letters*, vol. 42, no. 2, pp. 117-118, 2006.
- [32] J.-C. Gerbedoen *et al.*, "AlGaN/GaN HEMTs on (001) silicon substrate with power density performance of 2.9 W/mm at 10 GHz," *IEEE Transactions on Electron Devices*, vol. 57, no. 7, pp. 1497-1503, 2010.
- [33] H.-P. Lee, J. Perozek, L. Rosario, and C. Bayram, "Investigation of AlGaN/GaN high electron mobility transistor structures on 200-mm silicon (111) substrates employing different buffer layer configurations," *Scientific Reports*, vol. 6, no. 1, p. 37588, 2016.
- [34] T. Metzger *et al.*, "Defect structure of epitaxial GaN films determined by transmission electron microscopy and triple-axis X-ray diffractometry," *Philosophical Magazine A*, vol. 77, no. 4, pp. 1013-1025, 1998.
- [35] Y. Picard *et al.*, "Nondestructive analysis of threading dislocations in GaN by electron channeling contrast imaging," *Applied Physics Letters*, vol. 91, no. 9, 2007.
- [36] T. J. Ruggles, J. I. Deitz, A. A. Allerman, C. B. Carter, and J. R. Michael, "Identification of star defects in gallium nitride with HREBSD and ECCI," *Microscopy and Microanalysis*, vol. 27, no. 2, pp. 257-265, 2021.
- [37] J. Cheng *et al.*, "Growth of high quality and uniformity AlGaIn/GaN heterostructures on Si substrates using a single AlGaIn layer with low Al composition," *Scientific Reports*, vol. 6, no. 1, p. 23020, 2016.

Chapter 6 Comparative Study of GaN-Based micro-LEDs on Sapphire and Silicon by Direct Epitaxial Approach

This chapter presents a direct epitaxial approach for the fabrication of III-nitrides-based micro light-emitting diodes (μ LEDs) using MOCVD. The μ LEDs obtained by this method were investigated from different perspectives. This approach has been successfully applied to grow μ LEDs on both (111) silicon and (0001) sapphire substrates. Unlike conventional μ LED fabrication techniques, the approach presented in this chapter can avoid the sidewall damage caused by dry-etching process, thereby effectively enhancing the optical efficiency of the μ LEDs produced.

In this chapter, the direct selective overgrowth approach is described in detail and obtained the μ LED arrays on patterned templated using this direct selective epitaxial method. Furthermore, the influence of varying sizes and fill factor on identical structured μ LEDs, the impact of substrates on μ LEDs, and the effect of incorporating a proportion of hydrogen in the QB growth of μ LEDs have all been subjected to investigation. All samples presented in this chapter were grown using a MOCVD system.

6.1 Introduction

When the dimensions of an LED chip are reduced to a scale of tens or even just a few micrometres, it is referred to as a micro-LED chip. The use of micro-displays based on RGB (red, green, blue) micro-LED chips offers several advantages over traditional LEDs, including a compact size, high resolution, high brightness, fast response time, and low power consumption. Therefore, μ LEDs are particularly well-suited for small displays that require high resolution and brightness, which makes them ideal for a number of applications, including such as head-mounted displays, augmented reality (AR), high-speed visible light communication (VLC), micro-projectors, optogenetics, and wearable electronics. It is widely acknowledged that μ LEDs represent a significant technological advance, offering exceptional optical and electrical properties that are set to transform the next generation of display technologies.

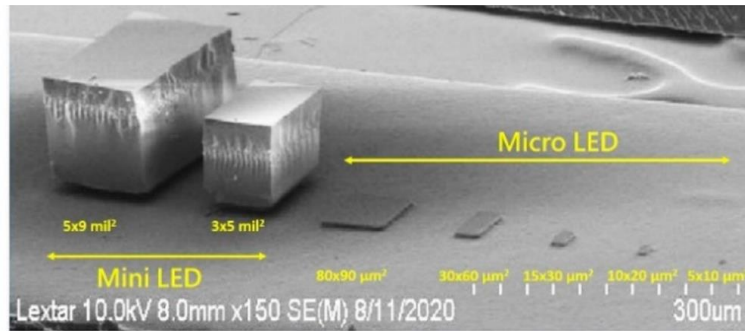


Figure 6-1 SEM image of the size comparison between Mini LED and Micro LED chips [1].

In comparison to organic light-emitting diodes (OLEDs) and liquid crystal displays (LCDs), micro-LED technology presents a number of distinctive advantages. In contrast to the "passive" nature of LCD technology, micro-LEDs are characterised by a self-emissive property, which enables them to offer high resolution, high efficiency and high contrast [2]. In the other hand, to achieve the requisite high brightness output from colour filters, OLED displays must operate at high injection currents. While this strong current drive meets the brightness requirements, it also introduces several issues, including reduced efficiency, heat generation, shorter lifespan, and colour unevenness. In contrast, μ LEDs are capable of delivering high brightness without compromising reliability or longevity due to their unique characteristics [2-5].

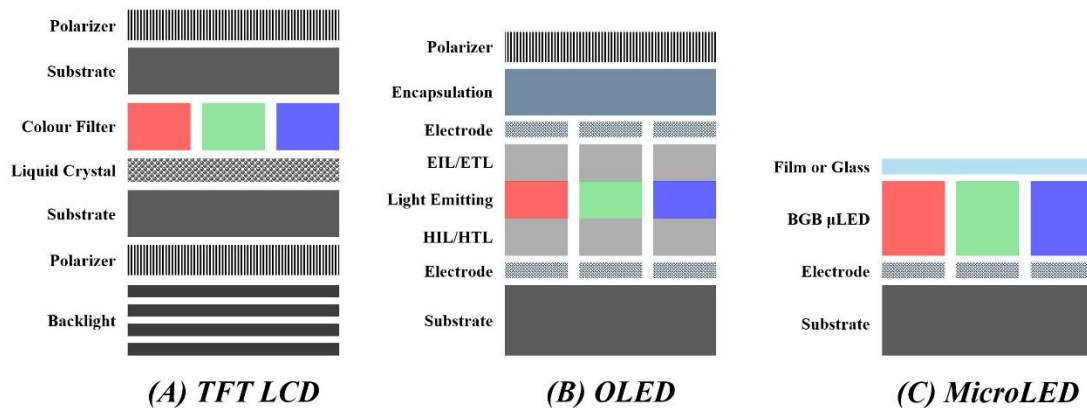


Figure 6-2 Comparative schematic cross-sections of display technologies: (A) TFT LCD, (B) OLED, and (C) MicroLED, illustrating the key layers and components in each technology.

The fabrication process of micro-LEDs still presents a number of significant challenges due to their extremely small size. Currently, the most prevalent fabrication process for μ LEDs is the application of photolithography and dry etching process to an as-grown planar LED wafer to obtain the desired

μ LED wafer [6, 7]. It is important to consider that the dry etching process inevitably causes sidewall damage, which results in a significant decline in the optical performance of μ LEDs. In case of the larger LEDs ($>100 \mu\text{m}$), this issue is generally negligible due to the small ratio of the damaged area to the light-emitting region. However, as the size of the LED decreases, the severity of this problem increases [7-10]. Atomic Layer Deposition (ALD) technology is an advanced surface passivation method that can mitigate sidewall damage caused by dry etching in the μ LED manufacturing process, but the extent of improvement remains limited [11]. Therefore, it is essential to modify the conventional μ LED fabrication process and optimise epitaxial growth in order to overcome the challenges in the achievement of extremely small μ LEDs. Based on this background, our experimental group has developed a novel method for fabricating μ LEDs by depositing LED structures on pre-patterned templates through selective epitaxy. This approach confines the epitaxial overgrowth to the pre-patterned micro-holes, thereby enabling the direct formation of μ LEDs without any dry etching process and avoiding potential damage caused by etching [4, 12, 13].

This chapter first introduces this novel method for achieving μ LEDs through direct epitaxial growth, followed by a series of comparative studies on the μ LED samples produced using this approach. The studies include the initial n-GaN layer and the final p-GaN layer of μ LEDs, followed by a comparative analysis of the impact of different substrates on the optical performance of μ LEDs. Furthermore, the impact of the fill factor of selective area patterns and the dimensions of μ LEDs on growth and optical performance was also investigated. Finally, the last section presents a comparative analysis of the differences between MQWs of μ LEDs grown using H_2 -doped QB methods (in which the appropriate amount of H_2 was introduced during the QB growth phase) and MQW structures grown in an N_2 atmosphere.

6.2 Direct Epitaxial Overgrowth Method for III-Nitrides μ LEDs on a Patterned Template

The μ LEDs employed in this project were all obtained through the implementation of a novel confined selective epitaxial overgrowth methodology on a patterned GaN template, which was developed by our research team [4, 12, 13]. This confined selective epitaxy method is distinct from recent conventional μ LED fabrication methods in that epitaxial deposition only occurs within pre-designed patterned silica micro-holes. By varying the etch depth, the shape of the template and the structure of the deposited μ LEDs, the μ LED array wafers with different requirements and structures can be realised, allowing for the production of μ LED that align with specific design specifications. The dry etching process is a fundamental step in conventional fabrication methods for the creation of μ LED arrays. However, the dry etching process inevitably results in sidewall damage in μ LEDs, and the percentage of sidewall damage increases significantly as the size of μ LEDs decreases, resulting in a significant degradation of optical performance. In contrast, the confined selective epitaxy method used in this project successfully avoids the essential dry etching process in the conventional μ LED fabrication method, which addresses the issue of optical efficiency degradation due to sidewall damage. Furthermore, it reduces the number of process steps associated with dry etching, simplifying the manufacturing process while lowering the generation cost.

Figure 6.1 depicts the schematic of preparation of the μ LED patterned template and the growth of μ LED by the confined selective epitaxial overgrowth method on a patterned template. Firstly, the standard GaN templates with sufficient GaN thickness need to be prepared by MOCVD on either a sapphire substrate or a Si substrate (Step A). For sapphire substrates, GaN layers are typically prepared using the traditional two-step method, whereas GaN layers on Si substrates are prepared using the optimised GaN-on-Si growth method described in Chapter 5. Once a standard GaN template had been obtained, a SiO₂ dielectric film with a thickness of 500 nm was deposited on the surface of GaN by PECVD (Step B). Subsequently, the templates with the deposited SiO₂ layer were patterned by photolithography, and then the SiO₂ film was selectively etched using standard inductively coupled plasma (ICP) techniques until the top surface of the GaN layer was exposed (Step C). In this project, all patterned templates were subjected to etching ICP at a chamber pressure

of 25 mTorr using a gas mixture of 20 sccm of CHF_3 and 30 sccm of Ar, with the etching power was set at 200 W. Upon completion of the process, the standard μLED patterned templates are prepared for the subsequent confined selective overgrowth. It is important to note that the fabricated μLED templates cannot be directly placed into the MOCVD for overgrowth. Prior to this, a meticulous cleaning treatment must be undertaken to remove any organic matter, photoresist, etching by-products and other contaminants that may remain on the surface. This is to avoid the impact of residues on the growth environment in the MOCVD reactor room and to achieve high-quality epitaxial growth. At last, the cleaned μLED templates are adequately prepared for the subsequent overgrowth by MOCVD (Step D).

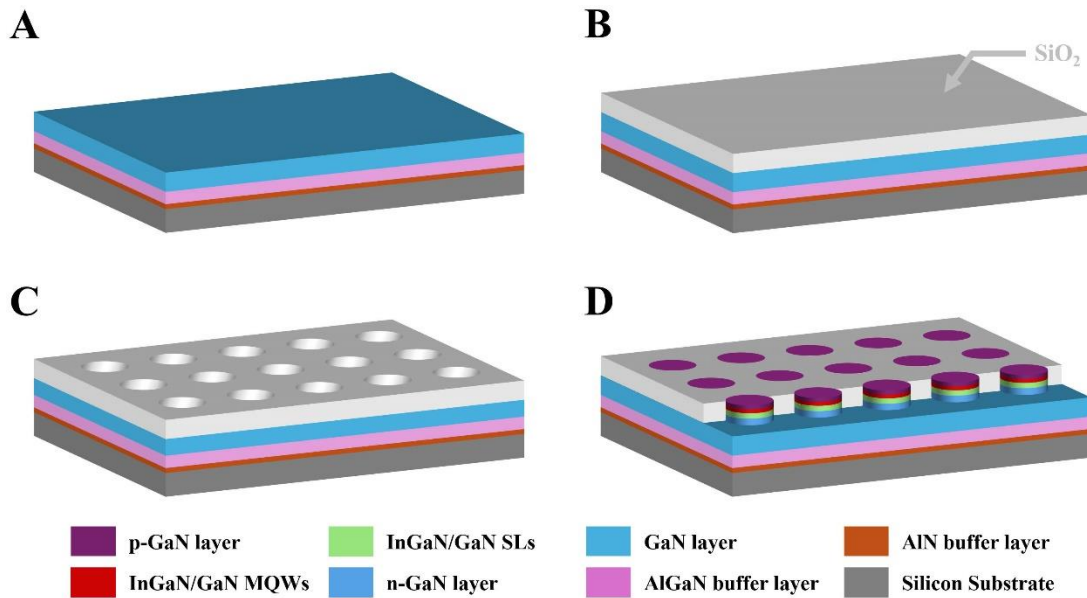


Figure 6-3 Schematic illustration of the preparation process for the μLED patterned template and the confined selective epitaxial overgrowth of μLED s on the patterned template. (A) Growth of a standard GaN layer on the substrate; (B) Deposition of the SiO_2 layer; (C) Photolithography and ICP etching; and (D) Selective epitaxial overgrowth of μLED s.

In comparison to the cleaning treatment of planar overgrown templates, the cleaning treatment applied to patterned templates will be slightly different and require a greater investment of time. This is due to the necessity of removing as much residual impurity as possible, particularly within the micro-holes. The application of HF will no longer be employed in this approach; instead, the KOH-PEC etching will be applied to treat the patterned templates. The detailed cleaning treatment for templated templates is provided below:

- i. Chemical solvent cleaning:** The patterned template was sequentially immersed in the following solvents in a beaker: n-butyl acetate, acetone, and IPA. Each beaker was then placed in an ultrasonic water bath for a period of 5 minutes each. Following this, the template was rinsed with DI water to remove any residual solvent.
- ii. PEC wet etching:** The patterned template was immersed in a beaker containing a 20% KOH solution and then the beaker was placed in a customised PEC unit and irradiated under a xenon lamp for 40 minutes. Thereafter, the template was rinsed with DI water to eliminate any residual solvent.
- iii. HCl neutralization treatment:** The patterned template was immersed in a 40% HCl solution for 5 minutes to neutralise and remove KOH residues and other surface contaminants. The templates were then rinsed in flowing DI water to remove the residue of the HCl solution.
- iv. Drying and baking:** The water droplets were blown off from the template by a dry nitrogen spray gun, and then baked in an oven at 100°C for 5 minutes to remove any residual moisture.

6.3 Direct Epitaxial Overgrowth to Achieving InGaN/GaN MQWs-Based μ LEDs on a Patterned Template

This section examines the growth characteristics and optical performance of InGaN/GaN MQWs-based μ LEDs grown on patterned templates using a direct epitaxial method. Given the distinctive challenges associated with μ LEDs in comparison to planar LEDs, a comprehensive investigation of the growth factors is essential to optimise the growth of μ LEDs. This study focuses on understanding the impact of key growth parameters, including the initial n-GaN layer and the final p-GaN layer, on the optical properties of μ LEDs. In particular, we investigate the impact of these layers on the defect density, surface morphology, and PL properties of μ LEDs. Furthermore, the performance of μ LEDs grown on different substrates (sapphire and silicon) is evaluated to elucidate the role of substrate choice on emission wavelength and intensity. The investigation also considers the impact of μ LED dimensions and fill factor on growth dynamics and device performance. The findings from this study will contribute to providing insights into the optimal conditions for the development of high-quality μ LEDs.

6.3.1 Investigation of the Initial n-GaN Layer in InGaN/GaN μ LEDs on Patterned Templates

In GaN-based LED devices, the structure comprising the n-GaN layer, quantum well structure, and upper p-GaN layer is typical. Theoretically, the n-GaN layer provides electrons, while the p-GaN layer provides holes. These two carriers then recombine in the quantum well structure to produce photons, resulting in the light-emitting function of the LED. Therefore, a sufficiently thick n-GaN layer needs to be deposited on the top of the GaN template when preparing it prior to the overgrowth of GaN-based LED structures. Furthermore, before overgrowing the MQW structure on the patterned template, a thin n-GaN layer must be deposited on top of the original n-GaN layer, serving as the initial layer for MQW growth. The objective of this section is to investigate the impact of the initial n-GaN layer on the optical properties of InGaN/GaN MQWs-based μ LEDs grown on patterned templates. It is hoped that this investigation will contribute to the further optimisation of the process for μ LED growth.

Experiment design

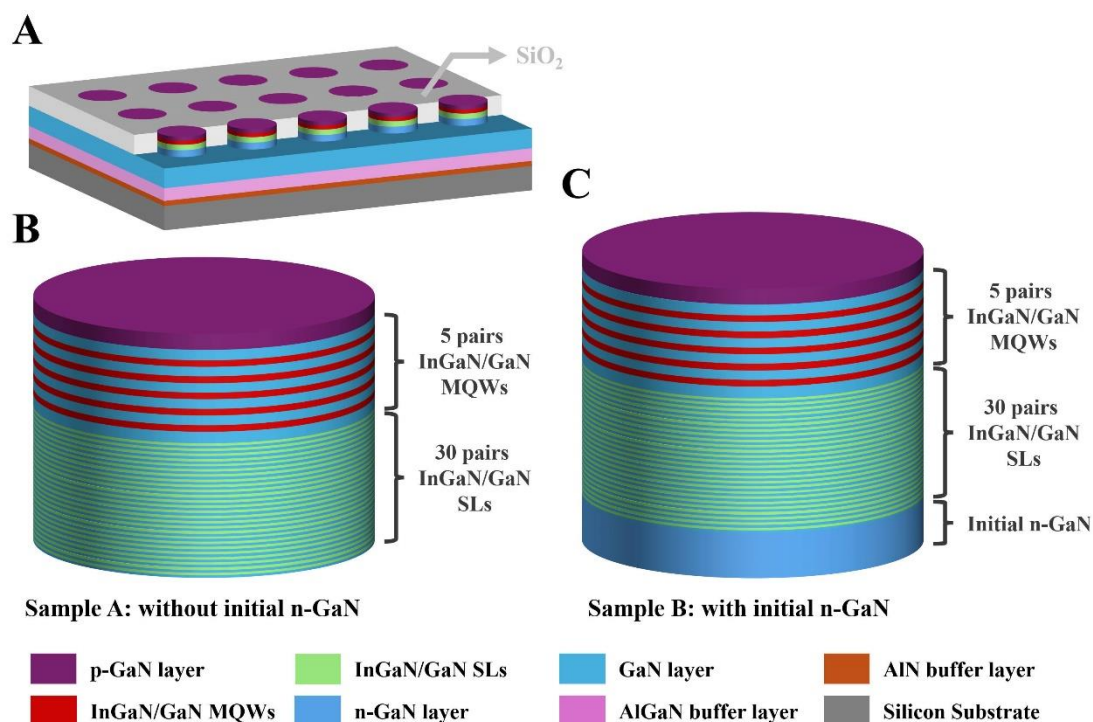


Figure 6-4 Structure schematic of (A) patterned template after overgrowth; (B) the single μ LED unit without the initial n-GaN and (C) the single μ LED unit with the initial n-GaN.

This experiment will involve the growth of two samples, designated as Sample A and Sample B, both prepared on GaN-on-Si μ LED patterned templates. For Sample A, the μ LED will be grown without an initial n-GaN layer, whereas Sample B will include an initial n-GaN layer of approximately 60 nm. The growth conditions for the subsequent SLs, MQWs, and the upper p-GaN layer will be identical for both samples, with the only difference being the presence of the initial n-GaN layer. Figure 6-4 presents the structural schematic of the patterned template after overgrowth (Figure 6-4A), along with the μ LED units of Sample A (Figure 6-4B) and Sample B (Figure 6-4C).

Results and Discussion

Figure 3 shows the Room-Temperature PL spectra of the two samples, which clearly indicate that Sample B (with initial n-GaN) exhibits a relatively strong luminous intensity in green emission at 500 nm and a wider spectral range. In contrast, the Sample A, which without initial n-GaN, does not show the distinct PL peak from MQW structure. Furthermore, both samples exhibit a higher peak at approximately 400 nm, which can be attributed to the SLs structure.

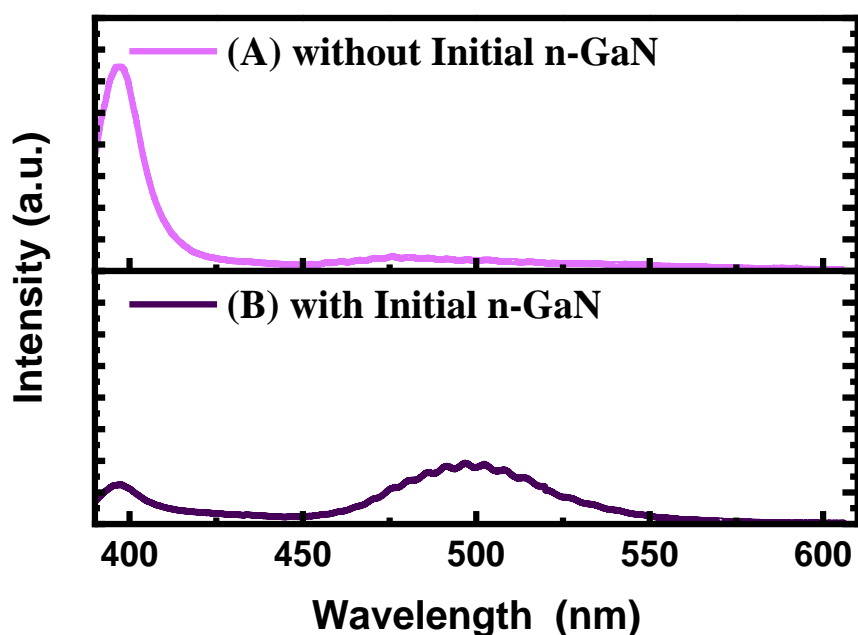


Figure 6-5 the standard room-temperature PL spectra of Sample A (without initial n-GaN layer) and the Sample B (with initial n-GaN layer).

Summary

The initial n-GaN layer has been shown to significantly enhance the optical performance of the μ LED during the overgrowth process. This is likely attributable to the increased crystal defect density that occurs when the μ LED structure is directly overgrown on the template, which in turn adverse effects the final optical performance. Therefore, the introduction of the initial n-GaN layer can effectively reduce the optical performance degradation caused by the increase in crystal defect density when the μ LED is grown directly on the patterned template.

6.3.2 Effect of Final p-GaN Growth on the Optical Properties of InGaN/GaN μ LEDs on Patterned Templates

The uppermost p-GaN layer plays a pivotal role in the light-emitting structure of a GaN-based LED. The quality of the p-GaN layer can influence not only the optical properties of the device but also significantly impact carrier distribution and recombination. In MOCVD deposition, a smooth and uniform crystalline surface is indicative of high crystal quality, which is the desired outcome during

the growth process. During the deposition of planar GaN-based LED structures, growth conditions are intentionally optimized to achieve high crystal quality. Based on previous experience, GaN materials typically exhibit better crystal quality and surface morphology when grown at relatively high temperatures and slower growth rates [14-16]. However, in the deposition of μ LEDs, as the dimensions decrease, each material layer also becomes significantly thinner, making the deposition process more sensitive to growth conditions. In the growth sequence, the p-GaN layer is deposited after the MQWs. Typically, the growth temperature for the p-GaN layer is significantly higher than that for the InGaN QWs to achieve higher quality. However, MQWs are particularly sensitive to high temperatures, and this sensitivity is likely exacerbated in the case of μ LEDs [17-22]. Therefore, this section will investigate whether the growth of the final p-GaN layer affects the photoluminescence characteristics of InGaN/GaN MQWs-based μ LEDs.

Experiment design

Table 6-1 Growth conditions of p-GaN layers for three samples; including growth temperature, reactor pressure, TMG and NH₃ flow rate.

Sample	Temperature (°C)	Pressure (mbar)	TMG (sccm)	NH ₃ (sccm)
A (GN4115)	1080	100	20	5600
B (GN4116)	1080	100	10	5600
C (GN4117)	1080	100	7.5	5600

In this experiment, three μ LED samples (GN4115, GN4116, GN4117) with different p-GaN layer growth rates were grown on patterned templates, while keeping the p-GaN growth temperature constant. The variation in growth rates was achieved by adjusting the TMG flow rates under the same growth temperature, allowing for the deposition of p-GaN layers with different surface roughness [14]. Table 6-1 outlines the growth conditions of the p-GaN layer for three samples, including growth temperature, reactor pressure, and the flow rate of TMG and NH₃. Furthermore, to ensure consistent thickness of the final p-GaN layer, the reflectance curve should be monitored in real-time during growth, allowing precise control of the growth duration.

Results and Discussion

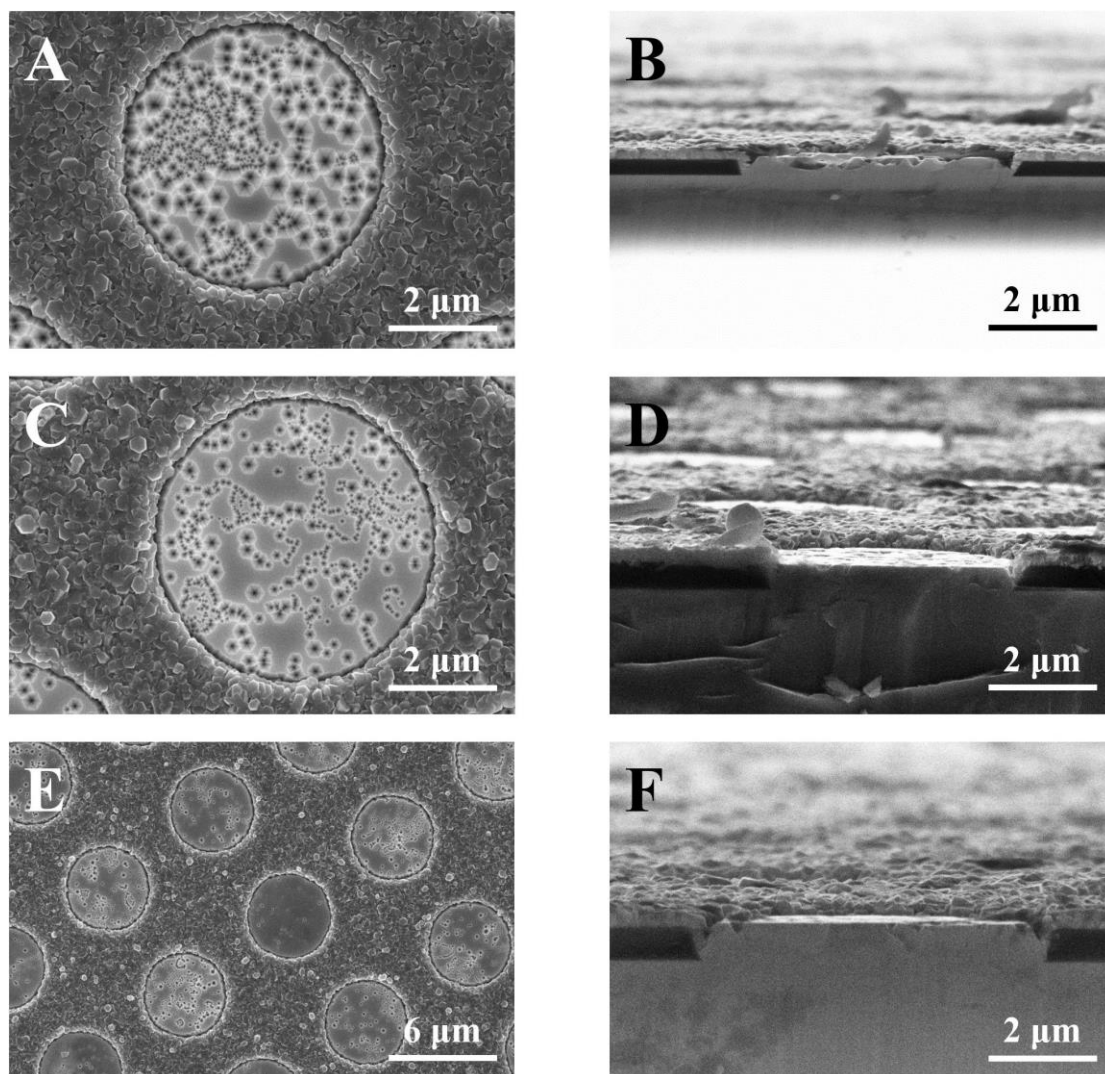


Figure 6-6 SEM images of GN4115: (A) top view and (B) cross-section; GN4116: (C) top view and (D) cross-section; and GN4117: (E) top view and (F) cross-section.

Figure 6-6 shows the top views and cross-sectional SEM images of the three samples. It is clearly observed that GN4115 (Figure 6-6A & B), which was grown using the highest TMG flow rate for p-GaN, displays the most significant surface roughness. In contrast, GN4117 (Figure 6-6E & F) which was grown with the lowest TMG flow rate, exhibits the smoothest surface, while the surface roughness of GN4116 (Figure 6-6C & D) falls between the two. Furthermore, as thicknesses of the p-GaN layers in the three samples are consistent, and the growth times are 450 seconds for GN4115, 910 seconds for GN4116, and 1213 seconds for GN4117, it can be concluded that GN4115 has the fastest p-GaN growth rate, followed by GN4116, with GN4117 having the slowest growth rate.

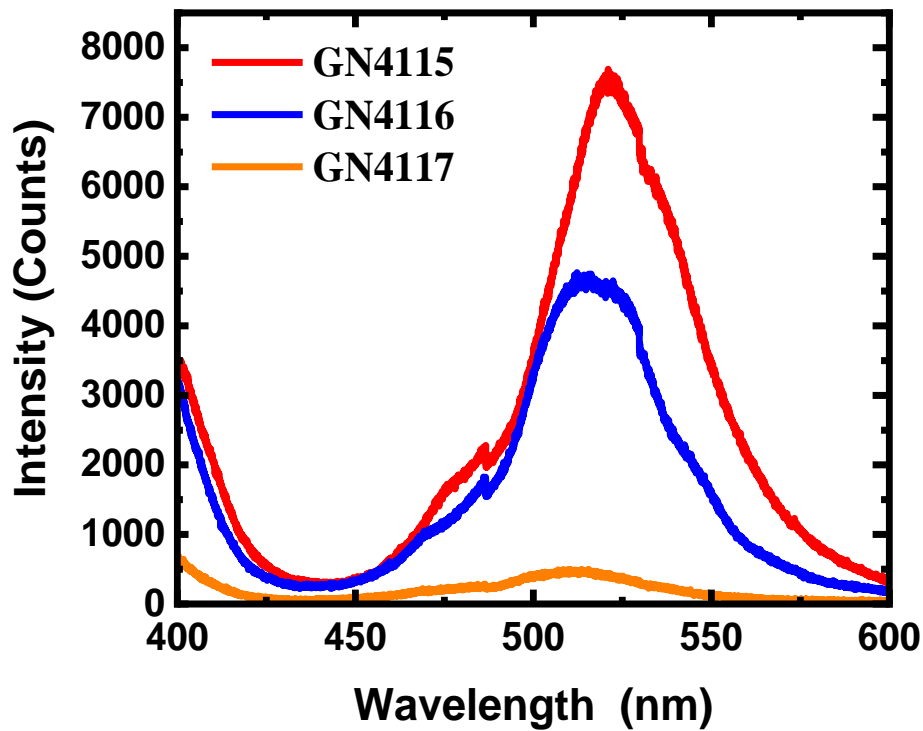


Figure 6-7 the standard room-temperature PL spectra of GN4115, GN4116 and GN4117 with different TMG flow rates for final p-GaN growth.

Figure 6-7 illustrates the standard room-temperature PL spectra of three samples. The emission peak of GN4115 is located at approximately 537 nm and exhibits the highest PL intensity among the three samples. GN4116 shows a second PL intensity with an emission wavelength of around 517 nm, while GN4117 has the lowest PL intensity with an emission wavelength of around 511 nm.

It can be observed that as the roughness of the p-GaN surface increases, the PL intensity strengthens and the emission wavelength red-shifts. This phenomenon may be attributed to an increased growth rate, which reduces the time required to achieve the same p-GaN thickness and thereby mitigates the thermal degradation of the MQWs caused by high-temperature growth of p-GaN over an extended growth time. In this experiment, the temperature differential between the growth of InGaN QB and p-GaN is 175 °C.

Summary

The findings of this study illustrate that variations in TMG flow rates at a consistent growth temperature have a considerable influence on the growth rate of p-GaN. It was observed that the

surface roughness of Mg-doped p-GaN increases with higher growth rates. Moreover, the findings suggest that while faster growth rates can reduce the risk of thermal degradation in MQWs, but it also results in a less uniform p-GaN surface with an increased density of defects, which could negatively affect subsequent device performance. Therefore, it is essential to achieve a balance between achieving a high-quality, smooth p-GaN layer and minimising the thermal degradation of MQWs by optimising both the growth rate and temperature.

6.3.3 Comparative Analysis of 5 μm InGaN/GaN μLEDs on Sapphire and Silicon by Confined Selective Epitaxial Overgrowth

After obtaining the patterned templates for selective regional overgrowth of μLEDs , the next objective was to achieve stable and reproducible growth of μLED structure by direct epitaxy methods. This section presents a comparative study of 5 μm InGaN/GaN MQWs-based μLEDs grown on both (0001) sapphire and (111) silicon substrates using the direct epitaxial overgrowth method. Sapphire serves as a commonly used substrate for the epitaxial GaN layer, and a number of studies have reported the successful preparation of μLEDs on sapphire substrates with excellent performance [23-26]. Sapphire exhibits excellent thermal and chemical stability, and the relatively low lattice mismatch with GaN favourable for the high-quality epitaxial growth of GaN-based materials. On the other hand, despite the large lattice and thermal mismatch between silicon and GaN, silicon represents an attractive alternative due to its cost-effectiveness and established infrastructure within the electronics industry. Furthermore, the confined selective epitaxial overgrowth technique employed in this chapter is designed to avoid sidewall damage resulting from the dry etching process used in conventional μLEDs fabrication. Consequently, the introduction of this technique into the fabrication process of μLEDs may prove beneficial in enhancing the optical performance of μLEDs .

In the previous chapter it was mentioned that the presence of tensile stresses in the GaN-on-Si templates results in a redshift in the wavelength of the obtained LEDs due to the presence of more indium doping than in the case of GaN-on-Sapphire templates under the identical growth conditions. In light of the aforementioned considerations, it is necessary to investigate whether InGaN/GaN

MQWs-based μ LEDs on sapphire and Si substrates exhibit comparable behaviour to that observed in planar LEDs. Furthermore, this study aims to effectively transfer the existing experience of sapphire-based μ LED growth to silicon substrates, thereby providing a valuable reference for the development of high-quality μ LEDs on silicon substrates.

Experiment design

Based on the pursuit of the development of ultra-small μ LED devices and the preceding research conducted by our experimental group on μ LED template shapes [4, 12, 13], a window size of 5 μ m has been selected for the overgrowth, with a circular mask pattern being employed. In this experimental group, the μ LED structures will be grown on two patterned templates designated Sample A and Sample B, with different substrates: (0001) sapphire and (111) Si. The two templates will be identical in terms of their mask pattern and parameters, except for the substrate material. Moreover, all patterned GaN templates employed in this chapter were fabricated from standard GaN-on-Sapphire and GaN-on-Silicon templates.

The prepared patterned templates with SiO₂ masks are initially subjected to the cleaning process described above section to ensure that the templates are completely clean and dry, and then placed treated templates into the MOCVD reactor for the subsequent overgrowth of the μ LED structures. Firstly, the deposition of the n-GaN layer was initiated when the reactor temperature reached 1270 °C in a H₂ atmosphere. The growth of n-GaN was divided into two phases: HP-nGaN and LP-nGaN, with reactor pressures of 233 and 186 mbar, respectively. Subsequently, the reactor temperature was reduced to 995 °C and the carrier gas was fully switched from H₂ to N₂, thereby initiating the growth of 30 pairs of InGaN/GaN superlattices. Subsequently, 5 pairs of InGaN/GaN MQWs structures as active region were grown at temperatures of 905 °C and 1040 °C, respectively. Following the deposition of MQWs, the carrier gases are switched back to H₂, and the reactor temperature is increased to 1080 °C for the growth of final p-GaN. Figure 6-8 illustrates the structure of the SiO₂ patterned template, the template following overgrowth, and the μ LED unit.

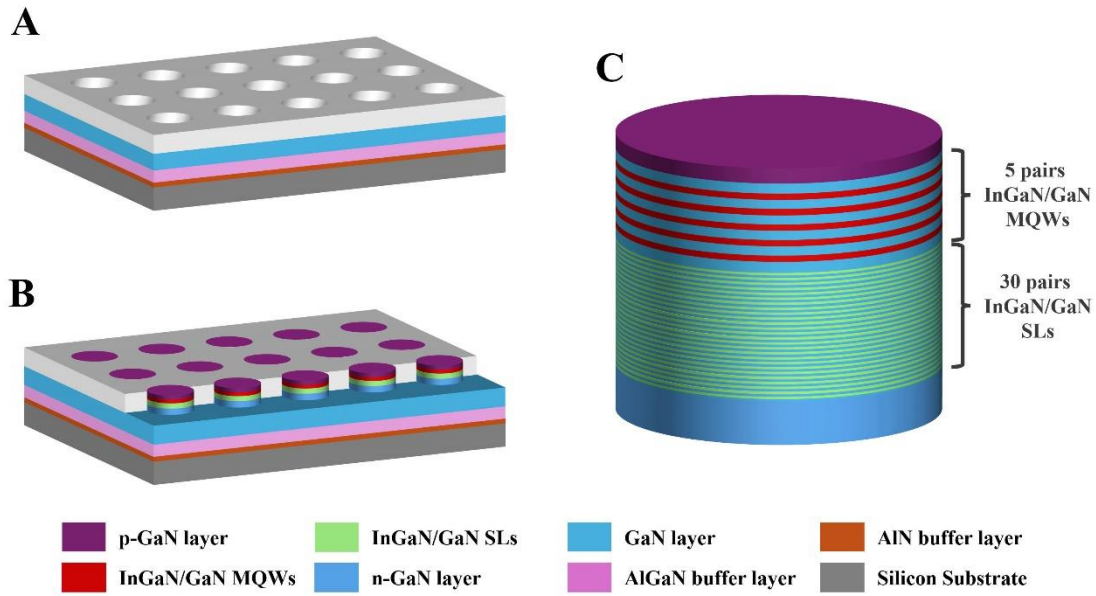


Figure 6-8 Structure schematic of (A) patterned template before overgrowth; (B) overgrown μ LEDs and (C) single μ LED unit with 5 pairs SLs and 30 pairs MQWs.

Results and Discussion

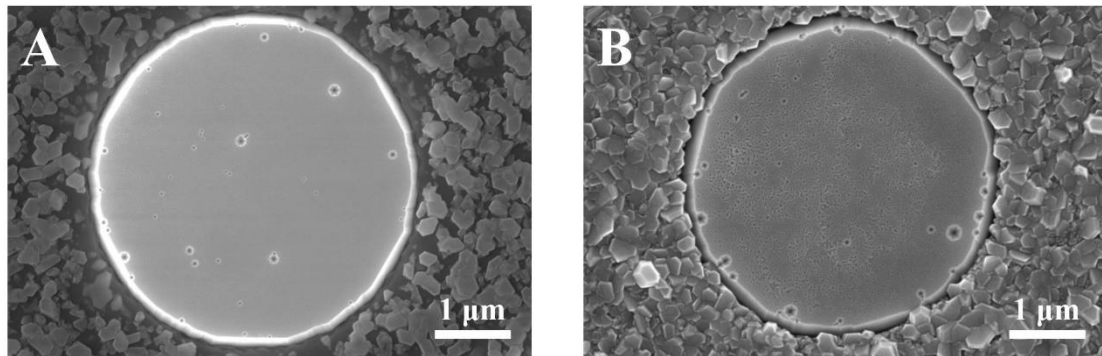


Figure 6-9 Plan view SEM images of (A) Sample A: 5 μ m LEDs on (0001) sapphire and (B) Sample B: 5 μ m LEDs on (111) Si.

Figure 6-9 shows the plan view SEM image of two samples. The AX161A (Figure 6-9A), which was grown on the GaN-on-Sapphire template, exhibits a flat surface with some deep pits. In contrast, the upper surface of AX161B (Figure 6-9B) which was grown on Si template displays not only a low density of deep pits but also some shallow pits. Overall, the surface of AX161B (Si substrate) is observed to be more surface and edge irregular than that of AX161A (sapphire substrate).

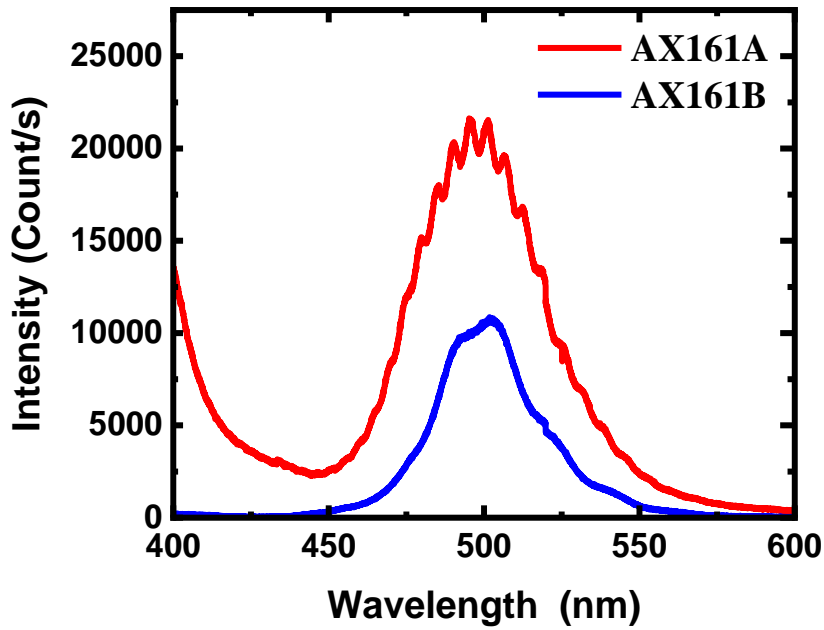


Figure 6-10 Standard RT-PL spectra of 5 μm μLEDs on sapphire template (AX161A) and the 5 μm μLEDs on silicon template (AX161B).

The standard RT-PL spectra of AX161A and AX161B are presented in Figure 6-10. It is evident that the PL intensity of AX161A is greater than that of AX161B, with both samples exhibiting an emission wavelength of approximately 500 nm.

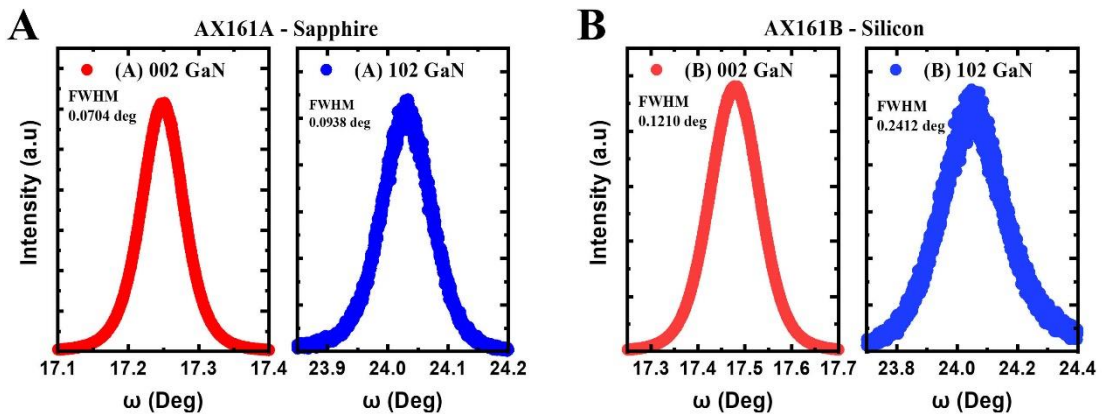


Figure 6-11 the XRD results of (A) AX161A - sapphire substrate, and (B) AX161B- silicon substrate with (002) GaN and (102) GaN.

Figure 6-11 illustrates the XRD results for the two samples, clearly showing the (002) GaN and (102) GaN reflections. For this two samples, the FWHM values of the GaN layer measured across

the (002) GaN reflection are 0.0704 degrees and 0.1210 degrees, respectively, while the FWHM values measured across the (102) GaN reflection are 0.0938 degrees and 0.2412 degrees, respectively. Based on obtained the FWHM values of (002) and (102) GaN, the screw dislocation density (D_{screw}) and edge dislocation density (D_{edge}) within the GaN layer can be determined as equation 5.1 and 5.2 [27, 28], form section 5.4.

Table 6-2 presents the FWHM values for the (002) and (102) GaN reflections, along with the corresponding calculated screw and edge dislocation densities for both samples.

Table 6-2 FWHM values and corresponding calculated screw and edge dislocation densities for the (002) and (102) GaN reflections in samples AX161A and AX161B.

Sample	Substrate	002 GaN FWHM (deg)	102 GaN FWHM (deg)	Screw Defects (cm^{-2})	Edge Defects (cm^{-2})
AX161A	Sapphire	0.0704	0.0938	1.3×10^8	6.1×10^8
AX161B	Silicon	0.1210	0.2412	3.8×10^8	4.4×10^9

Summary

As the findings presented in Chapter 5, the emission wavelength of c-plane LEDs grown on Si substrates is longer than that of those grown on sapphire substrates under identical conditions. This wavelength shift is primarily attributed to the differing stress statuses within the two kinds of templates, which affects indium incorporation in the InGaN layer, causing wavelength redshift. However, in the case of μ LEDs grown using the direct overgrowth approach, this wavelength shift between different substrate was not observed. It is assumed that the patterning process of the μ LEDs change the stress distribution within the template, resulting in similar levels of indium incorporation into MQWs on both substrates. This finding suggests that the patterning approach for μ LED overgrowth effectively mitigates the more pronounced stress effects observed in the growth of planar LEDs. Furthermore, the weaker emission intensity observed in μ LEDs on Si may be attributed to the lower crystal quality of the Si template compared to that of the sapphire template. The reduced quality of the GaN layer could result in an increase in defects that extend into subsequent epitaxial layers, ultimately leading to a decrease in the emission efficiency.

6.3.4 Effect of μ LED Dimensions on InGaN/GaN μ LEDs Grown on (111) Silicon

Among the various factors affecting the performance of μ LEDs, the dimensions of a single μ LED unit are one of the factors to be considered. Furthermore, as the demand of for μ LED applications continues to grow, the necessity for ultra-small μ LEDs is becoming increasingly apparent. The objective of this section is to investigate the effect of μ LED dimensions on InGaN/GaN MQWs grown on (111) Si. Specifically, the growth of μ LEDs may be affected by the physical dimensions (e.g., size, shape, and aspect ratio) of the μ LEDs. It is crucial to understand the relationship between μ LED dimensions and its growth status in order to optimise device performance and achieve the desired results in various applications. The findings of this study are expected to provide valuable insights into the design of ultra-small μ LEDs on (111) Si, thereby facilitating the widespread use and development of ultra-small μ LEDs on Si technology in the optoelectronics industry.

Experiment design

In this experiment, a 2-inch μ LED mask with three different dimensions (5 μm , 10 μm , and 20 μm) was designed, and a patterned template with three dimensions was fabricated from this mask based on the GaN-on-Si template. This design allows for the deposition of 5 μm , 10 μm and 20 μm μ LEDs on a single wafer under identical growth conditions. The cleaned patterned templates will be subjected to μ LED structure growth by MOCVD, the growth conditions used are identical to those described in Section 6.3.3. Figure 6-12 shows the schematic representation of a 2-inch μ LED patterned template with three different dimensions (5, 10 and 20 μm).

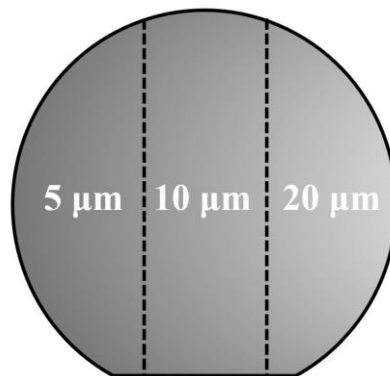


Figure 6-12 Schematic of a 2-inch μ LED patterned template (Si substrate) with three different dimensions.

Results and Discussion

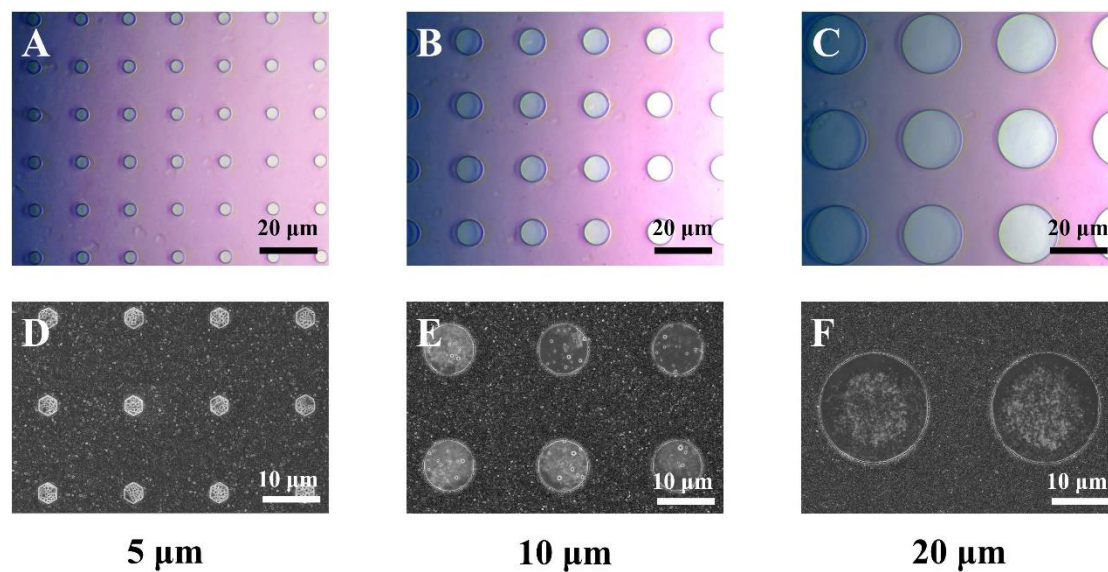


Figure 6-13 Optical images of the patterned template (Si substrate) with three different μ LED dimensions: (A) 5 μ m, (B) 10 μ m, and (C) 20 μ m, along with the corresponding SEM images after overgrowth: (D) 5 μ m, (E) 10 μ m, and (F) 20 μ m.

The optical images in Figure 6-13 illustrate the optical images of μ LED pattern templates with different dimensions (5 μ m, 10 μ m, and 20 μ m) and the corresponding SEM images of surface morphology after overgrowth. The images clearly show that a significant change in morphology occurs as the μ LED dimensions increase. The Figure 6-13D, E, and F illustrate the surface morphology of μ LEDs after MOVCD overgrowth on templates with different dimensions. The 5 μ m region displays a hexagonal structure after overgrowth, whereas the 10 μ m and 20 μ m regions retain their circular shape, consistent with the original template. Furthermore, all three dimensions of μ LEDs display a high density of pits on the surface, although this phenomenon appears to improve slightly as the μ LED dimension increases.

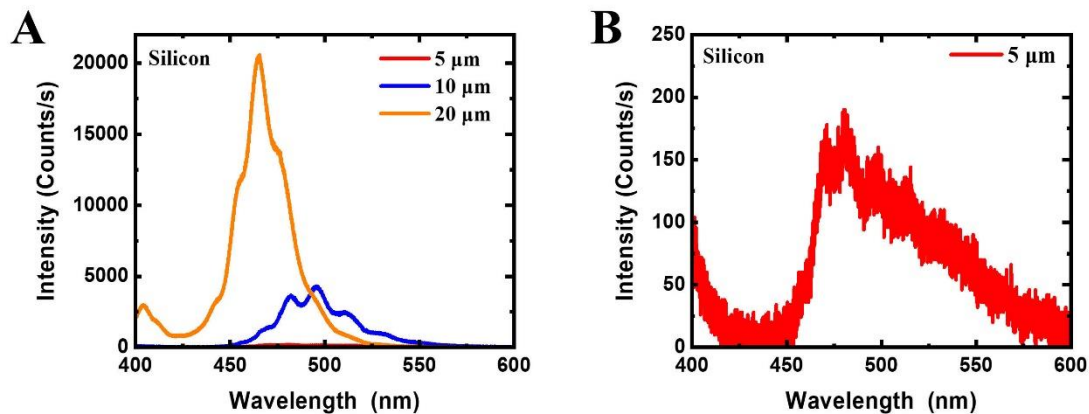


Figure 6-14 (A) RT-PL spectra of μ LEDs on Si templates with dimensions of 5 μ m, 10 μ m, and 20 μ m; and (B) a zoomed-in view of the PL spectrum for the 5 μ m μ LED.

The Figure 6-14A shows the PL spectra of three different μ LED dimensions. The spectrogram shows that the 5 μ m μ LEDs exhibit the lowest luminous intensity with a very weak peak. Figure 6-14B further zooms in on the spectrum of 5 μ m μ LED, revealing that its luminescence intensity is relatively weak, and its emission wavelengths are more broadly distributed. The emission intensity of the 10 μ m μ LEDs is significantly higher than that of the 5 μ m μ LEDs but lower than that of the 20 μ m μ LEDs. Furthermore, the 10 μ m μ LED also exhibits a broad emission spectrum, with the peak emission occurring at approximately 490 nm. The 20 μ m μ LEDs display the highest luminescence intensity and a significantly more concentrated emission spectrum than the other two μ LED dimensions, with an emission wavelength of approximately 475 nm.

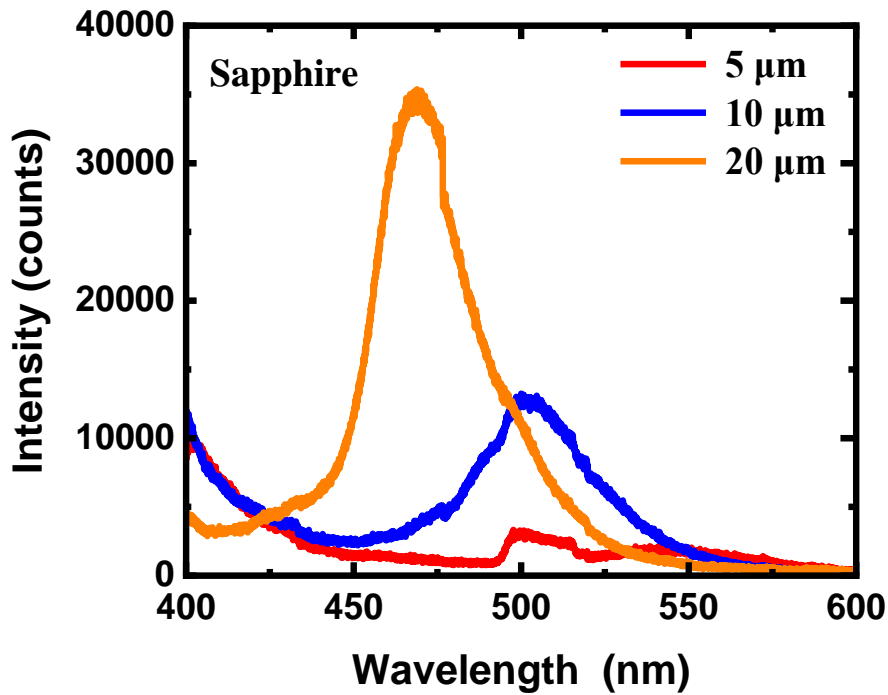


Figure 6-15 RT-PL spectra of μ LEDs on the control group (sapphire template) with dimensions of 5 μm , 10 μm , and 20 μm .

To investigate whether the wavelength shift observed on the Si template would similarly occur on the sapphire template, a control experiment was conducted using the identical mask and growth conditions on the sapphire template, followed by PL measurement. Figure 6-15 illustrates the PL spectra of the control experiment group on the sapphire. Similarly, a redshift phenomenon in the emission wavelength with decreasing μ LED dimension is also observed on the sapphire template.

Summary

In this section, a phenomenon was observed whereby μ LEDs grown on patterned templates using a direct overgrowth method exhibited a size-dependent shift in emission wavelength. Specifically, LEDs grown on dimensions of 5 μm , 10 μm , and 20 μm patterned templates demonstrated a redshift in emission wavelength as the template dimensions decreased. This effect is likely attributable to strain relaxation in the direct overgrowth process, which may result in leads to changes in the energy band structure and affect the emission wavelength.

6.3.5 Fill Factor Analysis of InGaN/GaN μ LEDs on Silicon

The fill factor (FF) represents a pivotal parameter in the fabrication of μ LEDs, defined as the ratio of all μ LED areas to the entire wafer area [29-31]. A higher fill factor may improve light output by increasing the active region, while a lower fill factor reduces wafer usage efficiency. However, the effect of fill factor on μ LED performance remains unclear, making it necessary to investigate any potential effects. It is hoped that this will provide a reference point for future μ LED fabrication and development. This study examines the influence of different fill factors on the optical properties and epitaxial growth of μ LEDs. The μ LED structures with different fill factors were deposited on patterned templates under the identical growth conditions. These samples were subsequently analysed to determine whether the fill factor exerts an influence on μ LEDs.

Experiment design

The fill factor is defined as the ratio of the area of all μ LEDs to the area of the entire wafer and can be calculated using the following equation:

$$\text{Fill Factor (FF)} = \frac{A_{\mu\text{LEDs}}}{A_{\text{Total}}} \times 100\% \quad (6.1)$$

Where $A_{\mu\text{LEDs}}$ represents the total area of all μ LEDs, whereas A_{Total} denotes the total area of the entire wafer or substrate.

In this experiment, two μ LED masks with different fill factors were designed and corresponding patterned templates were fabricated on GaN-on-Si templates using the designed mask. The dimensions of the μ LED unit in both masks are designed to be 5 μm in diameter and circular in shape, with the exception of the fill factor. The AX161B is a 5 μm μ LED on Si with a fill factor of 22.9%, while the AX161C is a 5 $\mu\text{m}/10 \mu\text{m}/20 \mu\text{m}$ μ LED on Si with a fill factor of 6.5% in the 5 μm area. Figure 6-16 shows the optical microscopy images of the two distinct patterned templates with a different fill factor.

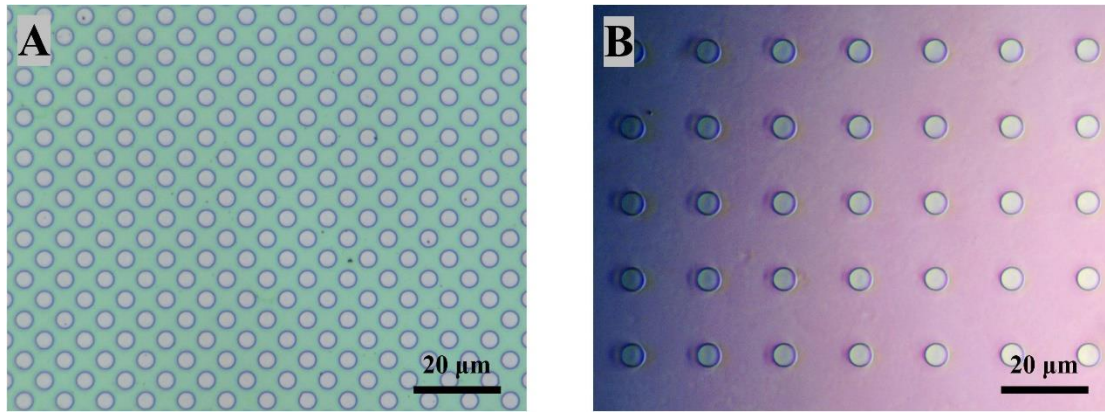


Figure 6-16 Optical microscopy images of the two μ LED patterned templates (before overgrowth) with different fill factor: (A) AX161B with fill factor of 22.9%; (B) AX161C with fill factor of 6.5%.

Table 6-3 The parameters of both μ LED patterned templates.

Sample	Substrate	Fill Factor (%)
AX161B	Si	22.9
AX161C	Si	6.5

Table 6-3 provides an overview of the parameters associated with both μ LED samples, including the substrate type and fill factor. In this case, the overgrowth recipe is the identical to that described in the previous section. The Si- doped n-GaN layer was deposited at 1270°C in a H₂ atmosphere in the first. Subsequently, the reactor temperature was reduced to 995°C, and the carrier gas was switched to N₂ to grow 30 pairs of InGaN/GaN superlattices. Following this, 5 pairs of InGaN quantum well and GaN quantum barrier were grown at temperatures of 905°C and 1040°C, respectively. Finally, the carrier gas was switched back to H₂, and the reactor temperature was raised to 1080°C for the growth of the p-GaN layer.

Results and Discussion

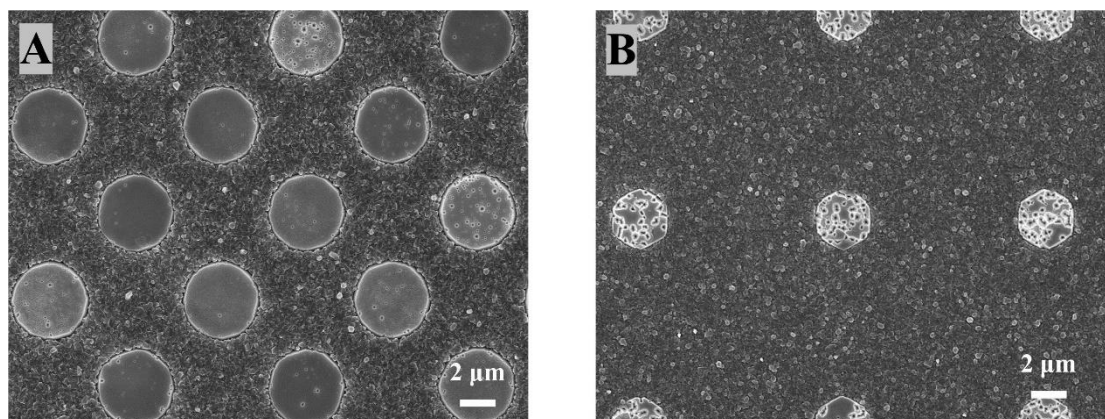


Figure 6-17 SEM top-view images of two μ LED samples (after overgrowth) with two fill factors: (A) AX161B with a fill factor of 22.9% and (B) AX161C with a fill factor of 6.5%.

Figure 6-17 presents the SEM top-view images of two samples after overgrowth. As shown in Figure 6-17A, AX161B, with a fill factor of 22.9%, displays a smooth surface, characterised by a relatively low density of deep pits, no significant morphological defects, and a well-defined circular contour. In contrast, AX161C (Figure 6-17B), with a fill factor of 6.9%, displays a hexagonal shape after overgrowth, with a relatively rough surface morphology and a higher density of deep pits.

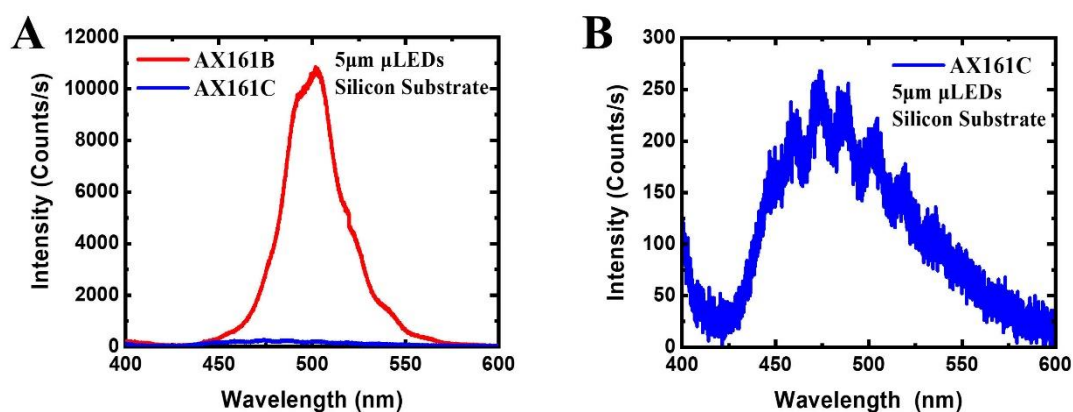


Figure 6-18 (A) RT-PL spectra of AX161B and AX161C; and (B) the zoomed-in PL spectrum of AX161C.

As illustrated in Figure 6-18, the RT-PL spectra presented a significant difference in emission intensity between the samples AX161B and AX161C. The spectrum demonstrates that AX161B exhibits a much higher emission intensity in comparison to AX161C, with the emission peak of AX161B is centred around 500 nm. The zoomed-in PL spectrum of AX161C further highlights the extremely weak emission intensity, with a broader and less defined peak.

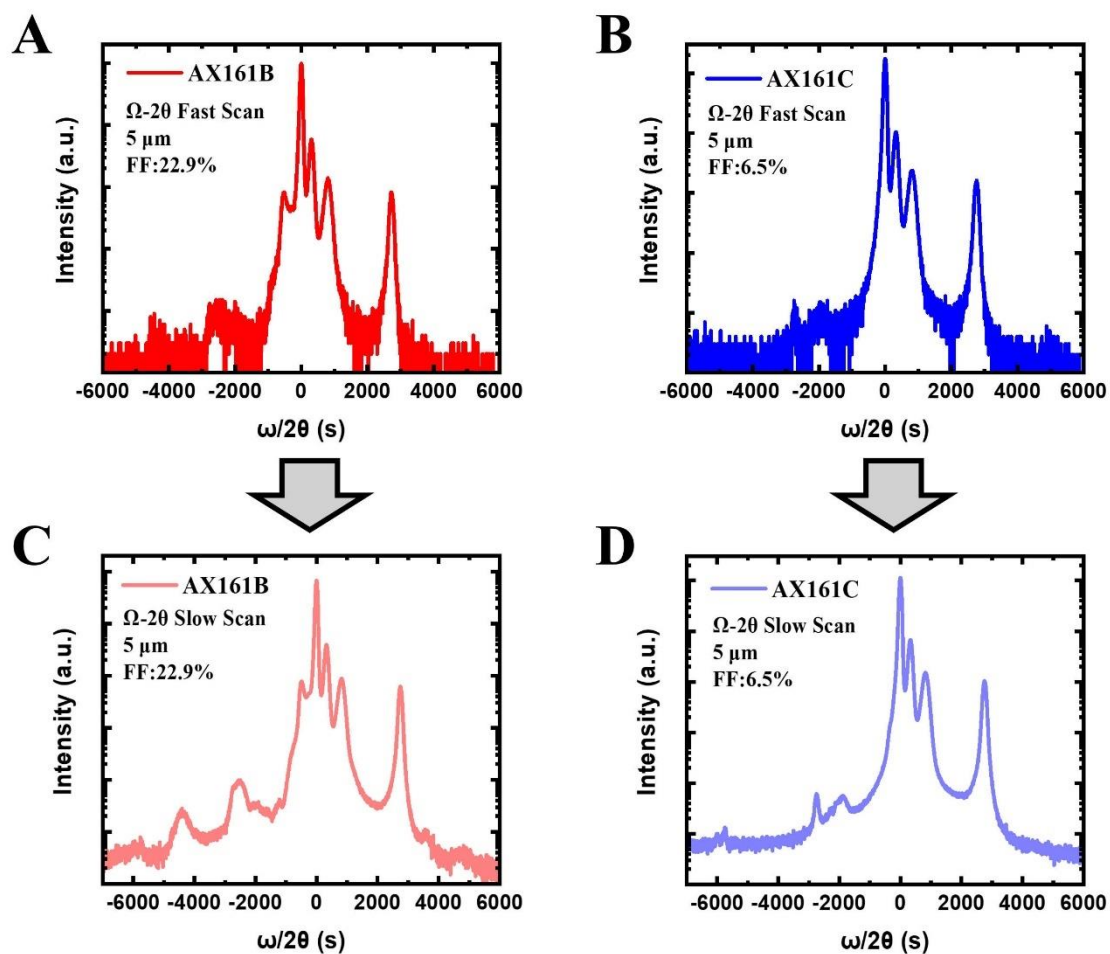
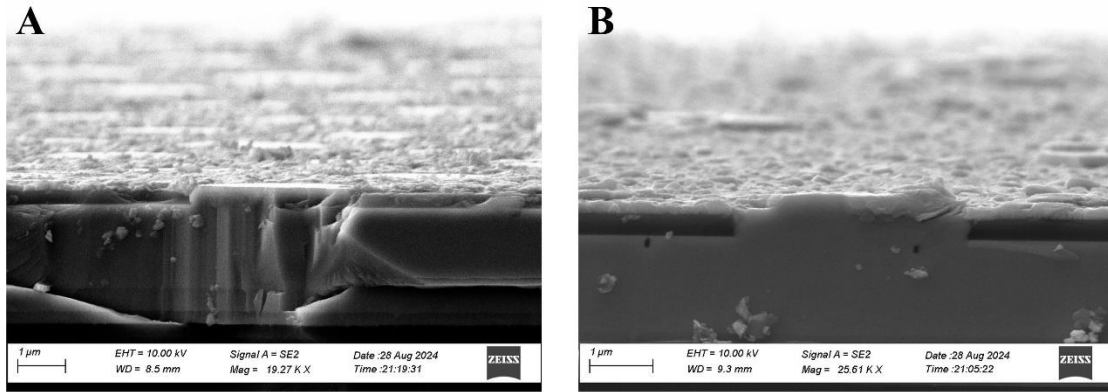


Figure 6-19 The XRD ω - 2θ spectra for samples AX161B and AX161C. (A) and (B) the fast scan of AX161B and AX161C; (C) and (D) the slow scan of AX161B and AX161C.

Figure 6-19 illustrate the XRD ω - 2θ spectra for both samples AX161B and AX161C. Figure 6-19A and B show the fast scan results for both samples, where AX161B displays some indistinct MQW and SL satellite peaks, while the image for AX161C is extremely blurred, with almost no visible satellite peaks. Therefore, in order to better observe the satellite peaks of both samples, the subsequent XRD ω - 2θ overnight slow scan (Figure 6-19C and D) was performed, the clear MQW and SL satellite peaks are observed for AX161B, whereas AX161C still lacks any distinct and regular satellite peaks for MQW and SL. This suggests that the growth in the 5 μm area with a 6.5% fill factor for AX161C was highly problematic, resulting in the undesirable deposition of the InGaN/GaN MQWs active region.



(A) AX161B 5 μ m μ LED

FF: 22.9%

(B) AX161C 5 μ m μ LED

FF: 6.5%

Figure 6-20 SEM cross-section images of (A) AX161B; FF: 22.9% and (B) AX161C; FF: 6.5%.

Figure 6-20 presents the SEM cross-section images of two samples. It is evident that the surface cross-section of AX161B is much flatter and shows no observable pits compared to AX161C. The surface of AX161C appears more uneven and slightly higher relative to AX161B, indicating that the growth rate of the two samples may exhibit differences. Combined with the SEM top-view images of the two samples (Figure 6-17), it can be concluded that the overgrowth status of the μ LEDs in the 5 μ m region of sample AX161C is less optimal.

Summary

The experiments revealed that even under identical growth conditions, different μ LED fill factors can have a significant impact on the growth of μ LED samples, leading to variations in surface defects. These phenomena may can be attributed to the influence of the μ LED pattern fill factor on the growth status within the overgrowth process. In particular, the sample with a lower fill factor demonstrates a decline in crystallinity and a high density of defects, which ultimately impact the optical performance of the μ LED samples. Furthermore, SEM cross-sectional images show that samples with lower fill factors exhibit more overgrowth, indicating a faster growth rate, which is closely associated with the increased presence of pits and defects.

6.4 Effect of H₂-Doped Quantum Barriers of InGaN/GaN μ LEDs on Patterned Templates

In the study of InGaN/GaN MQWs based LEDs, the design and optimisation of MQW structure represent a crucial aspect for the optical performance of the devices. The structure and growth environment of MQWs exert a profound influence on their optical properties and crystal quality. Optimisation of the optical properties of LEDs can be achieved by varying the number of MQWs pairs, the thickness of the layers, and the growth conditions [32-35]. During the MOCVD growth process, hydrogen (H₂) is commonly used as the ambient gas for GaN-based materials due to its ability to clean surfaces, promote the formation of smooth layers, suppress unfavourable surface reactions, and enhance atom mobility, all of which contribute to improved crystal quality of the GaN materials [36-38]. However, a significant drawback of hydrogen is its potential negative impact on the indium content in InGaN. H₂ gas readily combines with nitrogen atoms to form hydrides, leading to the volatilization or migration of indium, which in turn alters the composition of the quantum wells and affects their optical properties [38-40]. In contrast, nitrogen (N₂), as an inert gas, does not chemically react with the components of the quantum wells. In case of the growth of InGaN/GaN MQWs, nitrogen is more effective in preserving the integrity of the indium composition, minimizing the indium volatilization that can occur with hydrogen. It is therefore typically avoided that H₂ be used as the ambient gas in the growth of InGaN/GaN MQWs, and instead N₂ is employed as a safer alternative. However, a potential drawback of using a N₂ ambient is that it may reduce surface mobility rates, leading to increased interface roughness. This can result in non-uniformity at the QW/QB interfaces, thereby affecting carrier recombination efficiency. In recent years, H₂ doping ambient gases (N₂/H₂ mixer gases) has gained increasing attention in the growth of quantum barriers due to its ability to effectively regulate the quality of barrier layers and QW/QB interfaces, thereby enhancing the overall performance of MQWs [37, 39, 41-45].

This section will investigate the impact of utilising an H₂/N₂ mixed ambient during the growth of quantum barriers in InGaN/GaN MQWs-based μ LEDs on their optical performance, with a comparative analysis of the results on (0001) sapphire and (111) silicon substrates. This study compares the PL characteristics of μ LEDs with quantum barriers grown under different ambient

gases and evaluates their performance on various substrates. The objective is to elucidate the impact of H₂-doped quantum barriers on the optical properties and epitaxial quality of μ LEDs, as well as to explore the balance between H₂ and N₂ ambient gases. The findings aim to provide valuable insights for the future design of high efficiency μ LEDs

6.4.1 Impact of H₂-Doped Quantum Barriers on the Optical Properties of 5 μ m μ LEDs on Sapphire and Silicon

This study investigates the impact of H₂-doped quantum barriers on the optical properties of 5 μ m InGa_N/Ga_N μ LEDs grown on two different substrates: (0001) sapphire and (111) silicon. The optical properties of μ LEDs grown on the two substrates were compared by photoluminescence measurements, which were supplemented by a comprehensive XRD ω -2 θ scan to explore the layer parameters of the MQWs. The objective of this study is to elucidate how H₂-doped quantum barriers influence the growth of MQWs and their emission characteristics, and to ascertain whether there is a difference in these characteristics on different substrates.

Experiment design

Table 6-4 Overview of sample parameters, including substrate type, μ LED dimensions, QB growth ambient gas, and NH₃ flow rate.

Sample	Substrate	μ LED Dimensions (μ m)	Quantum Barriers Growth	
			Ambient Gas	NH ₃ Flow (sccm)
AX161A	Sapphire	5	N ₂	5840
AX161B	Silicon	5	N ₂	5840
AX162A	Sapphire	5	10% H ₂ /N ₂	5840
AX162B	Silicon	5	10% H ₂ /N ₂	5840

In this experiment, four samples were included: AX161A, AX161B, AX162A, and AX162B. Among them, the atmosphere gas used to grow QBs for AX161A and AX161B was N_2 , and both samples were grown on Sapphire and Si substrates, respectively. In contrast, the ambient gas employed for the growth of QBs for both AX162A and AX162B was a H_2/N_2 mixture containing 10% H_2 , and both samples were similarly grown on Sapphire and Si substrates, respectively. All samples were grown under consistent conditions, with the exception of the differing ambient gases employed during the QB growth. Table 6-4 presents the parameters of four samples, including the substrate type, μ LEDs dimensions, the ambient gas for QB growth, and the NH_3 flow rate.

Results and Discussion

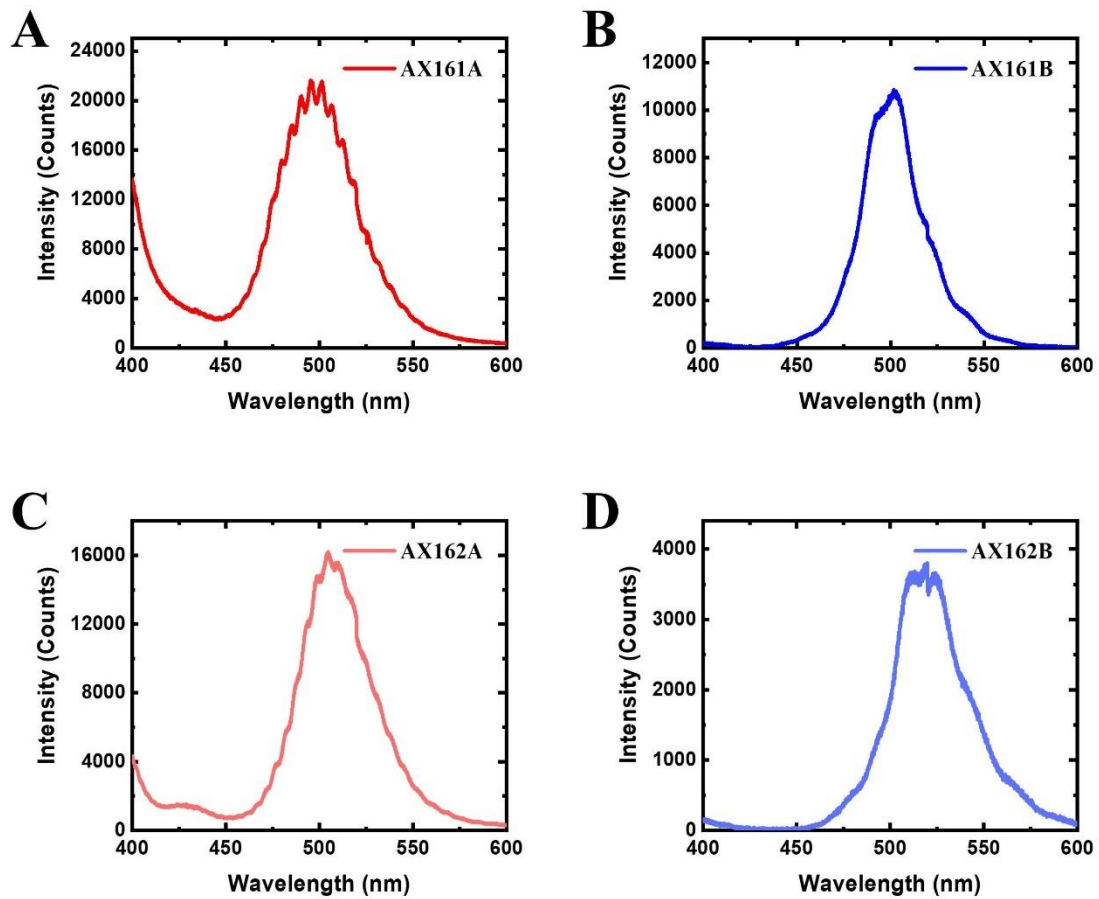


Figure 6-21 RT-PL spectra of (A) AX161A, (B) AX161B, (C) AX162A, and (D) AX162B μ LEDs with different QB growth conditions and substrates.

Figure 6-21 shows the RT-PL spectra of the four samples. It can be clearly observed that a significant redshift phenomenon occurs in the emission wavelength of the samples AX162A and AX162B which were grown QB layer with a H_2/N_2 mixture gas, in comparison to the samples AX161A and

AX161B, which were grown QB layer with N_2 ambient gas. Furthermore, a significant decrease in PL intensity was observed for the QB of samples grown with the H_2/N_2 mixture, exhibiting a value that was approximately half that observed for the QB grown with nitrogen exclusively.

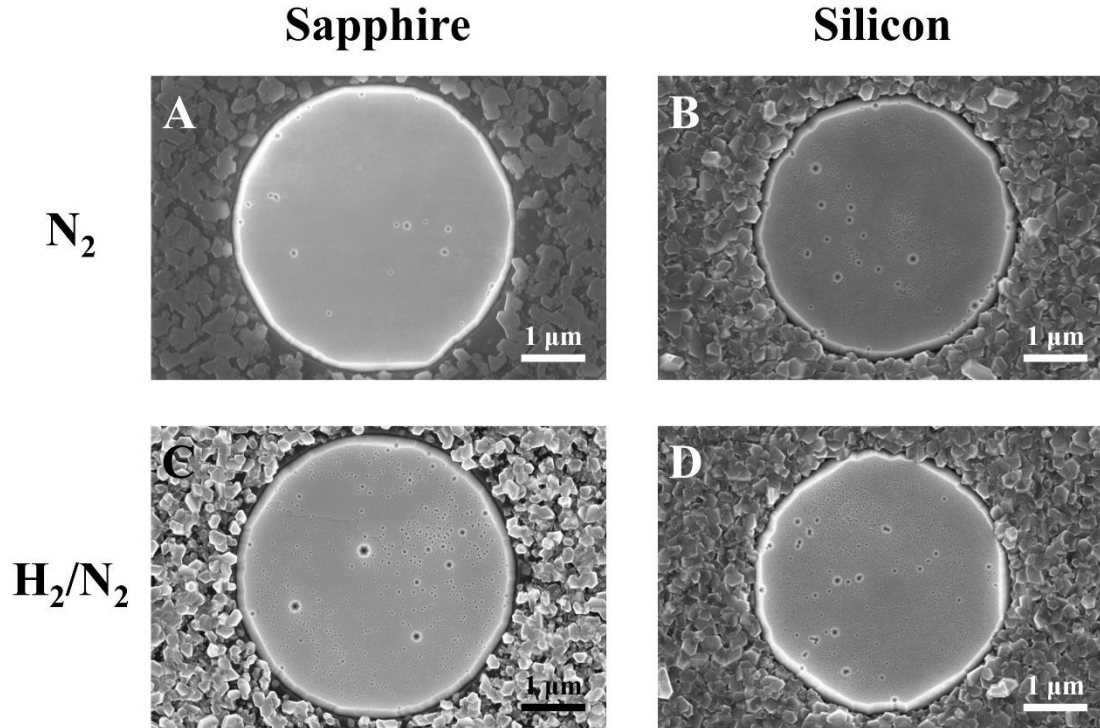


Figure 6-22 SEM top-view images of $5\mu\text{m}$ μLEDs with different substrates and quantum barrier growth conditions after overgrowth: (A) AX161A (sapphire, N_2), (B) AX161B (silicon, N_2), (C) AX162A (sapphire, H_2/N_2), and (D) AX162B (silicon, H_2/N_2).

The SEM images of the four samples presented in Figure 6-22 clearly demonstrate the existence of significant differences in surface morphology under different QB growth conditions. The samples that were grown QB layer in a H_2/N_2 gas mixture atmosphere (Figure 6-22C and D) exhibited a higher defect density compared to those grown in a N_2 atmosphere (Figure 6-22A and B). Additionally, the former μLED shape demonstrated less uniformity than the latter. The observed reduction in PL emission intensity and SEM images suggests that the introduction of H_2 into the QB growth may have resulted in the formation of additional defects or an increase in non-radiative recombination, thereby reducing the overall emission efficiency.

Summary

In this study, samples AX162A and AX162B, which were grown with H₂-doped QBs, exhibited a significant redshift in their PL spectra, accompanied by a decrease in intensity, in comparison to samples grown under N₂ ambient gas (AX161A and AX161B). Furthermore, SEM images revealed an increase in surface defects in the H₂-doped samples, suggesting that the introduction of H₂ during QB growth may have a detrimental impact on the surface quality and uniformity of μ LEDs, potentially leading to a decline in optical and electrical performance. In conclusion, while H₂-doped quantum barriers can induce a redshift in the emission wavelength of InGaN/GaN μ LEDs, it may also result in reduced emission intensity and compromised surface quality. Nevertheless, the controlled utilisation of H₂/N₂ mixed gases in the growth of MQWs represents a promising approach for developing longer-wavelength μ LEDs. Therefore, further optimisation of growth conditions is necessary to mitigate the adverse effects associated with the introduction of gas mixtures.

6.4.2 Impact of H₂-Doped Quantum Barriers on Optical Properties of InGaN/GaN μ LEDs on Silicon

In previous sections, the influence of different fill factors and μ LED unit dimensions on the optical properties of μ LEDs deposited using conventional MQWs growth method (MQWs growth under the N₂) has been investigated. The study demonstrated that under identical growth conditions, variations in fill factor can significantly influence the growth rate of μ LEDs. Furthermore, a correlation was observed between the PL emission wavelength of the μ LEDs and their dimensions. To further investigate whether fill factor and μ LED dimensions similarly affect μ LEDs grown with H₂-doped QBs, this section will conduct a comparative analysis of μ LEDs with varying fill factors and dimensions to elucidate their growth behaviour under H₂-doped QB conditions.

Experiment design

This section presents the design of two experimental groups, designated A and B, with the objective of investigating the effects of fill factor and μ LED dimensions on the optical properties of μ LEDs under H₂-doped QB conditions, and the results are also compared to the samples obtained from conventional MQWs growth method under an N₂ ambient. Group A consists of four samples:

AX161B, AX161C, AX162B, and AX162C, aimed at studying the influence of fill factor. Group B includes two samples: AX161C and AX162C, with the objective of examining the impact of μ LED dimensions. Among them, the QB growth conditions of the AX161 series was grown under an N₂ atmosphere, whereas the QB of the AX162 series was grown in a 10% H₂/N₂ mixed atmosphere. Furthermore, only the 5 μ m region of AX161C and AX162C was employed for comparison in the Group A. Table 6-5 provides an overview of the μ LED samples employed in each experimental group, accompanied by the respective parameters.

Table 6-5 Overview of μ LED Samples with Different Dimensions, Fill Factors and Quantum Barrier (QB) Growth Conditions on Silicon Substrates.

Group	Sample	Substrate	μLED Dimensions (μm)	Fill Factor (%)	QB Growth Ambient Gas
A	AX161B	Silicon	5	22.9	N ₂
	AX161C	Silicon	5	6.5	N ₂
	AX162B	Silicon	5	22.9	H ₂ /N ₂
	AX162C	Silicon	5	6.5	H ₂ /N ₂
B	AX161C	Silicon	5/10/20	6.5/13.9/29.9	N ₂
	AX162C	Silicon	5/10/20	6.5/13.9/29.9	H ₂ /N ₂

Results and Discussion

A. Investigation of Fill Factor in H₂-doped QB

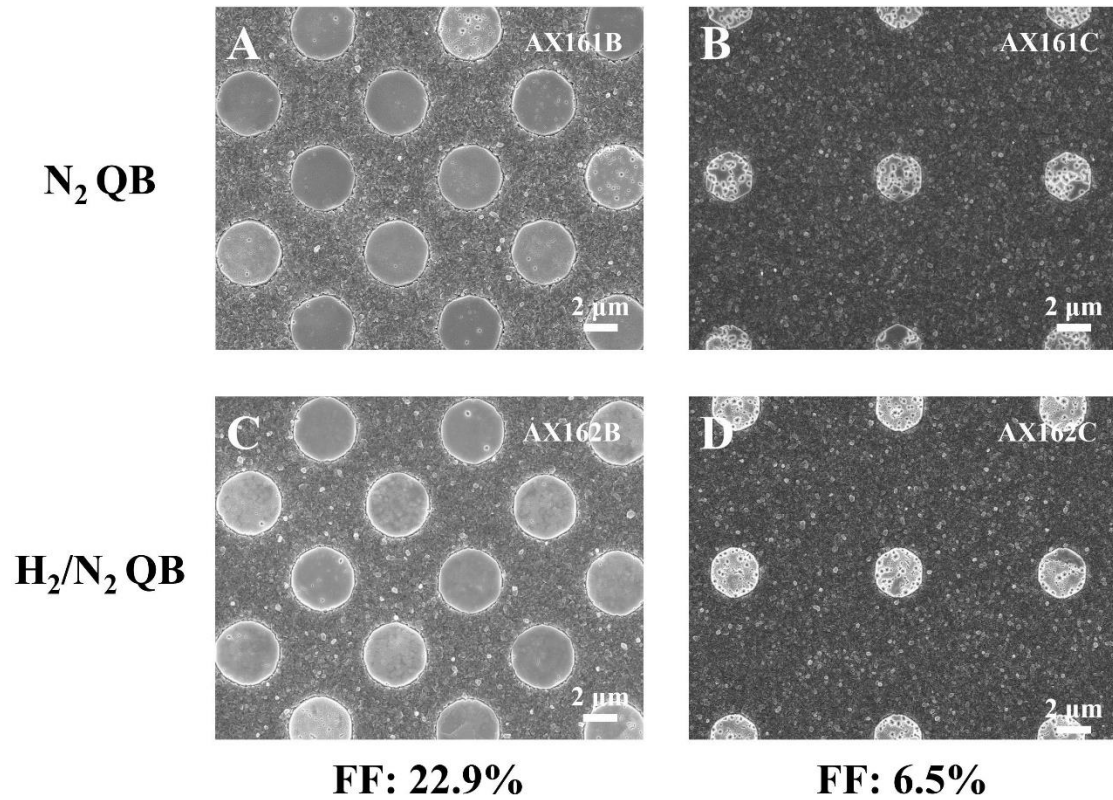


Figure 6-23 SEM images of μ LEDs grown on silicon substrates with different QB conditions and fill factors (FF): (A) AX161B (N₂, 22.9%), (B) AX161C (N₂, 6.5%), (C) AX162B (H₂/N₂, 22.9%), and (D) AX162C (H₂/N₂, 6.5%).

Figure 6-23 illustrates SEM images of μ LEDs grown on silicon substrates, which were prepared under different QB conditions and fill factors. In comparison to the N₂-grown QB samples (AX161B and AX161C), the H₂/N₂-grown QB samples (AX162B and AX162C) exhibited a more rougher surface morphology and a greater number of surface defects. Additionally, the μ LED unit shapes were observed to be more irregular, particularly in the samples with a lower fill factor.

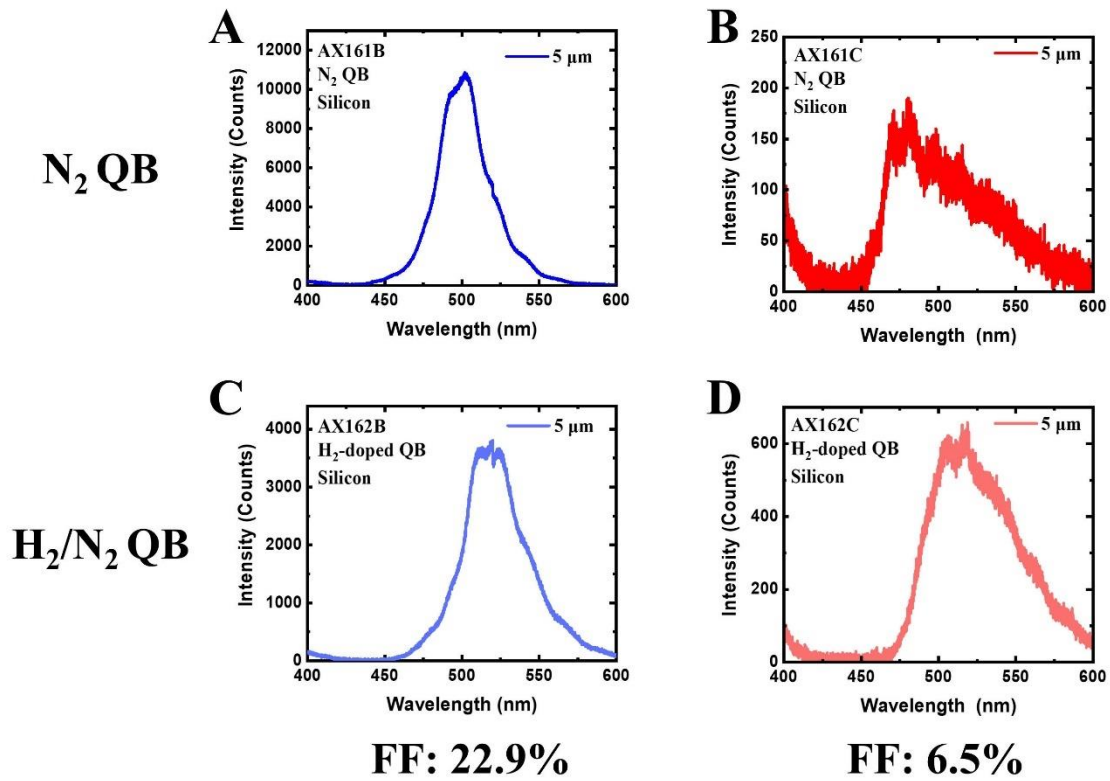


Figure 6-24 RT-PL spectra of μ LEDs grown on silicon substrates with different QB conditions and fill factors (FF): (A) AX161B (N_2 , 22.9%), (B) AX161C (N_2 , 6.5%), (C) AX162B (H_2/N_2 , 22.9%), and (D) AX162C (H_2/N_2 , 6.5%).

Figure 6-24 illustrates the corresponding RT-PL spectra of four samples that were grown under disparate quantum barrier conditions and fill factors. The PL spectra demonstrate that, in comparison to the samples AX161B and AX161C, which were grown with QBs in an N_2 atmosphere, the samples AX162B and AX162C, which were grown with QBs in an H_2/N_2 mixed atmosphere, exhibit a redshift in their emission peaks, with AX162B showing a significant decrease in emission intensity. Furthermore, upon visual inspection of the PL measurement, samples AX161C and AX162C exhibited emission of white light in the 5 μ m regions when excited by the laser source.

B. Investigation of μ LEDs Dimensions in H_2 -doped QB

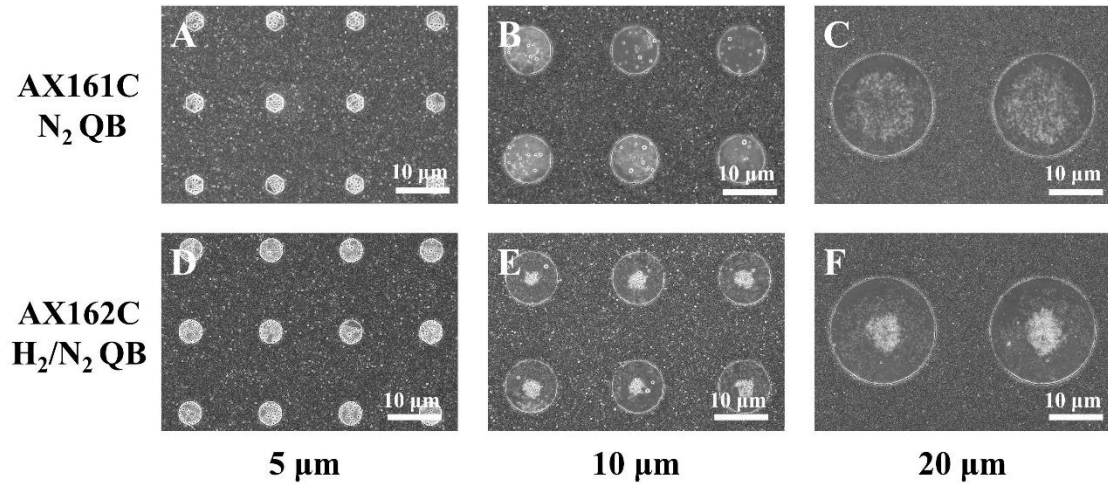


Figure 6-25 SEM images of μ LEDs with different dimensions ($5\ \mu\text{m}$, $10\ \mu\text{m}$, $20\ \mu\text{m}$) grown on silicon substrates under different QB conditions: (A-C) AX161C with N_2 QB, and (D-F) AX162C with H_2/N_2 QB.

Figure 6-25 presents SEM images of different dimension regions ($5\ \mu\text{m}$, $10\ \mu\text{m}$, $20\ \mu\text{m}$) for samples AX161C and AX162C. The SEM images reveal that both samples exhibit varying degrees of surface defects. Compared to sample AX161C, where the QB was grown in an N_2 atmosphere, the surface of sample AX162C with QB grown in a mixed H_2/N_2 atmosphere, exhibits a higher density of pits and defects, particularly within the central regions of the $10\ \mu\text{m}$ and $20\ \mu\text{m}$ μ LEDs.

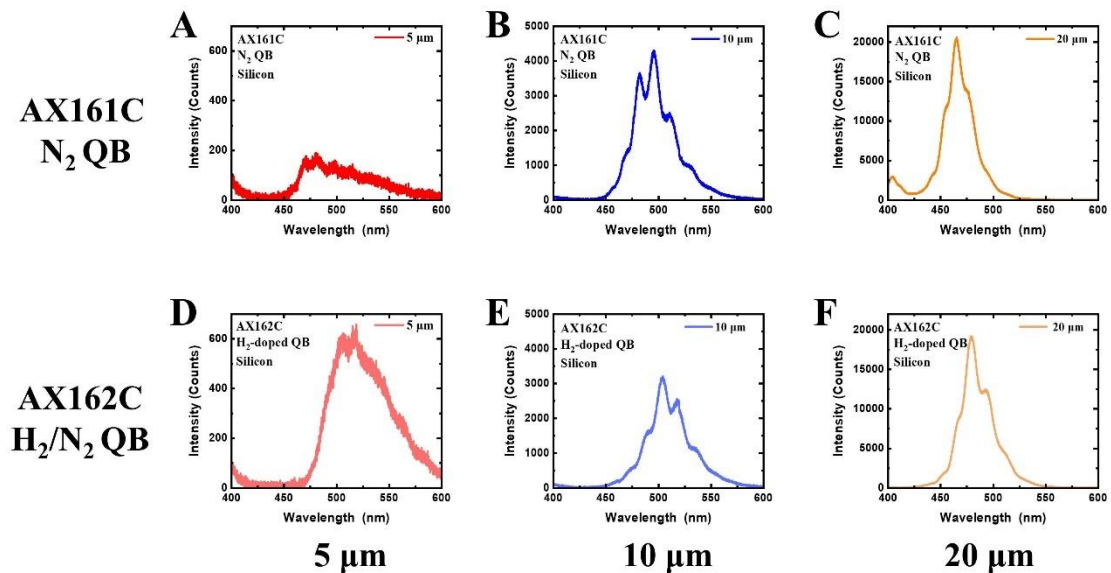


Figure 6-26 RT-PL spectra of μ LEDs with different dimensions ($5\ \mu\text{m}$, $10\ \mu\text{m}$, $20\ \mu\text{m}$) grown on silicon substrates under different QB conditions: (A-C) AX161C with N_2 QB, and (D-F) AX162C with H_2/N_2 QB.

Figure 6-26 shows the RT-PL spectra of μ LED samples grown under different quantum barrier conditions with different dimensions (5 μm , 10 μm , 20 μm). The PL spectra demonstrate that the luminescence intensity of the samples with QB layers grown in either an N_2 atmosphere (AX161C) and an H_2/N_2 mixed atmosphere (AX162C) increases with the μ LED dimensions. However, the samples grown under the H_2/N_2 mixed atmosphere exhibit a redshift in the emission peak and lower emission intensity in comparison to the samples grown under the N_2 atmosphere, and this phenomenon is particularly evident in the 20 μm μ LEDs.

Summary

This section presented an analysis of the effects of fill factor and μ LED size on the optical properties and surface topography of μ LEDs grown under different quantum barrier conditions on silicon substrate. The first part explored the effects of fill factor, while the second part focused on size-dependent effects. The results obtained from both parts were consistent with the observations from the previous section: μ LEDs with a higher fill factor exhibited fewer surface defects and better emission characteristics in comparison to samples with a lower fill factor, and larger μ LEDs demonstrated higher emission intensity and more defined emission peaks. However, samples grown under an H_2/N_2 mixed atmosphere showed a noticeable redshift in emission peaks and a reduction in emission intensity compared to those grown under an N_2 atmosphere. Additionally, the surfaces of samples grown in the H_2/N_2 mixed atmosphere exhibited a higher density of defects than those grown in an N_2 atmosphere.

It was observed that under our specified growth conditions, the H_2 -doped QB growth resulted in a redshift of the emission wavelength, but also led to a decrease in PL emission intensity. Therefore, while the H_2 -doped QB growth method shows potential for achieving longer-wavelength emitters, further optimisation of the growth conditions is necessary.

6.5 Conclusions

In this chapter, a direct epitaxial method was employed to grow μ LEDs on patterned templates, followed by a series of detailed studies. Unlike planar LEDs, the growth conditions for μ LEDs require more precise investigation and optimization. In Section 6.3, it was found that during the overgrowth process, the initial n-GaN layer effectively mitigated the degradation of optical performance caused by increased crystal defect density when μ LEDs were grown directly on patterned templates. Additionally, the growth of the final p-GaN layer also impacted the optical performance of μ LEDs. It was observed that faster p-GaN growth rates can reduce the overall growth time and decrease the risk of MQW thermal degradation, but it also results in a less smooth p-GaN surface with increased defects, potentially negatively affecting final device performance. Therefore, achieving a balance between high-quality, smooth p-GaN and minimizing MQW thermal degradation is crucial in μ LED growth.

Furthermore, a comparative study of μ LEDs grown under the same conditions on different substrates revealed that the PL emission wavelength of μ LEDs on both sapphire and silicon templates remained consistent, though the emission intensity of μ LEDs on silicon was lower than that on sapphire. This finding contrasts with the redshift observed in planar LEDs on silicon substrates in Chapter 5. This may be attributed to the patterning process of μ LEDs altering the stress distribution within the template, resulting in similar indium incorporation levels in the InGaN layers on both substrates. Additionally, the disparity in emission intensity is likely attributable to varying defect densities in the GaN layers grown on different substrates.

The study also examined the size-dependent effects of μ LEDs on silicon substrates, revealing that as the template size decreases, the emission wavelength undergoes a redshift. Finally, the impact of the fill factor on 5 μ m μ LEDs on silicon substrates was investigated. It was found that the template fill factor exerts a significant influence on the crystal quality of the samples. Therefore, selecting an appropriate template fill factor is critical for successful μ LED growth.

In Section 6.4, the study investigated the incorporation of H₂ into the QB growth and observed the resulting μ LED characteristics. It was found that samples grown with QB in with an H₂/N₂ mixed atmosphere exhibited a redshift in emission wavelength compared to those grown in an N₂

atmosphere, although the PL emission intensity decreased. Furthermore, the H₂-doped QB grown samples exhibited similar phenomena observed in the comparative studies in Section 6.3 (substrate, size-dependence, and fill factor effects). Therefore, although the utilization of an H₂/N₂ mixed atmosphere in QB growth demonstrates potential for achieving longer-wavelength emitters, further optimization is necessary.

Reference

- [1] L. Tzu-Yi *et al.*, "Technology and Applications of Micro-LEDs: Their Characteristics, Fabrication, Advancement, and Challenges," *ACS Photonics*, 0812 2022, doi: 10.1021/acsp Photonics.2c00285.
- [2] Z. Fan, J. Lin, and H. Jiang, "III-nitride micro-emitter arrays: development and applications," *Journal of Physics D: Applied Physics*, vol. 41, no. 9, p. 094001, 2008.
- [3] T. Wang, "Topical Review: Development of overgrown semi-polar GaN for high efficiency green/yellow emission," *Semiconductor Science and Technology*, vol. 31, no. 9, p. 093003, 2016.
- [4] J. Bai *et al.*, "A direct epitaxial approach to achieving ultrasmall and ultrabright InGaN micro light-emitting diodes (μ LEDs)," *ACS photonics*, vol. 7, no. 2, pp. 411-415, 2020.
- [5] M. Y. Soh *et al.*, "Design and characterization of micro-LED matrix display with heterogeneous integration of GaN and BCD technologies," *IEEE Transactions on Electron Devices*, vol. 66, no. 10, pp. 4221-4227, 2019.
- [6] Z. J. Liu, K. M. Wong, C. W. Keung, C. W. Tang, and K. M. Lau, "Monolithic LED microdisplay on active matrix substrate using flip-chip technology," *IEEE Journal of Selected Topics in Quantum Electronics*, vol. 15, no. 4, pp. 1298-1302, 2009.
- [7] F. Olivier, S. Tirano, L. Dupré, B. Aventurier, C. Llargeron, and F. Templier, "Influence of size-reduction on the performances of GaN-based micro-LEDs for display application," *Journal of Luminescence*, vol. 191, pp. 112-116, 2017.
- [8] M. S. Wong *et al.*, "High efficiency of III-nitride micro-light-emitting diodes by sidewall passivation using atomic layer deposition," *Optics express*, vol. 26, no. 16, pp. 21324-21331, 2018.
- [9] S. S. Konoplev, K. A. Bulashevich, and S. Y. Karpov, "From large-size to micro-LEDs: scaling trends revealed by modeling," *Physica Status Solidi (a)*, vol. 215, no. 10, p. 1700508, 2018.
- [10] J. M. Smith *et al.*, "Comparison of size-dependent characteristics of blue and green InGaN microLEDs down to 1 μ m in diameter," *Applied Physics Letters*, vol. 116, no. 7, 2020.
- [11] J. Park, W. Baek, D.-M. Geum, and S. Kim, "Understanding the sidewall passivation effects in AlGaInP/GaInP micro-LED," *Nanoscale research letters*, vol. 17, no. 1, p. 29, 2022.
- [12] Y. Cai, J. I. Hagggar, C. Zhu, P. Feng, J. Bai, and T. Wang, "Direct epitaxial approach to achieve a monolithic on-chip integration of a HEMT and a single micro-LED with a

- high-modulation bandwidth," *ACS applied electronic materials*, vol. 3, no. 1, pp. 445-450, 2021.
- [13] J. Bai *et al.*, "Ultrasmall, ultracompact and ultrahigh efficient InGaN micro light emitting diodes (μ LEDs) with narrow spectral line width," *ACS nano*, vol. 14, no. 6, pp. 6906-6911, 2020.
- [14] W. Lee, J. Limb, J.-H. Ryou, D. Yoo, T. Chung, and R. D. Dupuis, "Influence of growth temperature and growth rate of p-GaN layers on the characteristics of green light emitting diodes," *Journal of Electronic Materials*, vol. 35, pp. 587-591, 2006.
- [15] S. Li *et al.*, "Influence of growth rate in the early stage of high temperature GaN layer growth on quality of GaN films," *Journal of Crystal Growth*, vol. 310, no. 16, pp. 3722-3725, 2008.
- [16] D. Gogova, H. Larsson, R. Yakimova, Z. Zolnai, I. Ivanov, and B. Monemar, "Fast growth of high quality GaN," *Physica Status Solidi (a)*, vol. 200, no. 1, pp. 13-17, 2003.
- [17] S. Kim, K. Lee, K. Park, and C.-S. Kim, "Effects of barrier growth temperature on the properties of InGaN/GaN multi-quantum wells," *Journal of Crystal Growth*, vol. 247, no. 1-2, pp. 62-68, 2003.
- [18] G. Zhang *et al.*, "InGaN/GaN MQW high brightness LED grown by MOCVD," *Optical Materials*, vol. 23, no. 1-2, pp. 183-186, 2003.
- [19] C. Huh and S.-J. Park, "Effects of temperature on InGaN/GaN LEDs with different MQW structures," *Electrochemical and solid-state letters*, vol. 7, no. 11, p. G266, 2004.
- [20] C. Huh, W. J. Schaff, L. F. Eastman, and S.-J. Park, "Temperature dependence of performance of InGaN/GaN MQW LEDs with different indium compositions," *IEEE Electron Device Letters*, vol. 25, no. 2, pp. 61-63, 2004.
- [21] V. Hoffmann *et al.*, "Influence of MOVPE growth temperature on the structural and optical properties of InGaN MQW laser diodes," *Journal of Crystal Growth*, vol. 310, no. 21, pp. 4525-4530, 2008.
- [22] T. Hikosaka, T. Shioda, Y. Harada, K. Tachibana, N. Sugiyama, and S. y. Nunoue, "Impact of InGaN growth conditions on structural stability under high temperature process in InGaN/GaN multiple quantum wells," *Physica Status Solidi c*, vol. 8, no. 7-8, pp. 2016-2018, 2011.
- [23] D. Hwang, *Epitaxial Growth, Nanofabrication, and Mass Transfer of InGaN Micro-LEDs for Displays*. University of California, Santa Barbara, 2018.
- [24] R.-H. Horng *et al.*, "Study on the effect of size on InGaN red micro-LEDs," *Scientific Reports*, vol. 12, no. 1, p. 1324, 2022.

- [25] P. Li, "Micro-LEDs with MOCVD-grown tunnel junctions and properties of efficient InGaN red Micro-LEDs," PhD Thesis, University of California, Santa Barbara, 2022.
- [26] Y. Zhang, R. Xu, Q. Kang, X. Zhang, and Z.-h. Zhang, "Recent advances on gan-based micro-leds," *Micromachines*, vol. 14, no. 5, p. 991, 2023.
- [27] H.-P. Lee, J. Perozek, L. Rosario, and C. Bayram, "Investigation of AlGaIn/GaN high electron mobility transistor structures on 200-mm silicon (111) substrates employing different buffer layer configurations," *Scientific Reports*, vol. 6, no. 1, p. 37588, 2016.
- [28] T. Metzger *et al.*, "Defect structure of epitaxial GaN films determined by transmission electron microscopy and triple-axis X-ray diffractometry," *Philosophical Magazine A*, vol. 77, no. 4, pp. 1013-1025, 1998.
- [29] O. Kayser, R. Westphalen, B. Opitz, and P. Balk, "Control of selective area growth of InP," *Journal of Crystal Growth*, vol. 112, no. 1, pp. 111-122, 1991.
- [30] H. Marchand *et al.*, "Mechanisms of lateral epitaxial overgrowth of gallium nitride by metalorganic chemical vapor deposition," *Journal of Crystal Growth*, vol. 195, no. 1-4, pp. 328-332, 1998.
- [31] M. E. Coltrin and C. C. Mitchell, "Mass transport and kinetic limitations in MOCVD selective-area growth," *Journal of Crystal Growth*, vol. 254, no. 1-2, pp. 35-45, 2003.
- [32] S.-J. Chang, W.-C. Lai, Y.-K. Su, J.-F. Chen, C.-H. Liu, and U. Liaw, "InGaIn-GaN multiquantum-well blue and green light-emitting diodes," *IEEE Journal of Selected Topics in Quantum Electronics*, vol. 8, no. 2, pp. 278-283, 2002.
- [33] A. Laubsch, M. Sabathil, J. Baur, M. Peter, and B. Hahn, "High-power and high-efficiency InGaIn-based light emitters," *IEEE Transactions on Electron Devices*, vol. 57, no. 1, pp. 79-87, 2009.
- [34] J. Pereiro *et al.*, "Optimization of InGaIn-GaN MQW photodetector structures for high-responsivity performance," *IEEE Journal of Quantum Electronics*, vol. 45, no. 6, pp. 617-622, 2009.
- [35] K. Meel, P. Mahala, and S. Singh, "Design and fabrication of multi quantum well based GaIn/InGaIn blue LED," in *IOP Conference Series: Materials Science and Engineering*, 2018, vol. 331, no. 1: IOP Publishing, p. 012008.
- [36] Y. Cho *et al.*, "Effect of carrier gas on GaIn epilayer characteristics," *Physica Status Solidi c*, vol. 3, no. 6, pp. 1408-1411, 2006.
- [37] R. Czernecki *et al.*, "Effect of hydrogen during growth of quantum barriers on the properties of InGaIn quantum wells," *Journal of Crystal Growth*, vol. 414, pp. 38-41, 2015.

- [38] X. Zhou *et al.*, "Surface morphology evolution mechanisms of InGaN/GaN multiple quantum wells with mixture N 2/H 2-grown GaN barrier," *Nanoscale Research Letters*, vol. 12, pp. 1-8, 2017.
- [39] Y. Zhu *et al.*, "Effect of hydrogen treatment temperature on the properties of InGaN/GaN multiple quantum wells," *Nanoscale Research Letters*, vol. 12, pp. 1-7, 2017.
- [40] W. Lv, L. Wang, J. Wang, Z. Hao, and Y. Luo, "InGaN/GaN multilayer quantum dots yellow-green light-emitting diode with optimized GaN barriers," *Nanoscale Research Letters*, vol. 7, pp. 1-8, 2012.
- [41] C. G. Van De Walle and J. Neugebauer, "Hydrogen in semiconductors," *Annual Review of Materials Research*, vol. 36, no. 1, pp. 179-198, 2006, doi: 10.1146/annurev.matsci.36.010705.155428.
- [42] H. Ekinci, V. V. Kuryatkov, C. Forgey, A. Dabiran, R. Jorgenson, and S. A. Nikishin, "Properties of InGaN/GaN MQW LEDs grown by MOCVD with and without hydrogen carrier gas," *Vacuum*, vol. 148, pp. 168-172, 2018.
- [43] Y.-T. Moon *et al.*, "Effects of thermal and hydrogen treatment on indium segregation in InGaN/GaN multiple quantum wells," *Journal of Applied Physics*, vol. 89, no. 11, pp. 6514-6518, 2001.
- [44] S. Suihkonen, O. Svensk, T. Lang, H. Lipsanen, M. Odnoblyudov, and V. Bougrov, "The effect of InGaN/GaN MQW hydrogen treatment and threading dislocation optimization on GaN LED efficiency," *Journal of Crystal Growth*, vol. 298, pp. 740-743, 2007.
- [45] Y. Hou, F. Liang, D. Zhao, P. Chen, J. Yang, and Z. Liu, "Role of hydrogen treatment during the material growth in improving the photoluminescence properties of InGaN/GaN multiple quantum wells," *Journal of Alloys and Compounds*, vol. 874, p. 159851, 2021.

Chapter 7 Conclusions and Future Work

This chapter presents a summary of the main findings and achievements of this thesis, highlighting the contributions made to the fields of GaN on Si and μ LED technology. Furthermore, it outlines potential avenues for future work, suggesting strategies to further enhance the performance of the developed GaN-based technologies.

7.1 Conclusions

This thesis investigates and optimises the growth process for c-plane GaN on (111) Si substrates, achieving crack-free and high-quality GaN on Si. Next, the optical properties of planar InGaN/GaN MQWs on Si and sapphire substrates were compared, and a basic AlGaIn/GaN HEMT structure was also fabricated on a Si substrate. Furthermore, the growth of μ LEDs on silicon substrates using a novel selective epitaxy technique was demonstrated, and key growth factors were analysed. Finally, the growth of QBs under a mixed H_2/N_2 ambient gases was investigated, revealing that the μ LEDs grown with this gas mixture exhibited a red-shift in wavelength compared to those grown under the original N_2 atmosphere. The presented studies lay the foundation and provide valuable insights for future research on epitaxially integrated miniature full-colour microdisplay on silicon substrates.

7.1.1 Optimisation of GaN Growth on Silicon

Through the step-by-step optimisation of the GaN growth process on (111) Si, a high-quality, crack-free GaN-on-Si standardized template has been successfully developed, providing a solid foundation for the subsequent overgrowth of devices. By utilizing direct high-temperature annealing instead of chemical pre-treatment for Si substrate preparation, the process has been simplified while maintaining comparable levels of surface cleanliness. Subsequently, the optimised AlN growth process has led to AlN layers with enhanced crystalline quality, which in turn provides a strong base for subsequent epitaxial layers and effectively prevents melt-back etching. Furthermore, through the study of the single AlGaIn buffer layer, a specific single AlGaIn buffer layer was developed, which simplified the buffer growth process and enabling crack-free GaN growth. Finally, the growth of the GaN layer was investigated, leading to the successful formation of a high-quality and smooth GaN layer, with the GaN-1 layer playing a crucial role in the overall GaN growth.

7.1.2 Comparative Study of Optical and Electrical Devices on Sapphire and Silicon

This study presents a comparative analysis of planar InGaN/GaN MQW-based LEDs grown on sapphire and (111) Si substrates under identical growth conditions. It was found that the PL emission wavelength of MQWs grown on GaN-on-Si templates was significantly longer than that of MQWs grown on GaN-on-sapphire templates. Additionally, the corresponding XRD ω -2 θ measurements and simulated fitting curves confirmed that, under the same growth conditions, the InGaN/GaN MQWs on the GaN-on-Si templates exhibited a higher indium content and faster growth rates compared to those on the GaN-on-sapphire templates. This phenomenon can be attributed to the internal tensile strain within the GaN-on-Si templates, which has a beneficial effect on the incorporation of indium into the InGaN/GaN layers. Furthermore, this study also investigated the influence of utilising NH₃ instead of N₂ as the ambient gas during the final cooling phase on the optical characteristics of the resulting InGaN/GaN MQWs. The results indicated that InGaN/GaN MQWs grown on GaN-on-Si templates under N₂ cooling conditions exhibited a longer emission wavelengths than MQWs cooled in a NH₃ atmosphere. These findings provide a valuable information for further development of long-wavelength LEDs on Si substrates.

Furthermore, this section presents the fabrication and characterisation of a HEMT device using an AlGaIn/GaN structure grown on (111) Si. The cross-sectional SEM image revealed that the epitaxial layers of the sample exhibited well-defined growth interfaces. However, the overall crystal quality was poor with a high density of dislocations as determined by the XRD rocking curve and ECCI image. This high dislocation density is likely a significant factor contributing to the subpar performance of the fabricated HEMT, as the defects in the epitaxial layers significantly impacted the functionality of the device.

7.1.3 Comparative Study of μ LEDs on Sapphire and Silicon by Direct Epitaxial Approach

This study introduced and employed a direct epitaxial overgrowth method for the growth of μ LEDs on patterned templates, followed by a comprehensive analysis of the key factors influencing the

growth of μ LEDs. The study revealed that the initial n-GaN layer plays a crucial role in mitigating optical performance degradation caused by increased defect density during μ LED growth on patterned templates. The growth rate of the final p-GaN layer also exerts a significant influence on the optical performance. While a faster growth rate can mitigate MQW thermal degradation, it results in a less smooth surface with more defects, which may potentially affect device performance. Therefore, balancing high-quality, smooth p-GaN with minimisation of MQW thermal degradation is essential. A comparative study demonstrated that μ LEDs grown on sapphire and silicon under identical conditions exhibited consistent PL emission wavelengths, which differed from the redshift observed in planar LEDs on Si substrates in comparison with planar LEDs on sapphire. However, the emission intensity on silicon was lower, which was likely due to differences in defect density. The study also demonstrated that a reduction in μ LED size resulted in a redshift in emission wavelength. Furthermore, a reduced fill factor in 5 μ m μ LEDs led to faster growth rates and lower quality of the crystal form, thereby showing the importance of an appropriate template fill factor. The studies also investigated the H₂ incorporation into QB growth, revealing that samples with QB grown in an H₂/N₂ mixed atmosphere exhibited a redshift in emission wavelength but decreased PL intensity compared to those grown in N₂. Furthermore, similar substrate, size-dependence, and fill factor effects were observed in this case of growth of QB under mixed gases. While H₂/N₂ in QB growth shows potential for longer-wavelength emitters, further optimisation is needed.

7.2 Future Work

This section presents potential directions for future research and development, based on the findings of the present study. Although considerable advancement has been made in the growth of GaN on Si and μ LEDs, further investigation is still necessary. This section proposes future exploration based on the findings of this thesis, including the continued optimisation of GaN quality, optimisation of HEMT performance on Si substrate, exploration of monolithic integration of HEMTs and μ LEDs, and further study of the effects of growth ambient gases on MQWs. These efforts aim to push the boundaries of current technology and pave the way for next-generation μ LED applications.

7.2.1 Enhance Quality of GaN on (111) Si

Although crack-free GaN layers have been successfully grown on (111) Si substrates, the crystal quality still lower than that of GaN grown on sapphire substrates. Our research group has achieved a (002) GaN quality of approximately 248 arcsec (0.069 degrees) on sapphire, but the quality of GaN on Si substrates ranges between 432 arcsec and 612 arcsec (0.12 degrees to 0.17 degrees). This indicates that there is still significant room for improvement in the crystal quality of GaN on Si. Specifically, the quality of the AlN layer can be further optimised to improve the crystal interface, thereby providing a better foundation for the nucleation of subsequent growth layers. Additionally, further improvement of the GaN-1 layer can contribute to enhancing the overall quality of the GaN layer. Therefore, the future research will focus on optimising the growth temperature and V/III ratio of the AlN and GaN-1 layers.

7.2.2 Integration of μ LEDs and HEMTs on Silicon Substrate

To further enhance the performance of HEMTs on Si substrate, it is crucial to optimise the structure and growth conditions, with a focus on improving the quality of the epi-layer and reducing the density of defects. Furthermore, the integration of HEMTs and μ LEDs on a single chip could be explored. This process would begin by the deposition of the AlGaIn/GaN HEMT structure on a Si substrate, followed by the patterning of the HEMT template. Subsequently, a directly epitaxial growth would be employed to grow the μ LED structure on this pre-patterned HEMT template. Finally, the obtained samples would undergo fabrication processing to complete the integration.

7.2.3 Selective Epitaxy of μ LEDs on Patterned Templates

The fill factor of the pre-patterned template has a significant impact on μ LED growth, and further research is needed to determine the optimal fill factor for direct overgrowth of μ LEDs using pre-patterned templates. Given the small size of μ LEDs, it is crucial to fine-tune the growth conditions with greater precision. This could include adjusting the growth temperature and V/III ratio of the MQWs active region to enhance indium incorporation to achieving the longer emission wavelength. Furthermore, the dimensions of the μ LED units on the pre-patterned template could be further reduced, exploring the potential for the development of even smaller μ LEDs, potentially down to 1 μm in dimensions or even smaller. This would pave the way for the achievement of higher-resolution microdisplays.

7.2.4 H₂-Dope MQWs Growth Method

The utilisation of an H₂/N₂ mixed gas atmosphere for QB growth in μ LEDs has been shown to influence the emission wavelength. However, further in-depth studies are required to fully understand its effects. Further research could explore various aspects, such as the optimal mixing ratio of H₂/N₂ and different incorporation methods, for example the introduction of the H₂ can be pulsed-mode. Furthermore, the additional characterisation method could provide valuable insights, such as the SEM cross-section analysis, which could provide layer interface information of samples. Moreover, a transmission electron microscope (XTEM) can be used to gain a deeper understanding of the actual growth status within the structure. Finally, investigating the impact of using mixed gases in the growth of the QW layer on the overall emission performance could offer useful information for the further development of μ LEDs.